Experimental Study of Strongly Correlated Fermion Systems under Extreme Conditions: Two-Dimensional ^{3}He at Ultra-Low Temperatures and Graphite in the Magnetic Ultra-Quantum Limit

Frank Arnold

Royal Holloway,

University of London

A dissertation submitted to the University of London

for the degree of Doctor of Philosophy

March 2015

Declaration of Authorship

I, Frank Arnold, hereby declare that this thesis and the work presented in it is entirely my own. Where I have consulted the work of others, this is always clearly stated.

Signed: _____

Date: _____

Abstract

This work explores both the effect of strong correlations in two-dimensional fermion systems, using ^{3}He films on graphite at ultra-low temperatures as a model system, and the correlation induced phases of graphite in the magnetic ultra-quantum limit.

Two-dimensional ^{3}He is a strongly correlated Fermi system that undergoes a Mott transition from an isotropic neutral Landau Fermi liquid at low densities into a magnetically frustrated solid on a triangular lattice. The magnetisation, frequency shift and spin dynamics of a series of ^{3}He samples across the phase diagram were measured using pulsed low-frequency SQUID-NMR down to 200 μK. On increasing the density approaching the Mott transition the effective mass of the ^{3}He quasi-particles diverges. At the lowest temperatures the Mott insulator is preceded by an intervening phase, the nature of which is discussed. The Mott insulator is a highly frustrated quantum magnet, which shows a Fermi liquid-like magnetisation down to lowest temperatures, and other features, which support the formation of a gapless quantum-spin liquid.

In the second part of this thesis it will be shown how magnetic fields applied along the crystallographic c-axis of graphite influence its underlying band structure, incorporating electronic correlations. The quasi-one dimensional dispersion of the Landau levels gives rise to the formation of a series of charge-density waves below 10 K and above 30 T. Pulsed magnetic field magneto-transport experiments have been performed up to 60 T. These show the onset, commensuration and collapse of these charge-density wave states. The observations, in conjunction with theoretical calculations, conclusively identify these states.

Contents

1 Introduction **1**

2 Theory of Two-Dimensional Fermion Systems **8**

2.1 The Theory of Fermi Liquids 8

2.1.1 The Non-Interacting Fermi Gas 8

2.1.2 The Interacting Landau-Fermi Liquid 10

2.2 Band Theory 15

2.2.1 The Quasi-Free Fermion Model 15

2.2.2 The Tight-Binding Model 18

2.2.3 The Slonczewski-Weiss-McClure Model of Graphite 21

2.2.4 Fermi Surface Nesting Instabilities 24

2.2.5 The Hubbard model 28

2.3 The Magnetism of the Mott Insulator 33

2.3.1 Antiferromagnetism and Geometrical Frustration 33

2.3.2 Multiple Spin Exchange 34

2.3.3 High Temperature Series Expansion 36

2.3.4 Quantum Spin Liquids 37

2.4 Nuclear Magnetic Resonance 40

2.4.1 Spins in a Magnetic Field 40

2.4.2 Microscopic Origin of the Relaxation Times 43

2.4.3 Pulsed NMR and Relaxation Time Measurements 45

3 Experimental Methods **52**

3.1 Cryogenic Refrigerators 52

3.2 Helium Dilution Refrigerators 54

3.3 Adiabatic Nuclear Demagnetisation Cooling 59

3.4 Thermometry . . . 68
3.4.1 Resistive Thermometry . . . 68
3.4.2 ^{3}He Melting Curve Thermometers . . . 70
3.4.3 NMR Thermometers . . . 72
3.4.4 Johnson-Noise Thermometry . . . 73
3.5 SQUID NMR . . . 77
3.5.1 NMR at Ultra-low Temperatures . . . 77
3.5.2 SQUIDs . . . 79
3.5.3 The SQUID-NMR Setup . . . 83
3.6 ^{13}C NMR and Ultra-Low Temperature Thermometry . . . 90

4 The Metal-Insulator Transition in Two-Dimensional ^{3}He 103
4.1 Sample Preparation . . . 103
4.2 Pulsed NMR Measurements and Results . . . 108
4.2.1 Magnetisation . . . 113
4.2.2 Frequency Shifts . . . 115
4.2.3 Transverse Relaxation Times . . . 118
4.3 The Metal-Insulator Transition . . . 128
4.3.1 The Curie-Weiss Plus Fermi Fluid Model . . . 130
4.3.2 The Three Fermi Fluids Model . . . 133
4.3.3 Effective Mass Enhancement in the Fluid . . . 137
4.3.4 Fluid-Solid Cross-Over . . . 142
4.3.5 Microscopic Interpretation of the Metal-Insulator Transition - The Wigner-Mott Scenario . . . 147
4.4 The Mott Insulating State and Quantum Spin Liquids . . . 155
4.4.1 Low Temperature Magnetism . . . 155
4.4.2 Spin-lattice Relaxation Times . . . 164

5 Transport Phenomena in Graphite 169
5.1 Graphite Samples . . . 170
5.2 Low Field Transport and Quantum Oscillations . . . 171
5.3 Landau Quantisation and Charge Density Waves in the Quantum Limit of Graphite . . . 179

5.4 Point-Contact Spectroscopy . . . 191
5.4.1 Low Field Spectra . . . 192
5.4.2 Anomalous Spectra and Possible Superconductivity . . . 196
5.4.3 Point Contact Spectroscopy in Pulsed Magnetic Fields . . . 200

6 Conclusions and Outlook **204**

7 Acknowledgements **207**

A The Ultra-Low Temperature Setup **209**
A.1 New SQUID and Magnet Wiring of ND1 . . . 209
A.2 The ND1 SQUID-NMR Coil Set . . . 215
A.3 The NMR-Cell . . . 220

B Pulsed Magnetic Fields **223**
B.1 Generation of High Magnetic Fields . . . 223
B.2 Pulsed Field Transport Measurements . . . 225

C Point-Contact Spectrometers **227**
C.1 Low Field Spectrometer . . . 227
C.2 Point-Contact Needles . . . 230
C.3 High Field Spectrometer . . . 232

Bibliography **236**

List of Figures

1.1 Cuprate Mott-Hubbard Phase Diagram 2
1.2 High Temperature Phase-Diagrams of ^{3}He on Graphite 3

2.1 Fermi-Dirac statistics and Pauli susceptibility of a non-interacting Fermi gas. 10
2.2 Landau Quasi-particles in the vicinity of the Fermi surface. 11
2.3 Back-action of the Landau Parameters onto the Fermi surface. 13
2.4 The Quasi-Free Fermion Model 17
2.5 The Tight-Binding Model 19
2.6 Crystal Structure of Graphite 22
2.7 Tight-Binding Band Structure of Graphite 24
2.8 The Hubbard model: Site Occupancy and Phase Diagram 30
2.9 DMFT phase diagram of the maximally frustrated Hubbard model . . 32
2.10 Antiferromagnetic Ground States of the Isotropic Triangular Lattice . 34
2.11 Spin Liquid Phases in the Triangular Lattice Solids 40
2.12 Pulsed NMR and the Free Induction Decay 47
2.13 Spin Echo Pulse Sequence 50
2.14 T_1 Pulse Sequence 51

3.1 Properties of Liquid Helium 53
3.2 Schematics of a ^{3}He:^{4}He dilution refrigerator with attached nuclear demagnetisation stage. 55
3.3 ND1 Cooling Power 57
3.4 Entropy and the Demagnetisation Cycle 60
3.5 ND1 Submillikelvin Stage 63
3.6 Temperature Range of Low Temperature Thermometers 68
3.7 ^{3}He Melting Curve 71

3.8 Noise Thermometer . . . 75
3.9 Noise Thermometer Spectrum . . . 76
3.10 Josephson Junctions, SQUIDs and $V(\Phi)$-Charactersistics . . . 81
3.11 SQUID NMR Schematic . . . 83
3.12 Noise Level of the SQUID NMR Setup . . . 87
3.13 Transmitter Excitation and NMR Spectrum . . . 88
3.14 SQUID Recovery . . . 89
3.15 Frequency Dependence of the ^{13}C Transverse Relaxation Time . . . 91
3.16 Comparison of Ultra-Low Temperature Thermometers . . . 92
3.17 ^{13}C Paramagnetism . . . 93
3.18 Cooling Paths and Thermal Resistances . . . 94
3.19 Longitudinal Magnetisation Recovery of ^{13}C in Graphite . . . 95
3.20 Temperature Dependence of the T_1 of ^{13}C in Graphite . . . 96
3.21 T_1 Relaxation Rate Distributions for $\beta \leq 1$ . . . 97
3.22 Frequency Dependence of the T_1 of ^{13}C in Graphite . . . 99
3.23 ^{13}C NMR Thermometer Correction . . . 100
3.24 ^{13}C NMR Thermometer Correction . . . 101

4.1 ^{4}He Adsorption Isotherm on the Grafoil NMR-cell . . . 105
4.2 Tuning the ^{4}He Preplating . . . 107
4.3 Overstretched Free-Induction Decays . . . 109
4.4 Double Exponential Decays . . . 111
4.5 Temperature Dependence of the ^{3}He Magnetisation . . . 114
4.6 Temperature Dependence of the Frequency Shift . . . 116
4.7 Applied Frequency Shift . . . 117
4.8 Temperature Dependence of the Transverse Relaxation Time . . . 119
4.9 Simulated Transverse Relaxation Times in the Slow Diffusive Limit . 122
4.10 Spin Echo Measurement at 5.50 nm^{-2} and 100 mK . . . 123
4.11 Frequency Dependence of the Intrinsic Relaxation at 5.50 nm^{-2} and 100 mK . . . 124
4.12 Intrinsic Transverse Relaxation Time Isotherm . . . 125
4.13 ^{3}He Magnetisation, Relaxation Time and Frequency Isotherms . . . 127
4.14 2D and 3D Pauli vs. Dyugaev Magnetisation . . . 129

4.15 Curie-Weiss and Fermi Fluid Fits . . . 131
4.16 Curie-Weiss Fitting Parameters . . . 132
4.17 3 Fermi Fluids Fits . . . 134
4.18 Renormalised Fermi Temperatures and Fluid Magnetisations . . . 135
4.19 Scaled Magnetisations in the Three Fermi Fluid Model . . . 136
4.20 Renormalised Fermi Temperatures . . . 137
4.21 Susceptibility and Fermi temperature Renormalisation in ^{3}He . . . 138
4.22 Effective Mass Enhancement in ^{3}He|^{4}He|Graphite . . . 139
4.23 Quasi-Particle Band Structure of 2D ^{3}He . . . 141
4.24 Fluid and Solid Fractions on Approaching the Mott Transition . . . 143
4.25 Logarithmic Plot of the Fluid and Solid Fraction . . . 144
4.26 Frequency Shift as a Function of the Polarisation . . . 145
4.27 Reciprocal Space and Brillouin Zone Folding . . . 148
4.28 Wigner-Mott Transition and Superlattices . . . 150
4.29 Interaction Potential and Wigner-Mott Phase . . . 151
4.30 ^{3}He Superstructures around 7.0 nm^{-2} . . . 152
4.31 Excess Magnetisation and Temperature Exponent . . . 156
4.32 High Temperature Series Expansion Fits . . . 157
4.33 High Temperature Series Expansion Fit Parameters . . . 158
4.34 Excess Magnetisation in the Gapped Magnon Model . . . 160
4.35 Ultra-Low Temperature Spinon Magnetisation . . . 162
4.36 Magnetic Field Scaling of the Solid Polarisation . . . 163
4.37 Spin-Lattice Relaxation of ^{3}He . . . 165
4.38 Frequency and Temperature Dependence of the Spin-Lattice Relaxation Time in 6.80 nm^{-2} ^{3}He . . . 166
4.39 Spin-Lattice Relaxation Rates . . . 167

5.1 Zero-Field Resistance of Graphite . . . 172
5.2 Low Field Magneto-Resistance of Graphite . . . 174
5.3 De Haas-van Alphen Effect in Graphite . . . 178
5.4 The Pulsed Field Graphite Sample . . . 180
5.5 High Field In- and Out-of Plane Magneto-Resistance of Graphite . . . 181
5.6 Derivatives of the In-Plane Magneto-Resistance of Graphite . . . 183

5.7 Phase Diagram of the Charge-Density Waves in Graphite 184
5.8 Quantum-Limit Landau Level Structures of Graphite 186
5.9 Quantum Limit Charge Susceptibility of Graphite 187
5.10 Fermi and Charge-Density Wave Nesting Vectors in the Quantum Limit of Graphite 188
5.11 1st-Order Character of the Charge-Density Wave Transitions 189
5.12 Temperature and Magnetic Field Dependence of the Point-Contact Spectrum of Graphite 194
5.13 Anomalous Point-Contact Spectra of Grafoil 197
5.14 Magnetic Field Dependence of the Point-Contact Gap 199
5.15 High Field Point-Contact Spectrum of Graphite 201
5.16 High Field Point-Contact Spectrum of Exfoliated Graphite 202
5.17 Second Order High Field Point-Contact Spectrum of Grafoil 202

A.1 SQUID Wiring 210
A.2 SQUID Wiring Implementation 211
A.3 Persistent Switches and Heat Exchangers of ND1 214
A.4 Simulated NMR-Magnet Homogeneity 216
A.5 Transmitter Coil Simulation inside a Hechtfischer Shield 217
A.6 NMR Tip Angle Dependence of ^{3}He 218
A.7 NMR-Coil Set and Cell 219
A.8 NMR Cell Manufacture 221

B.1 Pulsed Field Schematics and Pulse Durations 224

C.1 PPMS Point-Contact Spectrometer 228
C.2 Piezo-stack Performance 229
C.3 Point-Contact Spectroscopy Needles 231
C.4 Pulsed Field Spectrometers 233
C.5 Pulsed Field Point-Contact Spectroscopy Data 234

List of Tables

2.1 Renormalisation of Landau Fermi Liquid Parameters 14
2.2 Slonczewski-Weiss-McClure Band Parameter 23
2.3 $2k_{\mathrm{F}}$ Fermi Surface Instabilities 25

3.1 Technical SQUID Parameters 84

5.1 Phonon Modes in Graphite 195

C.1 List of PCS Contacts 235

1 Introduction

Ever since the discovery of high-temperature superconductivity in the late 1980s by Bednorz and Müller *et al.* [1], physicists have been trying to explain the mechanism for high-temperature superconductivity in the quasi-two dimensional cuprates. It quickly emerged that the two-dimensional copper-oxide planes in these materials form a square lattice of tight-binding sites with strong on-site repulsion in the copper d-orbitals. Long before the discovery of cuprates Mott and Hubbard pointed out that systems with strong on-site repulsion become insulators at half band filling [2, 3, 4]. And indeed by changing the chemical composition of cuprates, i.e. electron or hole doping of the copper-oxide planes, it was possible to explore the entire Mott-Hubbard phase diagram (Fig. 1.1) [5, 6].

It appeared that the superconductivity observed in cuprates is masking a quantum critical point between the Fermi liquid at high doping and the antiferromagnetic Mott insulator at low doping [7]. In the following years several similar superconducting phases covering quantum critical points were discovered in heavy-Fermion compounds and iron pnictides. The critical temperatures of these superconductors were strongly enhanced over the expected BCS-value [8, 9, 10, 11, 12]. Thus the question arose how the proximity to a quantum critical point triggers high-temperature superconductivity [5, 13].

The study of these strongly correlated electron materials, is however complicated by the restricted access to the phase diagram by applying pressure or chemical doping. Furthermore substituting elements or chemical doping often causes disorder in these materials. Thus less complicated model systems were needed to explore the Mott-Hubbard phase diagram.

The system studied in this thesis is two-dimensional ^{3}He. Liquid ^{3}He is a charge neutral Landau Fermi liquid, which shows strong short range repulsion similar to electrons in cuprates or other d and f-electron materials. The dominant interaction in ^{3}He and in particular the strong short range repulsion arises from van der Waals

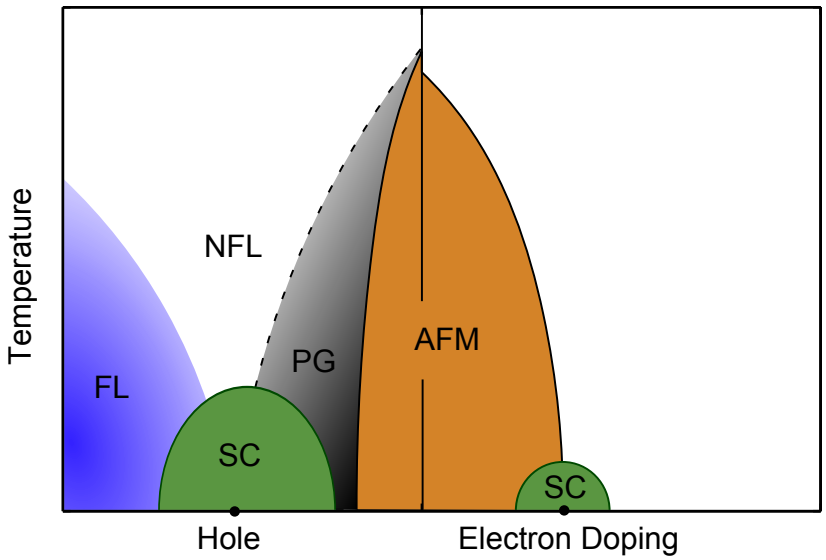

Figure 1.1: Cuprate Mott-Hubbard phase diagram showing the emergent superconductivity (SC) at the quantum phase transitions. The different phases mark the Fermi liquid (FL), non-Fermi liquid (NFL), pseudo-gap (PG), antiferromagnetic solid phase.

forces. Confining ^{3}He in thin cavities or adsorbing it onto atomically flat substrates leads to quasi-two and two-dimensional ^{3}He [14, 15]. In our experiments monoatomic films of ^{3}He are adsorbed onto graphite at low temperatures. The adsorption potential of ^{3}He in the first layer on graphite is $-200\,\mathrm{K}$ with a potential corrugation due to the graphite lattice of $40\,\mathrm{K}$ [15]. The large zero-point motion of the dimensionally confined ^{3}He allows the adsorbed atoms to overcome the potential corrugation and to delocalise within the film. At low densities these films are therefore behaving like an uncorrelated Fermi gas. Increasing the film density by adding ^{3}He increases the correlations within the system and eventually leads to its solidification [16, 17, 18]. Once the maximum capacity of a layer is reached atoms are promoted into the next layer forming a new two-dimensional Fermi system. The resulting phase diagrams of the first and second layer of ^{3}He on graphite are shown in Figure 1.2.

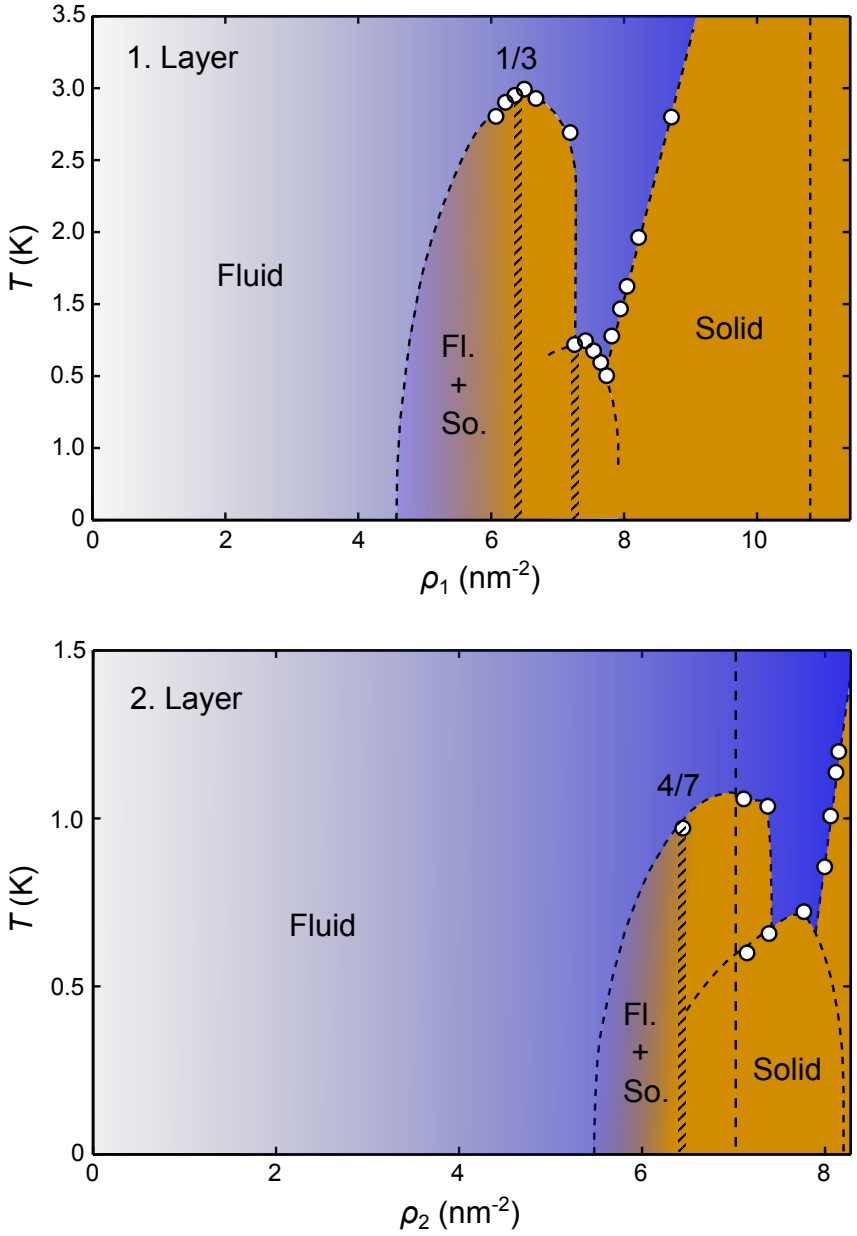

Figure 1.2: High temperature phase diagrams of ^{3}He on graphite [19]. The upper graph shows the first and the lower graph the second layer diagram. The blue regions at low densities refer to the Fermi liquids which become strongly correlated on approaching the yellow solid phases. The formation of the commensurate 1/3 and 4/7-solids is preceded by a fluid-solid phase coexistence region. The vertical dashed lines at 10.8 and 7.0 nm^{-2} mark the respective layer promotions.

The first and second layer phase diagrams of ^{3}He on graphite show extended Fermi fluid phases at low densities with adjacent solid phases at high densities. These solid phases form around commensurate superstructures with respect to the underlying substrate and are characterised by large phase-coexistence regions towards the low density fluids. Increasing the layer density beyond the commensurate densities compresses the solid until it eventually becomes incommensurate with respect to the under-layer.

The resemblance of the ^{3}He to the hole doped cuprate or Mott-Hubbard phase diagram suggests that the fluid-solid quantum phase transition in two-dimensional ^{3}He, could be accompanied by an intervening superfluid or other unconventional quantum phases. Even at low densities, far away from the phase transition, theoretical studies have predicted the emergence of a p and d-wave superfluid in two-dimensional ^{3}He [20, 21]. However such a phase has not been observed yet. This p or d-wave superfluid would be the first truly two-dimensional unconventional superfluid and is therefore subject of ongoing research.

In this thesis we study the increasing correlations and metal-insulator transition in two-dimensional ^{3}He adsorbed onto a ^{4}He preplated exfoliated graphite substrate. Preplating graphite with monolayers of inert gases generates a new composite substrate onto which ^{3}He films can be grown. The higher adsorption potential of these inert gases compared to ^{3}He ensures the seperation of inert gas and ^{3}He layers, where the inert gas occupies the lowest layers. The density of these under-layers is chosen such that the inert gas forms a full monolayer. The triangular lattice structure of these under-layers is incommensurate with respect to the graphite lattice and generates a weakend adsorption and corrugation potential for the ^{3}He film. At the same time the introduction of an intermediate layer reduces the substrate disorder experienced by the ^{3}He top-layer.

Previous work by Greywall, Godfrin, Fukuyama and our group have established the phase diagrams of ^{3}He on graphite preplated with ^{3}He, ^{4}He and hydrogen-deuteride (HD). Heat capacity and nuclear magnetic resonance experiments have shown the increasing quasi-particle interaction and effective mass in two-dimensional ^{3}He with increasing film density [16, 22, 23, 24]. Casey *et al.* were the first to demonstrate the effective mass divergence and solidification of two-dimensional ^{3}He at the commensurate 4/7-phase on a graphite substrate preplated with a bilayer of

HD [17]. The 4/7-phase corresponds to a triangular lattice superstructure formed on top of the HD under-layers whose density ratio is 4:7 (top:under-layer density) [25]. The mechanism of this quantum-phase transition was attributed to a Mott-Hubbard transition as described by the almost localised Fermion model [18, 17]. However since both the Hubbard and almost localised Fermion model rely on the existence of lattice sites, i.e. the 4/7-superstructure, the question remained how this symmetry breaking from an almost isotropic Fermi liquid into the triangular lattice solid takes place and which role the underlying corrugation potential plays. Furthermore it was proposed that the highly geometrically and magnetically frustrated triangular lattice Mott insulator, is a good candidate for a gapless quantum spin liquid [26, 27, 28, 29, 30, 31].

In order to clarify these questions renewed interest was paid to the bare and helium preplated systems. Unlike in HD preplated systems, these show extensive phase coexistence regions on approaching the commensurate solid. Recent heat capacity measurements by Matsumoto *et al.* on ^{4}He preplated graphite suggested a similar mass divergence as was observed on HD [24]. However, their analysis was complicated by an anomalous low temperature contribution to heat capacity on approaching the 4/7-density. Concurrent magnetisation and heat capacity measurements in the proximity of the 4/7-phase by Fukuyama *et al.* showed first signs of the proposed quantum spin liquid like behaviour of the 4/7-solid [31].

We undertook a new series of experiments probing the entire phase diagram of ^{3}He adsorbed onto ^{4}He preplated graphite to measure the magnetism and spin dynamics of two-dimensional ^{3}He using ultra-low temperature SQUID-NMR.

Another material studied in this thesis is the quasi-two dimensional electron system graphite. Graphite is described by a tight-binding model. However, it lacks the strong Coulomb or on-site repulsion of d and f-electron compounds [32, 33]. Its semi-metallic band structure gives rise to van Hove singularities and light charge carriers as have been reported in its two-dimensional allotrope graphene [34, 35].

Following the ideas of Peierls, Fröhlich and Overhauser, three-dimensional electron gases, like electrons in graphite, become unstable against the formation of charge or spin-density waves at low temperatures and high magnetic fields [36, 37, 38, 39, 40]. In semi-metals like graphite the critical fields of these instabilities are low due to their low charge carrier density. Graphite is therefore an ideal model system to study these instabilities. Preceding measurements by Iye [41], Yaguchi [42] and Fauqué *et al.* [43]

have found prominent magneto-resistance anomalies in the magnetic quantum limit of graphite above 30 T. The observed magneto-resistance anomaly was attributed to a density wave in the lowest occupied Landau levels, its nesting mechanism, however, remained subject of ongoing debates [44, 45, 46]. We have, therefore, studied the general transport properties of graphite, focusing on the magneto-resistance in magnetic fields up to 60 T and theoretical Landau level structure in this magnetic field range [47].

This thesis is structured as follows:

The second chapter introduces the theoretical frame work, which is necessary to interpret and understand strongly correlated Fermion systems. The chapter starts with the introduction of the Landau-Fermi liquid theory, followed by band structure models, which are used to describe Fermi fluids. Particular focus is paid to the tight-binding and Hubbard model, describing electrons in graphite and two-dimensional ^{3}He. The discussion of Fermi liquids is followed by the theory of magnetic exchange and magnetism in solids and particularly Mott insulators, like ^{3}He. Multiple spin-exchange and the notion of quantum-spin liquids are introduced. The final part of this chapter focuses on nuclear magnetic resonance and its underlying theory.

The third chapter introduces the low temperature experimental techniques, which were used in this thesis. After a brief introduction to cryogenic and dilution refrigerators the chapter will focus on ultra-low temperature techniques, such as nuclear adiabatic demagnetisation, thermometry and SQUID-NMR. Technical details and supplemental information to this chapter are given in the appendices.

Ultra-low temperature SQUID-NMR measurements of two-dimensional ^{3}He and their interpretation are presented in chapter four. The initial data analysis and results will be followed by a microscopic interpretation of the observed metal-insulator transition. The final part of this chapter focuses on the magnetism of the triangular lattice Mott insulator. Here a low temperature gapless quantum-spin liquid ground state will be proposed.

The fifth chapter presents transport measurements on different types of graphite. A comparative study of poly and nano-crystalline graphites at zero and low magnetic fields will be presented, showing the connection between magneto-transport properties and defect concentrations in graphite. Based on pulsed magnetic field

transport measurements up to 60 T and Landau level calculations the development of a collinear charge-density wave state in the lowest four Landau levels of graphite will be shown and discussed. The chapter closes with point-contact spectroscopy measurements on graphite, which were aimed to directly measure the opening of the charge-density wave gap in graphite.

A summary of our results and suggestions for future experiments on both two-dimensional systems can be found in chapter six.

2 Theory of Two-Dimensional Fermion Systems

In the following chapter a series of quantum mechanical models and concepts will be introduced that are used to interpret the physics of two-dimensional helium and graphite. In the first part of this chapter the general frame work for the interpretation of strongly correlated Landau Fermi liquids will be given, followed by a more detailed discussion of how an underlying periodic potential influences the fluid state and leads to the parameters postulated in the Landau Fermi liquid. A model will be presented which takes into account the effects of hard core repulsion in helium or Coulomb interaction in electron systems, i.e. the Hubbard model, which leads to the solidification of these systems at strong interactions and half filling. Finally we will discuss the magnetism of the resulting solid state and explain the basic principles of nuclear magnetic resonance techniques, which can be used to probe the fluid and solid state.

2.1 The Theory of Fermi Liquids

2.1.1 The Non-Interacting Fermi Gas

Classical gases such as air can be described as an ensemble of non-interacting point-masses with a kinetic energy of $\epsilon = p^2/2m$, where p is the particle momentum and m the particle mass. The energy distribution within such an ensemble is described by the familiar Boltzmann-distribution:

$$f_{\mathrm{B}}(\epsilon) \propto \exp\left\{\frac{-\epsilon}{k_B T}\right\}, \tag{2.1}$$

where the renormalisation of the Boltzmann-distribution depends on the dimensionality of the system.

In the limit where the interparticle spacing of the gas atoms or molecules reaches the thermal de-Broglie wave length $\lambda_{th} = h/\sqrt{2mk_BT}$ i.e. the quantum mechanical wave functions of the particles start to overlap, meaning that particles can no longer be described in a non-interacting classical picture. In this regime a classical gas becomes a quantum gas or more precisely a Fermi gas. In quantum mechanics the Pauli-exclusion principle forbids two half-integer spin particles to occupy the same quantum mechanical state. Thus at $T = 0$ states are successively singly occupied from the lowest to the highest energy up to the Fermi energy ϵ_{F}. The temperature dependence of the occupation probability is described by the Fermi-Dirac distribution:

$$f_{\mathrm{F}}(\epsilon) = \frac{1}{\exp\left\{\frac{\epsilon-\mu}{k_BT}\right\}+1}, \tag{2.2}$$

where μ is the chemical potential for adding an additional particle, marking the energy at which the distribution takes the value of one half (see Fig. 2.1). At $T = 0$ the chemical potential is equivalent to the Fermi energy and shifts towards lower energies for temperatures $k_BT \geq \epsilon_{\mathrm{F}}$. If we assume a non-interacting spin-$1/2$ Fermi gas with a quadratic energy dispersion $\epsilon(p) = p^2/2m$, the magnetisation of such a system can be calculated from the number difference of spin-up and down particles:

$$M = \mu_{\mathrm{F}}(n_\uparrow - n_\downarrow), \tag{2.3}$$

where μ_{F} is the magnetic moment of the spin-$1/2$ Fermion. In a magnetic field, the otherwise degenerate bands of the spin-up and down particles are offset to each other by the Zeeman energy $\mu_{\mathrm{F}}B$ leading to the following expressions for the respective particle numbers:

$$n_{\uparrow,\downarrow} = \int_0^\infty f_{\mathrm{F}}(\epsilon \pm \mu_{\mathrm{F}}B/2)g(\epsilon \pm \mu B/2)d\epsilon \tag{2.4}$$

In the low polarisation limit of $\mu B << \epsilon_F$ the magnetisation simplifies to the Pauli

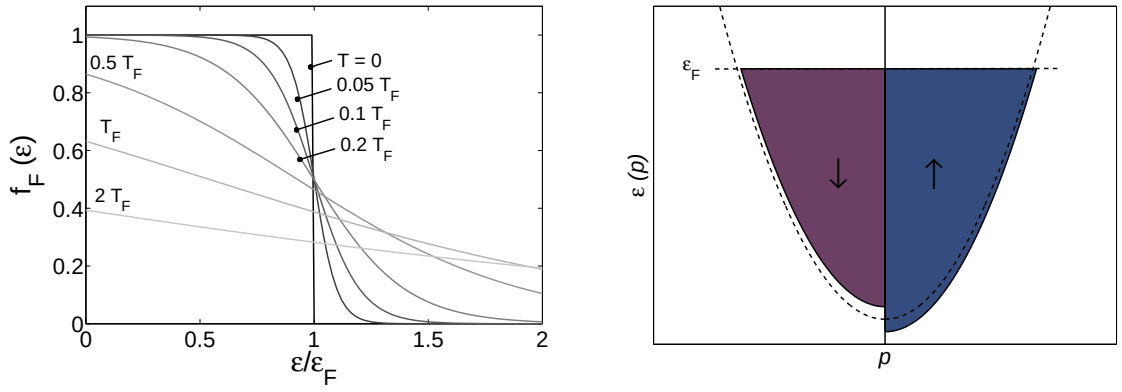

Figure 2.1: Fermi-Dirac statistics and Pauli susceptibility of a non-interacting Fermi gas. The left graph shows the effect of finite temperature on the Fermi-Dirac statistics. The schematics on the right-hand side shows how a magnetic field shifts the quadratic energy dispersion of a Fermi gas spin dependent, which leads to a finite spin imbalance, i.e. magnetisation of the system.

magnetisation:

$$M_0 = \mu_{\mathrm{F}}^2 g(\epsilon_F) B. \tag{2.5}$$

where $g(\epsilon_{\mathrm{F}}) = dn/d\epsilon|_{\epsilon_{\mathrm{F}}}$ is the density of states at the Fermi energy.

2.1.2 The Interacting Landau-Fermi Liquid

The previous model of non-interacting Fermions proved very successful for the description of the thermodynamic properties of many condensed matter systems, here in particular electrons in metals and bulk ^{3}He. However it was not understood, why the theory of non-interacting Fermions holds in the case of strongly-interacting systems.

In 1956 L.D. Landau postulated a model in which an interacting Fermi liquid could be described by a non-interacting Fermi gas with renormalised band parameters [48, 49, 50, 51]. The key idea of Landaus approach was the introduction of long-lived excitations close to the Fermi surface (FS) that enable scattering processes of the resulting quasi-particles, leading to the renormalisation of the single particle

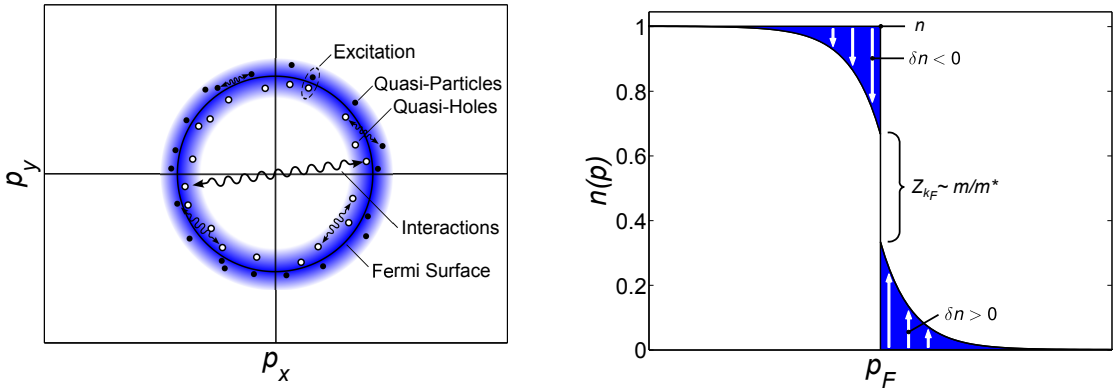

Figure 2.2: Landau Quasi-particles in the vicinity of the Fermi surface. The left schematics shows how quasi-particles are generated as particle-hole pairs (excitations) which then interact and give rise to the renormalisation within the Landau-Fermi liquid. The right plot shows how quasi-particles δn change the particle density n around the Fermi momentum p_F and give rise to a finite quasi-particle density above and quasi-hole density below the Fermi momentum, where the jump in the quasi-particle density at the FS i.e. the quasi-particle spectral weight Z_k is proportional to the inverse mass renormalisation.

energy dispersion.

In the non-interacting Fermi gas excitations above or below the Fermi energy have an infinite life-time due to the lack of interaction i.e. decay channels. If interactions are turned on an excited particle can decay by the generation of new low-energy excitations. These excitations are pairs of quasi-holes below and quasi-particles above the Fermi energy (see Fig. 2.2). The life-time of these excitations was found to follow $\tau^{-1} \propto (\epsilon - \mu)^2 + (k_B T)^2$, thus only becoming significant at $T \to 0$ and $\epsilon \to \epsilon_F$. As a result quasi-holes and particles are restricted to a thin shell around the FS.

If we assume the quasi-particles density $\delta n(p)$ with $p \approx p_F$ is small compared to the particle density $n(p)$, the total energy of the system E can be expanded in orders of the quasi-particle density:

$$E = \sum_p \epsilon_0(p) n(p) + \sum_p (\epsilon_0(p) - \mu)\delta n(p) + \sum_{p,p'} f(p,p')\delta n(p)\delta n(p') + \mathcal{O}(\delta n^3) \quad (2.6)$$

This is the Landau expansion, where the total energy of the non-interacting system (first term) is corrected by the creation and interaction of quasi-particles (second and third term respectively). Here $\epsilon_0(p)$ describes the non-interacting single particle dispersion relation and $f(p, p')$ gives the interaction between two quasi-particles with momentum p and p'. Thus the quasi-particle energy dispersion $\partial E/\partial \delta n$, or renormalised single-particle dispersion, is:

$$\epsilon(p) = \epsilon_0(p) - \mu + \sum_{p,p'} f(p, p')\delta n(p'). \tag{2.7}$$

As can be seen in Eqn. 2.7, the presence of quasi-particle interactions in the Fermi liquid renormalises the single particle energy dispersion relative to the non-interacting Fermi gas. The altered quasi-particle dispersion will feed back into the density of quasi-particles and generate a self-consistent loop. At this point, it is important to notice that the interaction function $f(p, p')$, in the limit of $p = p_{\mathrm{F}}$, is only a function of the enclosed angle between p and p'. Changes in $\epsilon(p)$ or δn will generally not feedback isotropically around the FS. Since $f(p, p')$ is symmetric in $p \cdot p'$ it can be expanded in terms of Legendre polynomials $P_l(p \cdot p')$:

$$f(p, p') = \sum_{l=0}^{\infty} (2l + 1) f_l P_l(p \cdot p'), \tag{2.8}$$

where $l = 0$ represents isotropic and $l = 1$ anti-symmetric case. Higher orders of the Legendre expansion are usually ignored. Normalising the Legendre coefficients f_l by the density of states $g^*(\epsilon_{\mathrm{F}})$ leads to the dimensionless Landau parameters F_l. Figure 2.3 shows how the first three Landau parameters influence the FS of a Landau Fermi liquid when an external fields is applied.

The result of the self-consistent Landau expansion Eqn. 2.7 is the renormalised single-particle dispersion for quasi-particles at the Fermi energy. Based on the renormalised single-particle dispersion it is possible to calculate the thermodynamic properties of a Landau Fermi liquid as a function of the Landau parameters (see Table 2.1).

Most importantly the renormalised band mass and density of states can be calcu-

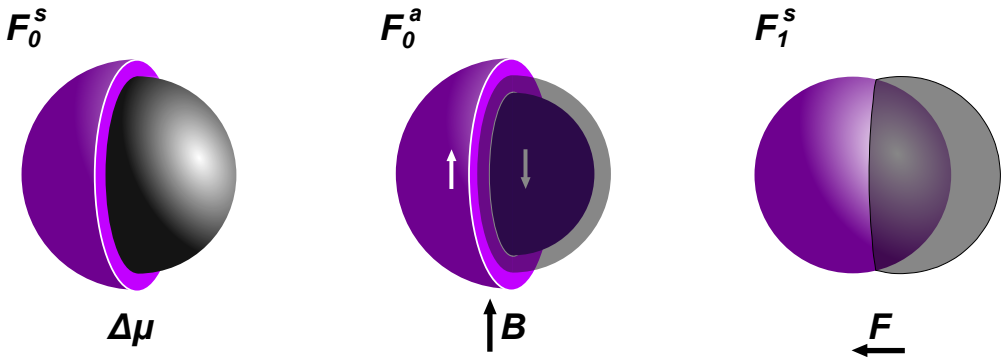

Figure 2.3: Back action of the Landau parameters onto the Fermi surface. The non-interacting FS is shown in grey whilst the purple coloured surfaces correspond to the renormalised surfaces. The spin-symmetric Landau parameter F_0^s leads to an spin independent isotropic expansion/contraction of the FS when the chemical potential is changed, whilst the spin-antisymmetric F_0^a leads to a splitting of the spin up and down FS i.e. FS polarisation when a magnetic field is applied. F_1^s, giving rise to the mass renormalisation, will generate a spin independent distortion of the FS in the direction of an externally applied force field or flow.

lated using:

$$m^* = p_\mathrm{F} v_\mathrm{F}^{-1} \qquad \text{with} \qquad v_\mathrm{F} = \left.\frac{\partial \epsilon(p)}{\partial p}\right|_{p_\mathrm{F}} . \tag{2.9}$$

In Table 2.1, it can be seen that the first order spin-symmetric Landau parameter F_1^s is responsible for the renormalisation of the effective mass, dispersion relation, density of states at the Fermi energy, heat capacity and magnetic susceptibility. In the case of the magnetic susceptibility the zeroth order spin-antisymmetric Landau parameter enters into the renormalisation. In the presence of a magnetic field F_0^a can lead to a polarisation of the FS beyond the Pauli susceptibility. The inverse proportionality of the spin susceptibility on $1+F_0^a$ gives rise to a magnetic instability when $F_0^a = -1$. This effect is known as the Pomeranchuk or ferromagnetic instability [52]. Before Landau's interpretation of the Fermi liquid, this instability was already postulated by Stoner, who introduced the Stoner enhancement factor of the magnetic

Table 2.1: Renormalisation of Landau Fermi Liquid Parameters

Property	Non-Interacting Fermi Gas	Landau Fermi Liquid
Fermi Momentum	p_F	unchanged
Particle Mass	m	$m^* = m(1 + F_1^S)$
Dispersion	$\epsilon(p) = p^2/2m$	$\epsilon(p \approx p_F) = p^2/2m^*$
Fermi energy	$\epsilon_{\mathrm{F}} = k_{\mathrm{B}} T_{\mathrm{F}}$	$\epsilon_{\mathrm{F}}^* = k_{\mathrm{B}} T_{\mathrm{F}}^* = \epsilon_{\mathrm{F}}/m^*$
Density of States	$g(\epsilon_{\mathrm{F}}) = 2m\pi/\hbar^2$	$g^*(\epsilon_{\mathrm{F}}) = g(\epsilon_F)(m^*/m)$
Heat Capacity	$c_v = \gamma_0 T = g(\epsilon_{\mathrm{F}}) k_B^2 (\pi^2/3) T$	$\gamma = \gamma_0 (m^*/m)$
Susceptibility	$\chi_0 = \mu^2 g(\epsilon_{\mathrm{F}})$	$\chi = \chi_0 (m^*/m)(1 + F_0^a)^{-1}$
Compressibility	$\kappa_0 = n^2/g(\epsilon_{\mathrm{F}})$	$\kappa = \kappa_0 (1 + F_0^s)(m^*/m)^{-1}$

susceptibility for strongly correlated electron systems $(1 - U g(\epsilon_{\mathrm{F}}))^{-1}$, where U is the on-site repulsion energy for two Fermions with opposite spin (see Section 2.2.5).

The dependence of thermodynamic properties (Table 2.1) on the quasi-particle interactions makes it possible to determine the Landau parameters *a posteriori* by measuring the the magnetic susceptibility, heat capacity and compressibility. We will later see how quasi-particle interactions lead to a strong effective mass and susceptibility enhancement in two-dimensional ^{3}He as we approach the commensurate 4/7-density.

It is important to notice that the Landau Fermi liquid theory, presented in this section, does not make any predictions about the microscopic origin of quasi-particle interactions in the system. Thus microscopic models need to be applied to determine the size and origin of correlations in a Fermi liquids.

2.2 Band Theory

In general any quantum mechanical system like two-dimensional ^{3}He or electrons in graphite are described by the solution of their Schrödinger equation,

$$\mathcal{H}\Psi = E\Psi, \qquad \mathcal{H} = \frac{-\hbar^2}{2m}\nabla^2 + V(r) + U(r, r'). \tag{2.10}$$

Where Ψ is the quantum mechanical many-body wave function, $V(r)$ and $U(r, r')$ are the underlying potential and interparticle interaction respectively. Once the precise eigenvalues or band structure $\epsilon_n(k)$ of the many-body system are solved it is possible to infer the associated Landau parameters and thermodynamic properties of the system.

Due to the mathematical complexity of this problem, approximations are introduced to simplify the kinetic, potential and interaction terms in the Hamilton operator $\mathcal{H}$.

In the following sections, different approximations of Eqn. 2.10 will be presented that are suitable to describe a Fermi liquid starting from the quasi-free Fermion model for weak periodic potentials, followed by the tight-binding and Hubbard model for strong periodic potentials and strong particle interaction. In the last part of this section an overview of possible Fermi liquid instabilities will be given, leading to the collapse of the Fermi liquid state and its associated FS.

2.2.1 The Quasi-Free Fermion Model

One of the simplest models which might be used to describe low density ^{3}He films or generally Fermions in a weak periodic potential is the quasi-free Fermion model. In this model, Fermions or electrons are approximated by planar Bloch waves:

$$\psi_k(r) = u(r)e^{ikr} \tag{2.11}$$

here k is the wave number and r the spacial coordinate of the particle wave function [53]. In the presence of a periodic potential or lattice, the underlying potential $V(r)$ and Bloch function $u(r)$ must be obey the translational symmetry of the lattice, $V(r + R_\mathrm{i}) = V(r)$ and $u(r) = u(r + R_\mathrm{i})$, where R_i are all possible crystal lattice

vectors, which can be expressed as a linear combination of primitive lattice vectors a_i:

$$R_\mathrm{i} = \mathrm{k_i} \cdot a_1 + \mathrm{l_i} \cdot a_2 + \mathrm{m_i} \cdot a_3 \qquad \text{with} \qquad \mathrm{k_i}, \mathrm{l_i}, \mathrm{m_i} \in \mathbb{Z}. \tag{2.12}$$

Thus under discrete Fourier transformation both functions can be written as:

$$V(r) = \sum_G v_G e^{iGr} \qquad\qquad \psi_k(r) = \sum_G c_G e^{i(k+G)r}. \tag{2.13}$$

in the basis of reciprocal lattice vectors G. By inserting them into the Schrödinger equation 2.10 we obtain:

$$\frac{\hbar^2}{2m} \sum_G (k+G)^2 e^{iGr} + \sum_G \sum_{G'} v_G c_{G'} e^{i(G+G')} = E_k \sum_G c_G e^{iGr}. \tag{2.14}$$

Which can be simplified to:

$$\left(\frac{\hbar^2 (k+G)^2}{2m} - E \right) c_G + \sum_G v_G c_{G-G'} = 0. \tag{2.15}$$

It follows that for a vanishing potential i.e. in free space, all components of v_G vanish and the Schrödinger equation returns the classical dispersion of a free particle $E(k) = \hbar^2 k^2 / 2m$. Secondly large values of k, outside the first Brillouin zone ($-G/2 \leq k \leq G/2$), can always be shifted back into the first Brillouin zone by adding or subtracting an integer number of reciprocal lattice vector nG with $n \in \mathbb{Z}$. Thus for a vanishing potential, the resulting band structure is a stacked superposition of free particle dispersions originating at all possible reciprocal lattice vectors (see Fig. 2.2.1). In points where these fundamental dispersions cross each other the resulting bands are degenerate. Since these points occur mostly at high symmetry planes, the degeneracy is usually lifted by the influence of an underlying periodic potential. For instance along the Brillouin zone boundary, degenerate energy levels will split symmetrically by the corresponding Fourier component of the potential $|2v_G|$ introducing a band gap between the degenerate energy levels as shown in Figure 2.2.1. Taking into account the two-fold spin degeneracy of Fermions, systems with an even number of valence electrons per unit cell will have a fully filled Brillouin

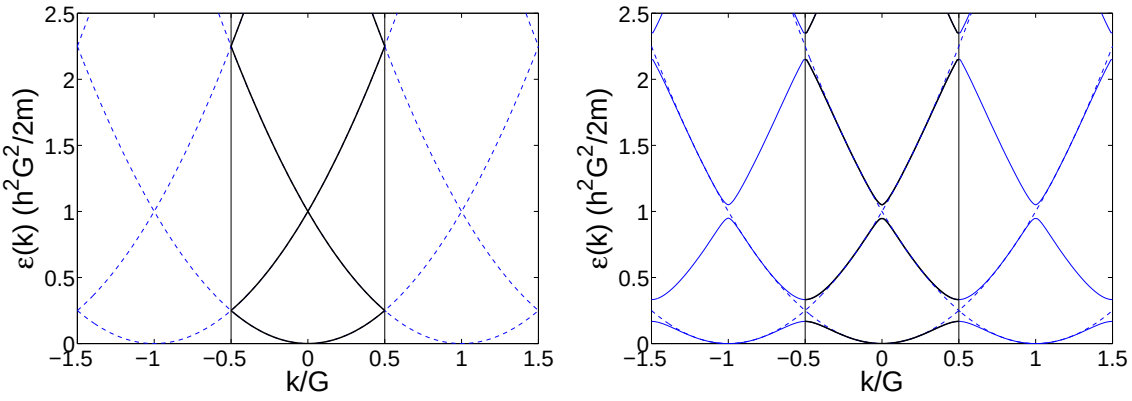

Figure 2.4: The quasi-free Fermion model: The graph on the left shows how the periodicity of the reciprocal space leads to the superposition of $\hbar^2(k+G)^2/2m$ dispersions in the first Brillouin zone $-G/2 \leq k \leq G/2$ in the absence of a periodic potential. The right-hand side graph shows how a finite periodic potential leads to the splitting of the energy bands close to the Brillouin zone boundary and centre.

zone with a Fermi wave vector close to the Brillouin zone centre or boundary and the Fermi energy will lie inside a band gap. Wilson therefore concluded that materials with even valence must be insulators whilst odd valent materials are metals. Thus applying this theory to single valent alkali-metals like lithium and sodium yields good agreement with the observed metallic character of these materials. Applying this simple model to carbon and its derivatives graphite and graphene however fails.

In low density ^{3}He films, where the potential corrugation arising from the graphite honeycomb lattice ($v(40\,\mathrm{nm}^{-1}) \approx 40\,\mathrm{K}$) or the triangular lattice structure of the ^{4}He under-layer ($v(23\,\mathrm{nm}^{-1}) \approx 3\,\mathrm{K}$), the effects of the periodic potential can be neglected since $k_\mathrm{F} \ll G/2$. Thus two-dimensional ^{3}He behaves like a Fermi gas at low-densities, neglecting any correlation effects.

One of the major restrictions of the quasi-free Fermion model is that the periodic potential has to be weak compared to the kinetic energy of the Fermions i.e. Fermions are unbound in the crystal and the periodic potential can be treated as a small pertubation. Let us thus consider the opposite limit of a very strong underlying potential. This will lead to the tight-binding model.

2.2.2 The Tight-Binding Model

One of the most successful models, which has been used to describe the electronic structure of quasi-localised systems i.e. presumed insulators is the tight-binding model. Here a general Bloch function is constructed from quasi-localised atomic states or so called Wannier states ϕ_n [54], which are the solution of the "atomic" Schrödinger equation:

$$\mathcal{H}_{At}\phi_n(r) = E_n\phi_n(r). \tag{2.16}$$

In the limit where these states are isolated from each other or are non-interacting, the energy spectrum of the solid would simply reflect the eigenvalues E_n of the "atomic" Schrödinger equation. However, if we allow the Wannier state wave functions to overlap, the eigenvalues of the atomic Hamiltonian will start to disperse and form bands. Due to the large energy separation of the atomic eigenstates it is adequate to assume that only the highest occupied eigenstates of ϕ_n will contribute to the global Bloch state. Thus the Bloch function ψ_k can be constructed from a linear combination of the highest occupied Wannier states:

$$\psi_k(r) = \frac{1}{\sqrt{N}} \sum_{\mathrm{i}} \phi(r + R_{\mathrm{i}}) e^{ikR_{\mathrm{i}}}, \tag{2.17}$$

where N is the total number of lattice sites in the system. Notice that unlike in the quasi-free electron model Eqn. 2.11, this is an expansion in standing rather than running waves to ensure the translational symmetry of the crystal. Inserting the Bloch state into the effective crystal Hamiltonian $\mathcal{H} = \mathcal{H}_{At} + V_{\Delta}(r)$, where $V_{\Delta}(r)$ is the residual crystal potential after subtracting the effective "atomic" potential, we obtain:

$$(\mathcal{H}_{At} + V_{\Delta}(r)) \sum_{\mathrm{i}} \phi(r + R_{\mathrm{i}}) e^{ikR_{\mathrm{i}}} = E \sum_{\mathrm{i}} \phi(r + R_{\mathrm{i}}) e^{ikR_{\mathrm{i}}}. \tag{2.18}$$

Subsequently the energy expectation value and dispersion relation of the tight-binding band can be derived by multiplying Eqn. 2.18 with $\phi^*(r)$ and integrating

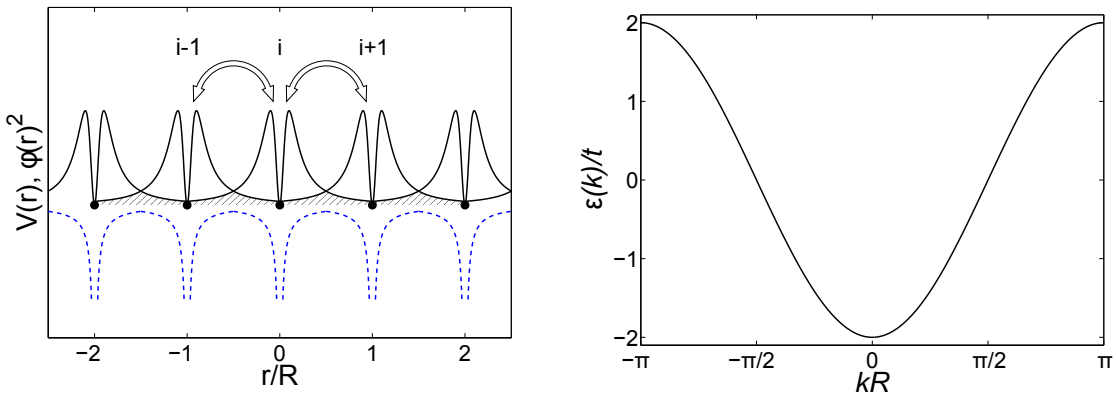

Figure 2.5: The Tight-Binding Model: The left graph shows a lattice of localised p-like atomic eigenstates (black) with their underlying atomic potential (blue). Particles can tunnel between neighboring lattice sites and give rise to the $\epsilon(k) = \cos(ka)$ dispersion relation in the right-hand graph. The tunneling constant $t_{\mathrm{i,j}}$ is proportional to the transfer integral (black shaded area).

out all spacial dimensions:

$$E(k) = E_\phi - B - 2t\cos(ka) \tag{2.19}$$

$$B = -\int \phi^*(r) V_\Delta \phi(r) dr^3 \tag{2.20}$$

$$t = -\int \phi^*(r) V_\Delta \phi(r+a) dr^3 \tag{2.21}$$

Here the tight-binding band dispersion is the sum of the highest occupied atomic eigenvalue E_ϕ, the expectation value of V_Δ and the transfer integral between neighboring sites weighted by V_Δ. The latter gives rise to a $-2t\cos(ka)$ dispersion of the Bloch state as shown in Figure 2.5.

Another interpretation of the tight-binding model can be derived from Fermions tunneling between neighboring lattice sites R_i and $R_{\mathrm{i}\pm1}$(see Fig. 2.5). Here the second quantisation creation and annihilation operators $\hat{c}^\dagger_{\mathrm{i},\sigma}$ and $\hat{c}_{\mathrm{i},\sigma}$ are used to express the vanishing of a particle at site R_i and its recreation at site $R_{\mathrm{i}\pm1}$ and vice

versa. Thus the Hamiltonian of the system can be written as:

$$\mathcal{H}_{TB} = -\sum_{\mathrm{i,j},\sigma} t_{\mathrm{i,j}} (\hat{c}^{\dagger}_{\mathrm{i},\sigma} \hat{c}_{\mathrm{j},\sigma} + \hat{c}^{\dagger}_{\mathrm{j},\sigma} \hat{c}_{\mathrm{i},\sigma}) \tag{2.22}$$

Fourier transforming the particle operators:

$$\hat{c}^{\dagger}_{k,\sigma} = \frac{1}{\sqrt{N}} \sum_{\mathrm{i}} e^{ikR_{\mathrm{i}}} \hat{c}^{\dagger}_{\mathrm{i},\sigma} \tag{2.23}$$

and inserting them into Eqn. 2.22 leads to the formulation of the tight-binding Hamiltonian in reciprocal space:

$$\mathcal{H}_{TB} = -\frac{1}{N} \sum_{k,k'} \sum_{\mathrm{i,j},\sigma} t_{\mathrm{i,j}} \left[e^{ikR_{\mathrm{i}}} e^{-ik'R_{\mathrm{j}}} + e^{ikR_{\mathrm{j}}} e^{-ik'R_{\mathrm{i}}} \right] \hat{c}^{\dagger}_{k,\sigma} \hat{c}_{k',\sigma} \tag{2.24}$$

Since the Wannier functions are quasi-localised to the sites R_{i} and are rapidly decaying for large distances, the tunneling amplitudes $t_{\mathrm{i,j}}$ are only finite for nearest and next-nearest neighbor processes. Thus Eqn. 2.24 can be reduced to $\mathrm{j} = \mathrm{i} \pm 1$ where $R_{\mathrm{i}} - R_{\mathrm{i}\pm1} = a_{\mathrm{i}}$ and it follows that:

$$\mathcal{H}_{TB} = -t \sum_{k,\sigma} \hat{c}^{\dagger}_{k,\sigma} \hat{c}_{k,\sigma} \left[2\cos(ka) \right] = -t \sum_{k,\sigma} n_{k,\sigma} \epsilon(k) \tag{2.25}$$

Here the same cosine dispersion of the tight-binding band as in Eqn. 2.21 is obtained. Remarkably for small fillings the tight-binding model returns a parabolic dispersion like the quasi-free Fermion model (Eqn. 2.15), where the flattening of the cosine-band towards the Brillouin zone boundary bears resemblance to the potential induced band splitting in the quasi-free Fermion model. However the bandwidth of the tight-binding band $W = 4t$ is much smaller than in the quasi-free Fermion model. Thus the tight-binding model is often referred to as narrow band model.

2.2.3 The Slonczewski-Weiss-McClure Model of Graphite

As has been pointed out in section 2.2.1 carbon and its derivatives can not be modelled using the quasi-free Fermion approach due to the localised nature of the $2p$-orbitals, thus we will show how the band structure of Bernal graphite can be derived from the tight-binding model.

Bernal graphite is a quasi-two dimensional material made of ABAB-stacked graphene sheets [55]. The graphene sheets are two-dimensional honeycomb lattices of carbon atoms, which can be described as a triangular lattice with a planar lattice vectors $|a_\mathrm{i}| = 0.246\,\mathrm{nm}$ with two atoms per unit cell. The two atoms are part of the two triangular sublattices A and A' (see Fig. 2.6). The spacing of the graphene sheets in graphite is $c_0 = 0.337\,\mathrm{nm}$ [32]. A representation of the crystal structure of Bernal graphite is shown in Figure 2.6.

The carbon atoms in graphite are sp^2-hybridised, meaning that one of the $2p$-valence electrons forms three planar hybrid orbitals with the two $2s$-core electrons. These three sp^2-orbitals form the covalent bonds between neighboring carbon atoms within the graphene layers. Due to the large energy difference between the low lying sp^2-orbitals and the unhybridised π-orbitals, we assume that the electronic structure close to the Fermi energy is only determined by the overlap of the remaining π-orbitals.

Here the tight-binding Hamiltonian of graphite, including all possible nearest and next-nearest neighbor hoppings, takes the form:

$$\mathcal{H} \;=\; \mathcal{H}_0 + \mathcal{H}_c + \mathcal{H}_{2c} \tag{2.26}$$

$$\begin{aligned}
\mathcal{H}_0 &= \gamma_0 \sum_{\mathrm{i,j}} \hat{c}^\dagger_{R^{\mathrm{A}'}_\mathrm{j}} \hat{c}_{R^{\mathrm{A}}_\mathrm{i}} + \mathrm{c.c.} \\
\mathcal{H}_c &= \gamma_1 \sum_{\mathrm{i}} \hat{c}^\dagger_{R^{\mathrm{B}'}_\mathrm{i}} \hat{c}_{R^{\mathrm{A}'}_\mathrm{i}} + \gamma_3 \sum_{\mathrm{i,j}} \hat{c}^\dagger_{R^{\mathrm{B}}_\mathrm{j}} \hat{c}_{R^{\mathrm{A}}_\mathrm{i}} + \gamma_4 \sum_{\mathrm{i,j}} \hat{c}^\dagger_{R^{\mathrm{B}'}_\mathrm{j}} \hat{c}_{R^{\mathrm{A}}_\mathrm{i}} + \mathrm{c.c.} \\
\mathcal{H}_{2c} &= \gamma_2 \sum_{\mathrm{i}} \hat{c}^\dagger_{R^{\mathrm{A}}_\mathrm{i}+2c} \hat{c}_{R^{\mathrm{A}}_\mathrm{i}} + \gamma_5 \sum_{\mathrm{i}} \hat{c}^\dagger_{R^{\mathrm{A}'}_\mathrm{i}+2c} \hat{c}_{R^{\mathrm{A}'}_\mathrm{i}} + \mathrm{c.c.}.
\end{aligned}$$

with $\mathcal{H}_0$ referring to hopping processes within the graphene layers and $\mathcal{H}_c$ and $\mathcal{H}_{2c}$ containing all terms arising from nearest and next-nearest plane hopping. Figure 2.6

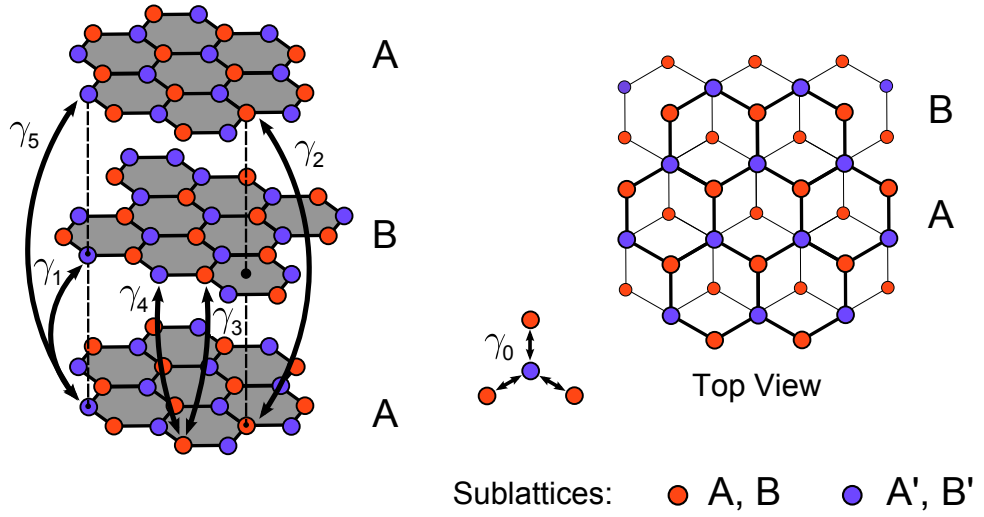

Figure 2.6: Crystal structure of graphite: The left figure shows the three dimensional crystal structure of ABAB stacked Bernal graphite where the B-layers are mirrored with respect to the A-layers. In the tight-binding model the band structure is calculated from the hopping terms related to the intralayer hoppings with γ_0 and the interlayer hopping processes with amplitude γ_1 to γ_5. In the centre the three intralayer hopping vectors associated with γ_0 are shown. The right-hand side figure shows a top down view of the ABAB-stacking.

gives an overview of all hopping processes included in the tight-binding Hamiltonian and their corresponding hopping amplitudes γ_0 to γ_5. A list of all hopping parameters as determined from magneto-transport and de Haas-van Alphen measurements [56] is given in Table 2.2.

If the interlayer hopping terms γ_1 to γ_5 are ignored, the Hamiltonian Eqn. 2.26 gives the band structure of a single graphene layer with its
$\epsilon(k) = \pm\gamma_0\sqrt{3 + 2\sum_{\mathrm{i}}\cos(k \cdot a_{\mathrm{i}})}$ dispersion for the lower and upper band. Here the two bands cross each other at the K and K' points in the hexagonal Brillouin zone, with the Fermi energy lying at the centre of the six Dirac cones.

Due to the large energy separation between the centre and HKH corners of the Brillouin zone within the bands, the band structure of graphite can be solved as an expansion around the HKH corners. Since the primitive lattice cell of graphite contains four atoms, the band structure will equally consist of four bands. Slonczewski, Weiss and McClure have solved the full Hamiltonian Eqn. 2.26 for graphite and

Table 2.2: Slonczewski-Weiss-McClure band parameter, as determined from quantum oscillation and magneto-transport [56].

$\gamma_0 =$	2.85eV	$\gamma_4 =$	0.18eV
$\gamma_1 =$	0.31eV	$\gamma_5 =$	-18.5meV
$\gamma_2 =$	-18.5meV	$\Delta =$	9meV
$\gamma_3 =$	0.29eV	$\epsilon_F =$	-22meV

found the following solution in the vicinity of the HKH corners [57, 32, 33]:

$$\begin{aligned}
\epsilon(k) &= \frac{1}{2}\left(\epsilon_1(k_z)+\epsilon_3(k_z)-\gamma_3\Gamma(k_z)\xi\cos(3\alpha)\right) \\
&\quad \pm\sqrt{\frac{1}{4}\left(\epsilon_1(k_z)-\epsilon_3(k_z)+\gamma_3\Gamma(k_z)\xi\cos(3\alpha)\right)^2+(\gamma_0^2-\gamma_4\Gamma(k_z))^2\xi^2} \\
\epsilon(k) &= \frac{1}{2}\left(\epsilon_2(k_z)+\epsilon_3(k_z)-\gamma_3\Gamma(k_z)\xi\cos(3\alpha)\right) \\
&\quad \pm\sqrt{\frac{1}{4}\left(\epsilon_2(k_z)-\epsilon_3(k_z)+\gamma_3\Gamma(k_z)\xi\cos(3\alpha)\right)^2+(\gamma_0^2-\gamma_4\Gamma(k_z))^2\xi^2}
\end{aligned} \tag{2.27}$$

where ξ is the distance away from the HKH-corner, α the polar angle around the HKH-corner and $\Gamma(k_z) = 2\cos(k_z c_0)$. The three functions $\epsilon_1(k_z)$ to $\epsilon_3(k_z)$ are the diagonal elements of the 4x4 Hamilton operator:

$$\begin{aligned}
\epsilon_1(k_z) &= \Delta+\gamma_1\Gamma(k_z)+\frac{1}{2}\gamma_5\Gamma^2(k_z) \\
\epsilon_2(k_z) &= \Delta-\gamma_1\Gamma(k_z)+\frac{1}{2}\gamma_5\Gamma^2(k_z) \\
\epsilon_3(k_z) &= \frac{1}{2}\gamma_2\Gamma^2(k_z),
\end{aligned} \tag{2.28}$$

here Δ is the chemical potential difference between atoms from different sublattices.

At the Brillouin zone HKH-corner, i.e. $\xi = 0$, the band structure reduces to $\epsilon_1(k_z)$, $\epsilon_2(k_z)$ and a doubly degenerate band $\epsilon_3(k_z)$. Due to the larger magnitude of γ_1 compared to γ_2, only the two ϵ_3-bands will give rise to significant FSs. The ϵ_1 band always lies above the Fermi energy and ϵ_2 only crosses the Fermi energy in the direct vicinity of the H-point giving rise to a minority hole pockets. The k_z dependence of ϵ_3 and resulting FSs are shown in Figure 2.2.3.

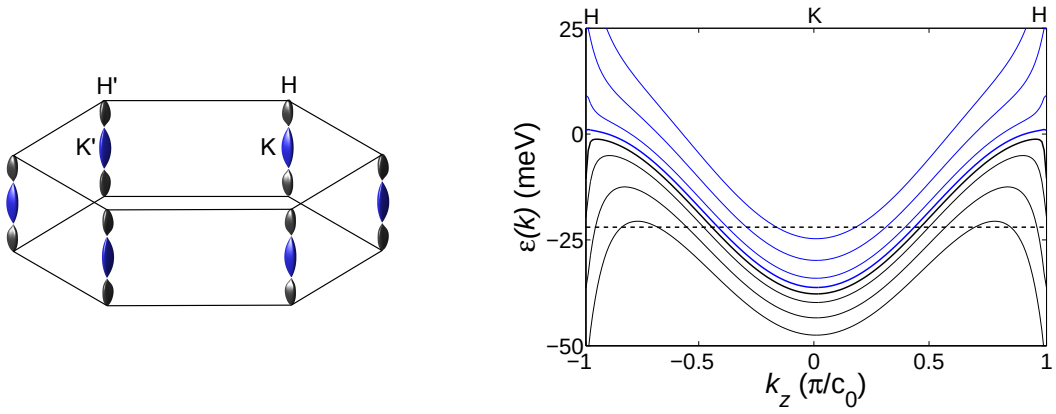

Figure 2.7: Tight-binding band structure of graphite: The left plot shows the hexagonal Brillouin zone of graphite with its three FSs arising in each HKH corner. The FSs consist of an electron pocket around the K-points and two hole pockets close to the H-points. All three FSs show a k_z dependent trigonal warping. The right-hand side graph shows the k_z and ξ dependence of the two degenerate ϵ_3 bands close the HKH-corner. The dark blue and black lines show the electron and hole band at the HKH corner respectively (split for better visibility). The weaker lines show the evolution of ϵ_3 away from the HKH-corner and the associated FS pinch-off.

Away from the HKH corner the ϵ_3 electron (hole) band falls quickly below (rises quickly above) the Fermi energy and gives rise to a cigar shaped electron pocket around the K-point (two cigar shaped hole pockets close to the H-point), where the interlayer hopping term γ_3 leads to a k_z-dependent trigonal warping of the three FSs.

2.2.4 Fermi Surface Nesting Instabilities

Right after Bloch had introduced his quasi-free Fermion model in 1928 [53] questions arose as to whether the proposed Fermi liquid ground state would be stable at low temperatures. One of the key problems in Bloch's model, which later led to a number of instabilities, is the negligence of electron-electron and electron-phonon interactions.

Table 2.3: $2k_F$ Fermi Surface Instabilities

Ground State	Pairing	Total Spin	Momentum	Broken Symmetry
Charge-Density Wave	elec.-hole	$S = 0$	$q = 2k_F$	translational
Spin-Density Wave	elec.-hole	$S = 1$	$q = 2k_F$	translational
Singlet Superconductor	elec.-elec.	$S = 0$	$q = 0$	gauge
Triplet Superconductor	elec.-elec.	$S = 1$	$q = 0$	gauge

In the following decades R. Peierls [36], H. Fröhlich [37], J. Bardeen, L.N. Cooper and J.R. Schrieffer (BCS) [58] and Overhauser [38] developed the theory of electron-electron and electron-phonon interactions and found that low dimensional Fermi fluids are unstable towards the formation of charge-density waves (CDW), superconductivity (SC) or spin-density waves (SDW) at low temperatures. A general overview of the resulting ground states is given in Table 2.3.

The general idea of all these models is that an electron with wave vector k (see Eqn. 2.11), or pairs of electrons in the case of SC with k_1 and k_2, at the Fermi level are allowed to interact with other holes or electrons via Coulomb and electron-phonon interactions. Fröhlich was one of the first to propose a more general Hamiltonian for this interacting system:

$$\mathcal{H} = \mathcal{H}_{\rm el} + \mathcal{H}_{\rm ph} + \mathcal{H}_{\rm el-ph} + \mathcal{H}_{\rm el-el} \tag{2.29}$$

$$\begin{aligned}
\mathcal{H}_{\rm el} &= \sum_{k,\sigma} \epsilon_{k,\sigma} c^\dagger_{k,\sigma} c_{k,\sigma} \\
\mathcal{H}_{\rm ph} &= \sum_{k} \hbar\omega_k b^\dagger_k b_k \\
\mathcal{H}_{\rm el-ph} &= \sum_{k,q,\sigma} u_q c^\dagger_{k+q,\sigma} c_{k,\sigma} (b_q + b^\dagger_{-q}) \\
\mathcal{H}_{\rm el-el} &= \sum_{k,k'} v_{k,k'} c^\dagger_{k,\uparrow} c_{k,\uparrow} c^\dagger_{k',\downarrow} c_{k',\downarrow}.
\end{aligned} \tag{2.30}$$

The first and second term represent the uncorrelated electron and phonon system.

The latter terms arise due to the electron-phonon and electron-electron interaction, where $\mathcal{H}_{\mathrm{el-el}}$ takes the form of the on-site repulsion of Eqn. 2.37. We might interpret the interaction constant $v(k,k')$ as the Fourier transformation of the screened Coulomb potential:

$$v(k,k') = \frac{4\pi e^2}{(k-k')^2 + k_s^2}\left(1 + \frac{\hbar^2\omega_{k-k'}^2}{(\epsilon_k - \epsilon_{k'})^2 - \hbar^2\omega_{k-k'}^2}\right). \tag{2.31}$$

In the presence of virtual phonon exchange between two particles, the screened potential is altered by the second term inside the brackets. Thus if $\hbar^2\omega_{k-k'} > |\epsilon_k - \epsilon_{k'}|$, the retarded Coulomb interaction becomes negative, giving rise to a bound state of the two particles close to the Fermi energy. This spin singlet particle pair with $k = -k' = \pm k_{\mathrm{F}}$ is generally known as Cooper pair. The formation of these pairs is associated with the opening of an energy gap Δ around the FS and the onset of superconductivity.

At the same time electrons at the FS can exchange phonons with the lattice in systems with strong electron-phonon interaction, leading to excited states $k \to k \pm q$ and holes k, which can interact with each other via Coulomb interactions. On the other hand, the emission and absorption of a phonons will lead to a local lattice distortion, which will act back on the electron density via Coulomb interactions. If the exchanged phonons connect two states from opposite sides of the FS i.e. $q = 2k_{\mathrm{F}}$ the interaction will be strongest due to the pile up of electrons and holes in the vicinity of k_F, thus the single-particle dispersion will be strongly renormalised. If the energy gain from the band renormalisation is greater than the energy loss due to the lattice distortion the system will undergo a Peierls transition into a macroscopically lattice distorted state. The periodic lattice distortion with wave length $\lambda = \pi/k_{\mathrm{f}}$ will introduce band gap at the Fermi edge, lowering the band energy of all occupied states for $k < k_{\mathrm{F}}$ and will lead to a reduced total ground state energy.

Overhauser generalised the ideas of Peierls and Fröhlich purely based on spin dependent electron-electron interactions [59, 39]. He replaced the electron-electron interaction in $\mathcal{H}_{el-el}$ by the single particle interaction with a generalised periodic potential (see also Kohn-Sham theorem and density-functional theory [60, 61]):

$$V(r) = \frac{\Delta}{2}\left[\sin(\phi)\sigma\sin(qr) - \cos(\phi)\cos(qr)\right], \tag{2.32}$$

which acts separately on the spin and charge density via the first and second term respectively. This potential leads to a spin dependent charge-density modulation of the form:

$$\rho_{\uparrow}(r) = \frac{1}{2}\rho_0 \left[1 + p_q \cos(qr + \phi)\right] \tag{2.33}$$

$$\rho_{\downarrow}(r) = \frac{1}{2}\rho_0 \left[1 + p_q \cos(qr - \phi)\right]. \tag{2.34}$$

$$\tag{2.35}$$

and opens a gap Δ at the Fermi energy for $q = 2k_{\mathrm{F}}$. If the spin-up and down modulation are in-phase ($\phi = 0$), the corresponding state is a CDW, whereas if they are out-of phase ($\phi = \pm\pi/2$) the net charge modulation is zero and only a SDW appears. It should be emphasised that these charge and spin-density waves are of purely electronic origin and do not necessarily cause a Peierls distortion.

It has been shown that due to the bosonic nature of all three proposed ground states, the temperature dependence of the induced gap follows the BCS temperature dependence:

$$\frac{\Delta(T)}{\Delta_0} = \left[1 - \frac{T}{T_c}\right]^{1/2} \qquad \text{with} \qquad k_{\mathrm{B}}T_c = 1.13\eta \exp\left\{-\frac{1}{\lambda g(\epsilon_{\mathrm{F}})}\right\} \tag{2.36}$$

where the parameters η and λ of the individual systems are connected to the Fermi and Debye energy and associated coupling constants respectively: and the zero

Ground State:	η	λ
Charge-Density Wave	ϵ_{F}	$2u^2_{2k_{\mathrm{F}}}/\hbar\omega_{2k_{\mathrm{F}}}$
Spin-Density Wave	ϵ_{F}	$v_{2k_{\mathrm{F}}}$
Singlet Superconductor	$\hbar\omega_{\mathrm{D}}$	$\bar{v}_{\mathrm{pair}}$

temperature BCS gap is connected to the critical temperature via $\Delta_0 = 1.764 k_{\mathrm{B}}T_c$.

2.2.5 The Hubbard model

So far all of the presented band structure models considered only the underlying periodic potential and kinetic terms of the Schrödinger equation 2.10. However in systems with strong particle interactions arising from e.g. Coulomb or hard-core interactions, the situation is more complex and we need to treat the full Schrödinger equation. In the case of short-range interactions and tight-binding conditions we can employ the Hubbard model [3]:

$$\mathcal{H} = -\sum_{\mathrm{i,j},\sigma} t_{\mathrm{i,j}}(\hat{c}^{\dagger}_{\mathrm{i},\sigma}\hat{c}_{\mathrm{j},\sigma} + \hat{c}^{\dagger}_{\mathrm{j},\sigma}\hat{c}_{\mathrm{i},\sigma}) + U\sum_{\mathrm{i}} \hat{c}^{\dagger}_{\mathrm{i},\uparrow}\hat{c}_{\mathrm{i},\uparrow}\hat{c}^{\dagger}_{\mathrm{i},\downarrow}\hat{c}_{\mathrm{i},\downarrow} + \sum_{\mathrm{i}} \mu\hat{c}^{\dagger}_{\mathrm{i},\sigma}\hat{c}_{\mathrm{i},\sigma}. \tag{2.37}$$

here $t_{\mathrm{i,j}}$ are the tight-binding hopping amplitudes (see Eqn. 2.21) and U represents the on-site repulsion energy arising from a double occupancy of the lattice site R_{i} and μ is the chemical potential. In the case where $U = 0$ the Hubbard Hamiltonian simplifies to the familiar tight-binding Hamiltonian Eqn. 2.22. Thus for $U \ll t$, the system resembles a Fermi liquid or metal with the familiar cosine dispersion relation.

In the case of $U \gg t$ however, the Hubbard Hamiltonian will be governed by the on-site interactions. Neglecting the kinetic terms the possible ground states of a single site are $\{|0\rangle, |\uparrow\rangle, |\downarrow\rangle, 1/\sqrt{2}(|\uparrow\downarrow\rangle + |\downarrow\uparrow\rangle)\}$ corresponding to non-, single- and double occupancy. By inserting these ground states into the partition function Z,

$$Z = \sum_{\mathrm{n}} \langle\phi_n|e^{-\frac{\mathcal{H}}{k_{\mathrm{B}}T}}|\phi_n\rangle \qquad \text{where} \qquad n = 0, 1, 2 \tag{2.38}$$

it is possible to calculate the expectation value of the occupation number for a single site $\langle n\rangle$ as a function of the chemical potential and temperature:

$$\langle n\rangle = \frac{1}{Z}\sum_{\mathrm{n}} \langle\phi_n|ne^{-\frac{\mathcal{H}}{k_{\mathrm{B}}T}}|\phi_n\rangle = 2\frac{e^{\mu/k_BT} + e^{(2\mu-U)/k_BT}}{1 + 2e^{\mu/k_BT} + e^{(2\mu-U)/k_BT}} \tag{2.39}$$

A graphical representation of the occupation number as a function of the chemical potential and temperature is shown in Figure 2.8. As can be seen, neglecting any underlying band structure the system consists of singly occupied sites at half filling. For higher fillings an additional energy U is needed to add another particle to the same site. This energy gap is called the Mott gap U [2]. Thus at half filling i.e. at

single occupancy $\langle n \rangle = 1$, where the smallest possible excitation energy is U, the system can no longer be described as a Fermi liquid but rather as a so called Mott insulator [2].

Even in the Mott insulating state the system can still lower its ground state energy by second order tunneling processes. These processes are virtual particle exchanges between two neighboring Fermions rather than single particles tunneling from site i to i $\pm$ 1. The Hamiltonian of these virtual particle exchanges can be written as:

$$\mathcal{H}_{ex} = \sum_{\langle \mathrm{i,j} \rangle, \sigma} \frac{t_{\mathrm{i,j}}^2}{U} \hat{c}_{\mathrm{i},\sigma}^{\dagger} \hat{c}_{\mathrm{j},\sigma'} \hat{c}_{\mathrm{j},\sigma'}^{\dagger} \hat{c}_{\mathrm{i},\sigma} \tag{2.40}$$

By using the relation $S_{\mathrm{z,i}} = n_{\mathrm{i},\uparrow} - n_{\mathrm{i},\downarrow}$. Eqn. 2.40 can be simplified to:

$$\mathcal{H}_{ex} = \frac{1}{2} \sum_{\langle \mathrm{i,j} \rangle} J_{\mathrm{i,j}} (\frac{1}{2} + 2 S_{\mathrm{z,i}} \cdot S_{\mathrm{z,j}}) \qquad \text{with} \qquad J_{\mathrm{i,j}} = \frac{2 t_{\mathrm{i,j}}^2}{U} \tag{2.41}$$

This is the exchange energy arising from virtual particle exchanges in the t-J model which goes back to P.W. Anderson [62]. Anderson derived in 1959 that a Mott insulator has an antiferromagnetically ordered ground state due to virtual tunneling processes [63](see Fig. 2.8).

So far we have only discussed the two limiting cases $U \ll t$ and $U \gg t$, which led to metallic and insulating behaviour respectively. It is clear that in between the two limits there must be a critical value of U/t at which the system undergoes a phase transition from the metallic into the insulating state the so called Mott transition. Unfortunately for intermediate U/t the Hubbard Hamiltonian can no longer be solved analytically and the precise ground state of the system can only be determined by variational or numerical methods.

The Almost Localised Fermion Model

Early variational studies by Gutzwiller and later Brinkman and Rice [64, 65] were able to approximate the ground state energy per particle $\bar{\epsilon}$ and density of double occupancies $\langle n_{\uparrow\downarrow} \rangle$ in the metallic state when the system is approaching the Mott

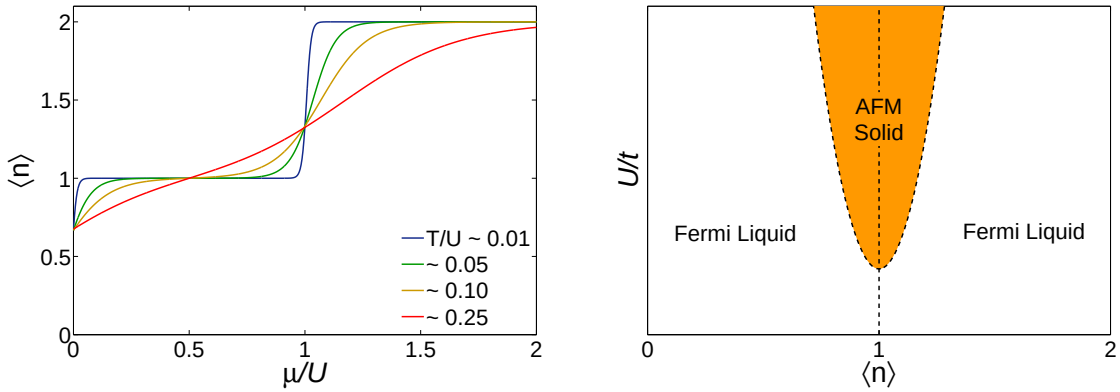

Figure 2.8: The left graph shows the statistical site occupation for the Hubbard model with $U \gg t$ for a varying chemical potential μ and temperature T. At low temperatures and energies sites are singly occupied and require an energy $\mu = U$ to become doubly occupied. This energy gap leads to the Mott insulating state. With increasing temperature fluctuations will increase double occupancy in the system and destroy the Mott insulating state. The right-hand side graph shows a qualitative phase diagram of the Hubbard Hamiltonian with its extended antiferromagnetic insulating phase around half filling.

transition $U \to U_c$:

$$\bar{\epsilon} = \frac{U_c}{8}\left(1 - \frac{U}{U_c}\right)^2 \qquad \text{and} \qquad \langle n_{\uparrow\downarrow}\rangle = \frac{1}{4}\left(1 - \frac{U}{U_c}\right). \tag{2.42}$$

Both quantities vanish when the system becomes critical i.e. $U = U_c$. Since U_c is generally a function of the filling n it is possible to tune Hubbard systems through a Mott transition by either increasing the particle interaction or density. In both cases Brinkman and Rice [65] calculated the dependence of the zeroth and first order Landau parameters on U/U_c. Here F_0^s, F_0^a and F_1^s are thought to follow:

$$F_0^s = \propto \left(\frac{m^*}{m}\right)^2 \qquad \text{with} \qquad \frac{m^*}{m} = \left(1 + \frac{F_1^s}{3}\right) = \frac{1}{1 - (U/U_c)^2} \tag{2.43}$$

$$\text{and} \qquad 1 + F_0^a = \frac{1}{(1 + \sqrt{1 - m/m^*})^2} \tag{2.44}$$

On approaching the Mott transition the system will show divergencies in the effective mass and compressibility, which is consistent with an increasing localisation tendency in the system. D. Vollhardt used the results of Hubbard, Gutzwiller, Brinkman, Rice and Anderson [3, 66, 65, 67, 68] and applied the results to measurements on three-dimensional bulk ^{3}He [69]. The resulting "Almost Localised Fermion Model" [18] showed that three-dimensional bulk ^{3}He, is not, as was believed, close to a ferromagnetic instability (see Sec. 2.1.2), but rather to localisation driven by the strong on-site repulsion.

It was shown that the observed susceptibility enhancement in ^{3}He on approaching solidification is driven by the effective mass renormalisation, on approaching the critical on-site repulsion, rather than the weak density dependence of F_0^a:

$$\frac{\chi}{\chi_0} = \frac{1 + F_0^a}{m^*/m}. \tag{2.45}$$

However, Vollhardts application of the Gutzwiller, Brinkman and Andersons result to bulk ^{3}He is purely empirical and based on the assumption that the Mott-Hubbard physics does not rely on tight binding sites but rather on short range spacial correlations. We will see in Section 4.3.5 how this negligence of the actual structure, leads to a different metal-insulator transition scenario in two-dimensional ^{3}He on graphite.

Phase Coexistence

As the Mott transition is a first order transition that breaks the translational or rotational symmetry of the paramagnetic Fermi fluid, hysteresis effects are expected to be observed as the system approaches this phase transition. Here the almost degenerate chemical potentials of the Mott insulator and strongly correlated fluid lead to extensive phase coexistence regions in the vicinity of the Mott transition. The precise nature of this fluid-solid coexistence region is still subject of intensive experimental and theoretical efforts. Particularly the role of finite temperature and preceding charge and spin ordering are of central interest.

Recently Vucicevic *et al.* have obtained a finite temperature phase diagram of the maximally frustrated Hubbard model by applying Dynamic-Mean-Field Theory

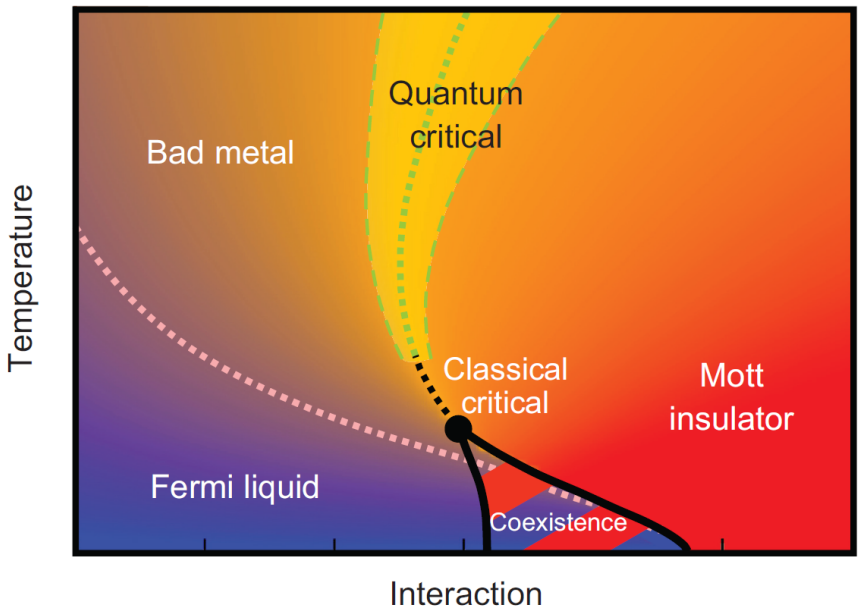

Figure 2.9: DMFT phase diagram of the maximally frustrated Hubbard model at finite temperature taken from [70].

(DMFT)(see Fig. 2.9) [70]. In this model magnetic ordering is suppressed by taking into account long-range and magnetically frustrating inter-site hoppings, which make it possible to study the Mott transition at low temperatures without being preceeded by a magnetic transition. This situation is equivalent to a magnetically frustrated triangular lattice Mott insulator as found in two-dimensional ^{3}He. In their phase diagram, upon increasing the on-site repulsion at low temperatures the system undergoes a phase transition from a strongly correlated Fermi liquid at $U < U_c$ to a Mott insulating state at $U > U_c$. In the region of $U \approx U_c$, however, the Mott transition is masked by the onset of a phase coexistence region, which was studied more closely for the isotropic triangular lattice by Liebsch *et al.* [71]. On increasing the temperature of the system, the phase coexistence region shrinks, and the two critical interactions for the onset of the phase coexistence and pure Mott insulator merge into a finite temperature critical point. The temperature of this critical end point T_c was argued to be much smaller than the typical energy scales of the system e.g. the Fermi energy ϵ_F and on-site repulsion U and might thus be regarded as a

quasi-zero temperature quantum critical point (QCP). Thus the question arises as to whether such a system shows signs of quantum critical scaling above the QCP. Stimulated by resistivity measurements on metal-oxide field-effect transistors and organic charge-transfer salts, Vucicevic *et al.* calculated the resistivity and found an extensive quantum critical region at high temperatures in which scaling takes place and the system behaves like a bad metal.

2.3 The Magnetism of the Mott Insulator

2.3.1 Antiferromagnetism and Geometrical Frustration

As we have already seen in section 2.2.5, the first order expansion of the Hubbard Hamiltonian to higher order hopping terms leads to an antiferromagnetic exchange in the Mott insulator. Here it follows that two-particle exchange between neighboring sites close to half filling leads to the familiar Heisenberg Hamiltonian:

$$\mathcal{H} = J_2 \sum_{\langle \mathrm{i,j} \rangle} S_\mathrm{i} S_\mathrm{j} + \frac{1}{2} \tag{2.46}$$

with an antiferromagnetic exchange constant J_2 as derived from Eqn. 2.41. In solids with a cubic crystal structures, this antiferromagnetic exchange will give rise to an antiferromagnetically ordered ground state.

In two-dimensional ^{3}He, however, the Mott insulator forms an isotropic triangular lattice. In this case, it is obvious that a strict antiparallel alignment of all three spins in each triangle, as would be favoured by the Heisenberg exchange, is impossible. Thus one might find two solutions to recover the antiferromagnetic exchange in this case: (1) in the limit of classical spins the system develops a 120^o order i.e. the system splits into three ferromagnetic sublattices whose spins have a relative orientation of 120^o (2) the system forms fluctuating singlet bonds between neighboring spins in analogy to electrons in a benzene molecule (see Fig. 2.10). In the first scenario the fundamental excitations of the systems are spin waves i.e. bosonic magnons, whereas in the latter case the excitations are spin-$^1/_2$ fermions, as shown in Figure 2.10, which can form a delocalised spin-liquid.

Even though the 120^o Neel ordered state seems to have the lower ground state

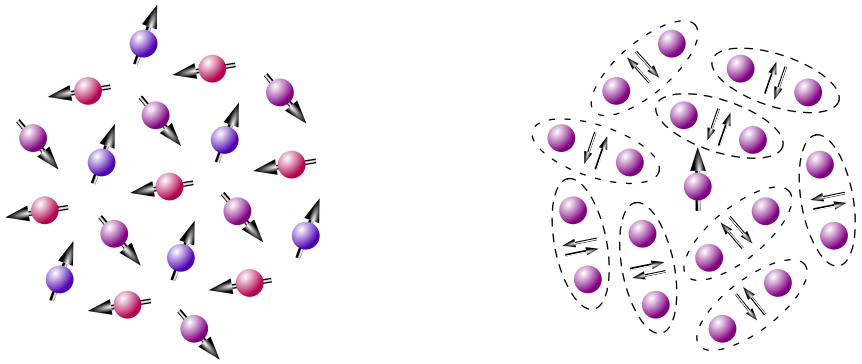

Figure 2.10: Antiferromagnetic Ground states of the Isotropic Triangular Lattice. Antiferromagnetic exchange on an isotropic triangular lattice leads to geometrical frustration of the magnetic ground state, thus the system might establish a 120^o spin order, as shown in the left, or resonating singlet bond state, as shown in the right-hand side graph.

energy compared to the resonating valence bond state, initial spin-wave theory and numerical calculations suggested the vanishing of the sublattice magnetisation and thus the destruction of the long-range ordered state [72]. Only recently by applying Greens function Monte Carlo and density matrix renormalisation group methods a finite sublattice magnetisation of $\langle S \rangle \approx 0.2$ was found, proving the existence of long range order in the 120^o triangular Heisenberg antiferromagnet [73].

Other authors realised the general importance of higher order particle exchanges for the stabilisation of either of the two phases [27, 28, 29]. Thus the following section will focus on higher order spin exchange processes in triangular lattice solids.

2.3.2 Multiple Spin Exchange

The idea of multiple spin exchanges was first proposed by Thouless in 1965 for solid ^{3}He [74]. In his paper Thouless argued that due to the large zero-point motion in ^{3}He higher order spin exchange processes of atoms are likely and will give rise to new magnetic interactions.

The underlying multiple spin exchange Hamiltonian can be derived by extending the t-J model or Heisenberg model to higher order particle exchanges:

$$\mathcal{H}_{\mathrm{MSE}} = \sum_{\mathrm{n}\geq 2} J_{\mathrm{n}} \left(\mathcal{P}_{\mathrm{n}} + \mathcal{P}_{\mathrm{n}}^{-1}\right), \tag{2.47}$$

here $\mathcal{P}_{\mathrm{n}}$ are the n-particle permutation operators. The multiple spin exchange model can thus be thought of as an expansion of the Hubbard Hamiltonian Eqn. 2.37 with $U \gg t$ close to half filling to an arbitrary order in $t_{\mathrm{i,j}}$, where the particle permutation operators can be expressed as virtual cyclic tunneling processes on a ring of n adjacent sites:

$$\mathcal{P}_2 = \sum_{\langle \mathrm{i,j}\rangle} \hat{c}^{\dagger}_{\mathrm{i},\sigma} \hat{c}_{\mathrm{j},\sigma'} \hat{c}^{\dagger}_{\mathrm{j},\sigma'} \hat{c}_{\mathrm{i},\sigma} \qquad \text{and} \qquad \mathcal{P}_3 = \sum_{\langle \mathrm{k,l,m}\rangle} \hat{c}^{\dagger}_{\mathrm{k},\sigma} \hat{c}_{\mathrm{m},\sigma''} \hat{c}^{\dagger}_{\mathrm{m},\sigma''} \hat{c}_{\mathrm{l},\sigma'} \hat{c}^{\dagger}_{\mathrm{l},\sigma'} \hat{c}_{\mathrm{k},\sigma} \tag{2.48}$$

where:

$$J_{\mathrm{n}} = (-1)^{\mathrm{n}} \mathcal{O}\left(\frac{t^{\mathrm{n}}_{\mathrm{i,j}}}{U^{\mathrm{n}-1}}\right). \tag{2.49}$$

Since this model is applied to Fermions, all permutations must obey the general anti-symmetry of the n-particle wave function for particle and spin permutations. Thus for exchanging two identical particles the spin part of the wave function is antisymmetric and it follows that even particle ring exchanges lead to antiferromagnetic exchange, whereas odd particle exchanges result in ferromagnetic exchange (see Eqn. 2.49).

In the case of three-particle ring exchange, $\mathcal{P}_3$ can be written as the sum of three two-particle exchanges $\mathcal{P}_2$, leading to an effective two-particle exchange constant $J = J_2 + 2J_3$.

Thus in triangular lattice systems with significant higher order ring exchanges, the system will not only show geometrical frustration but also magnetic frustration due to competing n-particle ring exchanges.

2.3.3 High Temperature Series Expansion

The magnetisation of an ensemble of spins can be derived from the partial derivative of its free energy $\mathcal{F}$ with respect to the magnetic field B

$$M = -\frac{1}{\mu_{\mathrm{F}}}\frac{\partial \mathcal{F}}{\partial B} \qquad \text{with} \qquad \mathcal{F} = -k_{\mathrm{B}}T \ln Z, \tag{2.50}$$

where the partition sum Z is defined in Eqn. 2.38. At temperatures $k_{\mathrm{B}}T > J$ well above the characteristic exchange energies, the partition sum i.e. the underlying multiple spin exchange Hamitonian:

$$\mathcal{H} = \mathcal{H}_{\mathrm{MSE}} - \sum_{\mathrm{i}} \mu S_{\mathrm{i}} B \tag{2.51}$$

might be expanded in terms of $1/k_{\mathrm{B}}T$ leading to:

$$\frac{\ln Z}{N} = \sum_{\mathrm{n}} \sum_{\mathrm{i,k,l}} \frac{a_{\mathrm{n,i,k,l}}}{\mathrm{n!}} \left(\frac{J}{2}\right)^{\mathrm{n-i-k-l}} \left(\frac{J_4}{8}\right)^{\mathrm{i}} \left(\frac{J_5}{16}\right)^{\mathrm{k}} \left(\frac{J_6}{32}\right)^{\mathrm{l}} \left(\frac{1}{k_{\mathrm{B}}T}\right)^{\mathrm{n}}. \tag{2.52}$$

Roger *et al.* have calculated the coefficients $a_{\mathrm{n,i,k,l}}$ for a triangular lattice system up to the sixth order in temperature [75]. Following his expansion the low field magnetisation of a two-dimensional triangular lattice magnet with multiple spin exchange can be written as:

$$\begin{aligned} M(T) &= N\frac{\mu^2 B}{3k_{\mathrm{B}}T}\left(1 + \sum_{\mathrm{n}\geq 1} \frac{J^{(\mathrm{n})}}{(k_{\mathrm{B}}T)^{\mathrm{n}}}\right) \qquad \text{with:} \\ & J^{(1)} = -3J - 9J_4 + 15J_5 - \frac{15}{8}J_6. \end{aligned} \tag{2.53}$$

In the non-interacting case where all $J_{\mathrm{n}} = 0$ i.e. in the paramagnetic state, the HTSE returns the well known Curie law. Whereas for finite J_{n} and first order in $1/k_{\mathrm{B}}T$ one obtains the Curie-Weiss law:

$$M(T) = \frac{C}{T + \Theta} \qquad \text{with} \qquad C = N\frac{\mu^2 B}{3k_{\mathrm{B}}} \qquad \text{and} \qquad \Theta = 3J^{(1)}, \tag{2.54}$$

where C is the Curie-Weiss constant and Θ the Curie-Weiss temperature.

2.3.4 Quantum Spin Liquids

As discussed in Section 2.3.1 the magnetic ground state of a geometrically frustrates triangular lattice solid is non-trivial. In the classical limit the triangular lattice or for dominating nearest neighbor exchange the solid will develop a 120^o Neel order, which can be described by the multiple-spin-exchange model and the high-temperature-series expansion outlined in the preceding two sections.

In a quantum mechanical spin-$1/_2$ system with strong magnetic frustration, however, the system might establish a quantum-spin liquid (QSL). The following description of QSLs is based on a talk by Yong-Baek Kim at the Perimeter Institute in Waterloo, Canada [76]. The QSL is chacterised by short or long-range correlations of spin-singlet pairs, in which, depending on the type of QSL, the individual spins are delocalised and form a fluid whilst the charge carriers themselves remain localised. The system can therefore be interpreted as a charge insulator and spin liquid with charge-spin separation.

A typical way of describing QSL is by the resonating valence bond model as introduced by Anderson [26]. Here the antiferromagnetically correlated spins from spin-singlet pairs. The excitation in such a system are characterised by fermionic spinon-antispinon, particle-hole pairs. In the case of a resonating valence bond solid, the singlet bonds extend over nearest neighbor pairs and form a lattice. This lattice formation might be triggered by anisotropies within the solid or exchange constants, i.e. $J \neq J'$. Thus the system reduces its translational symmetry and forms a non-magnetic ordered state. If these nearest neighbor singlets,however, are fluctuating the spin liquid ground state has the same symmetry as the charge insulator. This is usually the case for a gapped QSL, where spin-spin correlations or singlet bonds are restricted to short length scales. The spin-spin correlation in such a system decays as:

$$\langle S_\mathrm{i} S_\mathrm{j} \rangle \propto \exp\left\{-\frac{\Delta}{r_\mathrm{ij}}\right\} \tag{2.55}$$

where Δ is the spinon excitation gap. If the spinon dispersion is ungapped these correlations, singlet pairs, can extend over the entire sample and their correlation

function goes as:

$$\langle S_{\mathrm{i}} S_{\mathrm{j}} \rangle \propto \frac{1}{r_{\mathrm{ij}}^{\alpha}}. \tag{2.56}$$

In the former case, the magnetism of the system is characterised by a vanishing magnetisation and thermally activated heat capacity at low temperatures, whilst the latter case shows a Pauli-like Fermi fluid magnetisation and a heat capacity following a power-law in temperature.

A more theoretical classification of spin liquids is based on slave particle theories. Here the spin in the ususal Heisenberg Hamiltonian is replaced by fermionic operators:

$$\mathcal{H} = \sum_{\mathrm{i,j}} J_{\mathrm{i,j}} S_{\mathrm{i}} S_{\mathrm{j}} \qquad \Rightarrow \qquad \mathcal{H} = \sum_{\mathrm{i,j}} J_{\mathrm{i,j}} f_{\mathrm{i}\alpha}^{\dagger} f_{\mathrm{i}\beta}^{\dagger} f_{\mathrm{j}\beta} f_{\mathrm{j}\alpha} + \ldots. \tag{2.57}$$

Here the condition of single occupancy has to be satisfied, as the system is in a Mott insulating state. A mean-field treatment of the slave-fermion hamiltonian yields the mean-field Hamiltonian:

$$\mathcal{H} = \sum_{\mathrm{i,j}} \Big(\chi_{\mathrm{i,j}} f_{\mathrm{i}\alpha}^{\dagger} f_{\mathrm{j}\beta} + \Delta_{\mathrm{i,j}} \epsilon_{\alpha,\beta} f_{\mathrm{i},\alpha} f_{\mathrm{i},\beta} + h.c. \Big). \tag{2.58}$$

The first part of this Hamiltonian describes the kinetic energy, i.e. band structure, of the spinons as arising from particle-hole correlations. The second part of the equation is associated with pairing of spinons and gives rise to a gap in the spinon spectrum, much like in the case of BCS superfluids. The gap symmetry of this SL can be classed by the same s, p and d-like pairing wave functions as in superfluids. Here the short range singlets might be interpreted as incoherent cooper pairs.

In the unpaired case, $\chi \neq 0$ and $\Delta_{\mathrm{ij}} = 0$ the mean-field Hamiltonian is U(1) gauge invariant:

$$\mathcal{H} = \sum_{\mathrm{i,j}} \Big(\chi_{\mathrm{i,j}} f_{\mathrm{i}\alpha}^{\dagger} f_{\mathrm{j}\beta} \Big) \qquad \Rightarrow \qquad \mathcal{H} = \sum_{\mathrm{i,j}} \Big(|\chi| e^{i\alpha_{\mathrm{ij}}} f_{\mathrm{i}\alpha}^{\dagger} f_{\mathrm{j}\beta} \Big) \tag{2.59}$$

where $f_{\mathrm{i}\alpha} \rightarrow f_{\mathrm{i}\alpha} e^{i\theta_{\mathrm{i}}}$ and $\alpha_{\mathrm{ij}} \rightarrow \alpha_{\mathrm{ij}} + \theta_i - \theta_j$ are the gauge invariants.

In the pairing case,$\chi \neq 0$ and $\Delta_{ij} \neq 0$ the U(1) gauge symmetry reduces to a Z_2 Ising gauge field invariance, i.e. $\alpha_{ij} = 0$ or π resulting in a ± 1 gauge field. The following ground state shows topologically protected valence bond orders and fractionalised excitations.

Generally the thermodynamical properties of these spin liquids will be determined by their band structure and gap symmetry. Fully gaped system will, as mentioned before, develop a thermally excited heat capacity and vanishing zero-temperature magnetisation, whilst nodal systems and ungapped system with Dirac points in their band structure develop a finite zero-temperature magnetisation but a T^2 specific heat. In the simplest ungapped case with an extended spinon Fermi surface the system shows the same properties as a Fermi liquid with a T-linear heat capacity and constant Pauli-like susceptibility.

More recent calculations by Motrunich [29] have shown that gauge field fluctuations alter the T-linear specific heat to produce a $T^{2/3}$-dependence in two dimensional and $T \ln 1/T$-dependence in three-dimensional systems instead.

Misguich, LiMing and Motrunich *et al.* [27, 28, 29] have studied the influence of charge fluctuations on the magnetic ground state of a spin-$1/2$ triangular lattice solid. Such fluctuations will occur close to a metal-insulator and in particular Mott transition and give rise to higher order ring exchanges (see Sec. 2.3.2) and therefore long-range spin correlations. The suggested phase diagrams of of these calculations are summarised in Figure 2.11.

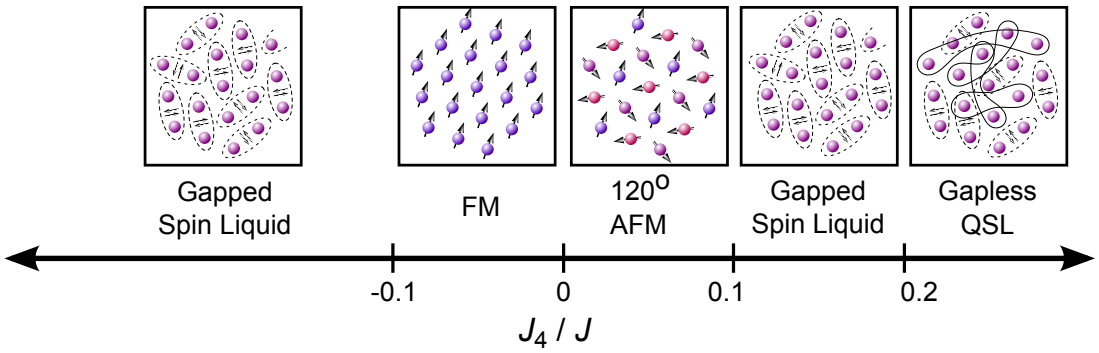

Figure 2.11: Spin liquid phases in the triangular lattice solid with competing multiple spin exchange.

2.4 Nuclear Magnetic Resonance

Nuclear magnetic resonance (NMR) is a powerful technique to probe the local environment of atoms and spins. Nuclei carrying a magnetic moment are polarised in an external magnetic field and brought out of equilibrium by applying a rf-tipping pulse. The following relaxation and Larmor-precession of the spins can be measured as free-induction decay (FID) and gives information about their spin-species, local fields and relaxation times. Nowadays NMR plays an important role in non-invasive imaging techniques such as magnetic resonance imaging (MRI) or chemical analysis i.e. NMR-spectroscopy. In our experiments NMR is used to characterise the magnetism and spin-dynamics of two-dimensional ^{3}He at ultra-low temperatures. Thus the following section is devoted to explain the basic theory behind these measurements and follows the book "Nuclear Magnetic Resonance and Relaxation" by B.P. Cowan [77].

2.4.1 Spins in a Magnetic Field

Most atoms with an odd number of protons or neutrons in their nucleus possess a nuclear magnetic moment $\mu_N = \gamma\hbar I$ which is proportional to the nuclear spin I and its gyromagnetic ratio γ. In an external magnetic field B this nuclear magnetic

moment will experience a torque proportional to:

$$\hbar \dot{I} = \mu_{\mathrm{N}} \times B = \frac{\dot{\mu}_{\mathrm{N}}}{\gamma}. \tag{2.60}$$

Let us assume that the nuclear moment has a large spin quantum number and behaves classically i.e. the nuclear moment has an infinite number of spin projections and the magnetic field is applied along the z-axis. In this classical case it is possible to solve the differential Eqn. 2.60 leading to:

$$\begin{aligned} \dot{\mu}_{\mathrm{N}}^{(x)} &= \gamma B \mu_{\mathrm{N}}^{(y)} & & & \mu_{\mathrm{N}}^{(x)}(t) &= \mu_{\mathrm{N}} \sin(\theta) \cos(\gamma B t) \\ \dot{\mu}_{\mathrm{N}}^{(y)} &= -\gamma B \mu_{\mathrm{N}}^{(x)} & \Rightarrow & & \mu_{\mathrm{N}}^{(y)}(t) &= -\mu_{\mathrm{N}} \sin(\theta) \sin(\gamma B t) \\ \dot{\mu}_{\mathrm{N}}^{(z)} &= 0 & & & \mu_{\mathrm{N}}^{(z)}(t) &= \mu_{\mathrm{N}} \cos(\theta) \end{aligned} \tag{2.61}$$

where θ is the polar angle with respect to the magnetic field. The solution on the right-hand side shows that a magnetic moment, tilted away from the magnetic field direction, develops a transverse component in the xy-plane, which starts to rotate around the magnetic field with a frequency $\omega = \gamma B$. This is the Larmor precession with its associated Larmor frequency. As a consequence of the lack of relaxation in Eqn. 2.61, magnetic moments with a finite angle θ to the magnetic field will continuously precess around the magnetic field axis and never recover to their equilibrium, parallel to the magnetic field. Even though this model is suited to describe the precession of spins in a magnetic field it fails to accommodate the relaxation observed in real systems.

Since NMR is usually applied to large systems of 10^{19} to 10^{24} nuclear spins, it is at this stage convenient to introduce the nuclear magnetisation M which in analogy to Eqn. 2.3 can be written as:

$$M = \mu_{\mathrm{N}}(N_{\uparrow} - N_{\downarrow}) \tag{2.62}$$

If we consider a non-interacting spin ensemble i.e. a paramagnet then its equilibrium magnetisation $M(B, T)$ is described by:

$$M = n\mu_{\mathrm{N}} \mathcal{B}\left(\frac{\mu_{\mathrm{N}} B}{k_B T}\right), \tag{2.63}$$

where n is the volume density of magnetic moments and $\mathcal{B}(x)$ the Brillouin-function. This relation can be derived from first principles from the thermal activation i.e. Boltzmann-distribution of Zeeman-split spin states in a magnetic field. In the small polarisation limit i.e. for high temperatures and low magnetic fields, this equation can be approximated to the familiar Curie law[78, 79]:

$$M = \frac{n\gamma^2\hbar^2 I(I+1)}{3k_B}\frac{B}{T}. \tag{2.64}$$

In the fully polarised limit Equation 2.63 reduces to:

$$M_0 = n\gamma\hbar I. \tag{2.65}$$

It can be shown from the application of the Heisenberg equation to the expectation value of the nuclear momentum operator that an ensemble of quantum mechanical spins behaves like a classical spin. In order to comply with the quantum mechanical nature of the nuclear moments, hereinafter the expectation value of the quantum mechanical spin ensemble i.e. its magnetisation is used rather than the nuclear moment.

As already mentioned, in a real system out-of equilibrium magnetisations relax back to their thermal equilibrium pointing along the magnetic field with a value of M_∞. During this process the transverse component of the magnetisation must vanish, whilst the longitudinal magnetisation recovers to its equilibrium value. Here the two time scales for the longitudinal and transverse relaxation are referred to as T_1 and T_2^* respectively. Bloch introduced the concept of these relaxation times in 1946 [80], leading to the formulation of the Bloch equations:

$$\begin{aligned} \dot{M}_x &= \gamma|M \times B|_x - M_x/T_2^* \\ \dot{M}_y &= \gamma|M \times B|_y - M_y/T_2^* \\ \dot{M}_z &= \gamma|M \times B|_z + (M_\infty - M_z)T_1. \end{aligned} \tag{2.66}$$

The solutions of the Bloch equations are:

$$\begin{aligned} M_x(t) &= M_\infty \sin(\theta)\cos(\gamma B t)\exp\left\{-\frac{t}{T_2^*}\right\}, \\ M_y(t) &= -M_\infty \sin(\theta)\sin(\gamma B t)\exp\left\{-\frac{t}{T_2^*}\right\}, \\ M_z(t) &= M_\infty - M_\infty(1-\cos(\theta))\exp\left\{-\frac{t}{T_1}\right\}. \end{aligned} \tag{2.67}$$

Here the Larmor precession in the xy-plane is damped by an exponential decay with a characteristic time T_2^* leading to the vanishing of the transverse magnetisation. The longitudinal magnetisation, however, recovers exponentially with the time scale T_1 to its thermal equilibrium. The microscopic origin of both of these relaxation processes will be described in the following section.

2.4.2 Microscopic Origin of the Relaxation Times

So far we have assumed that the nuclear spin ensemble is non-interacting and surrounded by a uniform, time independent magnetic field B. In reality, however, spins interact with each other via dipole-fields and magnetic exchange. Here the local field at each spin is a superposition of the mean external field B_0 and internal fields $b_\mathrm{i}(t)$ arising from sample inhomogeneities, fluctuating dipole-fields and field gradients of the external magnetic field. Thus spins from different positions "i" experience marginally different magnetic fields and precess at slightly different Larmor frequencies $\omega_\mathrm{i} = \gamma(B_0 + b_\mathrm{i})$.
In a system of spatially fixed spins and time independent local fields b_i, which point along B_0, the total precessing magnetisation can be expressed as the sum of all local precessing magnetisations:

$$M_\perp(t) = \frac{M_\perp(0)}{N}\sum_\mathrm{i}^N e^{i\gamma(B_0+b_\mathrm{i})t} = M_\perp(0)e^{i\gamma B_0 t}\langle e^{i\gamma b_\mathrm{i} t}\rangle \tag{2.68}$$

By separating out the mean Larmor frequency, it can be seen that spins from different sites "i" acquire a time dependent phase $\phi_\mathrm{i}(t)$ depending on the local field b_i (see also Eqn. 2.69). Thus after a characteristic time of $5T_2^*$ the spin ensemble will have

completely dephased and the transverse component of the magnetisation vanished. Here the relaxation time T_2^* is inversely proportional to the spread of local frequencies or fields $\gamma\langle b_\mathrm{i}\rangle^{1/2}$.

In mobile system, however, spins can diffuse through the system and experience an ensemble of local fields in the vicinity of their original position. Here the diffusive motion will lead to an averaging of the surrounding local fields and thus reduction of the spin dephasing. In order to incorporate the motion in this model the static local field b_i is replaced by a time dependent field $b_\mathrm{i}(t)$ and Eqn. 2.68 can be rewritten as:

$$M_\perp(t) = M_\perp(0)e^{i\gamma B_0 t}\langle e^{i\phi(t)}\rangle \qquad \text{with:} \qquad \phi_\mathrm{i}(t) = \int_0^t \gamma b_i(\tau)d\tau. \tag{2.69}$$

In the Gaussian limit where the $\phi_\mathrm{i}(t)$ are Gaussian distributed the phase expectation value can be replace by the transverse decay function:

$$F(t) = \langle e^{i\phi(t)}\rangle \qquad \text{with:} \qquad F(t) = \exp\left(-\int_0^t (t-\tau)G(\tau)d\tau\right) \tag{2.70}$$

where $G(\tau)$ is the auto-correlation function of the local magnetic field: $\gamma^2\langle b_\mathrm{i}(0)b_\mathrm{i}(\tau)\rangle$. Here the correlation time τ_c is introduced, which can be interpreted as the time over which b_i stays constant. For times $t \gg \tau_c$ the auto-correlation function tends to zero and Eqn. 2.70 reduces to an exponential decay. At short times $t \ll \tau_c$, however, the auto-correlation function is almost constant and $F(t)$ becomes Gaussian.

Thus we can summarise that transverse relaxation is a consequence of field inhomogeneity inside the sample, where the transverse relaxation time is a measure of the internal field distribution.

In order to understand the longitudinal relaxation, it is necessary to go back to the microscopic model of magnetic moments in a magnetic field. The Hamiltonian this system is described by:

$$\mathcal{H} = \mathcal{H}_Z + \mathcal{H}_{d-d} + \mathcal{H}_k \qquad \text{with:} \tag{2.71}$$

$$\begin{aligned}
\mathcal{H}_Z &= -\hbar\gamma I \cdot B_0 \\
\mathcal{H}_{d-d} &= \hbar^2\left(\frac{\mu_0}{4\pi}\right)\sum_{i\neq j}\gamma_i\gamma_j\left[\frac{I_i\cdot I_j}{r_{ij}^3} - 3\frac{(I_i\cdot r_{ij})(I_j\cdot r_{ij})}{r_{ij}^5}\right],
\end{aligned}$$

where $\mathcal{H}_Z$ is the Zeeman energy, $\mathcal{H}_{d-d}$ the dipole-dipole interaction and $\mathcal{H}_k$ the kinetic energy of the spins in a magnetic field. In the absence of dipole-dipole interactions the Hamiltonian Eqn. 2.72 leads to the continuous Larmor precession of Eqn. 2.61.

A finite dipole-dipole interaction, however, enables the exchange of energy and spin resulting in longitudinal relaxation. Here the dipole-dipole Hamiltonian includes all interactions between nuclear spins and hyperfine-coupling to electrons. The fluctuating fields that mediate the exchange are either induced by diffusion of a nuclear spin through a field gradient or time dependent local fields as produced by Larmor precessing nuclear spins and electrons. As in the case of the transverse relaxation the time dependence of these field fluctuations is of key importance. Transverse local fields oscillating at frequencies close to harmonics of the Larmor frequency can inducing spin flips, thus leading to energy and angular momentum exchange. Here the probability of a spin flip is proportional to the spectral density of the local field at integer multiples of the Larmor frequency where the spectral density is the Fourier transformation of the auto-correlation function of the local field b_i. For longitudinal relaxation, only those spin flip processes are of importance that change the net total energy or spin of the system. Spin exchange processes that conserve the total spin, however, will contribute to the transverse relaxation.

In conclusion the longitudinal relaxation time T_1 is a measure of how effectively a nuclear spin species can exchange energy and spin with its environment (lattice). Due to the resonant nature of spin flips involved in the longitudinal relaxation, T_1 can be used to probe the auto-correlation time of the local field. As for the transverse relaxation time, T_1 depends strongly on local field fluctuations and spin diffusion, thus both relaxation times can be used to probe the spin-dynamics of the system.

2.4.3 Pulsed NMR and Relaxation Time Measurements

In order to measure the magnetisation and spin dynamics of a nuclear spin species it is necessary to first generate an out-of equilibrium magnetisation and probe its subsequent Larmor precession and relaxation. The spin manipulation and measurement method deployed in this thesis is pulsed NMR.

Pulsed NMR

In pulsed NMR resonant magnetic field pulses at the Larmor frequency are applied perpendicular to external magnetic field to produce an out of equilibrium magnetisation which then undergoes Larmor precession as well as transverse and longitudinal relaxation. Here it is useful to introduce a coordinate system precessing around the external magnetic field at the mean Larmor frequency namely the rotating frame. By coordinate transformation from the resting into rotating frame:

$$r'(t) = \begin{pmatrix} \cos(\omega t) & \sin(\omega t) & 0 \\ -\sin(\omega t) & \cos(\omega t) & 0 \\ 0 & 0 & 1 \end{pmatrix} r \tag{2.72}$$

the apparent external magnetic field in the rotating frame $B_0(r')$ is zero whereas internal fields give rise to finite fields. Resonant magnetic fields applied along one of the axes in the xy-plane, can be modeled as two counter rotating waves in the xy-plane:

$$B_T(t) = B_T \cos(\omega t) = B_T \frac{e^{i\omega t} + e^{-i\omega t}}{2}. \tag{2.73}$$

In the rotating frame, one of these two waves rotates in unison with the frame and appears static, whereas the other counter rotates at double the Larmor frequency. Therefore it might be argued that the latter component can be neglected as its effect averages out. So to conclude, in the rotating frame the external magnetic field vanishes, magnetic fields applied perpendicular to the magnetic field direction appear as static fields in the xy-plane with half of their original amplitude and local fields depending on their direction and correlation time will produce effective fields along the rotation axis or in the xy-plane.

In the thermal equilibrium the magnetisation pointing along magnetic field has a value of M_∞. If a transverse magnetic field pulse at the Larmor frequency is applied, the magnetisation originally pointing along B_0 will start to Larmor precess around the apparent static transverse magnetic field in the rotating frame. Following Eqn.

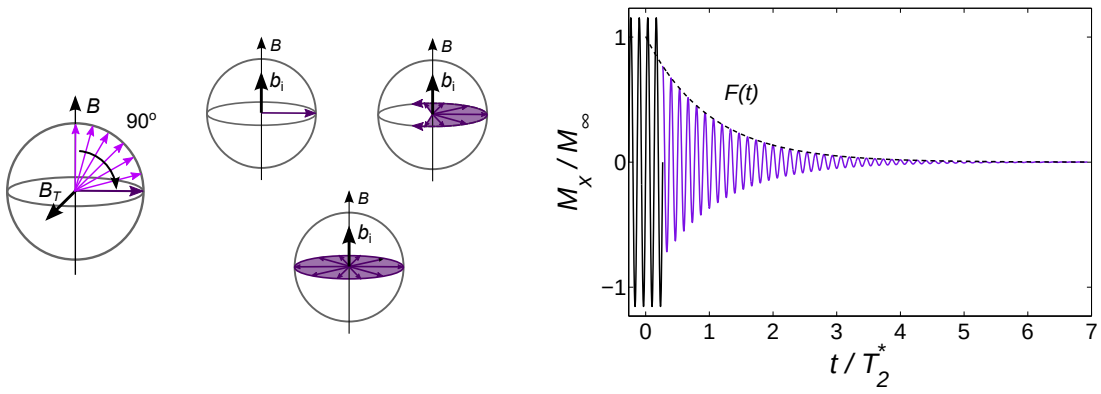

Figure 2.12: Pulsed NMR and the Free Induction Decay: The left-hand side shows how a transmitter pulse rotates the magnetisation in the rotating frame around the transmitter field B_T. The grey sphere represents the magnitude of M_∞. Local fields b_i will lead to a dephasing of the spins in the xy-plane leading to a vanishing transverse magnetisation with $F(t)$. The right-hand side graph shows a time-domain signal of the transmitter pulse and subsequent free induction decay i.e. dephasing of the spins in the xy-plane.

2.61 the time dependence of this rotation i.e. tip angle θ is:

$$\theta(\tau) = \frac{\gamma B_T}{2}\tau. \tag{2.74}$$

Here the magnetisation is rotated into the xy-plane after a time $\tau_{90^o} = \pi/\gamma B_T$ and points opposite to the magnetic field after $\tau_{180^o} = 2\pi/\gamma B_T$ (see Fig. 2.12). The transverse field pulses associated with these rotations are thus referred to as 90^o and 180^o tipping pulse respectively.

In order to measure the magnetisation M_∞ and transverse relaxation $F(t)$ of a spin species, a 90^o tipping pulse is applied, rotating the magnetisation into the xy-plane, where the Larmor precessing magnetisatioin can be measured as a flux change in a detection coil pointing along the x or y-axis. Tipping the magnetisation by less than 90^o will lead to a reduction of the observed magnetisation to $\sin(\theta)M_\infty$.

The signal induced by the precessing magnetisation in the detection coil is usually referred to as free-induction decay (FID). As the FID is a exponentially decaying sinusoidal function, its magnetisation, decay time and frequency might be anal-

ysed by means of its frequency spectrum. Here the frequency spectrum is obtained by Fourier transforming the FID. Here the fundamental Fourier transformations of the sine-wave and exponential decay are the delta function at frequency ω_0 and Lorentzian profile with full-width half-maximum 2δ and $t = 0$ magnitude of M respectively. By applying the convolution theorem, the complex Fourier transformation of the modulated sine-wave signal, i.e. the FID, is the convolution of the delta function with the Lorentzian profile:

$$\begin{aligned} L_{\text{abs}} &= \frac{M}{\pi} \frac{\delta}{\delta^2 + (\omega - \omega_0)^2} \\ L_{\text{disp}} &= \frac{M}{\pi} \frac{\omega - \omega_0}{\delta^2 + (\omega - \omega_0)^2} \end{aligned} \tag{2.75}$$

Here "abs" and "disp" refer to the absorption and dispersion of the Lorentzian profile. Depending on the initial phase ϕ of the FID, the observed complex components of the Fourier transformation are linear combinations of the absorption and dispersion profile. The coefficients for the real and imaginary part of the spectrum are $\cos(\phi)$, $\sin(\phi)$ and $-\sin(\phi)$, $\cos(\phi)$ respectively. The half-width half maximum δ of the Lorentzian profiles relates to the transverse relaxation time T_2^* as:

$$T_2^* = \frac{1}{\delta} \tag{2.76}$$

Examples of Lorentzian profiles and fits to measured FIDs are shown in Section 4.2.

Intrinsic Relaxation and Spin Echoes Measurements

As we saw in Section 2.4.2 the transverse relaxation function $F(t)$ depends strongly on the distribution of local fields, field gradients and diffusion of the spin species under consideration. One major source of field gradients are magnet inhomogeneities. In order to probe the intrinsic transverse relaxation it is desirable to find a method that cancels the effect of external field gradients or makes it possible to subtract their effect of the observed FID.

Two methods have been devised to achieve this. One works by measuring the magnetic field dependence of T_2^*, where the intrinsic transverse relaxation time T_2 is the zero-frequency limit of the measured T_2^* field dependence. Here it is crucial that

the intrinsic relaxation is frequency independent. In this case the total transverse relaxation time can be written as:

$$\frac{1}{T_2^*} = \frac{1}{T_2} + \gamma\overline{\Delta B_0} = \frac{1}{T_2} + \omega\frac{\overline{\Delta B_0}}{B_0}, \tag{2.77}$$

where $\overline{\Delta B_0}/B_0$ is the magnet inhomogeneity and is of the order of 10^{-5} to 10^{-3} in typical NMR magnets. The relaxation time associated with the magnet inhomogeneity $T_M = (\gamma\overline{\Delta B_0})^{-1}$ is often referred to as the magnet limit of the transverse relaxation time. If, on the other hand, the spin diffusion or intrinsic magnetic fields are magnetic field dependent, this approach is no longer valid as T_2 itself becomes frequency dependent. Here T_2 can only be determined from spin echo measurements.

As discussed in the previous sections, a magnetisation with a finite projection in the xy-plane, will precess at the Larmor frequency and dephase as a consequence of time dependent local fields. If a 180^o pulse is applied to the dephased system after a time τ, inverting all spins in the xy-plane, the spin ensemble will start to rephase if $b_i(\tau) \approx b_i(0)$ and form a spin echo after a total time of 2τ. Here static field gradients will not lead to a reduction of the spin echo height as compared to the zero-time magnetisation. Fluctuating intrinsic fields however will lead to a reduction of the spin echo amplitude. A schematics of the spin echo sequence is shown in Fig. 2.13. By repeating the spin echo sequence for various times τ is is possible to probe the intrinsic relaxation function $E(t)$ with its characteristic decay time T_2. In the spirit of Section 2.4.2, the echo relaxation function $E(t)$ depends on the auto-correlation function $G(\tau)$ as:

$$E(t) = \exp\left\{-\int_0^t (t-\tau)\left[G(\tau/2) - G(\tau)\right]\right\} \tag{2.78}$$

where by assuming a sinusoidal internal field with magnitude δ and wave length q across the sample and spin diffusion with a constant D we obtain:

$$E_s(t) = \exp\left\{-\frac{\gamma^2\delta^2 D}{12}t^3\right\} \qquad \text{and} \qquad E_f(t) = \exp\left\{-\frac{\gamma^2\delta^2}{q^4 D}t\right\}. \tag{2.79}$$

Here $E_s(t)$ is the echo relaxation function in the slow diffusion limit, whereas $E_f(t)$ is the limit for fast diffusion. It might be argued that in magnetically ordered solids

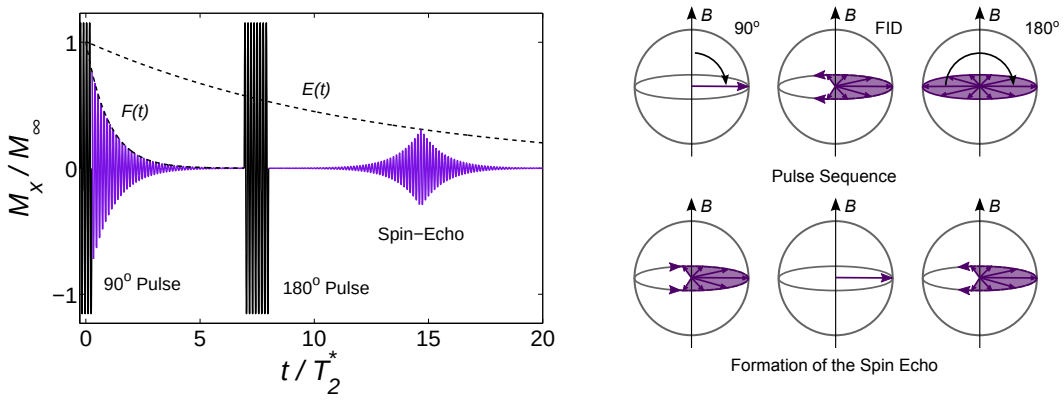

Figure 2.13: Spin Echoe Pulse Sequence: The left-hand graph shows the spin echo pulse sequence in the time domain. A 90^o pulse is applied to tip the magnetisation into the xy-plane where it starts to dephase with $F(t)$. After a time τ a 180^o pulse is applied inverting the magnetisation of each spin leading to the formation of a spin echo after a time 2τ. The magnitude of the spin echo decays with the intrinsic transverse relaxation function $E(t)$. The right-hand diagram shows the rotating frame Bloch spheres according to the pulse sequence.

with finite spin diffusion, where q is of the order of the lattice spacing, the latter case applies and the intrinsic relaxation is simply exponential.

T_1 Measurements

In order to measure the longitudinal relaxation, it is necessary to generate an out-of equilibrium magnetisation along the magnetic field direction. Using pulsed NMR, a 180^o tipping pulse can be applied to invert the equilibrium magnetisation from originally pointing along the magnetic field to being anti-parallel to the magnetic field. Subsequently the magnetisation will relax with the longitudinal relaxation function $L(t)$ back to its equilibrium. As it is technically challenging to probe the longitudinal magnetisation directly, a second tipping pulse, ideally a 90^0 pulse, has to be applied to tip the longitudinal magnetisation into the xy-plane, where it can be measured as the zero time magnitude of the following FID (see Fig. 2.14). By repeating this sequence for different delay times τ after the magnetisation has fully recovered to its equilibrium value, it is possible to probe the time dependence of the

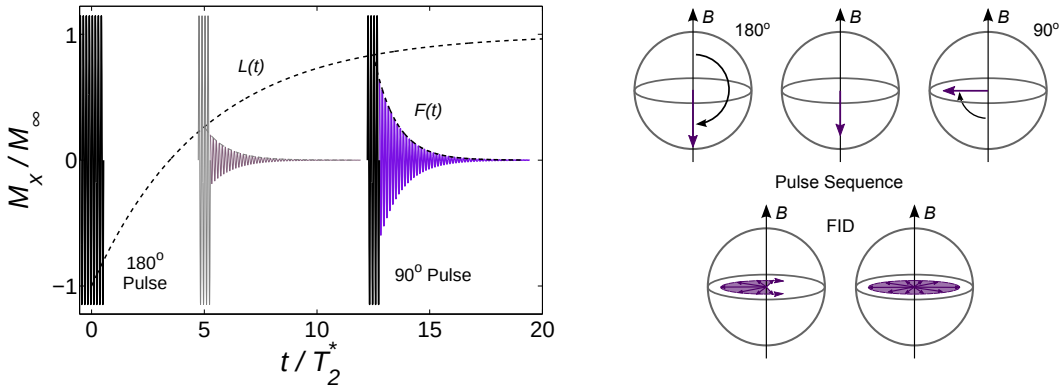

Figure 2.14: T_1 Pulse Sequence: The left-hand graph shows the T_1 180^o-90^o pulse sequence in the time domain. A 180^o pulse is used to invert the equilibrium magnetisation, which then starts to recover with the longitudinal relaxation function $L(t)$. At time the time τ a 90^o pulse is applied to tip the recovered longitudinal magnetisation into the xy-plane, where it can be measured as a FID. The right-hand diagrams shows the magnetisation in the frame Bloch spheres according to the various stages of the pulse sequence.

longitudinal relaxation function and to extract the longitudinal relaxation time T_1.

In systems where large angle tipping pulses can not be applied due to rf-heating concerns, the 180^o and 90^o pulse can be replace by almost arbitrarily small pulses limited only by the resolution of the spectrometer. However, in this case it has to be ensured that the delay time τ is longer the $5T_2^*$ to suppress the transverse magnetisation.

Secondly for systems with large longitudinal relaxation times a more time efficient pulse sequence can be used. Following a single 180^o pulse the recovering magnetisation is probed by a series of small angle tipping pulses and resulting FIDs. In this sequence the longitudinal recovery is accelerated for negative and slowed down for positive longitudinal magnetisations due to the enhancement or reduction of the longitudinal magnetisation by the sampling pulse. Here the error introduced by each sampling pulse is $\Delta M_z(t) = M_z(t)\sin(\theta)$ where θ is the angle of the sampling pulse. For small angle sampling pulses this error is negligible and the pulse sequence is thus probing the true longitudinal relaxation.

3 Experimental Methods

At the beginning of the previous century Heike Kamerlingh Onnes developed a technique to liquify noble gases using the Joule-Thompson effect in a multi-stage Linde liquifier. The boiling point of these gases and in particular liquid helium were as low as 4.2 K. This development laid the foundation of modern low temperature physics and lead to the discovery of quantum mechanical effects like superconductivity and others.

This chapter describes the ultra-low temperature platform and thermometry used in this work, and SQUID NMR spectrometer. Supplemental information is provided in Appendix A. As part of this project a major rebuild of the experimental space on an existing nuclear demagnetisation cryostat was undertaken. The goal was to extend the available experimental space and to add SQUID NMR capability.

The background theory and experimental details follow the books "Matter and Methods at Low Temperature" by Frank Pobell [81] and "Low Temperature Physics" by Christian Enss and Sigfried Hunklinger [82].

3.1 Cryogenic Refrigerators

Most modern low temperature experiments are based on liquid helium refrigerators. Generally there are two different types of refrigerators, so called "pot" and "flow-cryostats". Both these cryostats operate by controlled evaporation of ^{4}He.

Temperatures above 4.2 K are usually achieved by heating a regulated helium gas flow. Thus these systems are referred to as flow-cryostats. In flow-cryostats liquid helium is drawn from a helium reservoir through a needle valve and thin capillary into the sample chamber or annulus around the sample chamber. The temperature of the gas flow can be changed by applying heat to the inlet capillary or regulating the gas flow by adjusting the needle valve or pressure in the sample chamber. Cryostats

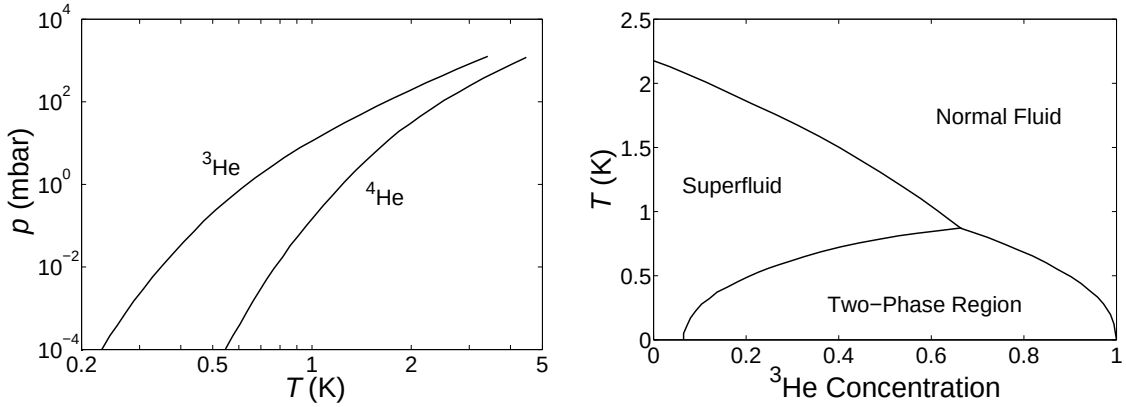

Figure 3.1: The left graph shows the vapour pressure of ^{3}He and ^{4}He as function of temperature. The right graph shows the miscibility of ^{3}He in ^{4}He and its miscibility gap below 800 mK. (Graphs are taken from [81]).

of this type were used in our high magnetic field experiments (see Chapter 5 and Appendix B).

Temperatures below 4.2 K are produced by reducing the vapour pressure above a helium bath. The reduction of the vapour pressure leads to a lowering of the boiling point and helium will start to evaporate. The latent heat of evaporation necessary to transfer helium atoms from the liquid into the gas phase generates a cooling power and reduces the temperature of the bath. With this method of evaporation cooling, temperatures as low as 1.2 K can be achieved in ^{4}He based refrigerators. Here the lowest temperature is limited by the exponentially decreasing vapour pressure with decreasing temperature, pumping power and heat leak into the cooling stage. In order to reduce the helium consumption, most ^{4}He refrigerators use separate ^{4}He-pots inside an inner vacuum chamber rather than pumping on the entire helium reservoir. Here the ^{4}He-pot is connected to the reservoir through a thin capillary whose impedance is matched to the evaporation rate and heat load to the pot [83].

By using ^{3}He instead of ^{4}He, it is possible to cool to even lower temperatures. Due to the higher vapour pressure of ^{3}He compared to ^{4}He (see Fig. 3.1) temperatures as low as 0.3 mK can be achieved. Since ^{3}He is a particularly rare and expensive noble gas, closed cycle refrigerator were introduced that recover the evaporated helium and recondense it into the pot. These closed cycle refrigerators follow the basic

principle of a Linde cooler, where the condensing gas is precooled in counter-flow heat exchangers by the cold evaporating gas from the ^{4}He or ^{3}He-pot.

3.2 Helium Dilution Refrigerators

Temperatures below 0.3 K can only be achieved by a few techniques. Several of these techniques are based on discontinuous thermodynamic cycles like adiabatic demagnetisation of paramagnetic salts or Pomeranchuk cooling. The most commonly used continuous technique relies on diluting ^{3}He into ^{4}He. Due to the increased zero-point motion of ^{3}He compared to ^{4}He, the van der Waals interactions between ^{3}He and ^{4}He atoms are stronger than between ^{3}He atoms. This solubility is limited to a ^{3}He concentration of 6.4 % at $T = 0$, arising from the increase of the Fermi energy of ^{3}He in solution with ^{4}He (see also Fig. 3.1).

In general helium dilution refrigerators bear resemblance to continuous ^{3}He refrigerators with the difference that the ^{3}He-pot is replaced by a mixing chamber and still. Sophisticated heat exchangers are necessary to ensure a sufficient precooling of the incoming ^{3}He condensate (see Fig. 3.2). Above 500 mK a dilution refrigerator behaves like a continuous ^{3}He evaporation refrigerator. The system is filled up to the still with a mixture of about 16% ^{3}He in ^{4}He. By pumping on the still, ^{3}He preferentially evaporates and generates local cooling power. The evaporated ^{3}He is recycled through pumps and cold traps before it is recondensed into the system.

Below 500 mK, however, the ^{3}He-^{4}He mixture will start to separate, depending on its ^{3}He concentration, due to the miscibility gap of ^{3}He in ^{4}He (see Fig. 3.1). The phase separation will occur first at the still and rapidly progress through the dilution unit. If the concentrations of ^{3}He and ^{4}He are set up correctly, the phase boundary will form inside the mixing chamber with the ^{3}He rich phase floating on top of the dilute ^{4}He-phase. At ideal working conditions, it has been shown, that the mixing chamber can reach temperatures as low as 2 mK whereas the still operates at 600 mK [84]. Commercial refrigerators usually reach a higher minimum temperature below 10 mK but above 5 mK depending on the details and number of heat exchangers used in their design. The osmotic pressure between the mixing chamber and still drives a ^{3}He-flow from the dilute phase in the mixing chamber to the still, replacing the ^{3}He pumped away at the still. This flow of cold liquid towards the still is also

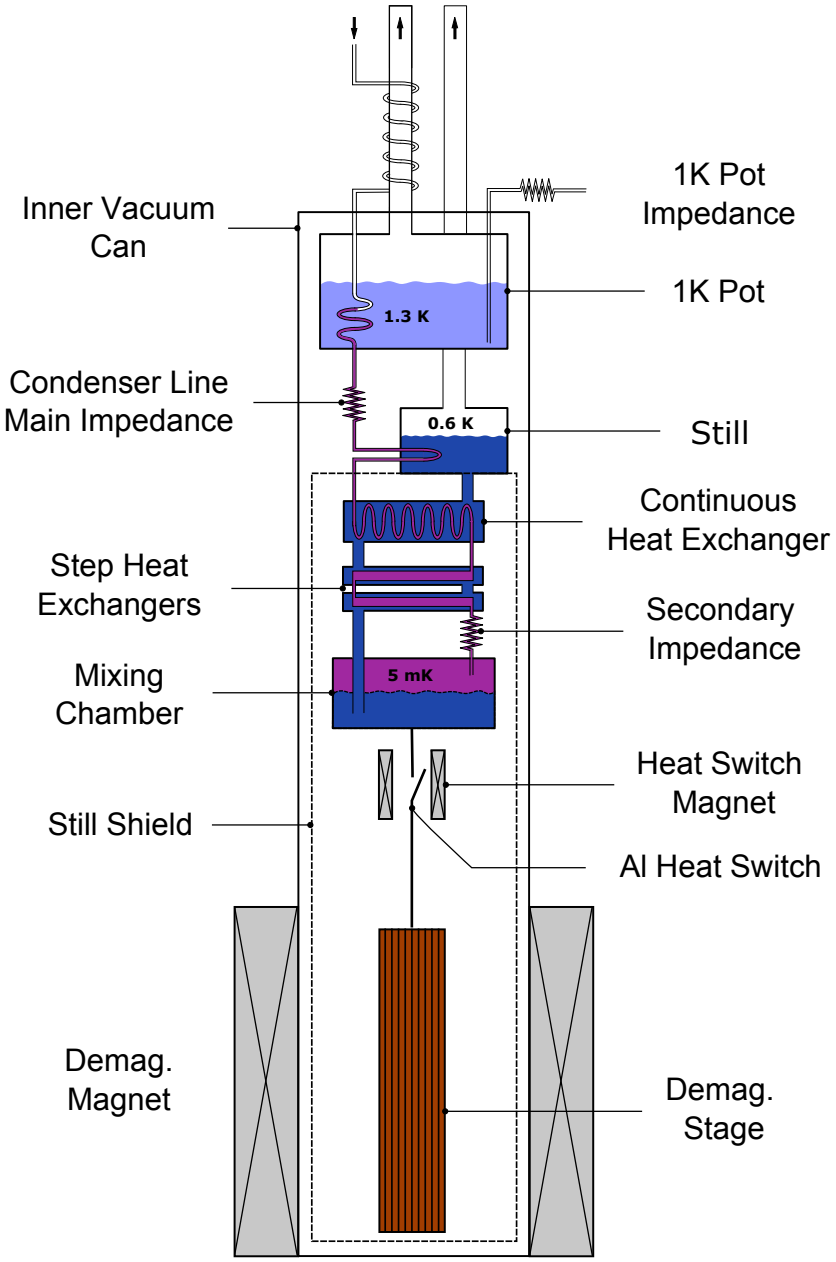

Figure 3.2: Schematics of a ^{3}He:^{4}He dilution refrigerator with attached nuclear demagnetisation stage.

used to precool the recovered ^{3}He in counter flow heat exchangers.

The returning ^{3}He gas is liquified at the 1K-pot and hydrostatically driven down through the condenser side of the dilution unit and precooled by a series of heat-exchanger. The heat load produced by the incoming ^{3}He condensate and additional heat applied by external heaters is used to control the temperature and hence evaporation at the still. Subsequently the liquid is further cooled in continuous, tube-in-tube, heat-exchangers down to about 50 mK.

To precool to even lower temperatures step heat exchangers are introduced. Rather than the continuous heat exchangers, step heat exchangers are made from sintered silver with an active surface area of a few 100 m^2. The large cross-section of open channels and large surface area of these heat exchangers reduces the viscous heating and increases the thermal contact. Thus it is possible to achieve precooling temperatures of a few millikelvin.

The cooling power of the mixing chamber can be calculated from the heat load to the mixing chamber and the cooling power at the phase boundary. The bare cooling power at the phase boundary can be derived from the enthalpy difference between the dilute $H_{3,\mathrm{d}}$ and concentrated ^{3}He-phase $H_{3,\mathrm{c}}$. Both of which are Fermi liquids whose Sommerfeld coefficients are experimentally known [69]. The enthalpy difference $\Delta H$of the two liquids is:

$$\Delta H \;=\; H_{3,d} - H_{3,c} \approx 95T^2[Jmol^{-1}] \tag{3.1}$$

The overall energy balance of the mixing chamber including all heat loads is:

$$\dot{Q} \;=\; \Delta H \times \dot{n_3} - (H_3(T_{\mathrm{ex}}) - H_3(T_{\mathrm{mx}})) \times \dot{n_3} \tag{3.2}$$

where $\dot{n_3}$ is the ^{3}He circulation rate and T_{ex} the temperature of the last heat exchanger. At the base temperature of the refrigerator the cooling power of the mixing chamber equals the sum of all external heat leaks. Due to the quadratic temperature dependence of the enthalpy the cooling power of the dilution refrigerator will increase quadratically with temperature. This quadratic temperature dependence can be measured in the cooling power of our dilution refrigerator "ND1" (Fig. 3.3).

The dilution unit of "ND1" was built by Oxford Instruments in the late 1970s.

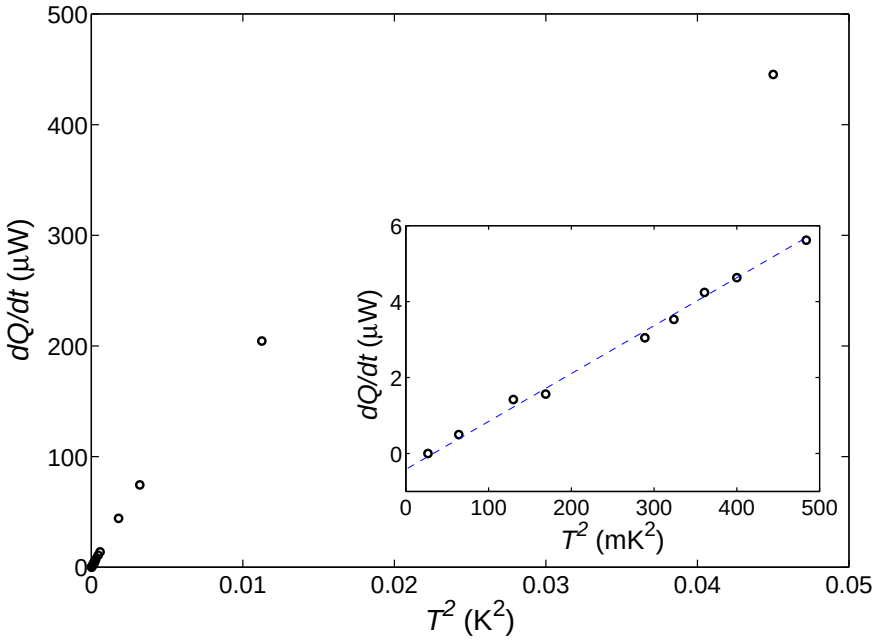

Figure 3.3: Cooling power of the ND1 dilution refrigerator at a ^{3}He circulation rate of 140 μmols^{-1}. The temperature at which the applied heat $\dot{Q}_{\text{ext}} = 0$ is the base temperature of the refrigerator. It is determined both by the heat load on the mixing chamber due to the incoming ^{3}He and the residual heat leak.

The basic setup of this unit is equivalent to the schematic shown in Figure 3.2, with the minor difference that the heat shield, surrounding the mixing chamber and submillikevin stage, is mounted to the cold plate between the continuous and step heat exchangers rather than to the still. The entire dilution unit is thermally and mechanically divided into four segments the 1K-pot, the still plate, the cold plate and mixing chamber. These segments are connected via stainless steel tubes thermally isolating by Vespel washers and serve to support the heat exchangers, heat sinks and experiments at the respective temperatures. The entire bundle is mounted to the IVC-flange.

In order to avoid heat leaks and mechanical noise the entire cryostat is mounted in a steel frame and rests on air mounts. The vacuum lines connecting the 1K-pot and still to their respective vacuum pumps are interrupted by stainless steel

bellows. Fill lines and wiring connecting experiments and the dilution unit to the room temperature connectors at the OVC-flange were heat sunk at the IVC-flange or 1K-pot to minimise the heat load into the lower parts of the dilution unit. A detailed description of the heat sinking and wiring of ND1 is given in Appendix A.1.

The operation of the dilution unit and 1K-pot were controlled by an external gas handling system.

A rotary vane pump was used to pump the 1K-pot. Typical pot-pressures ranged from 4 to 7 mbar corresponding to temperatures of about 1.45 to 1.60 K. The 1K-pot was fitted with an additional needle valve inlet, which could be used to fill the pot in the case of an input impedance blockage.

The performance of the dilution unit itself was controlled by the filling and circulation rate of the ^{3}He-^{4}He mixture and heat applied to the mixing chamber and still. Under normal conditions the still was pumped by an oil diffusion booster pump backed up by a sealed rotary vane pump. The returning ^{3}He gas was cleaned through liquid nitrogen and helium cold traps to freeze out any potential contaminants in the circulate and sent back into the condenser line.

Additional valves allowed to add or remove gas to the circulation from three separate gas tanks. By sequential recovering of the mixture it was possible to split the mixture into a ^{3}He rich and poor gas and store these in separate tanks. This way the concentration and volume of mixture in the unit could be adjusted. The key indicators for a well tuned mixture are the filling of the still, position of the ^{3}He-^{4}He phase boundary and base temperature of the dilution unit. These parameters were monitored by RuO_2 thermometers mounted at the still, mixing chamber and step heat exchangers (see Sec. 3.4).

The temperature of the mixing chamber and attached experiments was controlled by applying heat to the mixing chamber through a wire wound Constantan heater. The heater output was driven by a digital proportional-integral-differential (PID) controller based on the temperature of calibrated thermometers mounted at the mixing chamber or submillikelvin stage (see Sec. 3.4).

Under normal conditions the dilution unit was operated at a still pressure of 10^{-1} mbar and condensation pressure of > 60 mbar corresponding to a circulation rate of 100 to 180 μmols^{-1}. Under these conditions the natural heat leak into the still, due to returning the ^{3}He, was sufficient to drive the evaporation in the still.

Thus no additional heat was applied to the still during normal operation.

Figure 3.3 shows the cooling power of the dilution unit at an intermediate circulation rate of $140\,\mu\text{mols}^{-1}$. The cooling power was determined from the applied heat necessary to stabilise the mixing chamber at an elevated temperature. As can be seen the cooling power is proportional to T^2 at low temperatures and flattens off at higher temperatures. Typical base temperatures under these conditions were around 5.2 mK.

Nowadays the best dilution refrigerators with improved heat exchangers and mixing chambers reach base temperatures of about 1.7 mK [85]. In order to investigate the temperature range below 1 mK, more advanced techniques are required. Here adiabatic nuclear demagnetisation is the most commonly used method.

3.3 Adiabatic Nuclear Demagnetisation Cooling

Adiabatic demagnetisation cooling is based on the temperature and magnetic field dependence of the entropy of a paramagnetic spin system. The entropy of a non-interacting spin ensemble i.e. its degree of disorder can be tuned through applying a magnetic field or changing its temperature. High magnetic fields and low temperatures will both lead to an increased ordering of the spins along the magnetic field direction thus decreasing their entropy. The entropy of a paramagnetic ensemble of particles with spin-$^1/_2$ can be calculated from the partition sum to give:

$$S = Nk_B \ln\left[2\cosh\left\{\frac{\mu B}{k_B T}\right\}\right] - \frac{N\mu B}{k_\mathrm{B} T}\tanh\left\{\frac{\mu B}{k_B T}\right\}. \tag{3.3}$$

This entropy can be approximated in the low polarisation limit i.e. for $\mu B << k_\mathrm{B}T$ to:

$$S = Nk_B \ln\{2\} - N\frac{\mu^2 B^2}{8k_B T^2} \tag{3.4}$$

and its heat capacity reduces to:

$$C_v \;=\; T\frac{dS}{dT} = N\frac{\mu^2 B^2}{4k_B T^2}. \tag{3.5}$$

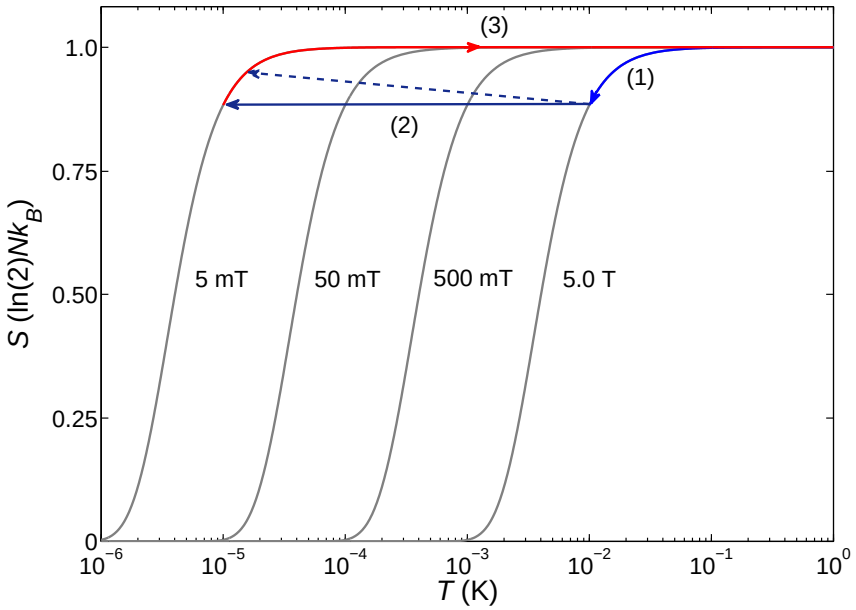

Figure 3.4: The graph shows the entropy of the ^{63}Cu and ^{65}Cu nuclei (grey) in the demagnetisation stage for temperatures between 1 μK and 1 K and magnetic fields up to 5 T. During precooling (1) heat is removed from the nuclei, lowering their entropy. By subsequently removing the magnetic field under adiabatic conditions (2) the temperature of the spin system is lowered below the precooling temperature. Eddy-current heating during the demagnetising can lead to an entropy increase i.e. loss of end temperature (blue dashed line). After the demagnetisation the spin system warms up under the influence of external heat leaks (3).

Under reversible adiabatic conditions i.e. for $\Delta S = 0$, temperature and magnetic field are proportional to each other. A magnetic field is applied, releasing heat of magnetisation and the system precooled to some initial temperature by the dilution refrigerator, at which the system reaches a state of lower entropy compared to its zero-field state. If the system is now thermally isolated from the mixing chamber and the magnetic field gradually removed, the temperature of the spin system will decrease conserving the entropy of the system. This process is the basis of adiabatic demagnetisation and is illustrated in Figure 3.4.

In nuclear adiabatic demagnetisation refrigerators, the paramagnetic spin ensem-

ble is a nuclear paramagnetic compound. Nuclear refrigerants are generally non-superconducting metals like copper, silver and $PrNi_5$, carrying a nuclear magnetic moment. Heat can be transferred from the nuclear spin to the electron system and vice versa by hyperfine coupling between the two. In thermal equilibrium the temperature of the spin system T_n equals the temperature of the electron system T_e. The time constant that governs the equalisation of the two temperatures is the Korringa-time τ_1:

$$\frac{dT_\mathrm{n}^{-1}}{dt} = \frac{(T_\mathrm{n}^{-1} - T_\mathrm{e}^{-1})}{\tau_1}. \tag{3.6}$$

This time is strongly temperature dependent and follows the Korringa-law[86]:

$$\tau_1 = K \times T_e^{-1}. \tag{3.7}$$

Here the thermal relaxation time is inversely proportional to the electron temperature, where K is the so called Korringa-constant. The Korringa constants of the nuclear magnetic isotopes of copper, silver and $PrNi_5$ for example are 1.09 to 1.27 Ks, 9 to 12 Ks and < 0.001 Ks respectively [81]. Due to the large Korringa constants of these metals their spin systems can be treated as almost isolated at ultra-low temperatures and show a large thermal resistance between the electron and spin system. As a result, the temperature of the electron system and experiment can saturate far above the nuclear spin temperature under a finite heat leak.

The Submillikelvin Stage of ND1

Before we started our experiments on two-dimensional ^{3}He the submillikelvin stage of the nuclear demagnetisation cryostat "ND1" was rebuilt to extend the available experimental submillikelvin space. This rebuild was preceded by the purchase of a longer helium dewar, which allowed us to extend the IVC and submillikelvin stage vertically by about 22 cm.

Before the rebuild, experiments could either be mounted directly onto the demagnetisation stage or a silver plate, which was located far above the stage. Mounting experiments directly onto the stage meant that experiments were exposed to the full demagnetisation field, thus superconducting shields would quench and trap flux.

Experiments on the elevated silver plate on the other hand did not suffer from the large stray field but from a too high thermal resistance to the nuclear demagnetisation stage. Thus one of the major objectives of this rebuild was to create a new experimental platform, the "100 μK-plate", which is well thermally connected to the copper demagnetisation stage and does not suffer from demagnetisation stray fields. Furthermore due to the new available space an additional "300 μK-plate" was added to the submillikelvin setup and the former mixing chamber "castle", i.e. the support structure for the submillikelvin stage that is bolted to the mixing chamber, was replaced by two separate mixing chamber plates. A picture of the new submillikelvin stage can be found in Figure 3.5. Here the new 100 μK-plate is raised 6 cm above the nuclear stage to remove it from the demagnetisation field and followed by the 300 μK, lower heat switch and the two mixing chamber plates.

All new structures of the submillikelvin stage were made from oxygen annealed oxygen-free high conductive (OFHC) copper to guarantee a high thermal conductance at ultra-low temperatures. Oxygen annealing was performed for 13 hours under ultra-high high vacuum at 850^{o}C followed by 24 hours under a 1.8^{-4} mbar dry air atmosphere at the same temperature [87].

Where a high thermal conductivity was required individual parts were connected by cone joints (see Fig. 3.5) or by screw connections. Niobium washers were used to separate individual copper parts if a low thermal conductivity was required. In order to prevent surface oxidation of the cone joints all copper plates were plated with 1 μm of gold. Resistance measurements of the bare and gold plated copper cone joints at 4.2 K have shown contact resistances of 20 to 35 nΩ. Here the gold plating did not lead to an increased resistance within the scatter of the tested joints. On the contrary gold plating as well as etching with nitric or acetic acid removes the surface oxide layer, which together with misalignment is the main cause for high contact resistances.

In order to achieve the lowest possible temperatures, the 100 μK and 300 μK-plate were both directly thermally grounded to the copper demagnetisation stage by three solid copper rods each. Importantly none of these rods or plates touch each other or are thermally connected. This way heat leaks into the individual plates are dumped directly into the demagnetisation stage and are not transferred to another plate. In the case of the 100 μK-plate connections between the 10 mm copper rods and

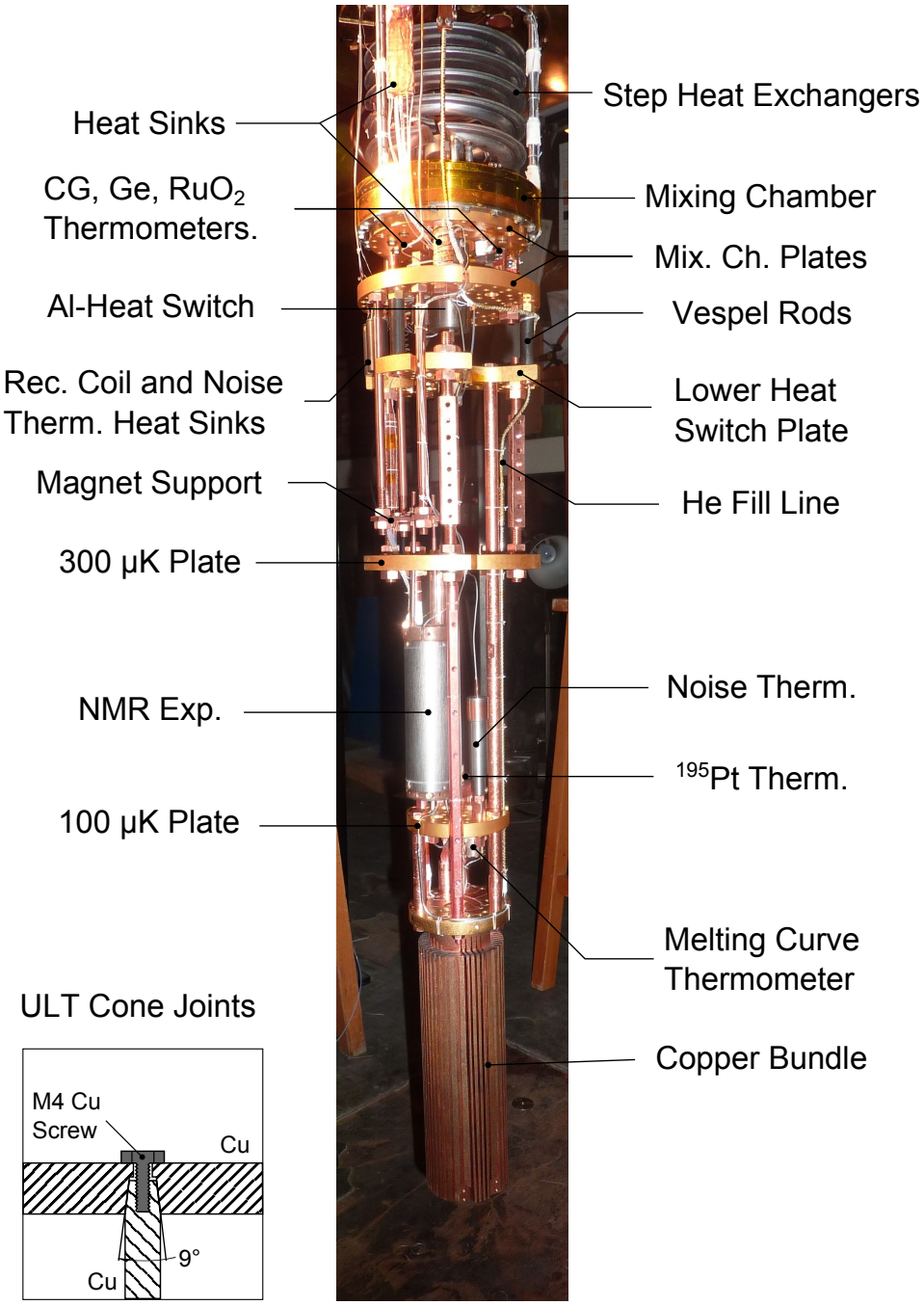

Figure 3.5: ND1 submillikelvin stage (Photo by courtesy of Jan Nyéki)

plate were made by cone joints, whereas the 300 μK-plate is connected via screw connections. The 300 μK-plate has an additionally flexible oxygen annealed copper wire link to increase its thermal contact to the demagnetisation stage.

The entire ultra-low temperature bundle is attached to the lower heat switch plate by three copper rods connected to the 300 μK-plate. These links are thermally isolated from the 300 μK-plate by thick niobium washers to avoid heat leaks into the 300 μK-plate. The lower heat switch plate itself is connected to the lower mixing chamber plate via three Vespel rods which thermally isolate the entire submillikelvin stage from the mixing chamber. A controlled thermal connection between the upper mixing chamber and lower heat switch plate can be made via a superconducting aluminium heat switch.

The main precooling link for the nuclear demagnetisation stage is established through a rigid copper link connecting the lower heat switch plate to the copper stage, bypassing the 100 μK and 300 μK-plates.

The actual nuclear demagnetisation stage, cooling the entire submillikelvin stage, is a cylindrical 2.4 kg copper i.e. 38 mols OFHC copper block centered in a superconducting magnet, with maximum field 8 T, usually operated at a highest field of 6 T. Periodic parallel slots have been cut into the copper stage to reduce eddy current heating during magnetic field sweeps. The entire submillikelvin stage is surrounded by a thermal shield mounted at the cold plate of the dilution unit. The alignment of the stage within the shield is secured by a spokewheel like structure at the bottom of the stage made from Nylon yarn.

For details about the experiments and thermometers installed on the submillikelvin stage please see Sections 3.4 to 3.6 and Appendices A.1 to A.3.

Heat Switches

In order to be able to precool and subsequently thermally isolate the nuclear demagnetisation stage a heat switch is installed between the mixing chamber and demagnetisation stage.

At dilution refrigerator temperatures superconducting heat switches are used. Superconducting heat switches are made from type-I superconductors whose thermal conductivity can be changed by factor of up to 10^6 by suppressing superconductiv-

ity through an applied magnetic field. Common heat switch materials are zinc and aluminium for ultra-low temperature and millikelvin applications respectively. Typically the material choice is governed by the maximal operation temperature of the switch. As a rule of thumb the critical temperature T_c of the switch material should be ten-times higher than the highest operation temperature to ensure a good isolation when open. Consequently most copper and $PrNi_5$ demagnetisation refrigerators use aluminium heat switches to separate the demagnetisation stage from the mixing chamber, whereas secondary demagnetisation stages and attached experiments use zinc heat switches.

Aluminium and zinc are classical BCS-superconductors [58] with critical temperatures of $T_c(\mathrm{Al}) = 1.18\,\mathrm{K}$ and $T_c(\mathrm{Zn}) = 0.88\,\mathrm{K}$ and critical fields of $B_c(\mathrm{Al}) = 10.5\,\mathrm{mT}$ and $B_c(\mathrm{Zn}) = 5.3\,\mathrm{mT}$ respectively. In the normal state the thermal conductivity of these metals is governed by electronic transport and thus strongly depending on its resistivity (see Wiedemann Franz-law[88]). Phononic thermal conductivity plays only a minor role at millikelvin temperatures and is typically a factor 10^4 to 10^6 lower than the electronic contribution. In the superconducting state the electronic contribution of the thermal conductivity vanishes due to pairing of electrons at the Fermi surface. At temperatures below $0.1\,T_c$ the electronic contribution of the remaining unpaired electrons approaches the level of the phononic thermal conductivity and the switch is maximally opened. Here the thermal conductivity is up to 10^6-times smaller than in the normal metal state. In order to close the switch, the superconducting state is artificially suppressed by applying an external magnetic field bigger than B_c. Now heat is conducted again in the normal state by the thermal excitation of conduction electrons even though $T \ll T_c$. If the magnetic field is removed the switch material reenters the superconducting state and the electronic thermal transport is suppressed i.e. the switch is open.

Our nuclear demagnetisation refrigerator uses an aluminium heat switch installed between the mixing chamber and submillikelvin stage (see Fig. 3.5). The heat switch is made of two oxygen annealed silver terminals connecting the aluminium heat switch foils thermally to the upper mixing chamber and lower heat switch plate. The vacuum annealed aluminium foils between the two terminals are mechanically clamped to the terminals on both sides to guarantee a good thermal contact. The heat switch magnet is a superconducting solenoid inclosed in a OD = 26 mm cylin-

drical niobium shield, which serves as well as mechanical stabilisation for the terminals and foils. The switch can be closed by applying a permanent current of about 250 mA to the magnet and is open if no current is applied. The use of aluminium restricts the operating temperature of our switch to below about 100 mK, above which the switch starts to leak through.

Minimal Temperature and Warm Up Rate

Following a demagnetisation the warm-up rate of a nuclear demagnetisation stage is governed by its heat capacity and the heat leaks into the stage. By applying Eqn. 3.5 and assuming a constant heat leak:

$$\dot{Q} = C_v \dot{T} = N \frac{\mu^2 B^2}{4 k_B T^2} \dot{T}. \tag{3.8}$$

Thus the inverse temperature follows a linear time dependence (see also Fig. 3.16), where the slope of the warm-up curve is proportional to the heat leak and inverse proportional to the magnetic field squared:

$$\frac{dT^{-1}}{dt} = -\dot{Q} \frac{4 k_B}{N \mu^2 B^2}. \tag{3.9}$$

This implies that demagnetising to an infinitesimally small magnetic field will not yield the lowest possible temperature. The temperature of the spin system would immediately rise after the demagnetisation, due to its low heat capacity.

The final field is generally chosen to match the experimental requirements on base temperature and warm-up rate. Typical final fields used in these experiments were of the order of hundreds down to tens of millitesla.

Furthermore parasitic heat capacities such as the nuclear spin heat capacity of structural parts and experiments can additionally limit the final temperature. As the electronic heat capacity vanishes linearly with temperature its effect on the final temperature is small. The nuclear heat capacity, however, diverges with T^{-2} above the Schottky anomaly.

In systems like ND1, where the ^{195}Pt NMR field (see Sec. 3.4) is applied to the entire submillikelvin stage the lowest temperature tends to be limited by the nuclear heat capacity of the support structures and experimental platforms exposed to this

field. In our setup, the entropy of the demagnetisation stage and support structures become comparable at demagnetisation fields of 20 mT. Thus demagnetising beyond this magnetic field will not yield a significantly lower temperature. For the present experiments this effect was mitigated by the use of ^{13}C-NMR thermometry. In the future this can be avoided by a self-contained Pt-NMR thermometer using a small magnet thermally anchored to the mixing chamber.

Given current technical limitations on superconducting magnets and the increased vibrational eddy-current heating of copper in high magnetic fields, most nuclear demagnetisation refrigerators do not exceed precooling fields of 9 T. Considering the limitations on the precooling and final field, demagnetisation ratios of up to 100 are common, leading to an almost hundred-fold reduction from the precooling temperature to around 100 μK.

Typical Operation

In order to reproduce similar conditions for all samples and experiments, e.g. the minimal temperature, stray field from the demagnetisation stage and warm up rate, a standardised demagnetisation cycle has been introduced.

Starting with the heat switch closed the copper stage is magnetised at 50 mT/min up to 3.3 and 5.0 T in later experiments. During this process the demagnetisation stage warms up to about 60 mK and is subsequently precooled for about 2.5 days down to 14 mK. Once satisfactory precooling conditions are reached, the heat switch is opened, and the magnetic field slowly removed. The demagnetisation is split into three steps. The first step down to about 500 mT or 2 mK is demagnetised at 13 mT/min followed by two steps down to 150 and 15 mT at 6.5 mT/min. The melting curve thermometer is calibrated during the initial demagnetisation step (see Sec. 3.4). Breaks of one to six hours were made in between the demagnetisation steps to ensure a good thermalisation of the submillikelvin stage with the copper nuclei.

Following a standard precool and demagnetisation, the 100μK-plate reached temperatures of about 160 to 200 μK and warmed up within six days to 20 mK. This slow warm up was used to measure the temperature dependencies of the ^{3}He and ^{13}C NMR magnetisation, frequency and relaxation times. By cross comparing warm

up rates of demagnetisations before and after the rebuild of the submillikelvin stage a heat leak of 5 nW into the demagnetisation stage was found. The second warm up shown in Figure 3.16 follows the described demagnetisation recipe starting from 3.3 T.

3.4 Thermometry

A central problem of low temperature and even more so ultra-low temperature physics is the precise determination of temperature. The following section will introduce the various types of thermometers that were employed in our experiments. Generally thermometers are distinguished into two classes, primary and secondary thermometers. Primary thermometers are based on fundamental physical laws and are self-consistently calibrated. Secondary thermometers, on the other hand, are calibrated against an external standard.

3.4.1 Resistive Thermometry

Resistive thermometers are based on the temperature dependence of electrical resistors. By measuring the resistance of the thermometer it is possible to infer its temperature. Generally all resistive thermometers are calibrated against external standards. The only primary resistance thermometers are superconducting fix-point thermometers. The resistance of these thermometer drops to zero at their material specific critical temperature.

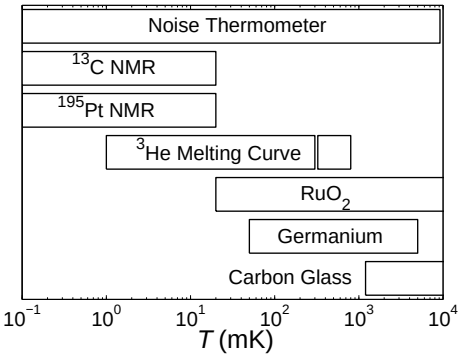

Figure 3.6: Temperature range of the low temperature thermometers installed on the nuclear demagnetisation cryostat ND1.

Depending on the sign of the temperature coefficient dR/dT normal resistive thermometers can be further classified in metallic (Pt100, RhFe) or semiconducting (Germanium, Silicon-Diode, RuO_2-Film, Cernox, Allen-Bradley, Speer, Carbon-Glas) thermometers. The main criterion for choosing a thermometer is its temperature sensitivity and thermalisation in the desired temperature range. Semiconducting thermometers show the best sensitivity at low temperatures but have a rather poor thermalisation due to their exponentially diverging resistance at zero temperature. Metallic thermometers, on the other hand, show a good thermalisation at low temperatures but lack the sensitivity. Thus metallic samples are used between room- and liquid helium temperature whereas semiconducting thermometers are used below 100 K down to about 20 mK (see Fig. 3.4).

In order to avoid overheating of thermometers at low temperatures metallic thermometers are measured in constant current mode whereas semiconducting thermometers due to their diverging resistance are measured with constant voltage excitation. In both cases the excitation is chosen as small as possible to reduce heat leaks into the thermometer.

In our experiments semiconducting thermometers were used to monitor the performance of the dilution refrigerator and to measure the sample temperatures at above 50 mK. The monitoring of the dilution refrigerator relied on a set of 2 kΩ RuO_2-thermometers installed at the IVC-flange, 1K-pot, still-plate, cold-plate, step heat exchangers, mixing chamber and SQUID-plate (see also Fig. A.3). All of these thermometers were from the same batch of thermally cycled SMD RuO_2-resistors. The self made thermometer packages contained an oxygen annealed copper body with an attached two pin connector. Cooper wire, wrapped around the body, was used to connect the resistors to the two pin connector an to heat sink the RuO_2-chip. Solder contacts to the resistors were made using indium to avoid overheating of the sensors.

Additional calibrated germanium [89] and carbon-glass thermometers were installed at the mixing chamber to measure its temperature above 50 mK and 1.1 K respectively.

All resistive thermometers were measured with an automated AVS-47 AC-Resistance Bridge [90]. Due to the limited number of input channels of these bridge a multiplexer was used to sample all thermometers with the same resistance bridge. The

calibrated germanium and carbon-glass thermometers were measured in four-wire configuration whereas the RuO_2-thermometers were measured using a pseudo-four wire configuration, where the respective voltage and current leads were joined between the 1K-heat sink and thermometer.

3.4.2 ^{3}He Melting Curve Thermometers

^{3}He melting-curve thermometers (MCT) rely on the temperature dependence of the melting pressure of ^{3}He. The melting-curve sensor is a high pressure helium cell with an integrated capacitive manometer. MCTs are commonly made of annealed silver and contain a large internal silver sinter heat exchanger to ensure good thermalisation of the helium.

The melting-curve sensor is loaded with ^{3}He via a narrow fill line at temperatures above 1 K and pressures around 35 bar. During loading the capacitive pressure gauge is calibrated against an external standard, in our case a high pressure oscillating quartz ParoScientific pressure gauge [91]. On cooling, the helium inside the fill line forms a solid plug between the still and mixing chamber at around 800 mK, enclosing the high pressure liquid in the sensor. Once the plug is formed the pressure inside the MCT follows the ^{3}He melting curve (Fig. 3.7). Its temperature dependence is described by the empirical formula:

$$p = p_{\mathrm{A}} + \sum_{i=-3}^{5} a_{\mathrm{i}} T^{\mathrm{i}} \tag{3.10}$$

where the temperature coefficients a_i are taken from Greywall *et. al* [69]. p_{A} refers to the pressure of the superfluid A-transition of 34.3380 bar at 2.5 mK.

Above the minimum in the melting curve at 312 mK and 29.32 bar, ^{3}He behaves like any ordinary fluid in the sense that its liquid entropy is bigger than its solid entropy and the gradient of the melting curve is positive. Below the minimum this relation is inverted and the entropy of the liquid is lower than the solid.

MCTs act as transferable standard of temperature given by the possibility to calibrate its temperature and pressure against the superfluid A-transition at 2.5 mK [69]. This corrects for the inevitable absolute error of the Paroscientific pressure gauge. Temperatures are then related to the superfluid A-transition. If a MCT is

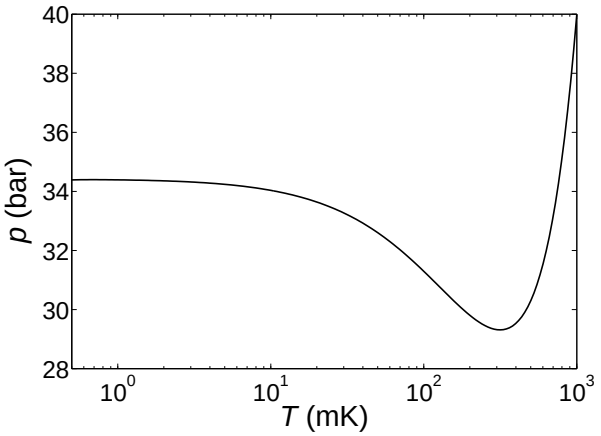

a_{-3}	=	-0.019652970
a_{-2}	=	-0.061880268
a_{-1}	=	-0.078803055
a_0	=	0.13050600
a_1	=	-0.043519381
a_2	=	$0.13752791 \cdot 10^{-3}$
a_3	=	$-0.17180436 \cdot 10^{-6}$
a_4	=	$-0.22093906 \cdot 10^{-9}$
a_5	=	$0.85450245 \cdot 10^{-12}$

Figure 3.7: ^{3}He melting curve and melting curve coefficients as taken from Greywall[69]

swept through this transition a change in the cooling rate can be observed due to the heat capacity jump associated with the 2nd-order phase transition.

In order to achieve a reasonable temperature resolution, pressure resolutions of less than 10 μbar on a background pressure of 35 bar are required. These resolutions are achieved by using thin CuBe-membranes as pressure sensor, forming one side of a capacitor measured by a highly sensitive capacitance bridges. The temperature range in which MCTs can be used is determined by the pressure resolution and gradient of the melting curve. Thus below 1 mK and around the melting-curve minimum at 312 mK, where the melting curve is flat MCTs can not be used.

The MCT used in our experiments is mounted at the 100 μK-plate directly next to the NMR-cell. Its fill line is heat sunk at the 1K-pot, still and mixing chamber and connected to a room temperature high pressure ^{3}He gas handling system. The MCT pressure, i.e. its capacitance, is measured by a home-made capacitance bridge using a reference capacitor at the still and an automated inductive voltage divider to balance the bridge. The imbalance of the bridge is measured using a lock-in amplifier and fed back to the automated voltage divider. The bridge ratio and off-balance voltage are subsequently used to calculate the temperature of the MCT [92]. Its temperature is used as calibration and measurement standard between 1 and 60 mK.

3.4.3 NMR Thermometers

Nuclear magnetic resonance thermometers are based on the Curie-law temperature dependence of the magnetisation of nuclear paramagnets in the low polarisation limit. Given prior calibration against an external temperature standard, like a MCT, the temperature of these thermometers can be inferred from their measured nuclear magnetisation (see Section 2.4).

Conventional NMR-thermometers use highly conductive metals like platinum with a high natural abundance of a nuclear magnetic isotope. The transverse relaxation time and hence measurability of the magnetisation by conventional NMR methods depends on the governing magnetic exchange interactions (see Sec. 2.4.2). In metals the dominant magnetic interactions are dipole-dipole and the Ruderman-Kittel-Kasuya-Yosida exchange interaction (RKKY) [93, 94, 95]. The transverse relaxation times of most metals are extremely short due to the dominance of the rigid-lattice dipole-dipole interaction. In highly conductive metals like platinum, however, the transverse relaxation time at 1 K is of the order of 1 ms due to an exceptionally high RKKY exchange and spin diffusion constant. Here two local nuclear magnetic moments couple with each other via the conduction electrons. The resulting exchange constant oscillates with the period length of a Fermi wave length and decays as the 4th power of the reciprocal distance.

Since nuclear magnetic moments predominantly thermalise by hyperfine coupling to conduction electrons, their longitudinal relaxation time is described by the Korringa-law [86](see Eqn. 3.7). In order to avoid magnetisation losses due to too frequent tipping of the nuclear spins, the NMR pulse repetition time must be adjusted to a multiple of the longitudinal relaxation time.

The NMR-thermometers used in our experiments are a conventional ^{195}Pt and SQUID NMR ^{13}C-thermometer.

The platinum thermometer is made of a bundle of thin platinum wires which are welded into a silver heat sink, mounted on the 100 μK-plate next to the helium NMR-cell and MCT. Platinum has a natural abundance of 33.8% ^{195}Pt with a Korringa-constant of 30 mKs [96]. Thus at ultra-low temperatures, around 200 μK, the T_1 of ^{195}Pt is of the order of 150 s, limiting the pulse repetition time to about 15 to 30 minutes for large tipping angles. Even though using small angle tipping, pulse

repetition times of our ^{195}Pt thermometer were of order of 5 to 30 minutes, below 5 mK, due to the thermal relaxation time following the eddy-current heating of the NMR pulse. The NMR field required for the ^{195}Pt thermometer is applied by an external magnet, whose magnet former, like the demagnetisation magnet, slips over the IVC. The NMR field extends over the entire 100 μK sample space and parts of the 300 μK-plate and can be shimmed by a pair of external gradient coils also located in the helium bath. The platinum wire bundle is mounted horizontally orthogonal to the external NMR field, with a superconducting coil directly wound onto a surrounding Mylar former. The superconducting coil is part of a tuned tank circuit operating at 250 kHz. Applying an rf-pulse to the tank circuit tips the ^{195}Pt-spins by typically a few degrees. The subsequent Larmor-precession and relaxation of the magnetisation can be measured as voltage across the tank circuit. By integrating the rectified tank circuit voltage over a fixed time window it is possible to infer the magnetisation of the ^{195}Pt-nuclei. A PLM4 Pulse NMR System [97] is used to drive and read the ^{195}Pt-thermometer. The measured magnetisation is calibrated against the MCT above 1 mK. Relying on Curie law this can be extrapolated to below 1 mK to determine temperatures.

The ^{13}C-thermometer is based on the graphite substrate in our helium-NMR cell and uses the broadband capabilities of our SQUID NMR setup (see Sec 3.5) [98]. The ^{13}C-nuclei inside the graphite substrate are simultaneously excited with the ^{3}He-spins by a broadband transmitter pulse and are measured as a parasitic signal on top of the ^{3}He FID. The operation and performance of the ^{13}C-thermometer are discussed in Section 3.6, following the description of the SQUID NMR spectrometer.

3.4.4 Johnson-Noise Thermometry

So far all thermometer discussed required some kind of excitation. Johnson-noise thermometers (NT), however, are based on thermal fluctuations or the Brownian-motion of electrons in metals and are purely passive. The electrical noise current generated by the conduction electrons is coupled to a highly sensitive dc-SQUID amplifier. The SQUID acts as a high gain-low noise current to voltage converter (see Section 3.5.2), making it possible to measure the noise current produced by the NT.

Johnson[99] and Nyquist[100] both derived the noise-voltage in a resistor at a given temperature from first principles:

$$\left\langle V_N^2 \right\rangle = 4k_B T R \Delta f \tag{3.11}$$

here $\langle V_N^2 \rangle$ is the mean squared voltage-noise and R and Δf the resistance of the sensor and bandwidth of the measurement. If the sensor is coupled to a SQUID via a superconducting flux-transformer, the voltage noise is converted into a current noise $\langle I_N^2 \rangle$:

$$\left\langle I_N^2 \right\rangle = \frac{4k_B T}{R} \left[\frac{1}{1 + (2\pi f L/R)^2} \right] \Delta f, \tag{3.12}$$

where L is the inductance of the flux-transformer circuit. The actual noise level or noise temperature is determined by fitting Eqn. 3.12 to an average of recorded noise frequency spectra.

If the resistance, inductance and bandwidth of the setup are known, NTs can be regarded as primary thermometers. Practically, however, the determination of these parameters proves to be difficult, and most NTs are calibrated against external standards at high temperatures. One possibility of implementing a calibration point in a NT is to inductively couple a superconductor with known T_c into the circuit. Here the onset of superconductivity in the standard reduces the inductance of the NT circuit compared to the normal state and increases its bandwidth [101].

The NT used on our cryostat is based on a 0.2 mΩ copper foil resistor mounted at the 100 μK-plate. Its read-out SQUID is a XL116T two-stage SQUID manufactured by the Physikalisch Technische Bundesanstalt Berlin [102] and controlled by a Magnicon XXF flux-locked loop electronic [103]. The coupled energy sensitivity of the SQUID was measured as $32h$ at 10 kHz. For the details about the SQUIDs their performance and wiring please see Section 3.5 and Appendix A.1. The noise spectra i.e. the Fourier transformed SQUID output signals were measured using a PXI-5922 digitizer [104].

The resistive element of our noise thermometer is made from an unannealed, u-shaped, 25 μm thick, 99.9 % purity copper foil [105]. A spare tap extending from one end of the resistive element was clamped and grounded to the copper body

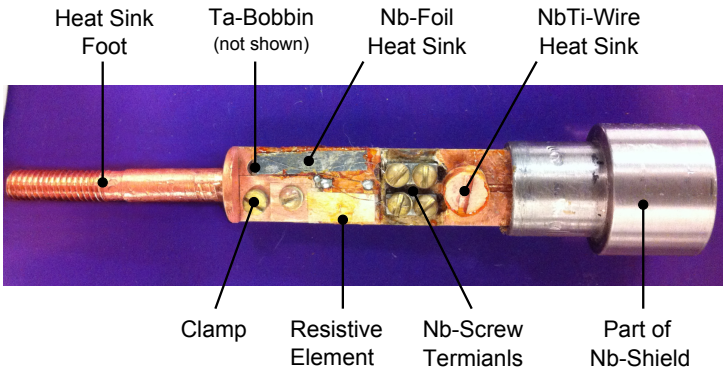

Figure 3.8: Ultra low temperature noise thermometer as installed on the 100 μK-plate of the nuclear demagnetisation refrigerator ND1. The self calibrating tantalum bobbin is missing on the photo (Photo by courtesy of Aya Shibahara).

of the thermometer to establish a good thermal contact (see Fig. 3.8). The rest of the sensor was glued flush on to the heat sink using GE-varnish and cigarette paper. Electrical contacts to the resistive element were made by CuNi-clad NbTi wires soldered to both ends of the u-shaped sensor. The floating end of the resistive element was additionally heat sunk via a large piece of niobium foil glued to the copper body. The wires on the grounded side were wrapped around a tantalum bobbin which acted as superconducting standard. Both sides of the resistor were finally connected to niobium screw terminals which were glued to the central body. The entire setup was encapsulated in a niobium shield with only a narrow hole for the heat sink foot and the niobium capillary connecting the wiring to the SQUID [101]. Once closed an annealed copper cone, matching the female cone in the 100 μK-plate, was screwed onto the heat sink foot and the thermometer was mounted.

Subsequently the sensor has been connected to the SQUID, which is mounted at the still, via a formvar-clad NbTi twisted pair shielded in a OD= 1 mm niobium capillary. An additional heat sink box was installed at the mixing chamber to reduce the heat leak into the thermometer. This heat sink box consisted of two copper pins and a pair of niobium screw terminals enclosed in a niobium shield. The in and outgoing twisted-pairs were wrapped around the posts and connected to the screw

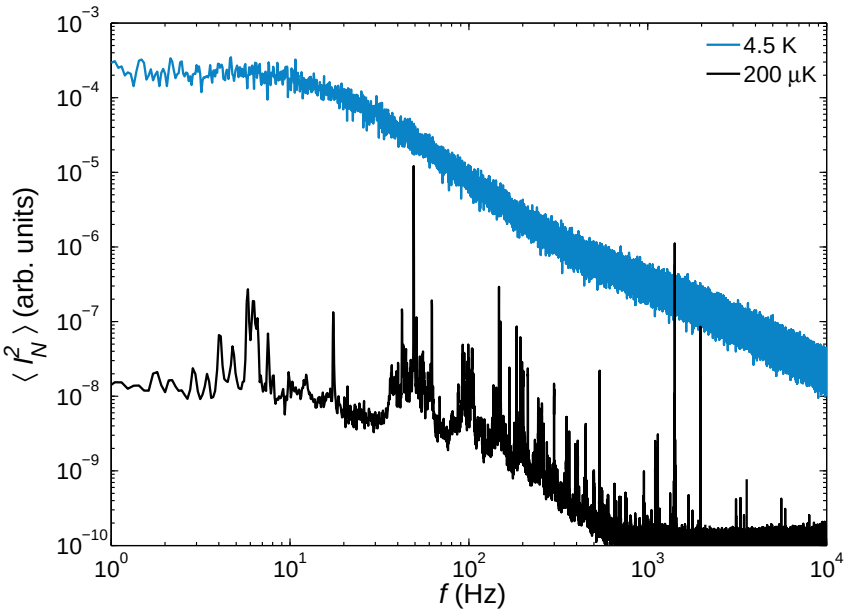

Figure 3.9: The graph shows the current noise spectrum of a 0.2 mΩ copper noise sensor at 4.5 K and 200 μK.

terminals. Both pins were heat sunk to the mixing chamber via annealed copper wires.

A typical noise spectrum of the sensor is shown in Figure 3.9. The noise power at low frequencies scales with the temperature, whilst the high frequency noise floor remains constant. The noise traces in Figure 3.9 have been averaged over 25 noise spectra. Individual spectra were calculated from the Fourier transformation of a 10 s noise trace measured at 50 kS/s. The thermometer was self-calibrated by the superconducting transition of the installed tantalum bobbin. On passing the critical temperature of the tantalum $T_c = 4.3$ K the inductance of the NT circuit dropped, visible in a shift of the cut-off frequency [101].

Following the calibration, the temperature was calculated from the fitted low frequency noise level. For this a special algorithm was deduced by A. Shibahara to exclude background noise peaks, visible at lowest temperatures. This way it was possible to measure temperatures as low as 170 μK with this thermometer (see Sec. 3.6).

3.5 SQUID NMR

In Section 2.4 we have already established the basis of pulsed NMR and how the magnetisation and spin dynamics of a nuclear magnetic system can be measured. Applying pulsed NMR to ultra-low temperature systems and two-dimensional ^{3}He in particular, however, is accompanied by a number of technical challenges. Various design constraints leave us with an exceptionally low number of nuclear spins and accessible magnetisation. Thus the following section gives an overview of the technical difficulties and their solution by performing SQUID NMR. For technical details of the wiring, coil set and NMR cell please see Appendices A.1 to A.3.

3.5.1 NMR at Ultra-low Temperatures

One of the biggest challenges of ultra-low temperature NMR is to ensure a good thermalisation of the sample. For two-dimensional ^{3}He this means that helium films are grown on a substrate which is a good thermal conductor at ultra-low temperatures and is itself well thermally connected to the nuclear demagnetisation stage. In our experiments this is achieved by using exfoliated graphite i.e. Grafoil [106], diffusion bonded to silver heat sink foils, which connect the graphite substrate to the well thermalised 100 μK-plate. The use of highly conductive materials inside the NMR cell, however, means that rf-fields like transmitter pulses, applied in the plane of the substrate, will generate eddy current heating. The heating power associated with a transmitter pulse can be derived from the eddy current density j induced in the metal surface. Here the deposited heat per unit area p is governed by the penetration depth δ, field amplitude B_T and frequency f of the rf-field:

$$p = \int_0^d \rho j^2(x) dx \qquad \text{where} \qquad j(x) \propto \frac{dB}{dt}\frac{1}{\rho}\exp\left\{-\frac{x}{\delta(f)}\right\} \qquad (3.13)$$
$$\text{and} \qquad \delta(f) = \sqrt{\frac{\rho}{\pi f \mu_r \mu_0}}$$

It followes that the dissipated heat per unit area p is proportional to:

$$p \propto \frac{2\pi^{3/2} f^{3/2} B_T^2}{\sqrt{\rho \mu_r \mu_0}} \left(1 - \exp\left\{-\sqrt{\frac{4\pi f d^2 \mu_r \mu_0}{\rho}}\right\}\right) \qquad (3.14)$$

where d is the thickness of the material. In the limit where the metal is much thicker than the penetration depth i.e. the exponential term becomes zero, the eddy current heating is proportional to the frequency as a power of $^3/_2$ and inversely proportional to the square root resistivity of the material. As the resistivity of the heat sink material has to be low in order to ensure a good thermal conductivity (see Wiedemann-Franz law [88]) the dominant eddy current heating is therefore expected to occur in the silver heat sink foils. However, it is possible to reduce the eddy current heating by reducing the frequency or the effective surface area of the foils e.g. by aligning the foils parallel to the transmitter field and slotting them in order to avoid large eddy current loops. A detailed description of our experimental NMR-cell is given in Appendix A.2.

In our cell we use about one gram of Grafoil with an effective surface area of about $12\,\mathrm{m}^2$. To see whether it is feasible to use conventional NMR i.e. a normal resistive receiver coil read out by an oscilloscope, we will estimate the signal size for the best case scenario based on our NMR cell. If we assume a fully polarised ^{3}He sample with a layer density of about $8\,\mathrm{nm}^{-2}$ i.e. 10^{20} ^{3}He-spins in total, the magnetisation of this system is of the order of $0.3\,\mathrm{A/m}$. If we further assume that the Larmor precessing magnetisation is measured by a normal conductive receiver coil, of about 100 turns, wound directly around the sample cell, the precessing magnetisation will induce a voltage of the order of $3\,\mathrm{mV}$ at a Larmor frequency of $100\,\mathrm{kHz}$ and is therefore measurable by conventional methods.

However, more realistically, the samples we are investigating are not fully polarised, but show polarisations of 10^{-6} to 10^{-2} (see Sec. 4.2). Here the signal size drops significantly below $1\,\mu\mathrm{V}$ and is thus no longer measurable with conventional techniques.

Thus a more sensitive technique is needed, amplifying the flux signal up to detectable voltages. Here highly sensitive low noise superconducting-quantum-interference devices (SQUIDs) are a natural choice. The following section will discuss the fundamental working principles of SQUIDs with flux resolutions of a few $\mu\Phi_0/\sqrt{Hz}$ and how they are incorporated into NMR setups.

3.5.2 SQUIDs

SQUIDs are based on superconducting loops interrupted by one or more superconductor-insulator-superconductor (Josephson) junctions. If the width of the insulator is thin compared to the superconducting coherence length, Cooper pairs can tunnel through the barrier and give rise to the ac and dc-Josephson effect [107, 108] (see Fig. 3.10).

If the superconductors either side of the junction are equivalent and their macroscopic Cooper pair wave function differs only by a phase δ, then the supercurrent through the junction is described by:

$$I = I_c \sin(\delta) \tag{3.15}$$

where I_c is the critical current of the junction. This is the dc-Josephson effect. If the current through the junction exceeds I_c the junction becomes ohmic and a voltage drop proportional to the bias current across the junction can be observed. Furthermore a finite voltage across the junction leads to a varying phase:

$$\dot{\delta} = 2eU/\hbar. \tag{3.16}$$

and its associated supercurrent. This is referred to as the ac-Josephson effect.

In real contacts, the situation is more complex and Josephson junctions can not be modelled as simple superconducting-ohmic switches. Here the resistively and capacitively shunted junction model (RCSJ) is applied to incorporate parasitic capacitances and shunt resistances of the contact [109]. In the RCSJ model the dc-Josephson effect is corrected by the current through the junction's capacitance C and resistance R:

$$I = C\dot{V} + \frac{V}{R} + I_c \sin(\delta) \tag{3.17}$$

The resulting phase evolution of the Josephson junction is described by a particle moving in a tilted washboard potential:

$$U(\delta) = \frac{\Phi_0}{2\pi}\left[I_c\left(1 - \cos(\delta)\right) - I\delta\right]. \tag{3.18}$$

Here the slope of the washboard is proportional to the applied current through the

junction. On exceeding I_c the particle, which was formerly trapped in a washboard potential well, accelerates along δ limited by its inertial mass and friction. Following the ac-Josephson effect an evolving phase is associated with a voltage drop across the junction. The inertial mass and friction in this model are proportional to the junction's capacitance C and conductance $1/R$. Here the Stewart-McCumber parameter is introduced to describe the dynamical behaviour of the Josephson junction:

$$\beta_c = \frac{2\pi}{\Phi_0} I_c R^2 C \tag{3.19}$$

In the over-damped limit $\beta_c \ll 1$, inertial terms are negligible and the junction behaves like an ideal Josephson junction. In the under-damped limit $\beta_c \gg 1$, however, the behaviour of the Josephson junction is governed by its dynamical constants C and R. This situation corresponds to weakly damped particle with high inertial mass moving through the washboard potential. Even though the washboard potential has tilted beyond its critical point the particle remains in its previous state. Junctions in this limit are thus highly hysteretic and remain super- or normal conductive far beyond I_c. In order to avoid such hysteresis of the $V(I)$-characteristic, Josephson junctions are usually shunted with parallel resistors. As a consequence the Johnson noise originating from these resistors limits the noise performance of SQUIDs.

In 1948 F. London derived the flux quantisation of ring-shaped superconductors exposed to a magnetic field based on the phase winding of the Cooper pair wave function induced by the circulating screening currents [110]. The total phase around the ring must be a multiple of 2π therefore leading to the quantisation of the screening current and flux penetrating the superconducting ring $\Phi = n\Phi_0$ where $n \in \mathbb{Z}$ and $\Phi_0 = 2e/\hbar$.

Considering a superconducting ring interrupted by two Josephson junctions and taking into account the total phase around the ring to be a multiple of 2π we can relate the phases of both junctions and calculate the total current through the SQUID:

$$I = 2I_c \cos\left(\pi \frac{\Phi}{\Phi_0}\right) \sin\left(\delta_1 + \pi \frac{\Phi}{\Phi_0}\right). \tag{3.20}$$

Here the critical current is modulated by $\cos(\pi\Phi/\Phi_0)$ and the phase δ_1 can be freely

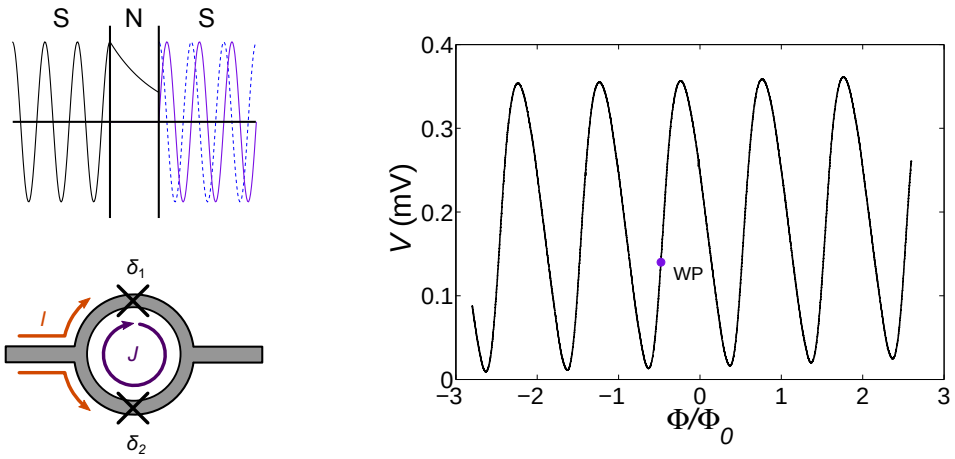

Figure 3.10: The upper left graph shows a cross section through a Josephson junction and the Cooper pair wave functions either side of it. The lower left schematic shows of a dc-SQUID with two Josephson junction. The bias current I splits around the ring whilst the screening current J circulates in the ring. The right-hand side graph shows the $V(\Phi)$-characteristics of the output stage of a PTB two-stage SQUID.

adjusted to fulfill the equation. If a SQUID is biased at its critical current, a penetrating flux will lead to a periodic suppression of I_c and drive the Josephson junctions ohmic. The modulation depth of the resulting $V(\Phi)$-characteristic is largest for bias currents $I \approx 2I_c$ and takes the value of $V_{\mathrm{pp}} = I_c R$ in SQUIDs with resistively shunted junctions. A typical $V(\Phi)$-characteristic of the SQUIDs used in our setup is shown in Figure 3.10.

In principle this voltage modulation alone could be used to measure the magnetic flux by e.g. counting $V(\Phi)$-periods or using the SQUID as a linear flux-to-voltage converter (open loop mode). However both methods lack either the precision or dynamical range required for NMR and other measurements. Thus SQUIDs are usually operated in the flux-locked loop mode, where the flux penetrating the SQUID is canceled by an external feed-back coil.

Flux-Locked Loop Mode

In flux-locked loop (FLL) mode the SQUID and attached feed-back electronics act as auto balancing null detector. The SQUID current biased at the largest $V(\Phi)$-

modulation depth is stabilised at a constant voltage corresponding to the steepest point of the $V(\Phi)$-characteristic. In this mode a flux change in the SQUID is transferred into a voltage offset from the predefined working point. This voltage offset is fed into an integrator circuit, whose output is driving the feed-back coil at the SQUID and cancels the flux change in the SQUID.

A basic schematic of the circuit used in our setup is shown in Figure 3.11. The SQUID shown in this schematic is a two-stage SQUID where the second stage amplifies the output voltage of the first stage. The bias currents of both stages are controlled by two separate current sources I_{b1} and I_{b2}. The working point of the two-stage SQUID is defined by the bias voltage V_b applied to one side of the differential amplifier. The output of this differential amplifier is integrated to produce the signal V_{out}, which serves as driver for the feed-back circuit and as output signal. The magnetic flux cancellation produced by the feed-back coil is proportional to its mutual inductance with the SQUID loop M_f and the feed-back current which is determined by V_{out} and the feed-back resistor R_f.

The gain and frequency response of the entire circuit are described by the feed-back gain G_F:

$$G_F = \left(\left. \frac{dV}{d\Phi} \right|_{WP} \right)^{-1} \cdot \frac{R_f}{M_f} \tag{3.21}$$

and gain-bandwidth product (GBWP) of the integrator circuit, where $dV/d\Phi|_{WP}$ is the slope of the $V(\Phi)$-characteristics at the working point. The unity-gain frequency f_1 at which the integrator loss cancels the feed-back gain is defined as:

$$f_1 = \mathrm{GBWP} * G_F^{-1}, \tag{3.22}$$

and is of the order of a few megahertz.

One technical challenge in high frequency SQUID applications is the time delay introduced by signals traveling between the SQUID and FLL electronics. Since most FLL electronics are computer controlled and are therefore TTL or CMOS based, their operating climate is limited to room temperature and atmospheric pressure. FLL electronics are therefore operated outside the cryostat and are connected to the SQUIDs at low temperatures via several meter long high frequency wiring. The

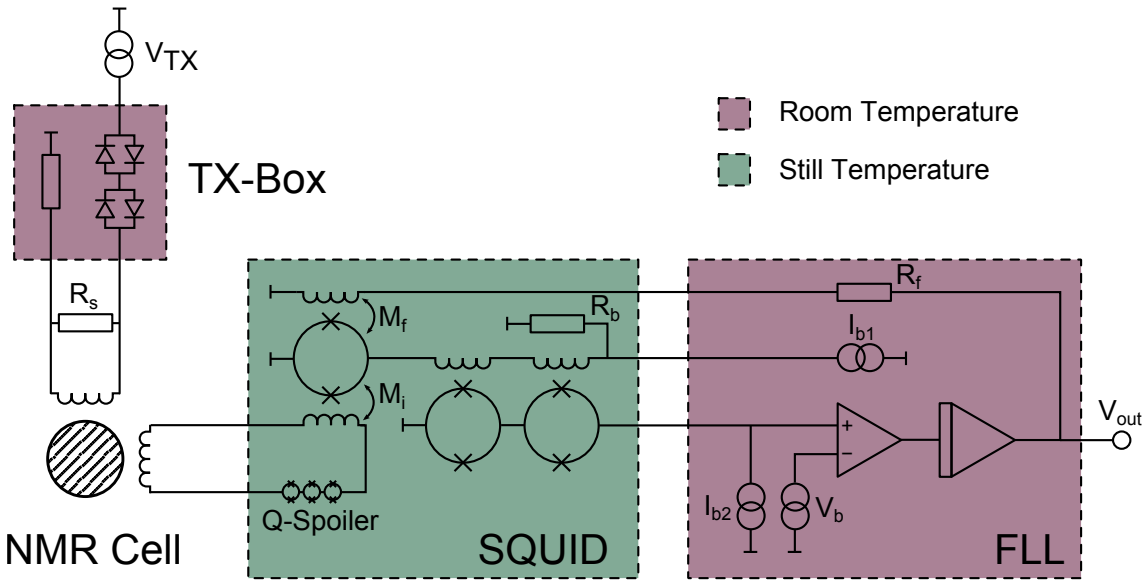

Figure 3.11: Schematic diagram the SQUID NMR setup.

travel time of signals from the SQUID to the FLL electronic and back can add between 10 to 30 ns to the intrinsic delay of the FLL electronic, suppressing the effective GBWP to lower frequencies. It is easy to imagine that an out-of phase feed-back signal, leads to zero or a negative gain. The resulting gain peak due to the positive feed-back can, for instance, be seen in the SQUID NMR noise spectrum Figure 3.12.

3.5.3 The SQUID-NMR Setup

Figure 3.11 shows a general overview of our SQUID NMR circuit. The circuit is divided in two parts, the excitation and detection circuit.

The excitation circuit controls the transmitter coil and is driven by a frequency or function generator. In our setup, transmitter pulses are applied through a saddle coil surrounding the sample (see also Appendix A.2). Depending on the pulse sequence and required amplitudes the excitation circuit is either driven by a PXI-5412 arbitrary waveform generator or two Agilent 33120A function generators in conjunction with a Stanford Research DG535 delay generator and PXI TE3222 wide-band amplifier. The transmitter wave form is fed through a set of cross-diodes to re-

move low-voltage noise and filtered by a 1st-order low-pass filter with 1 MHz cut-off. This 1st-order low-pass filter consists of the transmitter coil $L_{\mathrm{TX}} = 83\,\mu\mathrm{H}$ and a $R_{\mathrm{s}} = 410\,\Omega$ parallel shunt resistor mounted at the IVC. An additional $10\,\Omega$ shunt resistor is installed into the excitation circuit to monitor the transmitter current. The current reference is simultaneously measured the with NMR signal by a PXI-5922 digitizer.

On the detection side, the Larmor precessing magnetisation is coupled into the first stage of the SQUID amplifier via a superconducting flux transformer. This flux transformer consists of the receiver coil wound directly around the NMR-cell and the input coil of the SQUID connected by a superconducting twisted pair. The transfer ratio of this flux transformer is maximised by matching the inductances of the receiver and SQUID input coil (see Appendix A.2). In order to protect the micro-electronics of the SQUID from high currents a Q-spoiler made of a SQUID-array is installed into the flux transformer. The Q-spoiler is superconducting at low input currents and goes resistive when the critical current of the SQUID-array is exceeded. The critical Q-spoiler current can in principle be tuned by applying an external magnetic field to the Q-spoiler SQUID-array, but we did not use this facility in this work.

In our setup, we use a two-stage SQUID manufacture by the Physikalisch Technische Bundesanstalt Berlin (Germany) [102]. An overview of the technical parameters of the SQUIDs used in our experiments is given in Table 3.1.

Table 3.1: Technical SQUID Parameters: The table gives an overview of the technical parameters of the PTB XL116T SQUIDs used for the SQUID-NMR and noise-thermometry.

Exp.	Model	Serial No.	I_{c1} (μA)	I_{c2} (μA)	M_f ($\mu\mathrm{A}/\Phi_0$)	L_i (μH)	M_i ($\mu\mathrm{A}/\Phi_0$)	$\epsilon(10\,\mathrm{kHz})$ (h)
NMR	XL116T	C519E23	8.9	10.0	41.6	1.80	0.29	49
NT	XL116T	C636B23	13.7	9.5	43.5	1.80	0.31	32

In a SQUID-FLL circuit the two dominant noise sources are the Johnson noise of the Josephson junction shunts and the preamplifier noise of the FLL-electronic. The former is proportional to temperature whereas the latter is constant.

In order to achieve the lowest possible background noise, our SQUIDs were mounted

on a temperature controllable plate with a weak thermal link to the still. However, due to an almost temperature independent SQUID performance at lowest temperatures, the temperature control has not been used. The SQUID performance and its stability were monitored by cross-coupling measurements during Run 43 for various still temperatures.

At these temperatures the total noise of the SQUID-FLL circuit is dominated by the preamplifier noise of the FLL-electronics. Thus it is desirable to lower the preamplifier noise by reducing its gain and substituting it by a low temperature amplifier. In a two-stage SQUID this is done by the second SQUID-stage. The first stage is the detector stage to which the input and FLL feed-back are coupled. The output of this stage is fed into the second stage through a series of inductors. This second stage is an array of equivalent SQUIDs, whose total output voltage is the sum over all individual SQUID voltages in the array.

The biasing and feed-back of both SQUID-stages is provided by Magnicon FLL XXF-electronics [103]. The FLL-electronics are mounted on the outside of the cryostat and connected to the SQUIDs via high frequency shielded wiring. For detailed description of the SQUID wiring please see Appendix A.1. The output signal and control lines of the XXF-electronic can be accessed via a BNC break-out and computer interface box. The FLL output signal, i.e. the NMR-signal or NT signal, are measured by a PXI-5922 digitizer with 20-bit resolution at 5MS/s [104].

Operation and Performance

Before SQUID-NMR experiments can be performed it is necessary to tune the SQUID working point and to characterise the circuit characteristics.

As was already mentioned in the preceding sections, the optimal working point is defined by the maximal slope of the $V(\Phi)$-characteristic. Thus the first step is to maximise the $V(\Phi)$-modulation depth by tuning the SQUID bias current in open loop mode, followed by the selection of the bias-voltage corresponding of the maximal slope of the $V(\Phi)$-characteristic. The flux modulation necessary to plot the $V(\Phi)$-characteristic of the second stage can either be applied through the bias line of the first stage or a separate flux modulation coil built into the SQUID. For this the Magnicon FLL-electronics has built in function generators that can be used

to modulate all bias currents and voltages.

Figure 3.10 shows the optimised $V(\Phi)$-characteristic of the second stage of our NMR-SQUID. The maximal $V(\Phi)$-modulation depth of this SQUID is 345 mV. The working point in this example is fixed to 135 μV and locked to the positive slope of the $V(\Phi)$-characteristic.

Once the output stage is tuned, the procedure is repeated for the input stage. The output stage now acts as amplifier for the first stage. Finally the flux-locked loop is closed and the SQUID circuit is tested by applying an external flux modulation to the first stage.

Subsequently a fine tuning of the working point is performed to reduce the SQUID noise. Figure 3.12 shows two noise spectra of the NMR SQUID with optimised woring point. The NMR SQUID has a bare output noise of about 1 $\mu\mathrm{V}/\sqrt{\mathrm{Hz}}$ in the frequency range of our NMR experiments between 10 and 200 kHz, which is equivalent to a flux noise of about 1 $\mu\Phi_0/\sqrt{Hz}$. The sudden suppression of the SQUID noise and gain peaking around 4 MHz are connected to the finite bandwidth of our setup as induced by the signal travel time and bandwidth of the FLL-electronic. By selecting a lower GBWP the gain peak at 4 MHz can be suppressed, thus lowering the overall noise in the setup.

Following the characterisation of the detection circuit it is now possible to tune the NMR magnet to produce the desired Larmor frequency. Performing the SQUID characterisation with a magnetic field applied is usually avoided due to increased low frequency flux noise level due to mechanical vibrations.

Most of the data presented in the following chapters were measured in a NMR field of 3.09 mT corresponding to a ^{3}He Larmor frequency of 100.4 kHz and ^{13}C Larmor frequency of 33.2 kHz.

A standardised 40 μs NMR pulse at 100.0 kHz was used for magnetisation measurements to simultaneously excite the on-resonance ^{3}He and off-resonance ^{13}C-nuclei. The sinc-function like pulse power spectrum of this 40 μs-pulse is shown in Figure 3.13. The tipping angle of this 61 $\mu\mathrm{T}_{pp}$ pulse corresponds to 7.2^o for ^{3}He and 0.38^o for ^{13}C.

Following the tipping pulse the FID of both nuclear species was measured by the PXI-5922 digitizer for a duration of about $5T_2^*$s. In order to suppress low frequency signals arising from transient backgrounds the FLL-output was filtered by a 1st-order

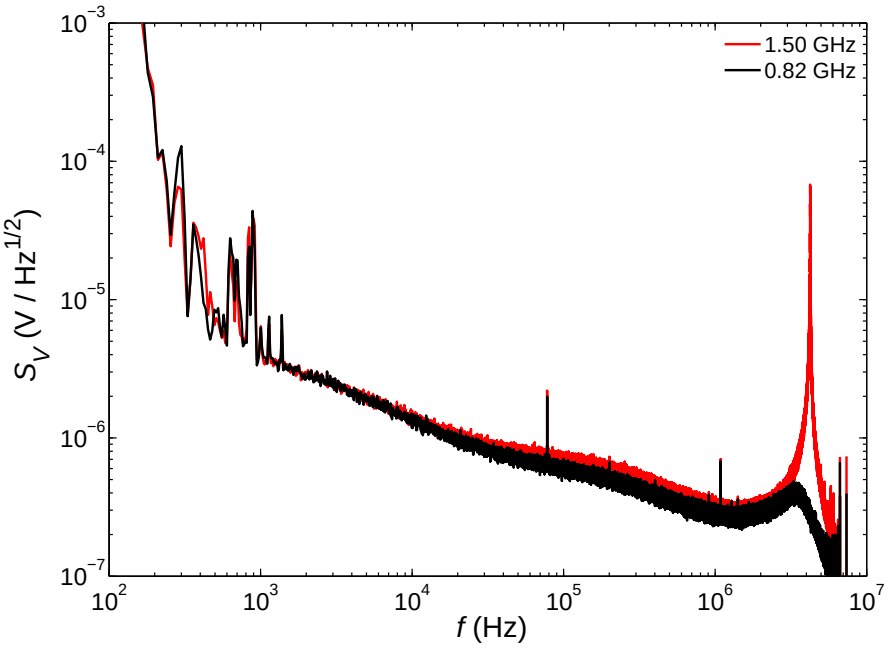

Figure 3.12: The graph shows the optimised noise spectrum of the SQUID NMR circuit measured at gain-bandwidth-products of 0.82 and 1.25 GHz. The transmitter circuit was grounded during the measurements.

4kHz high-pass filter.

The recorded signals were background subtracted by a zero field and high field off-resonance transient. Residual backgrounds were removed by a polynomial of 9 to 15 order. The high field off-resonance transient was measured using the standard NMR pulse at a magnetic field corresponding to the ^{3}He Larmor frequency of the first minimum in the sinc-function like pulse power spectrum at 125 kHz (see Fig 3.13). This way only magnetoacoustics and transients whose frequency is magnetic field independent are excited and can later be subtracted from the NMR signal.

A Fourier transformation of a 5 mK NMR-signal of a typical sample is shown in Figure 3.13. The observed NMR lines can be used to the determine the magnetisation and transverse relaxation time of the respective nuclear system by fitting Lorentzian line-shapes to the frequency spectrum (see Sec. 4.2). The "parasitic" ^{13}C-signal shown in Figure 3.13 was later used as thermometer (see Sec. 3.6). Examples

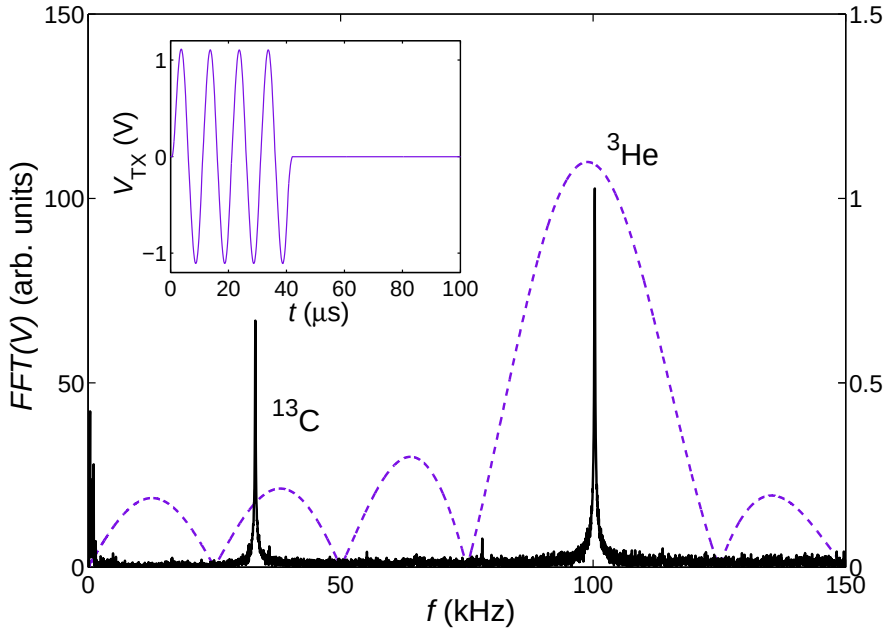

Figure 3.13: Transmitter excitation and NMR spectrum: The graph shows the Fourier transformation of the transmitter pulse (purple dashed line) and the resulting NMR signal of a $\rho_2 = 4.00\,\mathrm{nm}^{-2}$ ^{3}He|^{4}He|graphite sample at 5 mK (black line). The inset shows the transmitter shunt voltage as measured across a $10\,\Omega$ preresistor.

of time domain signals can be found in Figure 4.3 and 4.4.

Due to unavoidable cross coupling between the orthorgonal transmitter and receiver coil, the SQUID is exposed to a large rf-current during transmitter pulses. In order to protect the SQUID, the FLL is opened during the time of the transmitter pulse. The opening and closing of the FLL is controlled by the reset line of the Magnicon FLL-electronic connected to a TTL output of our PXI function generator. Even after the transmitter pulse, decaying eddy currents and magnetoacoustics continue to overload the SQUID circuit. Thus it is important to establish the SQUID recovery time, measured for the standard transmitter pulse. This is done by cross coupling a megaherz "buzz" signal into the receiver circuit whilst applying a NMR pulse. The FLL is closed immediately after the NMR pulse and the response of the SQUID to the buzz signal is measured.

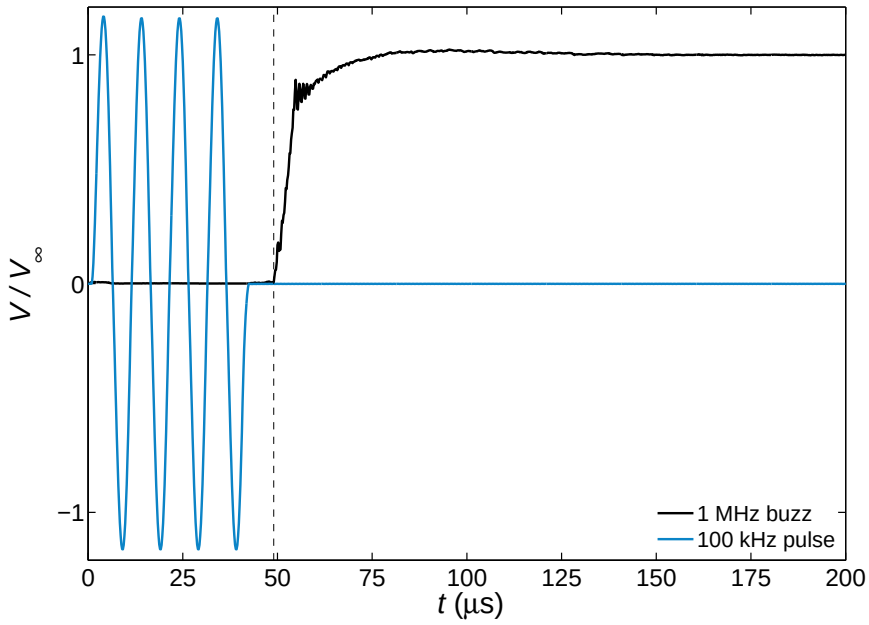

Figure 3.14: The graph shows the SQUID response to the standard four period 61 μT_{pp}, 100 kHz NMR pulse. The black curve is the amplitude of the 1 MHz buzz signal cross coupled into the receiver coil as measured by the SQUID. The black dashed line marks the time at which the FLL is closed.

Figure 3.14 shows an example of a SQUID recovery time measurement following a standard 100 kHz pulse. The amplitude of the 1 MHz buzz signal in this case was calculated by a digital lock-in procedure. The FLL is open during the pulse and closed 9 μs after the end of the NMR pulse. As can be seen the amplitude of the 1 MHz buzz signal subsequently starts to recover to its full magnitude within the following 40 μs. Counting from the centre of the pulse our NMR SQUID has a "dead time" of 70 μs. During this time the amplitude of high frequency NMR signal is distorted and can thus lead to wrong magnetisations and relaxation times when fitting to the frequency spectrum or FID envelope. In order to avoid these distortions and to reduce the effects of transient backgrounds, we truncated our time domain traces to 180 μs after centre of the pulse and used the fitted relaxation times and amplitudes to back extrapolate the centre of pulse values.

3.6 ^{13}C NMR and Ultra-Low Temperature Thermometry

As was shown in the preceding section, the broadband nature of our NMR setup allows us to probe multiple spin species at the same time, here in particular both the ^{3}He and ^{13}C-nuclei. ^{13}C in graphite is a simple weakly coupled spin-system due to its low natural abundance of 1.1 % [111]. Therefore its NMR signal can be used as a diagnostic tool for the magnetic field and temperature inside the NMR cell. Its low natural abundance leads to weak dipole-dipole interactions between the ^{13}C-spins and thus paramagnetic behaviour down to lowest temperatures and long transverse relaxation times and hence a sharp NMR line (unusual in solids).

The ^{13}C FIDs observed in our experiments were best described by single exponential decays. The ^{13}C-magnetisations, frequencies and transverse relaxation times were determined by fitting single Lorentzian line-shapes (Eqn. 2.75) to the complex Fourier spectra of the recorded FIDs.

Magnet Inhomogeneity

The frequency dependence of the transverse relaxation time T_2^* was measured at 8.5 mK in order to determine the magnet inhomogeneity $\Delta B/B$ of the new NMR magnet and the intrinsic spin-spin relaxation time T_2 of ^{13}C. For this transverse relaxation times were measured in magnetic fields ranging from 1.4 to 9.6 mT. Figure 3.15 shows the inverse transverse relaxation time as a function of the Larmor frequency. Following Equation 2.77, T_2 and $\Delta B/B$ have been determined as (3.17 ± 0.01) ms and (490 ± 20) ppm.

Ultra Low Temperature Thermometers

It emerged during the first experiments on the new NMR setup that except for the MCT above 1 mK neither of the other the other two thermometers (^{195}Pt-NMR and Johnson-noise thermometer) gave the correct temperature of the helium inside the NMR cell. The temperature of the NMR-cell, as measured by ^{13}C-NMR, saturated at a much higher temperature than the 100 μK-plate it was mounted on (see Fig. 3.16). This situation imprroved on adding a ^{3}He film.

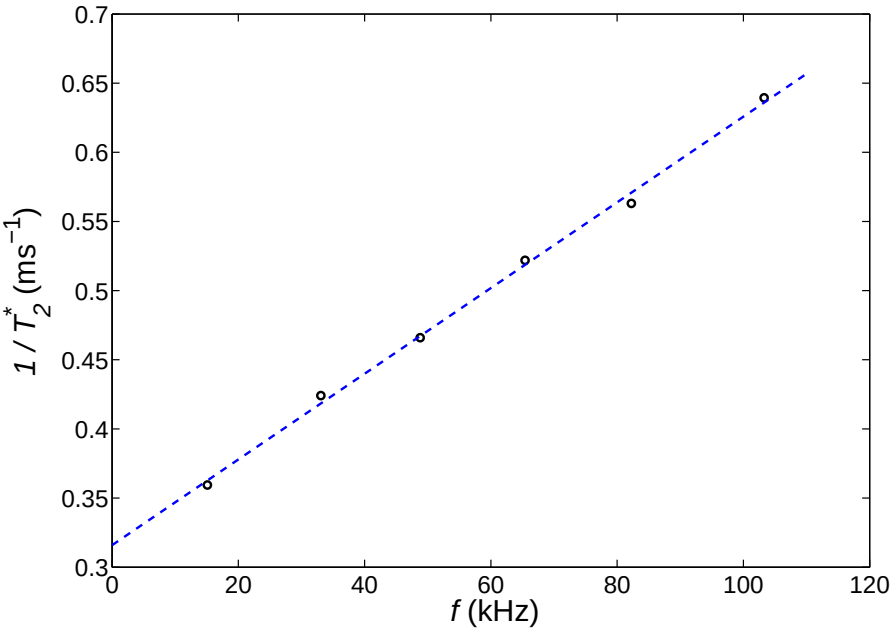

Figure 3.15: Frequency dependence of the transverse relaxation time of ^{13}C in graphite measured at 8.5 mK.

A comparison of the ^{3}He and ^{13}C-magnetisation, however, showed that the ^{13}C-nuclei in the graphite substrate are in good thermal equilibrium with the helium film and are paramagnetic down to at least 250 μK. Here a paramagnetic $\rho_2 = 1.82\,\mathrm{nm}^{-2}$ bilayer ^{3}He sample was used as reference (see Fig. 3.17). The ^{13}C-nuclei were therefore identified as a potential new NMR-thermometer, located directly inside the NMR cell. Its temperature, i.e. magnetisation could be inferred from the parasitic ^{13}C-signal, which is simultaneously excited and measured with the ^{3}He-signal [98]. Its Curie-constant is calibrated against the MCT at at least four stabilised temperatures in the temperature range of 5 to 20 mK allowing us to determine its temperature to within 4 % accuracy.

Figure 3.16 shows a comparison of the ultra-low temperature thermometers during two warm ups of "Run 43". In "Run 43" we have studied the spin dynamics of ^{3}He bilayer adsorbed onto graphite. The left graph of Figure 3.16 warm up corresponds to an empty cell whereas in the right-hand side graph a bilayer of ^{3}He with density

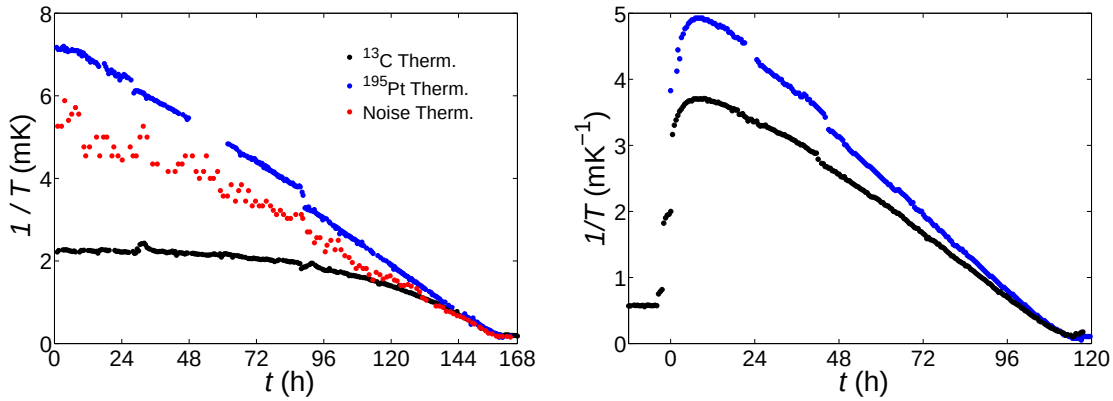

Figure 3.16: Comparison of ultra-low temperature thermometers: a) Time evolution of the temperatures measured by the ^{195}Pt NMR, Johnson-noise and ^{13}C NMR thermometer of an empty cell b) Comparison of the same thermometers in the presence of a $\rho_2 = 3.69\,\mathrm{nm}^{-2}$ bilayer ^{3}He sample.

of $\rho_2 = 3.69\,\mathrm{nm}^{-2}$ was adsorbed on to the graphite. As can be seen in the empty NMR-cell warm up, the ^{13}C-thermometer saturates at 450 μK far above the ^{195}Pt-thermometer, which shows a minimal temperature of 163 μK. In the filled NMR cell, even though the precooling conditions were poorer as evidenced by the higher ^{195}Pt temperature of 200 μK, the ^{13}C-thermometer cools much further to 270 μK. Thus the discrepancy between both thermometers is reduced. This effect can be attributed to: a) a reduced heat leak into the cell, through e.g. decaying time dependent heat leaks or b) an improved thermal coupling between the substrate and heat sink by the added ^{3}He bilayer.

The heat leak in case a) can be estimated by assuming that the silver foil heat link is the dominant thermal resistance between the cell and the 100 μK-plate. Its thermal resistance can be calculated from the known geometry and measured RRRs of the silver foils and is equivalent to 5 $\mu\Omega$ using Wiedemann-Franz law [88]. Using this thermal resistance and the temperature differences between the ^{13}C and ^{195}Pt-thermometer observed for the empty and filled cell, the heat leak in both cases corresponds to 500 and 75 pW respectively.

The unusually high heat leak into the empty cell case suggests that the thermal resistance in this case is not just governed by the silver heat sink. It is rather possible that some of the weakly coupled graphite platelets in the Grafoil substrate saturate

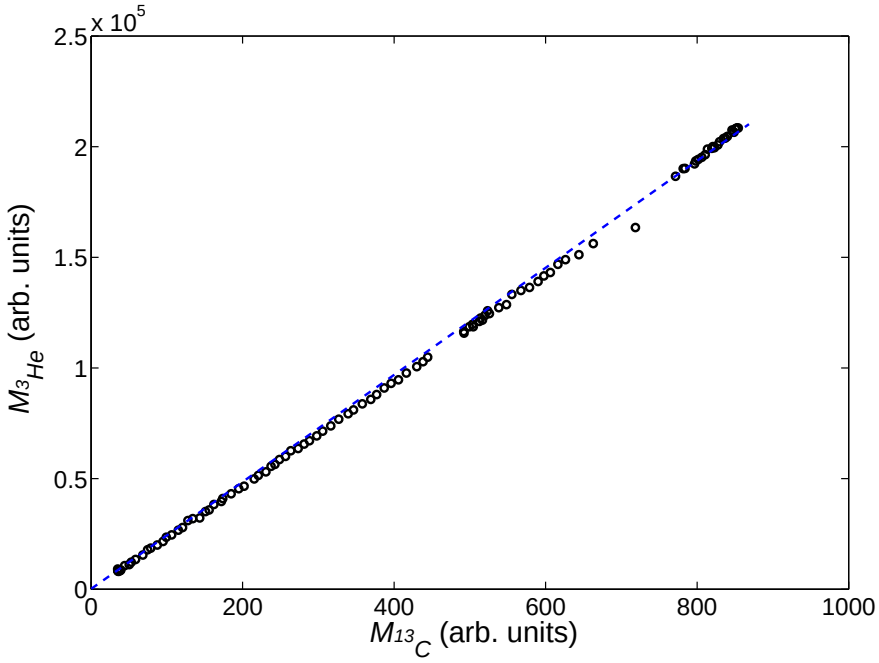

Figure 3.17: Linear relation between the ^{13}C and ^{3}He magnetisation of a $\rho_2 = 1.82\,\mathrm{nm}^{-2}$ ^{3}He bilayer sample. The linearity shows that ^{13}C is paramagnetic and in good thermal equilibrium with the ^{3}He bilayer down to at least $250\,\mu$K.

at a higher temperature due to a large thermal resistance towards the heat sink. On adding helium these weak links are strengthened by the thermal conductance of the helium layers allowing these hot spots to cool to lower temperatures, i.e. the entire cell cools to a lower average temperature.

Another possible explanation for the sudden drop of the thermal resistance between the ^{13}C-nuclei and the silver heat sink is that the added ^{3}He creates a new cooling path through weak dipole-dipole coupling to the ^{13}C-nuclei in the graphite surface. If this dipole-dipole interaction is stronger than the weak hyperfine coupling of the ^{13}C-nuclei to the graphite electron system a significant reduction of the longitudinal relaxation time T_1 and thermal resistance of the ^{13}C should be observed. However this model relies on a low or negligible thermal resistance between the ^{3}He and graphite. A schematic of the proposed cooling paths is shown in Figure 3.18.

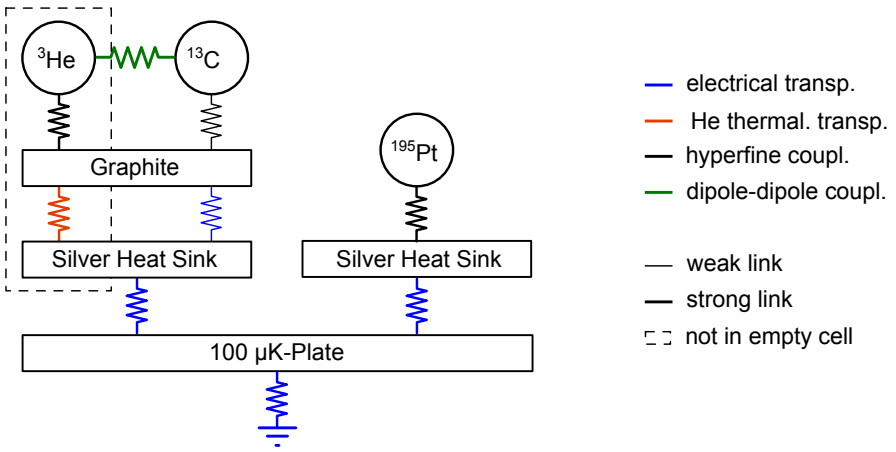

Figure 3.18: The schematic shows the cooling paths for the ^{3}He, ^{13}C and ^{195}Pt-spin systems towards the 100 μK-plate and nuclear demagnetisation stage.

It is known from the thermalisation following a demagnetisation, that the ^{3}He comes much faster into thermal equilibrium with the nuclear stage than the ^{13}C. Thus our assumption of a low thermal resistance between the ^{3}He and graphite might hold. The time scales for both processes are about 8 and 10 to 14 hours.

Longitudinal Relaxation of ^{13}C in Graphite

In order to characterise the time scales governing the ^{13}C-spin system further, its longitudinal relaxation time has been measured down to 250 μK. As was already mentioned in Section 3.3 and 3.4 the longitudinal relaxation time of metals can take values of up to 12, 000 s in metals like silver at millikelvin temperatures [81]. Thus to be more time efficient and to reduce eddy current heating during the measurements, a $180^o - \tau -$ read out $- \tau -$ read out $- \ldots$ pulse sequence was chosen to measure the ^{13}C T_1. This sequence inverts the equilibrium magnetisation only a single time by applying an initial 180^o-pulse and subsequently probes the recovering longitudinal magnetisation by a number of small angle read out pulses. We applied a 1 ms 180^o-pulse at the Larmor frequency of the ^{13}C and probed the recovering magnetisation by up to 2000 60 μs-pulses corresponding to 0.5^o to 3.5^o. Such extraordinary pulse lengths are possible due to the long T_2^* of ^{13}C in graphite. The tip angle of the read out pulse was increased at higher temperatures to account for the signal-to-noise

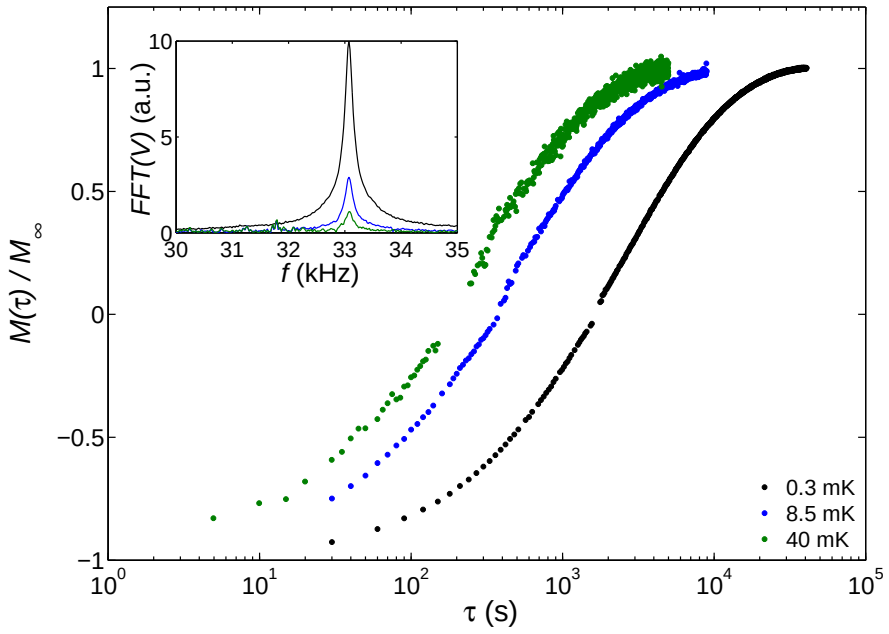

Figure 3.19: The graph shows the longitudinal magnetisation recovery of ^{13}C in graphite following a 180^o-pulse. The magnetisations have been renormalised by their equilibrium value M_∞. The inset shows the equilibrium ^{13}C NMR signal.

loss. The read out repetition rates of 5 to 20 s was chosen according to the expected T_1.

Figure 3.19 shows the recovering longitudinal magnetisation of ^{13}C in graphite for three different temperatures. T_1-sequences above 40 mK were repeated up to ten times and averaged together, to compensate for the exceptionally small signal-to-noise ratio at these temperatures.

The longitudinal recoveries shown in Figure 3.19 do not follow a simple exponential recovery as described by the Bloch equations (Eqn. 2.67 and 2.68). Their functional form is described by a stretched exponential recovery:

$$M(\tau) \;=\; M_\infty - (M_\infty - M(0)) \exp\left\{ \left(\frac{\tau}{T_1^\dagger} \right)^\beta \right\}, \tag{3.23}$$

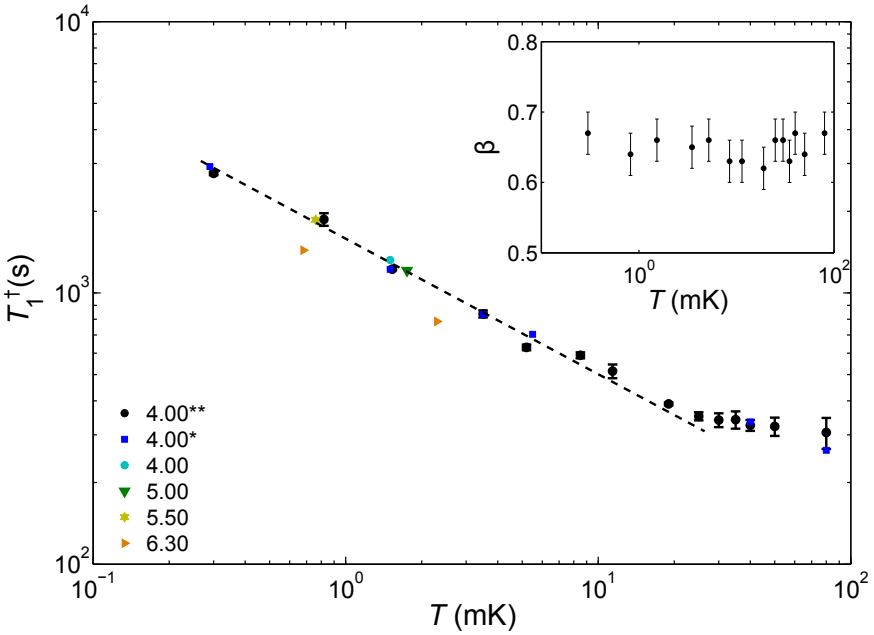

Figure 3.20: The graph shows the temperature dependence of the longitudinal relaxation time $T_1^\dagger$ of ^{13}C in graphite. The graphite was preplated with a $\rho_1 = 11.88\,\mathrm{nm}^{-2}$ monolayer of ^{4}He. Coverages marked with (*), (**) refer to a preplating densities of 11.47, $11.62\,\mathrm{nm}^{-2}$ respectively. The dashed line corresponds to $T^{-1/2}$. The inset shows the stretched exponent of the longitudinal relaxation.

where $T_1^\dagger$ is the generalised longitudinal relaxation time for arbitrary stretched exponents β.

The results for $T_1^\dagger$ and β are shown in Figure 3.20. The stretched exponent β has been determined as 0.66 ± 0.03, i.e. $2/3$ over the entire temperature range. Calculations by Prof. Brian Cowan show that a stretched exponent of $2/3$ can be explained by a distribution of spin-lattice relaxation rates of the form:

$$g(s) = \frac{1}{s}\frac{2^{4/3}}{3^{3/2}\sqrt{\pi}}\left(\frac{r}{s}\right)\exp\left\{-\frac{4}{27}\frac{r^2}{s^2}\right\}U\left(\frac{1}{6};\frac{4}{3};\frac{4}{27}\frac{r^2}{s^2}\right) \tag{3.24}$$

where g(s) is the relaxation rate distribution function, $r^{-1} = T_1^\dagger$ the observed stretched relaxation rate and U a confluent hyper-geometric function [112]. The

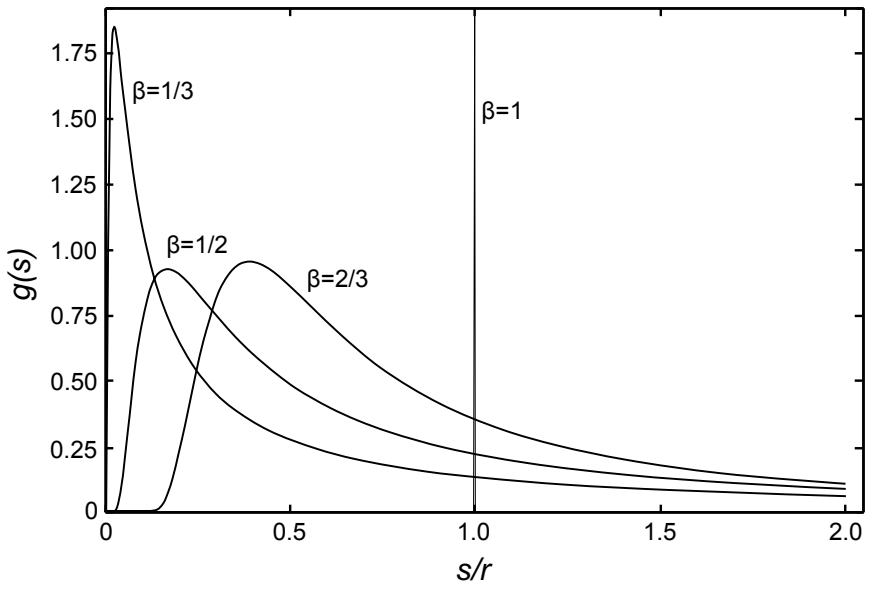

Figure 3.21: T_1 relaxation rate distribution $g(s)$ for stretched exponents $\beta \leq 1$ (data by courtesy of Prof. Brian Cowan).

distribution function $g(s)$ is shown in Figure 3.21 for the case of $\beta = 1; {}^2/_3; {}^1/_2$ and ${}^1/_3$. Such a distribution of T_1 relaxation rates can be caused by the random spatial distribution of ^{13}C-nuclei within graphite.

As can be seen in Figure 3.20 the temperature dependence of $T_1^\dagger$ below 20 mK is well described by a power law with exponent ${}^1/_2$. Thus showing a highly non-Korringa law behaviour of ^{13}C below 20 mK. Above 20 mK the spin-lattice relaxation time appears to be almost temperature independent up to the highest temperatures. A study by Carver *et al.* [113] of single-crystalline graphite found a similar temperature dependence of T_1 for temperatures well above 1 K up to room temperature. Here the temperature exponent of ${}^1/_2$ was attributed to the "semiconductor-like" band structure of graphite [114, 115].

As T_1 is governed by spin-flip processes of free electrons in the vicinity of the magnetic nuclei the probability for a spin-flip in metals i.e. the spin-lattice relaxation rate is proportional to the temperature and density of states at the Fermi-energy

[86]. This is the well known Korringa law. Bloembergen [114] later generalised the Korringa-law for semiconductors by considering the thermal excitation and Boltzmann distribution of free electrons in the presence of a band gap. He found that:

$$\frac{1}{T_1} = B \times n_e(T) \times T^{1/2} \tag{3.25}$$

where B is the Bloembergen-constant containing the gyromagnetic ratios and hyperfine constant. Here the factor $T^{1/2}$ arises from the integration of the governing Boltzmann distribution as opposed to the T-linear term of the Korringa law, which follows from the Fermi-Dirac distribution of charge carriers in normal metals [86]. The Bloembergen relation only leads to a $T^{1/2}$ temperature dependence of T_1 if the charge carrier concentration is constant e.g. in the temperature regime where all "donor states" of a semiconductor are fully ionised [116].

In addition to the temperature dependence the frequency dependence of T_1 has been measured at 8.5 and 40 mK, representing the $T^{1/2}$ and almost temperature independent T_1 regime.

The results of both measurements are shown in Figure 3.22. A linearly increasing $T_1^\dagger$ has been found at both temperatures, starting at a finite zero frequency intercept. The gradient of these curves is to first approximation proportional to the to the measured $T_1^\dagger$ in Figure 3.20.

To conclude, we have measured the longitudinal relaxation time of ^{13}C in graphite. The observed longitudinal relaxations follow stretched exponential recoveries with a stretched exponent of $2/3$. This exponent can be explained by a random spatial distribution of ^{13}C in graphite. The $T_1^\dagger$ follows a $T^{-1/2}$ power law below 20 mK and does thus not obey the Korringa law. The observed temperature exponent of $1/2$ was predicted by Bloembergen for semiconductors and might also be applied to semimetals like graphite, which can be interpreted as a zero gap semiconductor. At ultra-low temperatures $T_1^\dagger$ reaches values of up to 3000 s at 33 kHz. This and the observed temperature dependence shows evidence for a weak hyperfine coupling to the graphite electron system.

However the presence of ^{3}He in the close proximity of the ^{13}C-nuclei might lead to a significant contribution to the spin-lattice relaxation, shortening of T_1 through weak dipole-dipole interactions between the two spin-species. The observed dependence

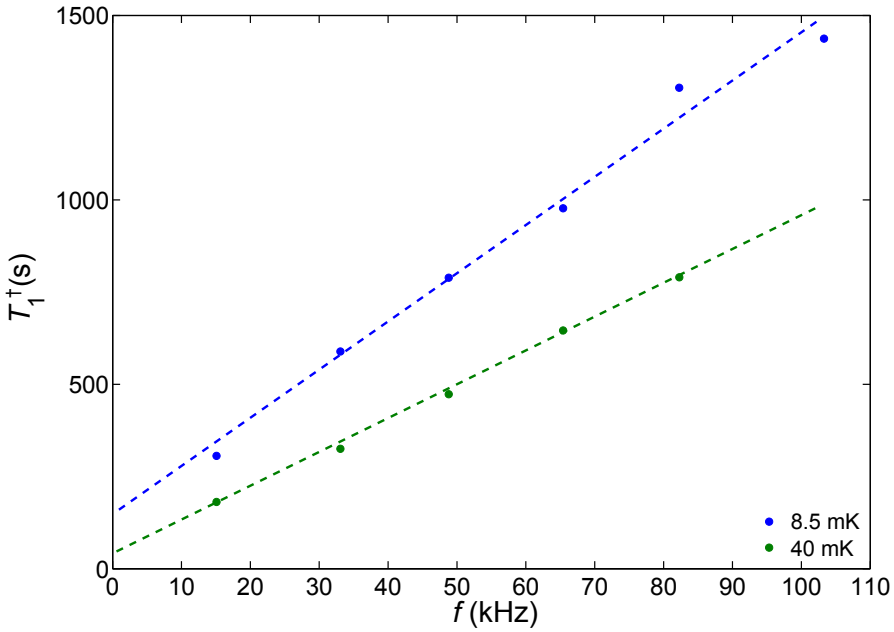

Figure 3.22: The graph shows the frequency dependence of the longitudinal relaxation time of ^{13}C in graphite at 8.5 and 40 mK.

on the ^{3}He covergae is weak, since the graphite, in this case, is preplated with a monolayer of ^{4}He. Further measurements on an empty and ^{3}He filled cell are pending. There have been previous studies of the longitudinal relaxation times of ^{19}F and ^{1}H in insulators like Teflon and Stycast 1266 submerged or surrounded by ^{3}He [117, 118, 119, 120]. In these cases the ^{3}He has been demonstrated to provide the dominant relaxation mechanism.

Thermometer Lag

As we saw in the previous section the ^{13}C-spin system is characterised by extraordinarily long longitudinal relaxation times. In order to use the ^{13}C as a thermometer the NMR pulse rate must be adjusted to a multiple of $T_1^\dagger$ to guarantee good thermal equilibrium. However significantly shorter pulse repetition times might be used if small angle tipping pulses are used.

In our case 0.38^o transmitter pulses were applied, at a repetition time of 30 minutes

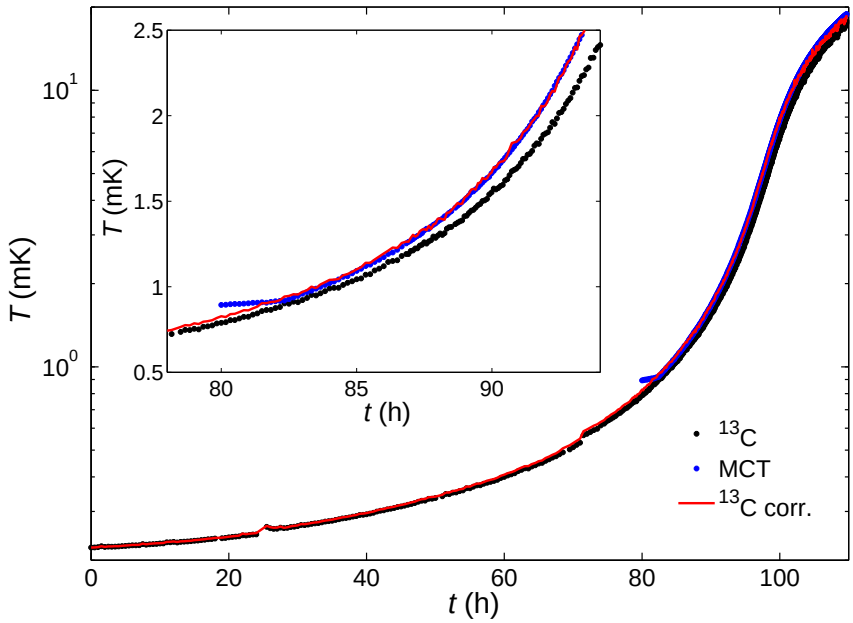

Figure 3.23: The graph shows the temperatures of the ^{13}C NMR thermometer and MCT during the warm up of a $\rho_2 = 6.16\,\mathrm{nm}^2$ ^{3}He:^{4}He sample following a standard demagnetisation cycle.

at sub-500 μK temperatures, which was gradually increased to 2 seconds at 5 mK and above. At these pulse rates the magnetisation suppression induced in the ^{13}C-thermometer is less than 600 ppm and can therefore be neglected.

In addition to the pulse rate limitation, the high T_1 of ^{13}C also limits the response time of the thermometer. A first indication of this thermometer lag was already discussed in the previous section based on the thermal relaxation times following a demagnetisation of the copper stage. These experiments were conducted with pure ^{3}He films, were the paramagnetic first layer could be used as thermometer. The experiments on ^{4}He preplated monolayers of ^{3}He showed an additional developing discrepancy between the ^{13}C-thermometer and MCT at temperatures above 1 mK. In the interval below 10 mK data are taken following the natural warm up after a demagnetisation, for which $\mathrm{d}/\mathrm{d}T(1/T)$ is constant, so the temperature sweep rate accelerates above 1 mK. Here the MCT follows the helium temperature almost in-

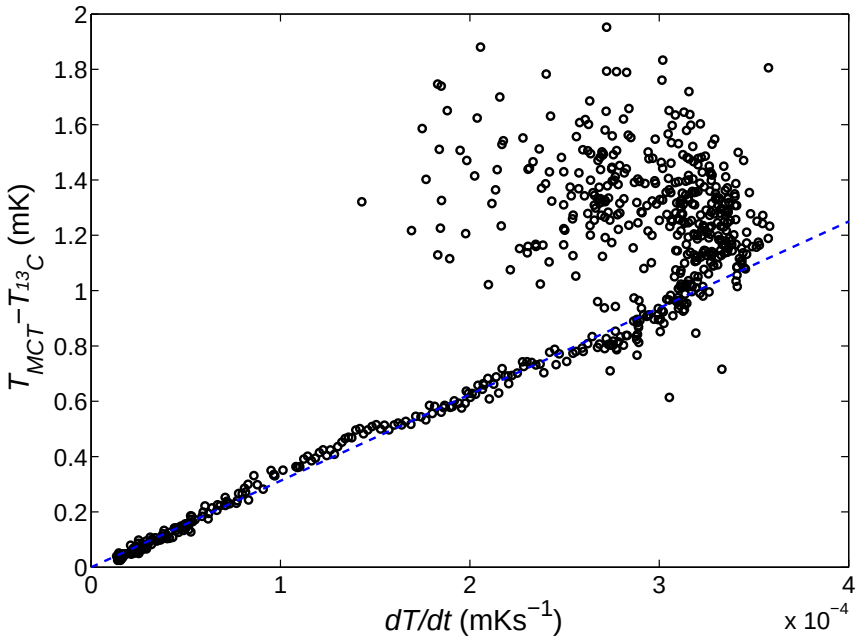

Figure 3.24: The lower graph shows the temperature difference between the two thermometers as a function of the warm up rate during the warm up of the $\rho_2 = 6.16\,\mathrm{nm}^2$ ^{3}He:^{4}He sample.

stantaneously, whereas the ^{13}C-thermometer shows higher and lower temperatures during cool downs and warm ups respectively. As the temperature difference between the thermometers changes sign the observed discrepancy can not be attributed to a static heat leak into either of the two thermometers. A more plausible explanation is that the long T_1 of ^{13}C limits the rate at which the thermometer can change its magnetisation or temperature. Thus the long T_1 induces a lag in the ^{13}C-thermometer at high sweep rates and low temperatures. An example of such behaviour can be seen in the natural warm up of the $\rho_2 = 6.16\,\mathrm{nm}^{-2}$ ^{3}He|^{4}He|graphite sample in Figure 3.23). The black and blue points in this graph are the ^{13}C-thermometer and MCT as measured. The inset shows a close up of the difference between the ^{13}C and MCT.

If the observed lag is a T_1 effect the induced temperature lag must depend on the temperature sweep rate. Figure 3.24 shows the developing temperature difference is indeed proportional to the rate of temperature change. This rate is zero at the

lowest temperatures, when the cell reaches its thermal equilibrium following a demagnetisation. Here the ^{13}C-thermometer shows the correct temperature. At higher temperatures, however, where the rate of temperature change speeds up, due to the linear warm up in $1/T$, the ^{13}C-thermometer develops a lag of up to 1.5 mK.

We therefore propose a correction of the ^{13}C-thermometer that interpolates between its true temperature at lowest temperatures and the MCT temperature at high temperatures and is proportional to the warm up rate:

$$\Delta T = -\alpha \frac{dT}{dt}. \tag{3.26}$$

Here α is the slope of the graph in Figure 3.24. The break down of the linearity at highest sweep rates has been ignored as these sweep rates correspond to temperatures between 10 and 20 mK where the ^{13}C-thermometer looses its sensitivity. The proposed correction is applied over the entire temperature range, but will have a negligible effect at lowest temperatures. The corrected ^{13}C-temperature is shown as red curve in the upper graph of Figure 3.23. As can be seen the correction generates a smooth transition form the ^{13}C thermometer at lowest temperatures to the MCT at higher temperatures. The ^{13}C-correction was applied to all ^{3}He samples of Run 44 with $\rho_2 \geq 5.86\,\mathrm{nm}^{-2}$. The proportionality constants α ranged from 1500 to 3500 s. A systematic of these values was not observed, however, most corrections were applied with $\alpha \approx 2800$ s.

Finally, as the sensitivity of the ^{13}C-thermometer decreases rapidly above 10 mK and the applied corrections become large, we limited the use of the ^{13}C-thermometer to below 2 mK. We generally switched to the MCT between 1 and 2 mK and used this up to 60 mK above which we used the calibrated germanium thermometer.

4 The Metal-Insulator Transition in Two-Dimensional ^{3}He

As was outlined in the Introduction and Section 2.2 two-dimensional ^{3}He is a strongly correlated Fermion system, in which strongly repulsive short range interactions result in its solidification at a density of about $6\,\mathrm{nm}^{-2}$ depending on the underlying substrate lattice. Here we study the increasing correlations and magnetism of the fluid and solid phase of two-dimensional ^{3}He on graphite preplated with a full monolayer of ^{4}He on tuning the layer density.

The objective of this study was to develop a microscopic model for the fluid-solid quantum phase transition, observed in two-dimensional ^{3}He, based on our new NMR measurements and to clarify the influence of the $^4/_7$-superstructure on this transition. Furthermore fundamental questions concerning the structure and correlations within the coexistence phase, on approaching the fluid-solid phase transition, will be addressed. The final part of this chapter discusses the possibility of a gapless quantum-spin liquid in the highly frustrated spin-$^1/_2$ triangular lattice ^{3}He solid.

4.1 Sample Preparation

The helium samples presented in this thesis are prepared by adsorbing helium onto an exfoliated graphite substrate, Grafoil [106, 121]. The graphite is encapsulated in a leak tight NMR cell which is described in Appendix A.3. This cell is connected to a room temperature gas handling system via a 3 mm o.d. fill line which narrows down to a 1.0×0.25 mm silver capillary at lowest temperatures. By admitting doses of helium gas to the cell, controlled monolayer films can be grown at low temperatures. The amount of helium adsorbed onto the substrate is measured by the room temperature gas handling system, which consists of a precisely calibrated dosing volume and highly sensitive Paroscientific oscillating quartz pressure gauge

[91].

In order to determine the total surface area of the Grafoil substrate, a 4.2 K adsorption isotherm was measured (see Fig. 4.1). For this, the NMR-cell was stabilised at 4.2 K using a heater and carbon glass thermometer mounted to the mixing chamber of the dilution refrigerator. ^{4}He was added in small precise doses of about 1.5 μmol and adsorbed onto the substrate. The equilibrium vapour pressure $p(n)$ above the growing ^{4}He film was measured using the room temperature quartz pressure gauge. At 4.2 K and submonolayer coverages the recorded vapour pressures are in the sub-microbar range due to the large binding potential [122]. On approaching the coverage at which promotion to a second layer occurs, the vapour pressure increases sharply. The admitted amount of ^{4}He n_{admit} must be corrected by the amount of ^{4}He in the vapour phase:

$$n_{\mathrm{ads}} = n_{\mathrm{admit}} - \frac{V_{\mathrm{D}} * p(n)}{R * 300\,\mathrm{K}}, \tag{4.1}$$

to obtain the amount of adsorbed ^{4}He n_{ads}. The total parasitic volume V_{D} of the fill line and NMR-cell was estimated from previous experiments on a similar cell (Run38). An empirical helium bath level dependence was included for the effective fill line volume[1] yielding a total room-temperature equivalent volume of 317 to 307 cm^3. The uncorrected and corrected adsorption isotherm are shown in Figure 4.1.

Each ^{4}He film was annealed at a vapour pressure of 1 mbar for at least two hours in order to guarantee a good film homogeneity, and subsequently cooled down at rate of less than 1 K/h. Due to a comparably large parasitic volume compared to the capacity of the substrate, annealing of low density films leads to the desorption of large fractions of the adsorbed film. In order to avoid this desorption ballast cells, containing a large quantity of the graphite substrate, may be introduced into the system.

The corrected adsorption isotherm (Fig. 4.1) was used to determine the total surface area of the Grafoil substrate inside the NMR cell. At second layer promotion the vapour pressure above the helium film increases sharply due to the reduction of the binding energy in the second layer [122]. In thermal equilibrium the chemical

[1] As determined by J. Nyeki and A. Phillis during Run38

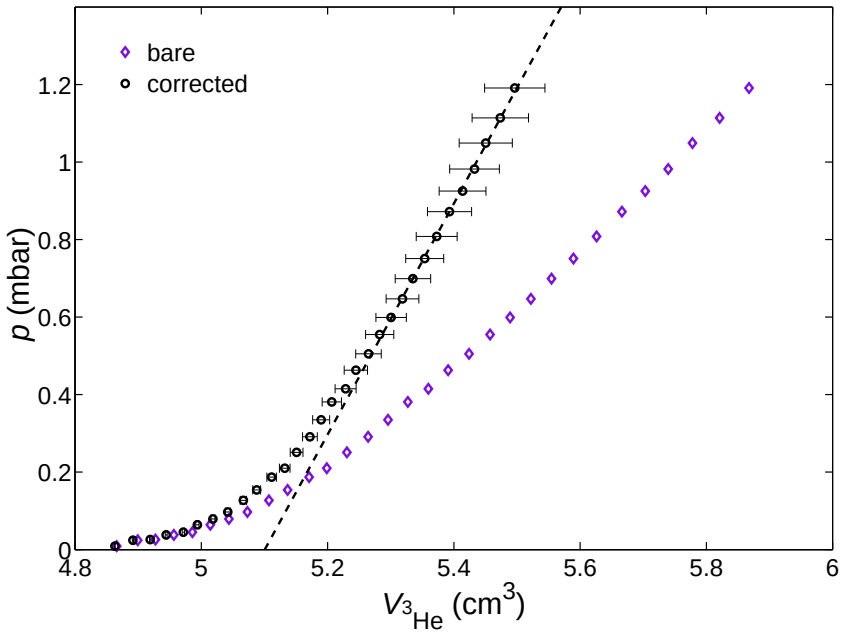

Figure 4.1: ^{4}He Adsorption Isotherm on the Grafoil NMR-cell: The graph shows the vapour pressure isotherm of ^{4}He on Grafoil at 4.2 K. Purple diamonds are raw data, black circles have been corrected by a helium bath level dependent parasitic volume of 306 to 317 cm^3. The point where the dashed line meets the isotherm at (5.26 ± 0.03) cm^3 is point-B i.e. monolayer completion.

potential of the adsorbed film and the vapour are equal. At constant temperature the vapour pressure thus reflects the chemical potential of the film. The point at which the sharp vapour pressure upturn, in the adsorption isotherm, becomes linear again is called point-B and is conventionally taken as the fiducial point marking second layer promotion (see Fig. 4.1). In ^{4}He adsorbed onto graphite this corresponds to a fixed density of 11.4 nm^{-2} [2]. This fixed-point in conjunction with the adsorbed amount of ^{4}He can be used to calculate the total surface area of the substrate. In our case the total adsorption area of the Grafoil substrate inside the NMR cell has been calculated as (12.23 ± 0.07) m^2. This value was confirmed by a preceding ^{3}He

[2] RHUL internal coverage scale, based on the monolayer completion densities of ^{3}He and ^{4}He as measured by neutron scattering [123], see also [16, 124]

adsorption isotherm and NMR experiments on the same graphite substrate (Run43).

Once the ^{4}He adsorption isotherm was finished, ^{4}He was removed from the cell to adjust the coverage of the preplating to one full monolayer of $11.4\,\mathrm{nm}^{-2}$ ^{4}He. Later ^{3}He was added to the cell to grow a second layer ^{3}He film on top. Here the increased zero-point motion of ^{3}He compared to ^{4}He in the van der Waals like surface binding potential leads to a lower binding energy of the ^{3}He with respect to ^{4}He. Thus in mixed systems, ^{4}He will preferentially adsorb onto the substrate, occupying lower layers and displacing ^{3}He into higher layers. In order to grow such a layered structure it is extremely important to ensure that the film is in equilibrium, i.e. with the ^{4}He in the lower layers. To do so the same thermal annealing procedure, i.e. such that the vapour pressure is of the order of 1 mbar, is applied as for growing monolayer samples.

Furthermore special attention needs to be paid to the ^{4}He under-layer density. A neutron diffraction study by Roger *et al.*, measuring the lattice constant of the underlayer solid through the observable Bragg peaks, has shown that the first layer of helium, irrespective of the isotope, compresses by about 3.5 to 4.5 % when a second layer film is grown on top [125, 126]. In order to avoid ^{3}He inclusions in the first layer, we therefore tuned the density of the ^{4}He under-layer at a top-layer density of $4.00\,\mathrm{nm}^{-2}$ (about 50 % of second layer completion). ^{3}He inclusions in the first layer correspond to localised spin-$^1/_2$, with a Curie law magnetisation, which tends to mask signals of interest from the second layer, particularly at lowest temperatures. Here the magnetisation and frequency shift of the ^{3}He top-layer were measured by pulsed NMR as the ^{4}He coverage was changed (see also Sec. 4.2). Figure 4.2 shows the temperature dependence of the top-layer magnetisation for three different ^{4}He preplatings.

Here the intermediate temperature magnetisation plateau and high temperature magnetisation decrease are attributed to the second layer Fermi fluid (see also Sec. 4.2.1 and 4.3), whereas the observed ultra-low temperature magnetisation upturn is thought to originate from paramagnetic ^{3}He inclusion in the under-layer. In a simple displacement model the amount of these ^{3}He inclusions and its magnetisation should linearly decrease by adding ^{4}He into the under-layer. However, the inset of Figure 4.2 shows that the ultra-low temperature magnetisation does not respond linearly to adding ^{4}He and approaches the intermediate magnetisation plateau only

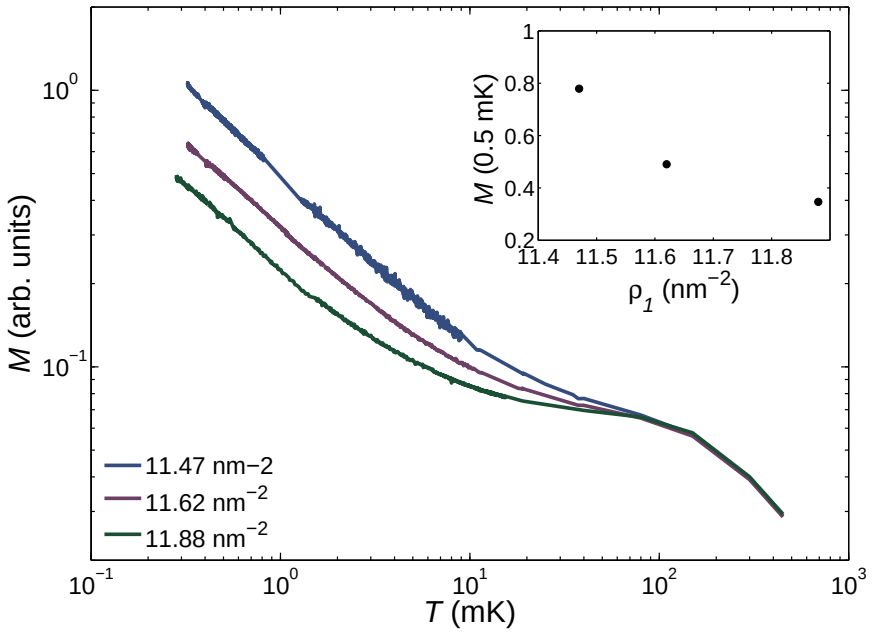

Figure 4.2: Tuning the ^{4}He Preplating: The graph shows the temperature dependence of the magnetisation of a 4.00 nm^{-2} ^{3}He sample. The low temperature magnetisation attributed to ^{3}He atoms in the under-layer vanishes non-linearly with increasing density of the ^{4}He bottom-layer.

assymptotically. Thus the low temperature upturn can not be fully compensated. At the same time the frequency shift induced by the ^{3}He inclusions has reduced by an order of magnitude (Fig. 4.6).

Assuming the observed upturn originates from localised spins in the first layer Curie-Weiss plus Fermi fluid magnetisation fits, as will be discussed in Section 4.3.1, can be used to determine the amount of ^{3}He particles trapped in the first layer. Here the calculations show a reduction of the number of localised spins from 2.6 % in the 11.47 nm^{-2} to 1.0 % in the 11.88 nm^{-2} sample.

Since neither of the two measurements indicates a precise ^{4}He preplating at which there are no ^{3}He inclusions in the first layer, we based our final preplating on the measured first layer compression by Roger *et al.*. Hence all ^{3}He samples with a density above 4.00 nm^{-2} are based on a ^{4}He preplating of 11.88 nm^{-2} corresponding

to 104.2 % of the second layer promotion density.

A question of interest is whether there is an intrinsic effect like interlayer particle exchange or low temperature Fermi fluid instabilities in two-dimensional ^{3}He giving rise to a low temperature magnetisation upturn. The latter is addressed in the subsequent sections.

4.2 Pulsed NMR Measurements and Results

The ^{3}He magnetisation, transeverse relaxation time and shift in Larmor frequency were inferred from Lorentzian fits to the complex Fourier spectrum (see Eqn. 2.75 Sec. 2.4.3) or from stretched and double exponential fits to the free induction decay (FID) envelope function. Due to a finite SQUID recovery time of about 100 μs in our system and decaying eddy-current transients after the NMR tipping pulse, FIDs were truncated to 160 μs after the NMR pulse. The true magnetisation was calculated from back extrapolations of the truncated fits to the centre of the NMR pulse according to the fitted transverse relaxation.

Stretched Exponential Decays

In order to determine the precise shape of the ^{3}He FID envelope function, a digital lock-in procedure was applied to the recorded FIDs. A reference sine-wave was fitted to the time-domain signals at the Larmor frequency. The time-domain signals are subsequently multiplied by the reference sine-wave and integrated over three Larmor periods to eliminate any beating effects introduced by the superimposed ^{13}C-signal and $2f$-component of the lock-in procedure. The resulting FID envelope is fitted to a stretched exponential decay of the form:

$$F(t) \;=\; M_0 \exp\left\{-\left(\frac{t}{T_2^{\dagger}}\right)^{\alpha}\right\}, \tag{4.2}$$

using the MatLab least-squares nlinfit() regression, yielding the magnetisation, transverse relaxation time and stretched exponent of the FID.

As an example, the FID of a $\rho_2 = 6.45\,\mathrm{nm}^{-2}$ sample is shown in Figure 4.3. Here FID is fitted by a stretched exponential decay with an exponent of $\alpha = 1.289 \pm 0.001$

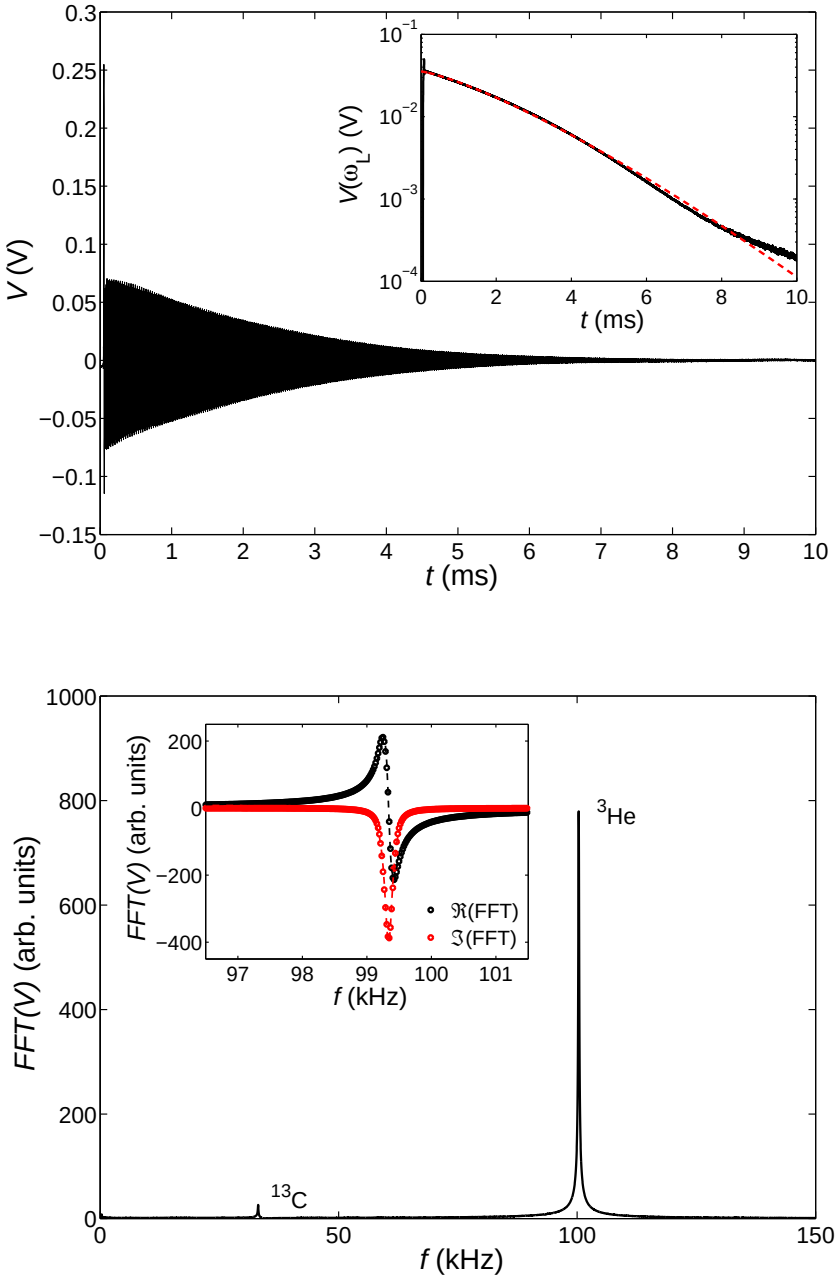

Figure 4.3: Stretched exponential free-induction decay of a $\rho_2 = 6.45\,\mathrm{nm}^{-2}$ sample preplated with ^{4}He at 0.25 mK following a 7.2^o tipping pulse. The upper graph and shows the recorded signal and envelope function (inset) of the FID. The lower graph shows the magnitude of the complex Fourier transformation and a Lorenzian line fit to the complex spectrum (inset).

(see red dashed line in the upper inset). The graph below shows the corresponding Fourier spectrum and a Lorentzian line-shape fit through the spectrum. As can be seen even though the stretched exponent of the FID differs significantly from unity, the complex Fourier spectrum can still be fitted by a simple exponential decay, i.e. Lorentzian line. The Pearson coefficients of both fits are of the order of $R^2 > 0.9995$ and $R^2 \approx 0.995$ for stretched and simple exponential decays respectively. The minor deviations of the stretched exponential fit at long times are ignored due to their negligible contribution to the total signal. Typical standard deviations of the fitted parameters range between 10^{-3} and 10^{-4}. Thus, in order to reduce systematic errors, the lock-in procedure and stretched exponential fits have been employed wherever possible.

Due to a comparably poor signal-to-noise ratio of the NMR signals for coverages up to 4.0nm^{-2}, the lock-in analysis could not be applied and the data were fitted by single Lorentzian lines in the frequency domain. The magnetisations of these samples were rescaled to the same arbitrary units as used by the lock-in program. However, for consistency, transverse relaxation times are only presented for coverages above $4.0\,\mathrm{nm}^{-2}$.

In general we observed stretched exponents ranging from $\alpha = 0.85$ to 1.45. Short transverse relaxation times were accompanied by a low stretched exponent, whereas long transverse relaxation times produced stretched exponents of up to 1.45. Figure 4.8 shows an overview over all stretched exponents as function of the corresponding transverse relaxation time. Here an almost linear dependence of α on $T_2^\dagger$ can be observed. The origin of this dependence will be discussed in Section 4.2.3.

Double Exponential Decays

For completeness, I also discuss the different behaviour following third layer promotion at $7.00\,\mathrm{nm}^{-2}$. Above a coverage of $7.20\,\mathrm{nm}^{-2}$ the formerly stretched exponential FIDs, become a superposition of two exponential decays. The magnetism and spin dynamics of this density region will be discussed elsewhere. However, the onset of the effects involved is already visible at the highest coverages presented in this thesis.

A prominent example of a double exponential decay in a third layer sample is shown in Figure 4.4. The envelope function in Figure 4.4 shows a clear transition

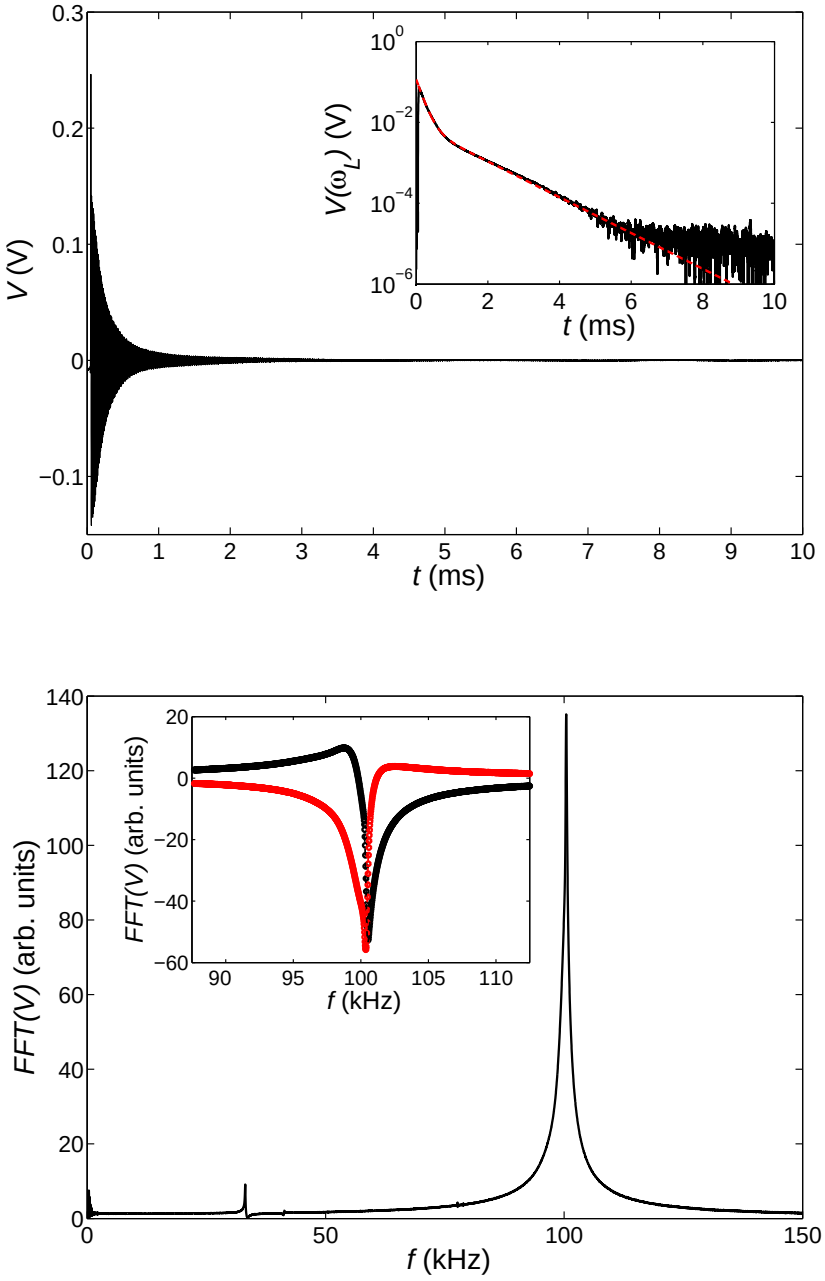

Figure 4.4: Double exponential free-induction decay of a $\rho_2 = 7.61\,\mathrm{nm}^{-2}$ sample preplated with ^{4}He at 0.25 mK following a 7.2^o tipping pulse. The upper graph shows the recorded signal and envelope function (inset) of the FID. The lower graph shows the magnitude of the complex Fourier transformation and a two-Lorenzian line fit to the complex spectrum (inset).

from a fast to a slowly decaying regime at around 1 ms associated with two magnetic subsystems decaying at different rates. Due to a frequency difference between the two NMR-signals, the lock-in procedure can no longer be applied and FIDs have to be fitted in the frequency domain by a superposition of two Lorenzian lines (see Fig. 4.4).

Multiple Lorentzian lines are fitted, by truncating the time domain signal at multiple times and simultaneously fitting to the complex Fourier spectra of all these truncations [127]. Each of the two Lorentzian lines is defined by a zero-time amplitude, frequency, phase and relaxation time. The magnetisations and phases of the truncated signals are then calculated from these initial parameters by using the exponential decay of the initial magnetisation and linear progression of the phase with time. Thus the fits of all three truncation times are linked to one set of initial parameters, which is determined by a least-square error fit.

Due to the dominance of the second layer signal over the minute third layer signal in the 7.20 nm^{-2} ^{3}He sample, double Lorentzian fits were not possible and data from this coverage were fitted by stretched exponentials. However, it is thought that the increasing relevance of the third layer signal at lowest temperatures leads to fitting errors and accounts for some of the changes observed in the magnetisations and relaxation times, here in particular the abrupt shortening of $T_2^\dagger$ at lowest temperatures (see Fig. 4.13).

In a preceding sample series (Run 43) we have studied a pure double layer ^{3}He system adsorbed on graphite. Here the solid first layer is a paramagnetic solid whilst the second layer shows the same fluid-solid phase transition as the ^{3}He|^{4}He|graphite system presented in this thesis. In a weakly coupled limit one would expect that both layers follow their intrinsic spin dynamics and relaxation.

Therefore the FID of the double-layer system is expected to be double exponential, where the solid has a short transverse relaxation time due to its rigid lattice dipole-dipole interaction and the fluid top-layer shows a longer relaxation time due to the motional averaging. In the real system the situation is complicated by interlayer exchange, which leads to an effective mixing of the two relaxations depending on the interlayer exchange rate.

The analysis of the FID was further made difficult by the relative weight of the two components and their partially short relaxation times. At lowest densities,

where the paramagnetic bottom-layer dominates the fluid top-layer magnetisation, the system does only show minute deviations from Curie law and an analysis of the fluid magnetisation is extremely prone to errors. At higher densities where the fluid magnetisation gains in importance and grows due to the increasing correlations within the fluid the measured relaxation times are so short that the magnetisation has already significantly decayed within the SQUID dead time. Thus the determination of the corresponding relaxation times and following back-extrapolation of the magnetisation were subject to huge errors. Furthermore given the stretched nature of the FIDs presented in this thesis it must be assumed that the observed FIDs in the double layer system are stretched too thus invalidating the back-extrapolations based on the double exponential fits.

As the data and analysis of the ^{3}He double layer system of Run 43 are still subject of ongoing debate, it has been decided to defer its presentation to a later point and exclude it from this thesis.

4.2.1 Magnetisation

Figure 4.5 shows the temperature dependence of the magnetisation of all ^{3}He samples. Samples with a ^{3}He second layer density $\rho_2 \geq 4.0\,\mathrm{nm}^{-2}$ are preplated with $11.88\,\mathrm{nm}^{-2}$ ^{4}He, the $1.95\,\mathrm{nm}^{-2}$ sample on the other hand with $11.47\,\mathrm{nm}^{-2}$ ^{4}He. As previously discussed the magnetisation was determined from the centre-of-pulse value of a stretched exponential fit to the FID envelope function (see for example Fig. 4.3). The magnetisations of the lowest density samples (dashed lines) were determined from a Lorentzian fit to the complex Fourier spectrum and rescaled to convert between the different arbitrary units of the two fitting programs. The dominant part of this conversion factor arises from the scaling of the Fourier spectrum with the sampling rate (5 MS/s). The conversion factor of $(2.94 \pm 0.02) \times 10^6$ was determined by cross-calibrating the high temperature magnetisation of samples with coverages in the range of 5.00 to $5.61\,\mathrm{nm}^{-2}$.

Starting at high temperatures, the low density magnetisations in Figure 4.5 increase initially with a temperature exponent close to -1 indicating an almost Curie-like behaviour. This initial increase is followed by a magnetisation plateau at temperatures between 10 and 100 mK before the magnetisation starts to grow again

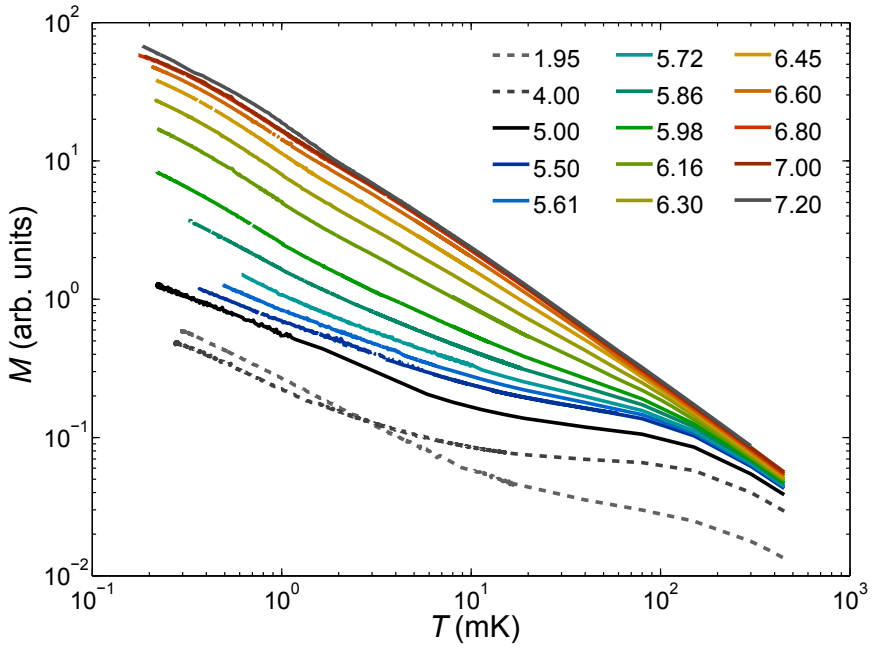

Figure 4.5: Temperature dependence of the ^{3}He magnetisation for the coverages studied. Curves are labeled by ^{3}He coverage in nm^{-2}

at ultra-low temperatures. With increasing ^{3}He density this ultra-low temperature magnetisation upturn increases strongly and starts to dominate the observed magnetisation plateau. The three distinct temperature regions are attributed to the non-degenerate Fermi fluid at high temperatures, the degenerate Fermi fluid at intermediate temperatures and a solid-like magnetisation at ultra-low temperatures [16, 22, 23, 128]. A detailed analysis and discussion of this temperature dependence will be given in Section 4.3.

In order to highlight deviations from simple paramagnetic behaviour, the product of temperature and magnetisation is plotted as a function of temperature (Fig. 4.15 and Fig. 4.13). The precision of the SQUID-NMR measurements means that useful insight is obtained from such a plot, which is more sensitive than the log-log plot of Figure 4.5. Here MT can be thought of as an effective, generally temperature dependent, Curie constant of the system. At temperatures well above the characteristic temperatures of the magnetic system, MT approaches a constant value and

the system follows Curie law as outlined in Equation 2.64.

The ultra-low temperature and solid magnetisations on the other hand are better shown in inverse coordinates, i.e. $1/MT$ against $1/T$ (see Fig. 4.17). Here $1/MT$ follows an almost linear function of $1/T$ at lowest temperatures. Such a behaviour is usually attributed to Curie-Weiss law, where the slope is proportional to the Curie-Weiss temperature divided by the Curie constant. However, we will show in Section 4.3.2 that the observed behaviour seems to be better described by two ultra-low temperature Fermi fluids.

Curie Constant and Saturated Magnetisation

As will be seen in the MT-isotherms (Fig. 4.13) at low densities the apparent Curie constant is strongly temperature dependent, which is consistent with the interpretation as a Fermi liquid (see also Sec. 2.2.5). At densities above $6.80\,\mathrm{nm}^{-2}$, however, the high temperature MT-isotherms collapse on to one curve, showing that the system behaves almost like an ideal paramagnet. The density dependence of these isotherms has been used to determine the effective Curie constant per spin in our system. Averaged over the three highest densities the Curie constant is $C_0 = 3.618\,\mathrm{a.u./nm}^{-2}$ (a.u. = arbitrary units) or $C_0 = 2.96 \times 10^{-19}\,\mathrm{a.u./spin}$ (MT are given in mV × mK). By applying Equations 2.64 and 2.65 it is possible to infer the specific signal size for a fully polarised ^{3}He sample. Here a constant of $M_0 = 1.5034 \times 10^3\,\mathrm{a.u./nm}^{-2}$ has been calculated (M given in mV).

In between the two density regimes, lies a region from 5.5 to $6.8\,\mathrm{nm}^{-2}$ where the low temperature isotherms interpolate between the Fermi fluid at low densities and Curie-like solid at high densities.

As we will see in Section 4.3 the three coverage regions can be attributed to the Fermi liquid, phase coexistence and Mott insulator phases of a Wigner-Mott system.

4.2.2 Frequency Shifts

In addition to the magnetisation, the NMR frequency shift relative to the Larmor frequency, as probe for local magnetic fields in the samples, was measured. In order to distinguish between the frequency shift introduced by external NMR field changes and internal fields the observed ^{3}He NMR frequencies have been corrected, using the

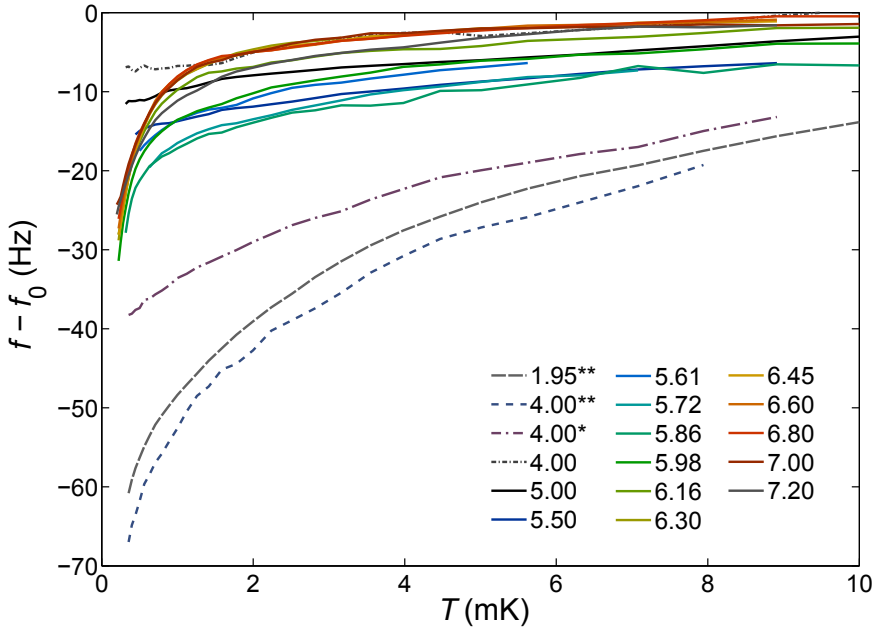

Figure 4.6: Temperature dependence of the frequency shift corrected for changes in the ambient field

frequency of the ^{13}C NMR-signal, to determine the magnitude of the external NMR field.

Minor changes of the ^{13}C frequency, were observed when the nuclear demagnetisation stage has been magnetised or demagnetised as well when the nuclear demagnetisation stage heat switch has been closed. The former is due to the magnetic field of the demagnetisation solenoid penetrating the non-ideally shielded NMR-magnet. The latter effect is so far unexplained. Both effects led to field changes of the order of 2.5 and 1.5 μT corresponding to a change of the ^{3}He NMR frequency of up to 100 Hz.

The frequency shifts shown in Figure 4.6, are the measured ^{3}He NMR frequencies relative to f_0:

$$f_0 = f_{^{13}C}\frac{\gamma_{^{13}\mathrm{C}}}{\gamma_{^3\mathrm{He}}} + f_\Delta. \tag{4.3}$$

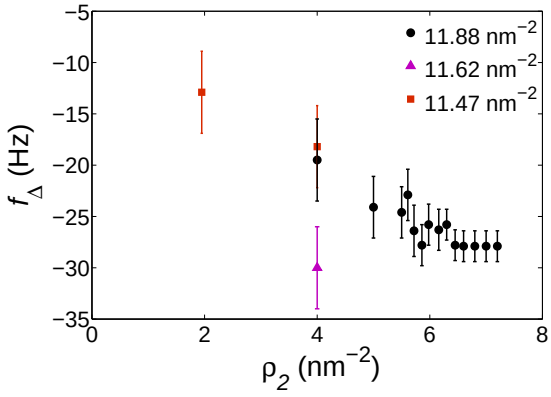

Figure 4.7: Additional frequency shift as calculated from the back-extrapolation of the frequency Fig. 4.26 to zero polarisation.

Here f_0 is the sum of the ^{3}He Larmor frequency according to the measured magnetic field and an additional frequency correction f_Δ. The magnetic field has been calculated from the measured ^{13}C-frequency $f_{^{13}C}$ and its gyromagnetic ratio $\gamma_{^{13}C}$. The additional frequency correction was determined by extrapolating the observed frequency shifts to infinite temperature, i.e. zero polarisation. If the frequency shifts arise due to dipolar fields, their magnitude must be zero at infinite temperature. Examples of the frequency shifts plotted against the ^{3}He-polarisation can be found in Figure 4.26. As this additional frequency correction is of the order of $f_\Delta/f \approx 10^{-4}$, which is the precision of our gyromagnetic ratios, a contribution due to an uncertainty of the gyromagnetic ratios can not be excluded. However the coverage dependence is thought to originate from a Knight shift of the ^{13}C-frequency. The additional frequency correction f_Δ is shown in Figure 4.2.2 and the gyromagnetic ratios of ^{13}C and ^{3}He are 10.71 MHz/T and 32.44 MHz/T respectively [77].

Due to a large frequency scatter, induced by the fitting uncertainty of the ^{13}C-frequency, the frequency shifts shown in Figure 4.2.2, 4.13 and 4.26 have been averaged over 40 successive NMR traces. The initial scatter of the corrected frequency data was about ±3 Hz.

Thus, whithin the uncertainties of the procedure described above, the frequency shifts in ^{3}He NMR shown in Figure 4.6 are intrinsic to the ^{3}He film.

On cooling all frequency shifts in Figure 4.6 diverge towards negative frequencies. This effect can be understood as an increasing polarisation of the ^{3}He spins, leading to increasing dipolar local fields within the ^{3}He films. The negative sign of the

induced frequency shifts is a consequence of the planar configuration of the spins, whose magnetisation points along the magnetic field normal to the plane. The field experienced by a spin is the sum of the external and all neighboring dipolar fields and the tensor dipole-dipole interaction gives a negative shift in our orientation. Due to the r^{-3} spatial dependence of the dipolar fields their lattice sum is dominated by nearest and next-nearest neighbours converging relatively slowly. Nevertheless the frequency shift is probing the local magnetism in the sample and does not scale with the system size.

As has already been shown in Section 4.1, composite ^{3}He films with non-ideal ^{4}He preplating show signs of localised ^{3}He atoms in the ^{4}He under-layer. Their concentration and accordingly magnetisation could be suppressed by adding ^{4}He into the under-layer. The local dipole fields induced by these impurity atoms is thought to be the cause of the comparably large frequency shifts observed in the 1.95 to 4.00 nm^{-2} samples which vanishes with increasing ^{4}He coverage. Similarly to the low temperature magnetisation upturn, these frequency shifts were also suppressed by adding ^{4}He to the under-layer.

The frequency shifts of the subsequent samples, with the highest ^{4}He preplating of 11.88 nm^{-2}, show a much weaker temperature dependence, originating from the two-dimensional Fermi liquid in the second layer, ranging between zero and 15 Hz. This frequency shift grows with increasing second layer density up 5.86 nm^{-2}. Above 5.86 nm^{-2} the high temperature frequency shifts decreases, whilst the low temperature shifts are increasing. Above 6.16 nm^{-2} all frequency shifts collapse onto one general curve. Similarly to the magnetisation data, these temperature dependencies might be grouped into three density regions, Fermi fluid, phase coexistence and Mott insulator densities. An interpretation of the observed frequency shifts can be found in Sections 4.3.4 and 4.4.

4.2.3 Transverse Relaxation Times

As has been introduced in Section 2.4.2, the transverse relaxation time is a powerful probe for spin diffusion and local fields in a sample. We determined the transverse and intrinsic relaxation times in our ^{3}He samples by fitting stretched exponential decays to the FIDs and by measuring the time dependence of the intrinsic relaxation

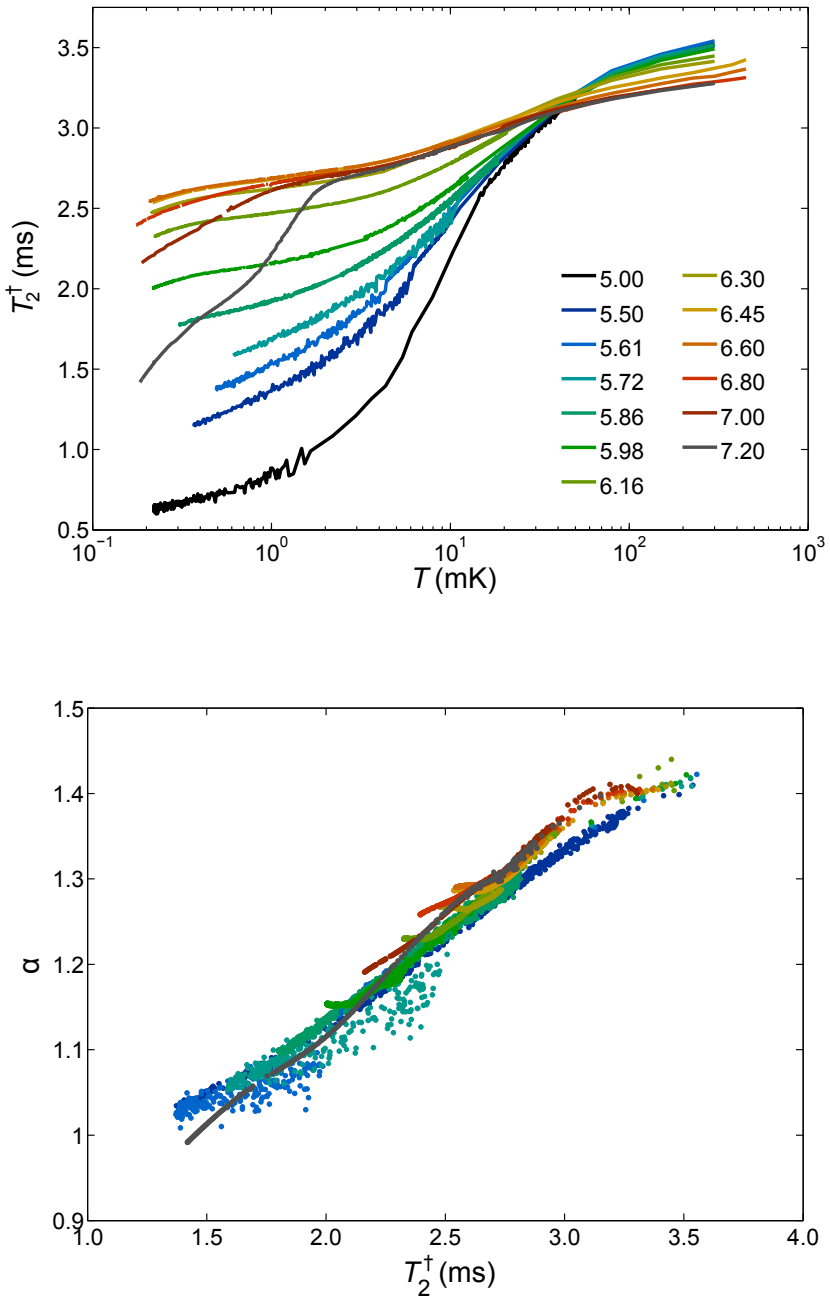

Figure 4.8: The upper graph shows the temperature dependence of the transverse relaxation time $T_2^\dagger$ of ^{3}He|^{4}He|graphite as extracted from stretched exponential fits to the FID envelope function for ^{3}He coverages above $5.00\,\mathrm{nm}^{-2}$. The lower graph shows the stretched exponent as a function of the transverse relaxation times.

by spin echoes. Figure 4.8 shows the fitted transverse relaxation times and stretched exponents of our samples. The transverse relaxation times $T_2^\dagger$ in Figure 4.8 are the stretched exponential relaxation times and are generally not equivalent to the transverse relaxation times T_2^* as introduced in Section 2.4.2.

Both of these relaxation times might be interpreted as the time at which the transverse relaxation function $F(t)$ has decayed to $1/e$ of its initial value. In the case of an unstretched decay, i.e. $\alpha = 1$, both relaxation times are equivalent.

In Fig. 4.8 the stretched exponent is shown as a function of the transverse relaxation time $T_2^\dagger$. As can be seen the stretched exponent depends strongly on the transverse relaxation time. The stretched exponent is one for short relaxation times and increases linearly up to the magnet limit of about $T_M = 3.25\,\mathrm{ms}$ (see magnet inhomogeneity, Sec. 3.6, and Eqn. 2.77), where it takes a value of $\alpha = 1.45$. The magnet limit is calculated from the measured magnetic field inhomogeneity (Sec. 3.6). This dependence of the stretched exponent can be explained by considering that the observed transverse relaxation is the sum of the intrinsic and external relaxation channel due to local motionally narrowed internal fields and external field gradients.

In the following we assume that we are in the limit $t \gg \tau_c$, the motional narrowed limit (for which $1/T_2 = M_2\tau_c$), so that the intrinsic relaxation is exponential.

Most of our measurements focus on $T_2^\dagger$, which has additional contributions arising from magnetic field gradients. The first is the well known contribution of magnet inhomogeneity, a conventional discussion of which is provided in Section 2.4.2. The second more complex effect is field gradients arising from the diamagnetism of the graphite substrate combined with edges/mosaicity of the surface. These lead to susceptibility artifacts at the platelet edges, and a randomicity of field gradients due to the sample morphology. Both of these terms scale with applied magnetic field. The fact that the current NMR experiments are undertaken in magnetic fields up to hundred times smaller than those conventionally used is helpful to reduce the impact of these effects.

The influence of substrate diamagnetism is more complex to deal with since it involves a second correlation time τ_d - the time needed to diffuse towards a platelet edge. In the following model we assume that we are in the slow diffusion limit ($\tau_d \gg 1/\Delta\omega$, where $\Delta\omega$ are the rms variations in local field). In this limit, Gaussian

relaxation is likely to be a reasonable approximation to T_2^* processes arising from local gradient field distribution originating from both the magnet inhomogeneity and graphite morphology.

Since it can be shown that different relaxation channels multiply in $F(t)$, we therefore model $F(t)$ as the product of an exponential term (arising from intrinsic relaxation) and a Gaussian term (arising from magnet/substrate field gradients). It can be shown that a product of exponential ($\alpha = 1$) and Gaussian relaxation ($\alpha = 2$) can be approximated by a stretched exponential relaxation with $1 < \alpha < 2$.

Since the external field gradients are time independent and their correlation time is only determined by spin diffusion through the field gradient, one might assume, that the correlation time of the external fields is much larger than the Larmor period in the slow diffusive limit. The resulting external relaxation, would therefore follow a Gaussian relaxation. At the same time the correlation time of the local fields might be much shorter due to intrinsic field fluctuations combined with the spin diffusion. Thus the transverse relaxation function of this channel is simple exponential. Depending on the relative time scales of the two relaxation channels the overall relaxation will be governed by either of the two or an admixture of both. Thus it is believed that at short $T_2^\dagger$ the relaxation is exponential due to the dominance of the intrinsic relaxation whereas at $T_2^\dagger \approx T_M$ the relaxation function tends towards a Gaussian relaxation due to the increasing effect of external fields gradients.

Simulations of this mixed relaxation in the slow diffusion limit are shown in Figure 4.9. Here the transverse relaxation function is thought to follow:

$$F(t) \approx \exp\left\{-\frac{t}{T_2(\omega)} - \frac{t^2}{2\sigma(\omega)^2}\right\}. \tag{4.4}$$

The half-width half maximum σ of the Gaussian relaxation was chosen such that the high temperature stretched exponents and relaxation times agree with the measurements (Fig. 4.8).

The simulation shows a good agreement with the experimentally observed stretched exponents. Furthermore it can be seen that $T_2 \approx T_2^\dagger$ for transverse relaxation times shorter than 1.5 ms. At higher T_2 the calculated $T_2^\dagger$ go asymptotically towards the magnet limit.

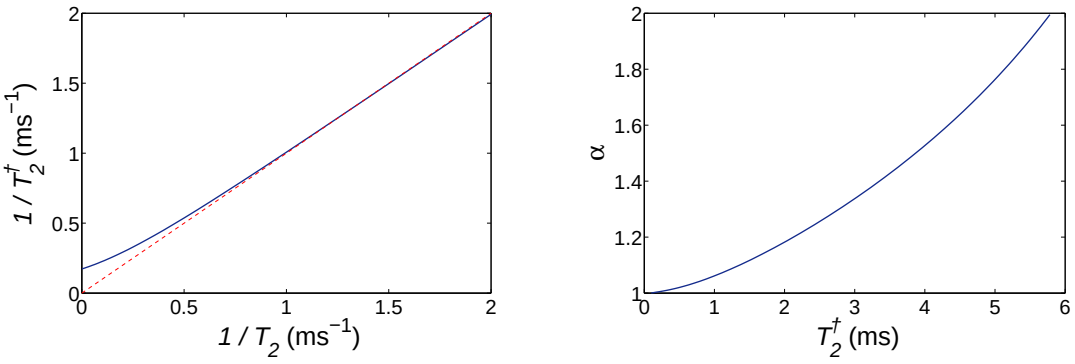

Figure 4.9: Simulated transverse relaxation times in the slow diffusive limit. The half width half maximum of the Gaussian contribution has been chosen a 4.1 ms. The left graph shows the transverse relaxation time $T_2^\dagger$ as a function of the intrinsic relaxation time T_2. The right-hand side graph shows the resulting stretched exponent of the relaxation function.

The slow diffusion hypothesis is also reinforced by T_2 spin echo measurements (see also Sec. 2.4.3). Here the forming spin echoes appear as Gaussians rather than back-to-back exponential decays (see inset of Fig. 4.10).

We determined the intrinsic T_2's of samples with second layer densities of 5.50 to 7.20 nm by measuring the time evolution of the spin echo height (see Fig. 4.10 and 4.11). A 90^o-τ-180^o pulse sequence was applied to produce spin echoes at times 2τ after the initial 90^o pulse. The 90^o and 180^o-pulses were applied at the precise ^{3}He Larmor frequency with a pulse length of 40 Larmor periods or approximately 400 μs. The amplitudes of the pulses were 0.274 A_{pp} and 0.558 A_{pp} corresponding to 77 μT_{pp} and 154 μT_{pp} for the 90^o and 180^o pulse respectively. The experimentally determined transmitter fields are in excellent agreement with theoretically predictions (see Eqn. 2.74).

Figure 4.10 shows the forming spin echoes of a 5.50 nm^{-2} ^{3}He sample at 20 mK. Here the amplitude of the echoes decreases exponentially with the delay time τ. Figure 4.11 shows the spin echo amplitudes of the same sample measured at three different Larmor frequencies as a function of their delay time. The echo amplitudes were obtained from Gaussian fits to the envelope function of the recorded spin echoes. Here the same lock-in procedure as described in the previous section was applied to calculate the envelope function.

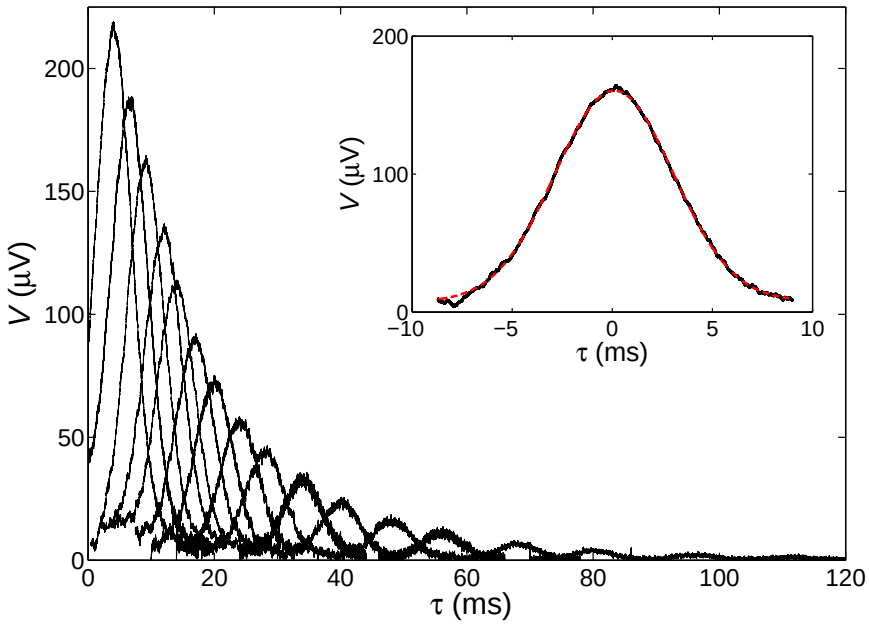

Figure 4.10: Spin echo measurement at $5.50\,\mathrm{nm}^{-2}$ and 100 mK: The graph shows the spin echoes measured at a second layer density of $5.50\,\mathrm{nm}^{-2}$ and temperature of 100 mK. The center position of the echoes have been shifted to the delay time τ. The inset shows the Gaussian shape of the spin echoes with a half-width of half-maximum of $\sigma = 2.96$ ms.

As can be seen in the figure, the extracted spin echo amplitude does not decay as a simple exponential function but rather as a superposition of two exponential functions. The slow relaxation time of the double exponential decay is plotted as a function of frequency in the inset of Figure 4.11. The intrinsic transverse relaxation rate of the slow component increases with increasing magnetic field and decreases with temperature. The fast component, however, is temperature and frequency independent and gives a value of about (15 ± 2) ms. The magnetisation ratios of the two components are shown in the inset of Figure 4.12. Here the slow component makes up a third to a half of the observed total spin echo amplitude.

Spin echo measurements by Takayoshi *et al.* in a magnetic field of 172 mT corresponding to a Larmor frequency of 5.5 MHz and the same temperature and density range found a pronounced double exponential behaviour of the decaying spin echo

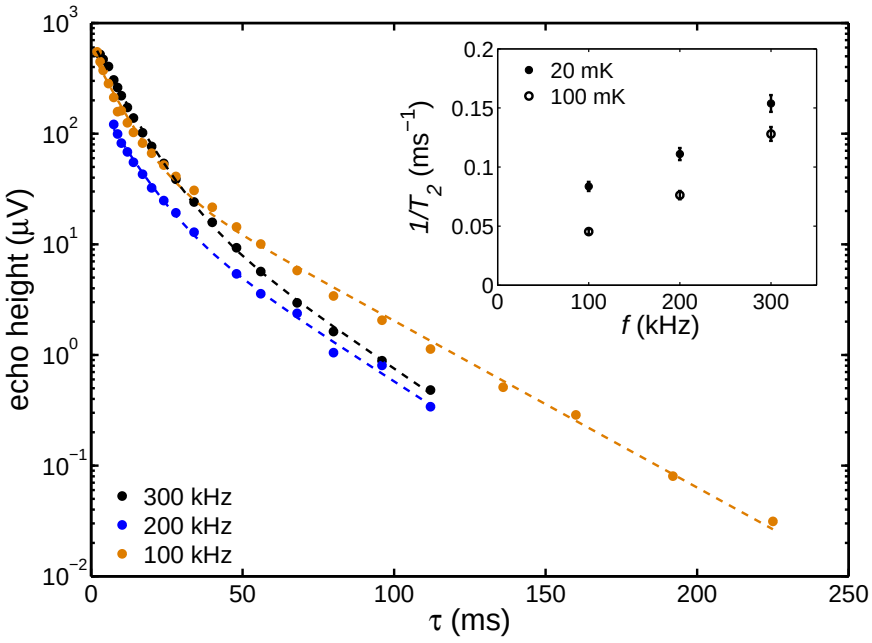

Figure 4.11: Frequency dependence of the intrinsic relaxation at 5.50 nm^{-2} and 100 mK: The graph shows the time dependence of the spin echo amplitude for a Larmor frequency of 100, 200 and 300 kHz. The inset shows the inverse of the long fitted relaxation times as a function of frequency.

amplitude [129]. There the magnetisation of their fast component, however, exceeded the magnetisation of the slow component by orders of magnitude. In their paper Takayoshi *et al.* showed that by filling their NMR-cell with bulk ^{3}He the slow component vanished and hence argued that the slow component is the intrinsic property of the two-dimensional system. By the same arguments and the observed temperature, density and frequency independence of the short relaxation time, following discussion will only focus on the long relaxation time. The origin of the short relaxation time will be discussed elsewhere.

In the light of the slow diffusion arguments brought forward to describe the observed stretching of the FID, it is clear that as the spin echo amplitude probes the intrinsic relaxation the observed decay is simple exponential, whilst the shape of the spin echoes, which is determined by re- and dephasing in magnetic field gradi-

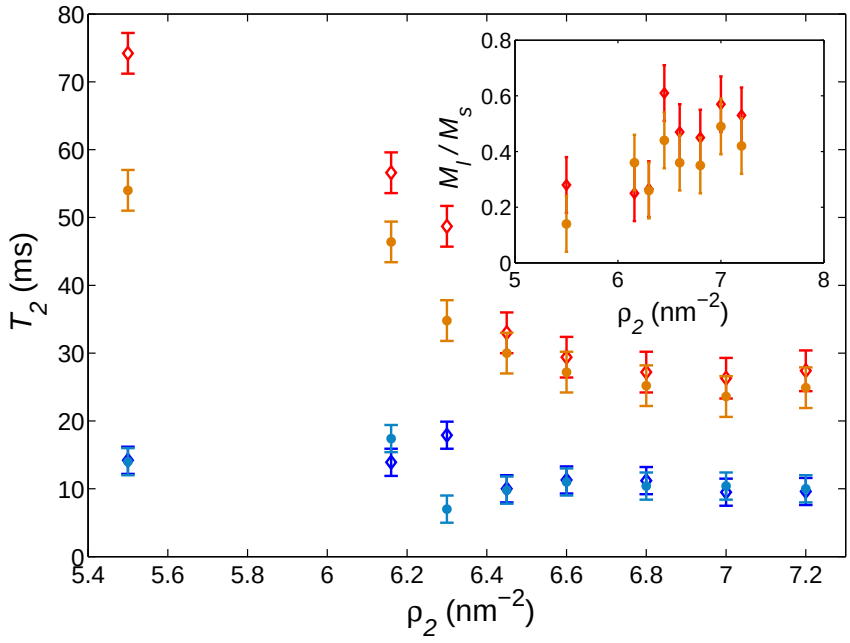

Figure 4.12: The graph shows the density dependence of the intrinsic transverse relaxation times of ^{3}He|^{4}He|graphite measured at 20 mK (closed symbols) and 100 mK (open symbols) and a Larmor frequency of 100 kHz. The inset shows the magnetisation ratio of the long to the short component.

ents, is Gaussian. Linking the observations of both methods we can conclude that two-dimensional ^{3}He is an example of a slowly diffusing spin system.

The density dependence of the intrinsic transverse relaxation times at 20 and 100 mK is shown in Figure 4.13. The isotherms show a strong reduction of T_2 on approaching a second layer density of 6.80 nm^{-2} similar to the $T_2^\dagger$-isotherms in Figure 4.13. Above this density the transverse and intrinsic transverse relaxation time remain constant.

Unfortunately the study of the intrinsic relaxation times was limited to temperatures well above 1 mK, due to eddy current heating at ultra-low temperatures (see also Sec. 4.4.2). A conversion from $T_2^\dagger$ to T_2, by subtracting the magnet contribution (see Equ. 2.77) is not possible, as it is only valid for simple exponential decays, i.e. stretched exponents of $\alpha = 1$. Attempts to map T_2 on to $T_2^\dagger$ by applying the

simulated relaxation times failed, as there was no single σ for which the calculated 20 and 100 mK T_2s agreed with the measurements. Therefore the low and ultra-low temperature spin dynamics can only be discussed on the basis of the stretched transverse relaxation times.

As can be seen in Figure 4.8, we observe a continuous increase of $T_2^\dagger$ with temperature for all coverages and temperatures. The gradient of this temperature dependence is strongly reduced with increasing second layer density. At around 40 to 60 mK all of these temperatures dependencies cross each other. In this temperature region $T_2^\dagger$ becomes almost density independent as can be seen in the 40 mK-isotherm (Fig. 4.13). At 5.86 nm^{-2} the temperature dependence of $T_2^\dagger$ develops a downward bend at lowest temperatures. The onset temperature of which shifts upwards with increasing coverage, whilst its magnitude stays almost constant up to a coverage of about 6.80 nm^{-2}. We will later see that the onset of this feature coincides with the growth of solid in the system. The general behaviour of $T_2^\dagger$ is also reflected in the isotherms (Fig. 4.13).

The observed density and temperature dependence of T_2 and $T_2^\dagger$ will be further discussed in the context of the Mott-Hubbard phase diagram in the following sections. However a precise interpretation of both relaxation times in terms of a microscopic model is challenging due to the competing effect of internal fields and spin diffusion.

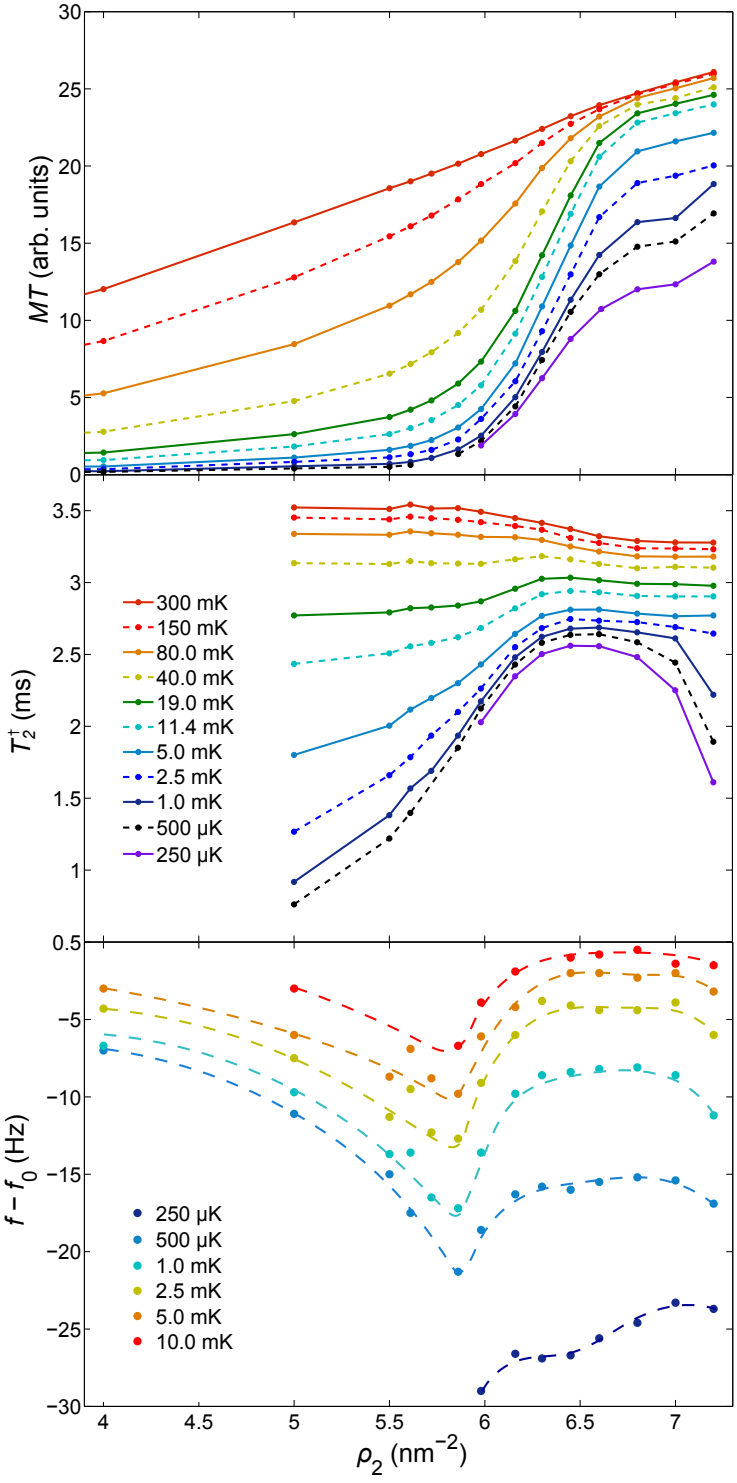

Figure 4.13: Isotherms of the ^{3}He magnetisation, transverse relaxation time and frequency shift

4.3 The Metal-Insulator Transition

As we saw in Section 2.1.2 the interactions i.e. correlations in Landau-Fermi liquids can be expressed by a series of Landau parameters. In two-dimensional ^{3}He, F_1^s and F_0^a are the Landau parameters leading to the renormalisation of its quasi-particle effective mass and spin susceptibility. These parameters may be determined by a combination of heat capacity and magnetisation measurements.

Earlier heat capacity measurements on ^{3}He|^{4}He|graphite were able to determine the effective mass of the ^{3}He quasi-particles up to fluid densities of about $6\,\mathrm{nm}^{-2}$ [24]. However, for densities above $6\,\mathrm{nm}^{-2}$, the low temperature Fermi liquid heat capacity was superimposed by a large spin contribution, the origin of which we will discuss, which made a further analysis impossible [130].

We measured the magnetisation of two-dimensional ^{3}He on graphite using pulsed NMR (see Fig. 4.5). As has been shown in Section 2.1.2 and 2.2.5 the low temperature magnetisation of a Landau-Fermi liquid is proportional to its density of states at the Fermi energy, determined by the effective mass m^*or equivalently the spin symmetric Landau parameter F_1^s. Furthermore we saw that the spin anti-symmetric Landau parameter F_0^a can lead to an additional enhancement of the spin susceptibility. Combined heat capacity and NMR experiments on two-dimensional ^{3}He [16, 19] have already shown that F_0^a follows the almost localised Fermion model by Vollhardt et al. [18]. Here F_0^a is weakly effective mass dependent and takes a value of approximately -0.75.

The key feature of our analysis is to apply Dyugaev's empirical temperature dependence of the Fermi liquid magnetisation, which interpolates between the degenerate and non-degenerate Fermi liquid far below and above the Fermi temperature (see Fig. 4.14) [131].

In Figure 4.14 it can be seen that the Dyugaev temperature dependence follows exactly the shape of the Pauli susceptibility for a 3D parabolic band. Here the 3D and 2D Pauli magnetisations have been calculated by numerical integration of Equations 2.2 to 2.4, where the chemical potential was iteratively calculated conserve the total particle number. The characteristic Dyugaev fluid temperature of the best fitting curve (black dashed line), however, lies 36% below the theoretical Fermi temperature (red dashed line). Similarly in 2D, the Dyugaev formula follows

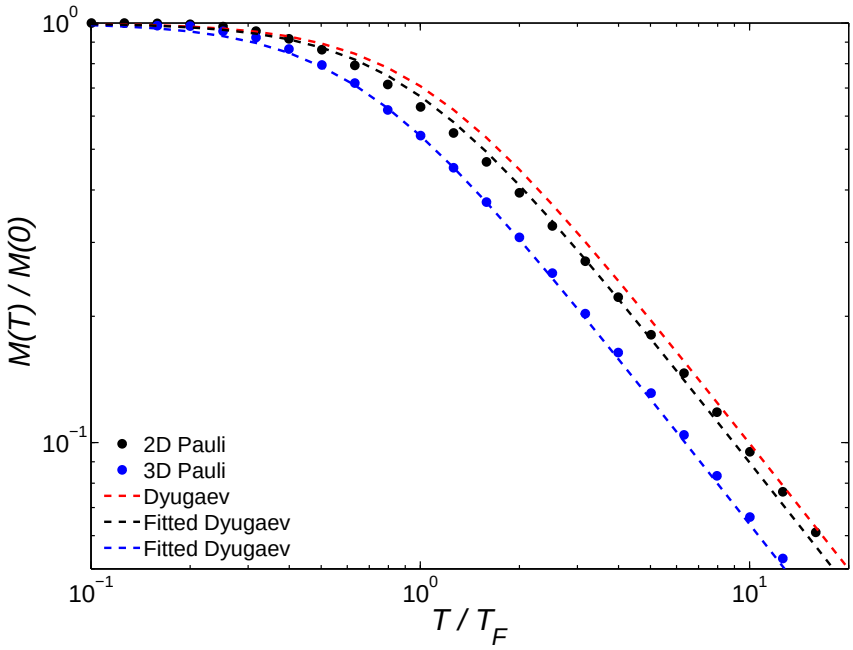

Figure 4.14: The graph shows the numerically calculated Pauli magnetisations for a 2D and 3D parabolic band and the corresponding Dyugaev formula fits. Here the red, blue and black dashed lines correspond to the Dyugaev magnetisations (see e.g. Eqn. 4.7) where $T_{\mathrm{Fl}} = 1$, 0.64 and 0.9.

the simulated temperature dependence, but shows minor discrepancies around the Fermi temperature. In part these discrepancies can be as large as 12%. Due to this discrepancy a fitting error of about 5% for the Dyugaev fluid temperature is induced, depending on the weighting of the fit. In these cases the characteristic temperature is about 88% of the theoretical Fermi temperature. We will thus correct the fitted Dyugaev fluid temperatures T_{Fl} by this 88% to obtain the renormalised Fermi temperature T_{F}^{**}.

The renormalised Fermi temperature T_F^{**} of the ^{3}He quasi-particles in our system is determined by:

$$T_F^{**} = T_F \frac{1 + F_0^a}{m^*/m}. \tag{4.5}$$

Using the theoretical mass dependence of F_0^a predicted by the almost localised

Fermion model (Eqn. 2.44), we can calculate the effective masses of the ^{3}He quasiparticles in our system. Thus m^*/m is essentially determined from the higher temperature data, through the onset of quantum degeneracy. The success of the Dyugaev model demonstrates the rational for this approach, for magnetisation data. It avoids the more anomalous behaviour observed deep into the quantum degenerate regime.

Thus as was already mentioned in Section 4.2.1, our measured magnetisations do not show a clear Pauli magnetisation plateau for temperatures well below the degeneracy temperatures of the Fermi liquid (see Fig. 4.5). The fluid magnetisation is rather dominated by an unexpected low temperature magnetisation upturn which increases throughout the phase diagram. In order to account for the low temperature upturn additional magnetisation terms were added to the Dyugaev Fermi fluid magnetisation. The most successful models were the Curie-Weiss solid plus Fermi fluid and three Fermi fluids models. Both are presented in the following two sections.

4.3.1 The Curie-Weiss Plus Fermi Fluid Model

The first approximation used to describe the low temperature magnetisation upturn is a simple Curie-Weiss contribution. The Curie-Weiss model is used to describe the magnetisation of a weakly interacting localised spins far above their ordering temperature. Its temperature dependence is described by the Curie-Weiss law:

$$M(T) = \frac{C}{T + \Theta} \tag{4.6}$$

where the Curie-Weiss temperature Θ is directly proportional to the exchange constant J of the solid (see Sec. 2.3.3) and C is proportional to the number of participating spins. As this is a high temperature approximation of Equation 2.50 its range of validity is limited to about $T > 5J \approx 2\Theta$. Due to the relatively high exchange constants in two-dimensional ^{3}He, fits had to be restricted to temperatures above 5 mK. The functional form fitted to the magnetisation data is the sum of a Curie-Weiss solid and Dyugaev Fermi fluid magnetisation:

$$M(T) = \frac{C_{\mathrm{CW}}}{T + \Theta} + \frac{C_{\mathrm{Fl}}}{\sqrt{T^2 + T_{\mathrm{Fl}}^2}}. \tag{4.7}$$

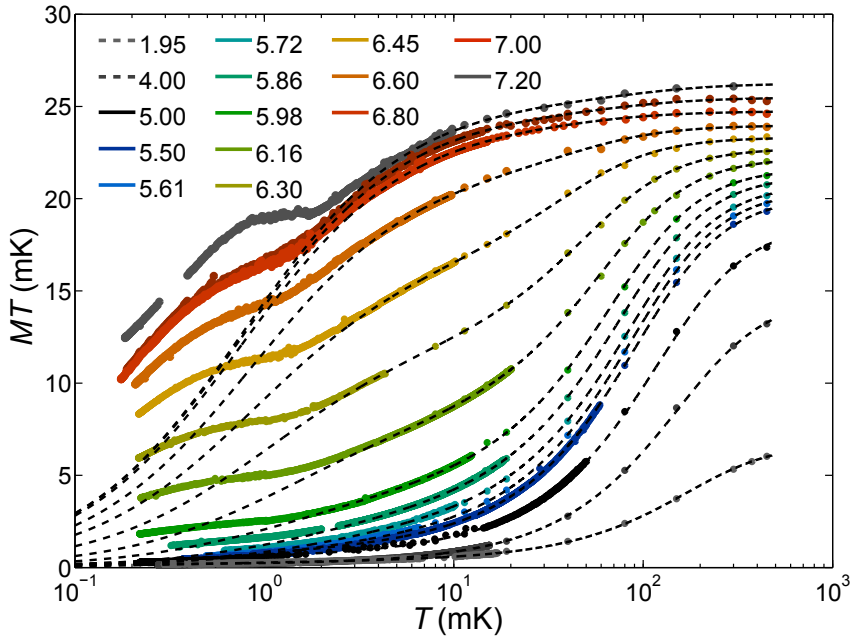

Figure 4.15: Curie-Weiss and Fermi fluid fits to the magnetisation data: The grey dashed lines show the Curie-Weiss and Dyugaev magnetisation fits to the magnetisation of two-dimensional ^{3}He. The data has been fitted above 5 mK, fits are shown over the entire temperature range. The corresponding fit parameters are shown in Fig. 4.16 and 4.20.

The magnetisation fits and raw data are shown in Figure 4.15. The fitted Curie-Weiss and Fermi temperatures as well as associated Curie constants of the solid and fluid are shown in Figure 4.16 and 4.20.

As can be seen in Figure 4.15, the high temperature data is well described by the Curie-Weiss plus Fermi fluid model. However, below 5 mK the data and fits quickly diverge. A more involved analysis in terms of a high temperature series expansion, with an extended fitting range down to 1 mK will be presented in Section 4.4 for the high density samples.

As shown by the Curie constants (Fig. 4.16) the magnetisation of the system is dominated by the Fermi fluid contribution at low coverages. Its magnitude grows linearly with second layer density up to about 5.0 nm^{-2} followed by a steep decline. Above 5.0 nm^{-2} the magnetisation of the Curie-Weiss contribution grows rapidly,

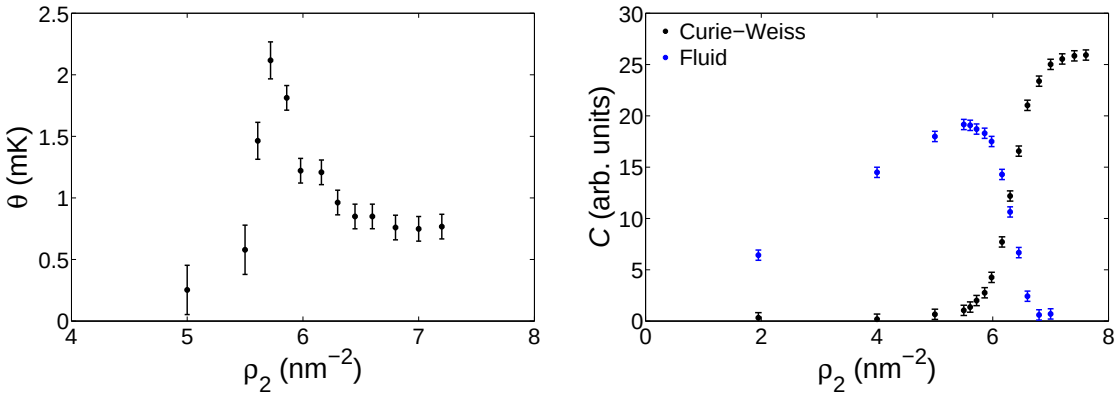

Figure 4.16: Curie-Weiss fitting parameters of ^{3}He|^{4}He|graphite: The left-hand side graphs shows the density dependence of the Curie temperature as determined from Curie-Weiss magnetisation fits to the low temperature excess magnetisation above 5 mK. The right-hand side graph shows the corresponding magnetisations.

becomes equal to the declining Fluid magnetisation at around 6.2 nm^{-2}. At coverages beyond 6.80 nm^{-2} the fluid contribution vanished and the system is entirely described by the solid. Here the fitted magnetisations reveal the first sign of a density driven metal-insulator transition in two-dimensional ^{3}He on graphite. The observation of a vanishing Fermi temperature of the fluid at around 7.0 nm^{-2} (Fig. 4.20), discussed in Section 4.3.3, confirms this picture. The precise density dependencies of the Fermi temperature and magnetisations and their interpretation will be discussed in Section 4.3.3 and following.

The fitted Curie-Weiss temperatures (Fig. 4.16) are positive for all samples showing that the magnetism of the putative solid contribution is predominantly antiferromagnetic. The observed Curie-Weiss temperatures start around 200 μK at low densities and peak at 2.2 mK at a second layer density of 5.72 nm^{-2}. Above 5.72 nm^{-2} the temperatures drop quickly to about 750 μK and plateau at the highest densities shown. The observed change in the Curie-Weiss temperatures and associated exchange constants hint towards a structural transition at a density of 5.72 nm^{-2}. A second indication of a structural transition is given by pronounced dip in the isotherms of the coverage dependence of the frequency shift (Fig. 4.13) around this density. Based on the upturn of the solid magnetisation and peak in the Curie-Weiss

temperatures, it will be argued that $5.72\,\mathrm{nm}^{-2}$ marks the onset of solid growing in the sample, as might be expected on entering a two-phase coexistence region associated with a first order fluid-solid transition. However, this hypothesis will be challenged by an observable exponential density dependence of the solid fraction in Section 4.3.4.

4.3.2 The Three Fermi Fluids Model

As we saw in the previous section the Curie-Weiss model for the low temperature magnetisation upturn (Fig. 4.15) showed a poor convergence with our data at lowest temperatures. Here we propose a new phenomenological model based on the existence of three distinct Fermi fluids in the system. The fluid with the highest degeneracy temperature will take the place of the Fermi fluid in the previous model. The two low and ultra-low temperature fluids replace the Curie-Weiss component and describe the low temperature magnetisation upturn. A microscopic justification for the existence of these two low temperature fluids rather than a solid magnetisation will be presented in Section 4.3.5 and 4.4. Here the lowest temperature fluid will be interpreted as the quantum-spin liquid in the triangular lattice solid whilst the mid temperature fluid is attributed to zero-temperature vacancies in the solid. For each of these contributions we use the Dyugaev form of the magnetisation, as previously discussed for fitting purposes.

Figure 4.17 shows the three Fermi fluid fits to the magnetisation data based on the fitting function:

$$M(T) = \frac{C_{\mathrm{HT}}}{\sqrt{T^2 + T_{\mathrm{Fl}}^2}} + \frac{C_{\mathrm{LT}}}{\sqrt{T^2 + T_{\mathrm{LT}}^{*2}}} + \frac{C_{\mathrm{ULT}}}{\sqrt{T^2 + T_{\mathrm{ULT}}^{*2}}}. \tag{4.8}$$

Here the magnetisation was remarkably fitted over the entire temperature range of $\approx 200\,\mu\mathrm{K}$ to $450\,\mathrm{mK}$. Except for the last coverage, $7.20\,\mathrm{nm}^{-2}$, which is the first sample with ^{3}He atoms in the third layer (see Sec. 4.2), all fits converged and reproduced the data. The fitted Curie constants C of all three fluids are shown in Figure 4.18 together with the degeneracy temperatures of the two low temperature fluids. A comparison of the high temperature renormalised Fermi temperatures with those obtained from the Curie-Weiss fits is shown in Figure 4.20.

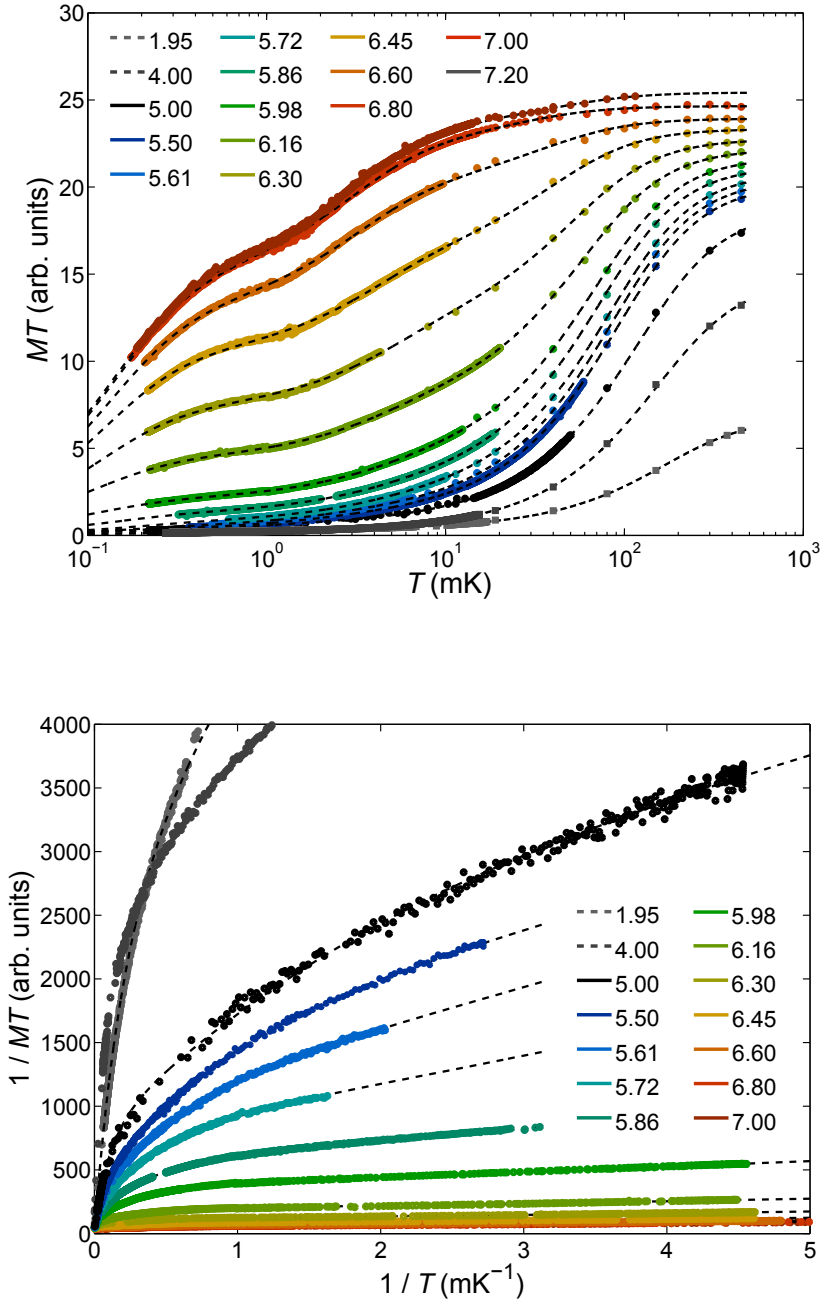

Figure 4.17: The graphs show the magnetisation of ^{3}He|^{4}He|graphite and the three Fermi fluid fits to the data. The grey dashed lines correspond to the three Fermi fluid fits which have been applied to the full temperature range. The corresponding fit parameters are shown in Fig. 4.18 and 4.20.

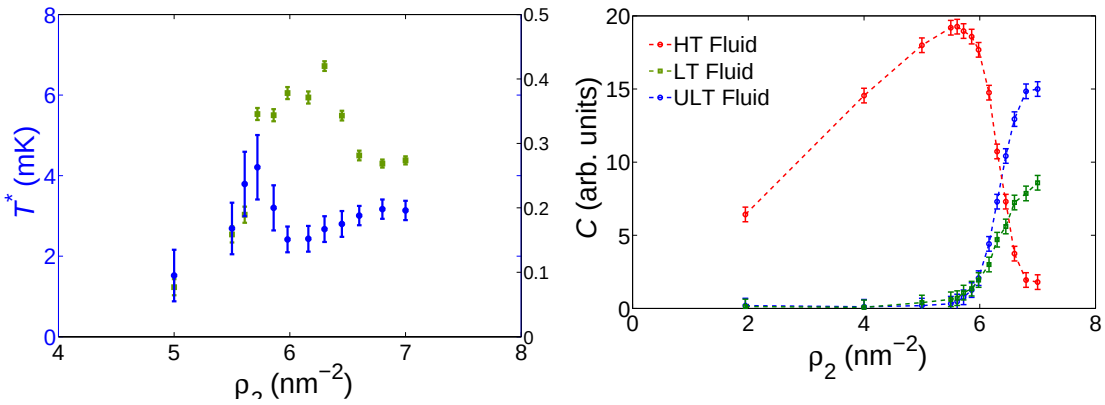

Figure 4.18: The graphs show the renormalised Fermi temperatures and magnetisations of ^{3}He|^{4}He|graphite as determined by the three Fermi fluid model. The left graph shows the Fermi temperatures of the low and ultra-low temperature fluid. The Fermi temperature of the highest temperature fluid is shown in Fig. 4.20. The right-hand side graph shows the corresponding Curie constants of the three fluids.

Similarly to the Curie-Weiss fits the high temperature fluid magnetisation, extracted from the three fluids model, increases linearly with density up to a second layer density of about $5.00\,\mathrm{nm}^{-2}$. Above $5.00\,\mathrm{nm}^{-2}$ the magnetisation of this fluid starts to decrease sharply before it vanishes, within the error bars of our fits, at around $7.0\,\mathrm{nm}^{-2}$. In the same density region the magnetisation of both low temperature fluids grows rapidly. As will be shown in Figure 4.24 the total Curie constant of the two low temperature fluids equals the Curie constant of the solid as was determined by the Curie-Weiss model.

At high densities the component of the low and ultra-low temperature fluid account for $(35 \pm 2)\,\%$ and $(65 \pm 2)\,\%$ of the solid magnetisation respectively. At present the physical origin of this approximately $\frac{1}{3}$-$\frac{2}{3}$ splitting of the solid magnetisation is unclear. The Fermi temperatures of the high temperature fluid determined by the three fluid model are equivalent, within estimated fitting errors, to the values obtained from the Curie-Weiss fits (see Fig. 4.20). Thus we conclude that both models yield, within a fitting error of $\Delta C = \pm 0.5$, the same results for the Fermi fluid and solid magnetisation (see also Sec. 4.3.3 and 4.3.4). The Fermi temperatures of the two lower Fermi temperatures follow the general trend of the Curie-Weiss

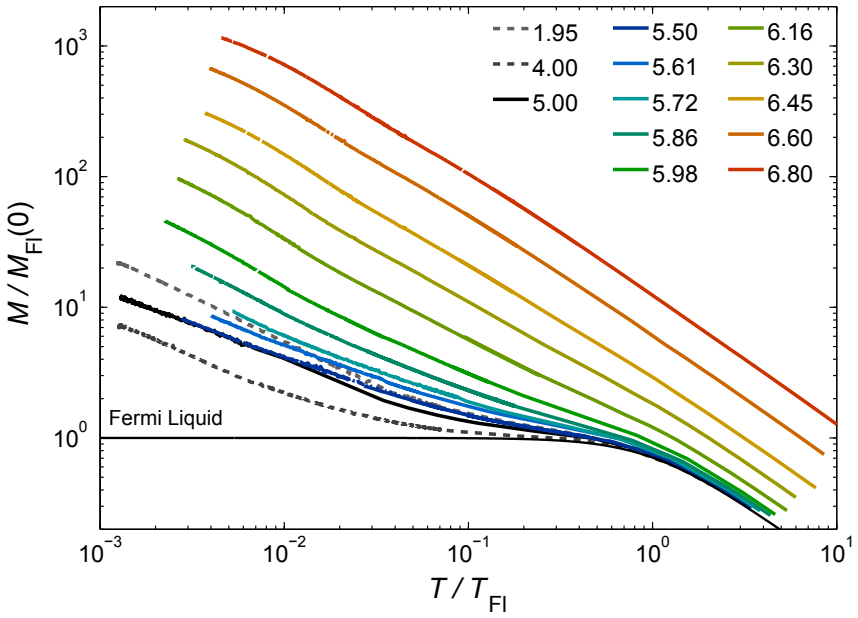

Figure 4.19: The graph shows the magnetisation plotted in relative units. The temperature and magnetisation are normalised by the Fermi temperature and zero temperature Pauli magnetisation. The black curve shows the ideal Fermi fluid magnetisation following Dyugaev [131].

temperature, i.e. both peak in the region of $\approx 6\,\mathrm{nm}^{-2}$, albeit their absolute values are different. Here we find a lowest Fermi temperature of about 150 to 300 μK and a intermediate temperature of about 4 to 7 mK.

For further analysis we will mostly rely on the parameters fitted by the three Fermi fluid model. The justification for the use of these parameters is purely based on the striking convergence over the entire temperature and density range. Physical interpretations of why the three Fermi fluid model is more appropriate to describe the low temperature magnetisation of the growing solid are currently being worked on. The quantum spin liquid as one possible scenario for an ultra-low temperature fluid will be discussed in Section 4.4.

Figure 4.19 shows the magnetisation of ^{3}He|^{4}He|graphite plotted in relative units of $M(T)/M_{\mathrm{Fl}}(0)$ and T/T_{Fl}. In this plot the low density high temperature magnetisation data collapse on to the curve of the ideal Fermi fluid as described by the

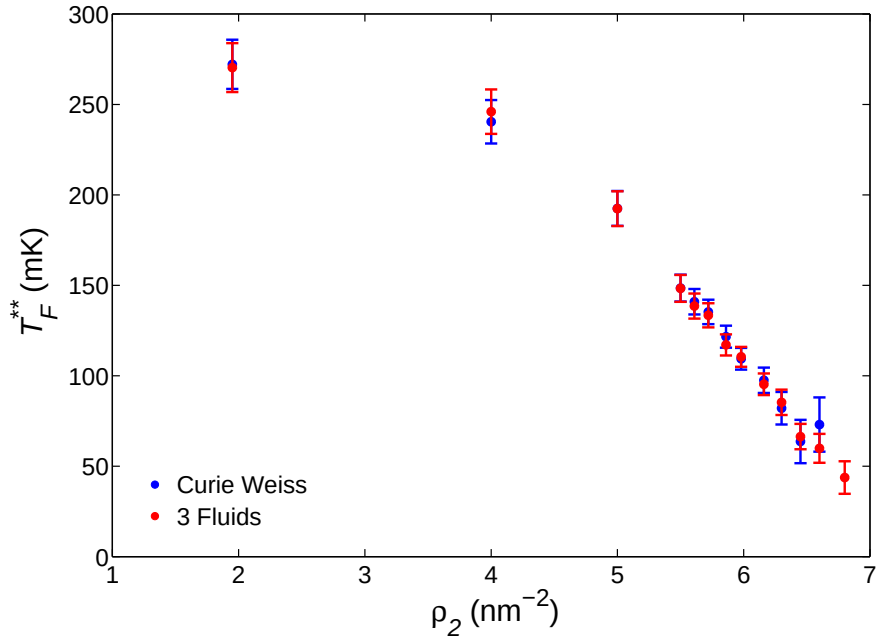

Figure 4.20: Density dependence of the renormalised Fermi temperature in two-dimensional ^{3}He. Blue data are taken from the Curie-Weiss, red data from the 3 Fluids model. Both Fermi temperatures are in good agreement with each other and vanish at the metal-insulator transition.

Dyugaev form [131], showing the validity of this model in this range. The low temperature and high density data, however, is characterised by the growing ultra-low temperature magnetisation, which gradually shifts the magnetisation curves away from the ideal Fermi liquid behaviour.

4.3.3 Effective Mass Enhancement in the Fluid

By fitting the measured magnetisation to the two models presented in the previous sections, we were able to determine the renormalised Fermi temperatures of the high temperature two-dimensional ^{3}He Fermi fluid (Fig. 4.20). As was seen both magnetisation models lead to almost identical degeneracy temperatures showing their reliability.

At lowest densities the renormalised Fermi temperatures start at about 240 mK

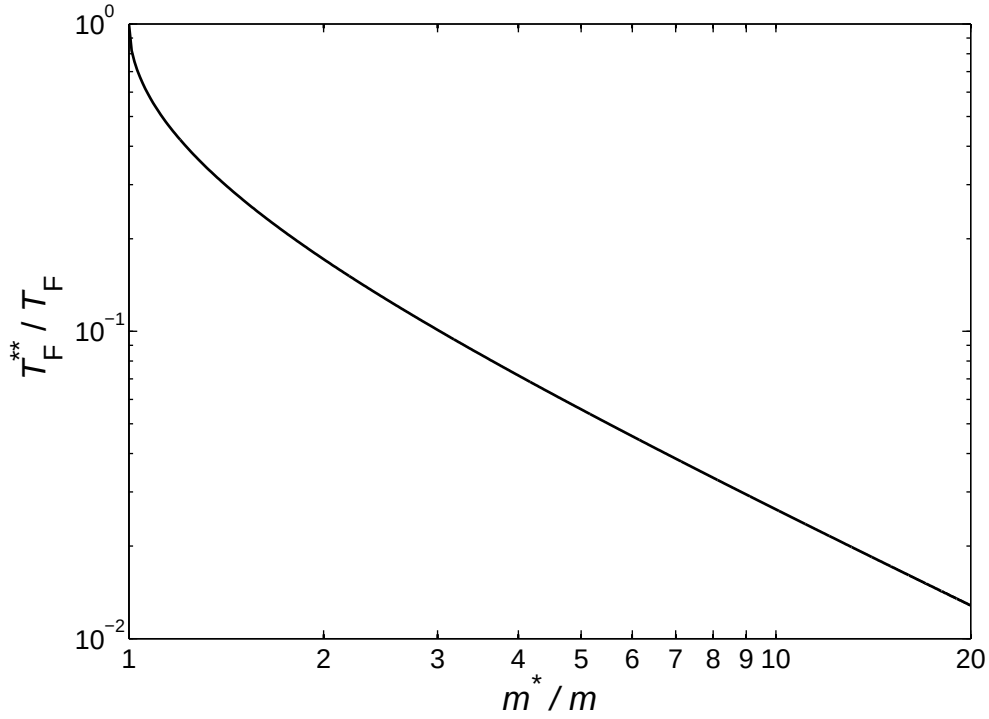

Figure 4.21: Susceptibility and Fermi temperature Renormalisation in ^{3}He

and decrease rapidly to 40 mK at a second layer density of 6.80 nm^{-2}. In comparison the ideal Fermi gas temperatures increasing linearly with second layer density, with a proportionality factor of 505 mK/nm^{-2} [18, 17]. The observed renormalisation of the Fermi temperature is a consequence of the increasing correlations within the two-dimensional Fermi liquid as the system approaches the metal-insulator transition.

We have only measured the magnetisation of our samples and wish to extract the density dependence of the effective mass ratio. Here we rely on previous work [17], which demonstrated that F_0^a depends only weakly on density. We use the almost localised Fermion model to correct for this weak density dependence of F_0^a (see Sec. 2.2.5 [18]. The resulting renormalisation of the Fermi temperature with respect to the effective mass is shown in Figure 4.21. The effective masses of the quasi-particles in the two-dimensional Fermi liquid were calculated by applying Equation 4.5 to the fitted renormalised Fermi temperatures.

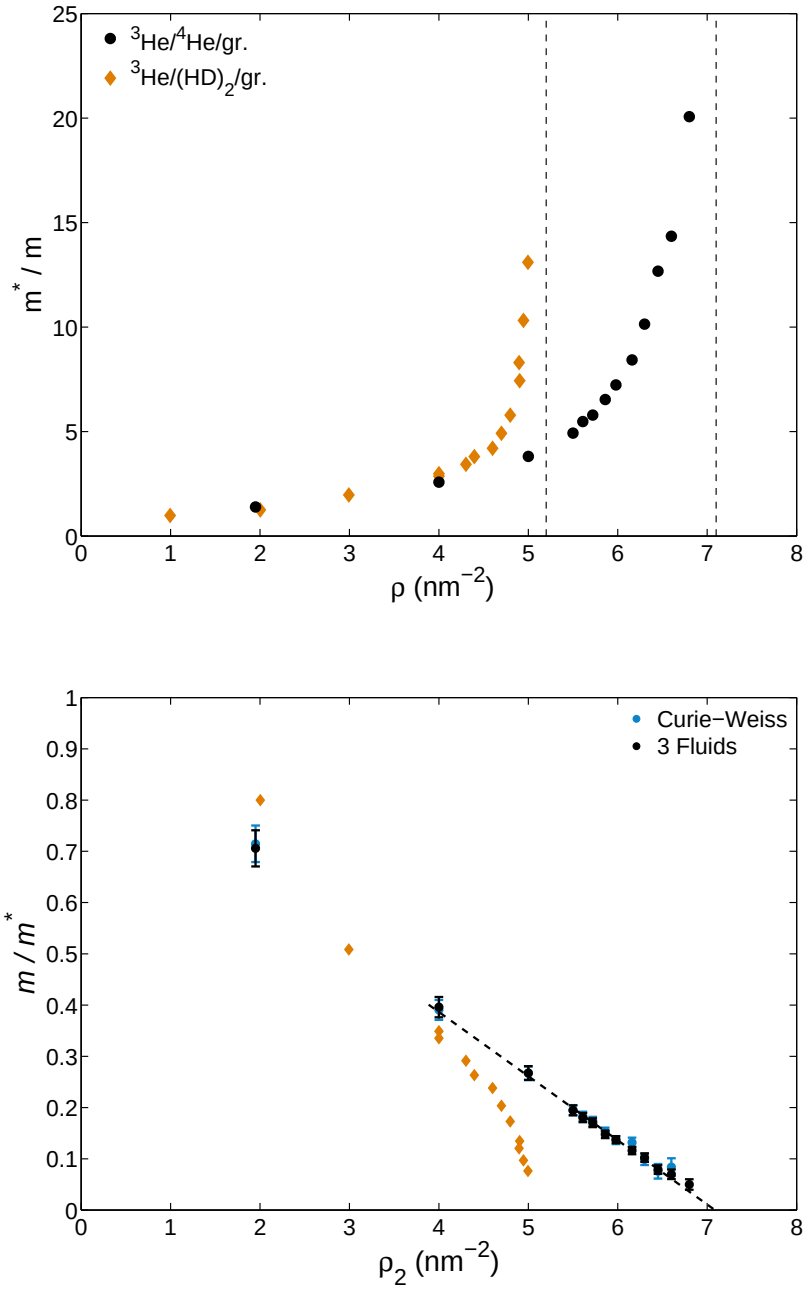

Figure 4.22: The graphs shows the density dependence of the effective and inverse effective mass in ^{3}He|^{4}He|graphite (circles) and ^{3}He|$(HD)_2$|graphite (diamonds) as reference as measured by A. Casey *et al.* [17].

The density dependence of these effective masses is shown in Figure 4.22. As can be seen the effective mass ratio in ^{3}He|^{4}He|graphite is starting from about one at lowest densities and diverges rapidly on approaching $7\,\mathrm{nm}^{-2}$. A similar behaviour was already reported by Casey *et al.* for ^{3}He|$(HD)_2$|graphite.
Here the effective masses also started around one at lowest densities but diverged on approaching $5.2\,\mathrm{nm}^{-2}$. It was argued that the critical density in their system is connected to the formation of the $\frac{4}{7}$-phase, which in $(HD)_2$|graphite occurs at much lower densities compared to ^{3}He|graphite. Furthermore, ^{3}He|$(HD)_2$|graphite is characterised by a much narrower phase coexistence region on approaching the critical density and hence facilitates fluid magnetisation and effective mass measurements right up to the critical density.

Similar studies by our group, Greywall, Godfrin and Fukuyama et al. showed divergences of the effective mass in two-dimensional ^{3}He on bare, ^{3}He, ^{4}He preplated graphite by heat-capacity and NMR measurements [19, 22, 132, 16, 23, 24]. However these measurements were complicated by the extensive phase coexistence regions in these systems, which prohibit the extraction of m^*/m from the low temperature heat capacity data.

We were able for the first time to follow the effective mass divergence in ^{3}He|^{4}He|graphite up to a density of $6.80\,\mathrm{nm}^{-2}$ where the effective mass reaches a value of $(20 \pm 4)m_0$. At this density the high temperature fluid fraction in the system is already suppressed to $\approx 5\,\%$ (see Sec. 4.3.4).

The inverse effective mass in our system is almost linearly decreasing with the second layer density over the entire density range (see lower graph of Fig. 4.22). A back-extrapolation of the inverse effective mass to zero density, based on the 1.95 and $4.00\,\mathrm{nm}^{-2}$ samples, leads to a value of $m^*/m = 0.97 \pm 0.05$. This result is in good agreement with the effective mass expected for an uncorrelated Fermi gas in the zero density limit. Throughout the second layer, the system develops an increasing effective mass with increasing density, as caused by increasing correlations in the two-dimensional Fermi fluid.

Extrapolating the linear dependence to even higher densities, we find an effective mass divergence at a second layer density of $(7.1 \pm 0.1)\,\mathrm{nm}^{-2}$. This effective mass divergence is attributed to the solidification of the system and identifies the density of the Mott transition. A microscopic model will be discussed in Section 4.3.5.

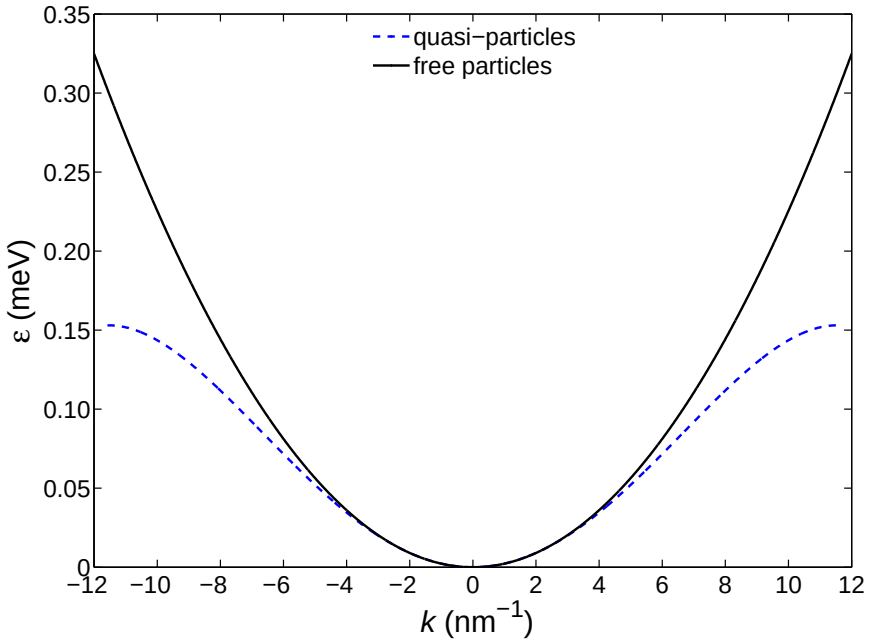

Figure 4.23: Quasi-particle band structure of 2D ^{3}He as calculated from the observed effective mass divergence. The black and blue curve show the non-interacting and renormalised band structure of 2D ^{3}He on graphite. Both are shown as doubly degenerate bands for better comparibility.

Comparing our results to Casey *et al.*, we find that the observed mass divergence in our system does as well coincide within 4 % with the formation of the $^4/_7$-solid at 6.85 nm^{-2}, showing the importance of the adsorption potential corrugation and resulting Brillouin zone size to the density driven metal-insulator transition.

Due to the observed linear density dependence, the inverse effective mass in our system can be described by the approximate formula:

$$\frac{m}{m^*} = \left[1 - \frac{\rho}{\rho_c}\right] \qquad \text{where:} \qquad \rho_c = 7.1\,\text{nm}^{-2}. \tag{4.9}$$

By applying the formula for the band mass:

$$\frac{m_b^*}{m_b} = \hbar^2 k \left(\frac{\partial \epsilon}{\partial k}\right)^{-1} \tag{4.10}$$

we can model the effective quasi-particle band structure for two-dimensional ^{3}He on graphite:

$$\epsilon(k) = \frac{\hbar^2}{2m_0}\left(k^2 - \frac{1}{2}\frac{k^4}{k_c^2}\right). \tag{4.11}$$

Where $k_c = 11.5\,\mathrm{nm}^{-1}$ is the critical Fermi surface radius and is proportional to the square root of the critical density. The resulting quasi-particle band structure is shown in Figure 4.23.

At the critical k_c the quasi-particle band structure is renormalised by an energy equivalent to $\Delta \approx 1.8\,\mathrm{K}$ or half of the uncorrelated bandwidth. We will later see that the charge gap at the critical density, is close to the charge gaps estimated from heat capacity measurements ($\Delta = 1.94\,\mathrm{K}$ [19]) and of the same order as theoretical calculations ($\Delta = 3.0\,\mathrm{K}$ [133]) (see Sec. 4.3.5).

4.3.4 Fluid-Solid Cross-Over

In addition to the mass divergence observed in our system, both magnetisation fitting models (Sec. 4.3.1 and 4.3.2) showed a pronounced cross-over of the fluid and solid magnetisations at densities higher than $5.0\,\mathrm{nm}^{-2}$. In order to discuss the precise nature of this cross-over the fluid and solid Curie constants have been renormalised by the total Curie constant of the system (see Sec. 4.2). The resulting fluid and solid fractions are shown in Figure 4.24.

As can be seen in Figure 4.24 the magnetisation of low density samples is dominated by the Fermi fluid. Here the fraction corresponding to the Fermi fluid is almost 100 %. At densities above $5.0\,\mathrm{nm}^{-2}$, a solid-like contribution starts to grow in the system simultaneously diminishing the fluid fraction. In this cross-over region the solid fraction grows almost exponentially before it reaches 100 % at the critical density (see Fig. 4.25). At this point the entire system is solidified and the fluid has vanished. This cross-over indicates the ongoing metal-insulator transition in the system.

In a classical model, phase coexistence between two phases occurs if their corresponding chemical potentials are equal. At equal chemical potential, increasing the system density leads to the growth of solid until the entire system is solidified. The

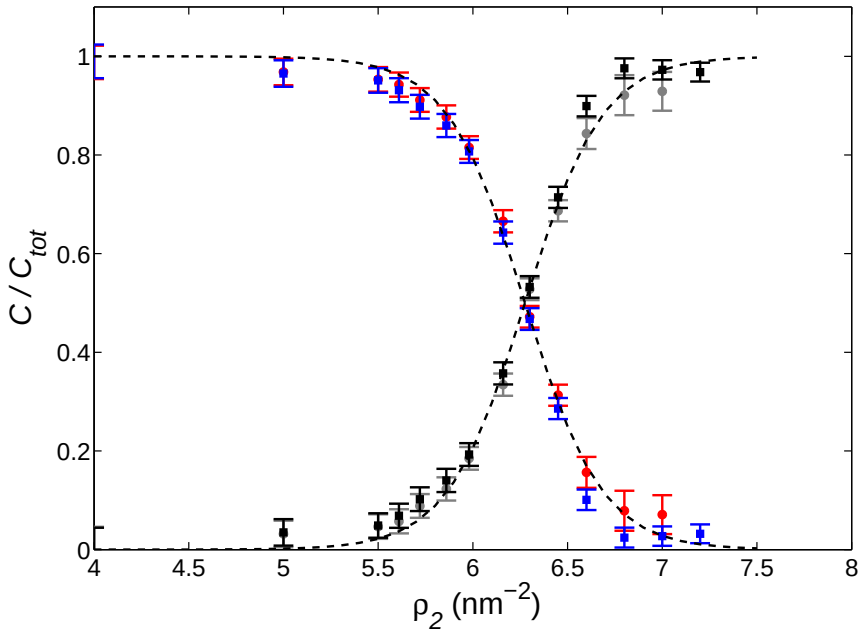

Figure 4.24: The graph shows the fluid and solid magnetisations of ^{3}He|^{4}He|graphite renomalised by the total magnetisation as determined by Dyugaev and Curie-Weiss magnetisations fits. Squares and circles represent data obtained from Curie-Weiss and 3 Fermi fluid fits respectively.

width of the coexistence region is determined by the density difference of the fluid and solid at the critical density. Throughout this transition the chemical potentials of both subsystem remain constant. This implies that the fluid-solid cross-over is characterised by a linear growth of solid with increasing density and constant effective mass of the fluid.

Both effects are absent in our measurements. In Section 4.3.3 we saw that the effective mass of the strongly correlated fluid diverges right up to the critical density of the metal-insulator transition. Here we see that the cross-over in the fluid and solid fraction follows a non-linear density dependence. The observed behaviour might be referred to as quantum coexistence rather than classical coexistence.

A closer analysis of the density dependence reveals that both fractions follow the

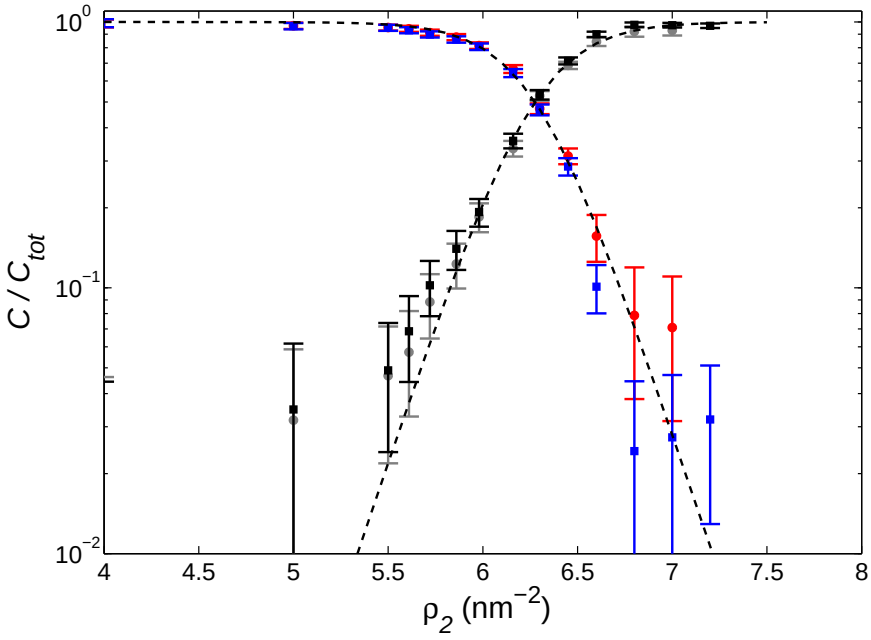

Figure 4.25: The graph shows the fluid and solid fractions of ^{3}He|^{4}He|graphite in Fig. 4.24 plotted logarithmically. Squares and circles represent data obtained from Curie-Weiss and 3 Fermi fluid fits respectively.

form:

$$F_s(\rho) = \frac{1}{1+\exp\{f(\rho_2)\}} \qquad \text{and} \qquad F_{fl}(\rho) = \frac{1}{1+\exp\{-f(\rho_2)\}}. \tag{4.12}$$

The semi-classical two-phase coexistence model can thus be rejected. The fits in Figure 4.24 (dashed lines) show $F_s(\rho_2)$ and $F_{fl}(\rho_2)$, where $f(\rho_2)$ has been approximated by the linear function:

$$f(\rho_2) = 4.9\,\mathrm{nm}^2(6.27\,\mathrm{nm}^{-2} - \rho_2). \tag{4.13}$$

Here $6.27\,\mathrm{nm}^{-2}$ marks the point at which the system consists to equal parts of fluid and solid an takes the place of the chemical potential in a Fermi-Dirac distribution. If the observed cross-over can be described by a Fermi-Dirac distribution, the question arises whether the observed dependence arises due to an increasing fluid potential

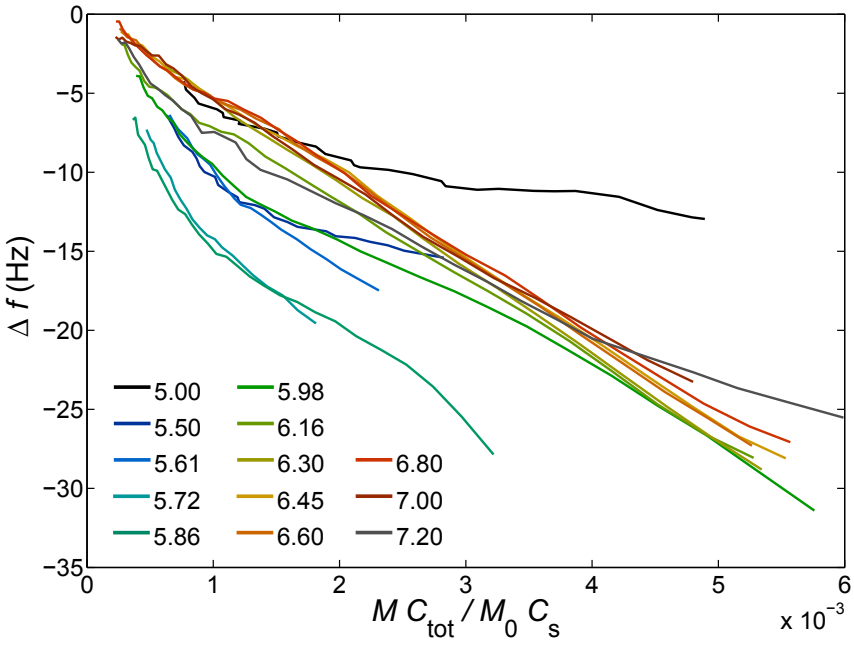

Figure 4.26: Frequency Shift as a Function of the Polarisation

transiting through the chemical potential of the solid or the vanishing of an internal energy scale like T_F in the presence of a gap? We will see in the following section that the latter might be excluded due to the extraordinary size of the Mott gap in two-dimensional ^{3}He which would require characteristic temperatures far above the Fermi temperature.

Based on the antiferromagnetic exchange constants (Fig. 4.16 and the renormalised frequency shifts (Fig. 4.26), we propose that the forming solid above $6.00\,\mathrm{nm}^{-2}$, is structurally equivalent to the insulator state at the critical density. In Figure 4.26, we plot the frequency shift as a function of the spin polarisation in the presumed solid. We can collapse all frequency shifts above $6.00\,\mathrm{nm}^{-2}$ on to one generic curve, where the frequency shift is proportional to the spin polarisation in the sample. The low temperature spin polarisation is calculated by rescaling the total polarisation of the ^{3}He film by the solid fraction. This renormalisation can be applied due to the dominance of the solid magnetisation at low temperatures. Here the polarisation of the ^{3}He layer and the associated frequency shift originate from

the solid polarisation. The fluid polarisation can be neglected in this limit.

The common proportionality between the frequency shift and spin polarisation for coverages between 6.0 to 7.0 nm^{-2} shows that the spin structure of the solid remains the same. Above 7.0 nm^{-2}, the low polarisation limit agrees with the collapsed data, but diverges at high polarisations. This shows the potential tendency to form a new spin structure above 7.0 nm^{-2}, which is expected due to the promotion of ^{3}He-atoms into the third layer. This third layer fluid leads to the ferromagnetic coupling of the solid second layer by the introduction of RKKY exchange and eventually results in the ferromagnetic anomaly at 7.5 nm^{-2} [134, 31, 135, 136].

4.3.5 Microscopic Interpretation of the Metal-Insulator Transition - The Wigner-Mott Scenario

As was outlined in Section 2.2, correlated Fermi liquids can become unstable towards the formation of various kinds of ordering and ultimately a MIT. The previous Sections showed that two-dimensional ^{3}He undergoes a metal-insulator transition as evidenced by the divergence of the quasi-particle effective mass at $7.1\,\mathrm{nm}^{-2}$ and fluid-solid cross-over between 5.0 and $7.1\,\mathrm{nm}^{-2}$.

It was shown in the introduction that interactions in ^{3}He arises due to van der Waals forces, which can be described by a Lennard-Jones (LJ) or Aziz potential (see Fig. 4.29). Here the potential is attractive for large interparticle distances and becomes strongly repulsive for short distances. This short distance repulsion is often referred to as hard core repulsion in ^{3}He and drives the Mott-Hubbard transition in two-dimensional ^{3}He (see 2.2.5).

In the conventional Hubbard Model, half filling is defined as the single occupancy of all tight binding sites or a degenerate Fermi surface (FS) volume corresponding to half of the first Brillouin zone (BZ). However, in two-dimensional ^{3}He such sites do not exist *a priori*. The BZ of the two-dimensional system is either defined by the honey-comb lattice of the graphite substrate or the triangular lattice of the ^{4}He under-layer. In the second layer it is the latter which counts. A schematic of the second layer BZ based on the ^{4}He under-layer is shown in Figure 4.27. Here black crosses correspond to the reciprocal lattice vectors of the ^{4}He under-layer and the black hexagon shows the resulting first BZ. The green circle indicates the isotropic doubly degenerate FS of ^{3}He at the critical density of $7.1\,\mathrm{nm}^{-2}$.

As can be seen, the critical FS does not correspond to half-filling of the under-layer lattice. Here half-filling would be expected around $12\,\mathrm{nm}^{-2}$. Therefore the question arises, whether the observed MIT in two-dimensional ^{3}He is of the Mott-Hubbard type or whether the observed effects are due to nesting instabilities of the Fermi fluid?

In order to answer this question, let us briefly go back to the first and second-layer phase diagram of ^{3}He on graphite (see Fig. 1.2 Sec. 1). In both layers the Fermi fluid phase is interrupted by a solid phase around $6\,\mathrm{nm}^{-2}$. Comparing the associated lattice constants of these two solid phases ($a_{2D} = 0.44\,\mathrm{nm}$) with the lattice constants

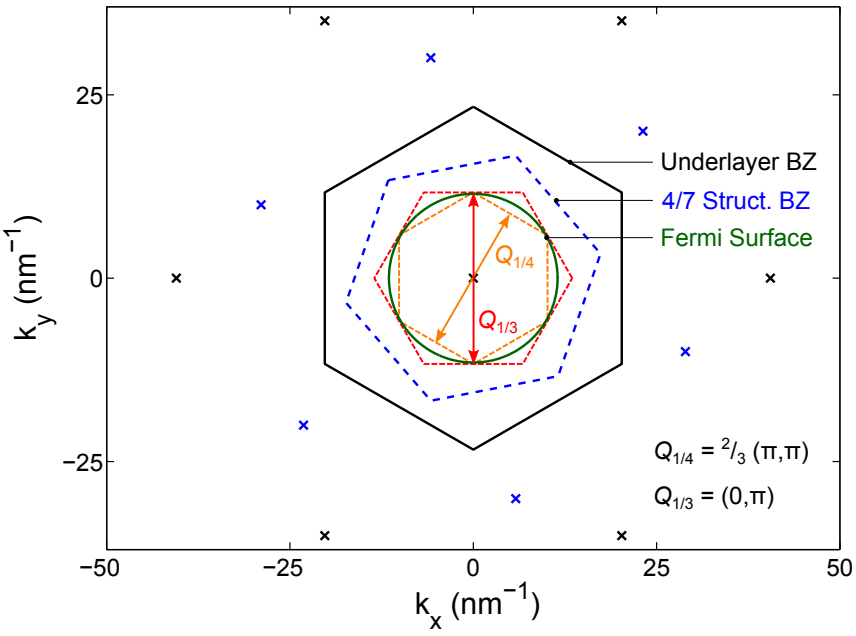

Figure 4.27: Reciprocal space and Brillouin zone folding in two-dimensional ^{3}He|^{4}He|graphite. Black crosses and lines show the reciprocal lattice vectors and Brillouin zone of the ^{4}He under-layer. The orange and red hexagon are integer fractions of the original Brillouin zone. Blue crosses and lines correspond to the reciprocal lattice vectors and Brillouin zone of the $^4/_7$-phase.

of bulk bcc ^{3}He at solidification ($a_{3D} \approx 0.40\,\mathrm{nm}$ [81, 82, 137]), it can be seen that both are almost identical. Thus the question arises whether both solids are driven by the same effects, i.e. the solidification is mediated by the interactions arising due to the minimum in the LJ potential.

Short-range interactions in ^{3}He are strongly repulsive, due to the divergence of the LJ-potential at zero interparticle distance, much like Coulomb interactions in electron systems. However, contrary to the latter, long-range interactions in ^{3}He are weakly attractive and charge fluctuations are enhanced in the vicinity of the LJ-potential minimum.

As has been shown in Section 2.2.4, strong charge or spin fluctuations can lead to the stabilisation of a $Q = 2k_\mathrm{F}$ charge or spin-density wave and opening a DW gap at

the Fermi energy. Depending on the size of the induced density wave gap and quality of the nesting (fraction of the FS covered by the nesting vectors) such a system can establish a density wave order (DWO) and become an insulator. In Figure 4.27, the folded BZs arising from a $Q_{^1/_4} = (\pi, 0, 0)$ and $Q_{^1/_3} = {}^2/_3(2\pi, \pi, 0)$ nesting vector are shown. Here the indices $^1/_4$ and $^1/_3$ refer to the size of the folded BZ with respect to the under-layer BZ. As can be seen the doubly degenerate critical ^{3}He FS lies close to both proposed BZ boundaries and is therefore prone to the opening of a DW gap and DWO in this region. However, due to the large on-site repulsion in ^{3}He, neither of the two solutions is stable. The strong on-site repulsion lifts the spin degeneracy of the band structure at large filling, doubling the effective FS volume and introduces a Mott gap between all reconstructed bands (see Fig. 4.28 b)). Therefore the doubling of the FS volume causes the occupation of the second band separated by the Mott gap, leading to a much higher ground state energy than the isotropic fluid.

In order to avoid the occupation of the upper Hubbard band, but still gain kinetic energy, the system undergoes a DW transition into a $Q = 2\sqrt{2}k_\mathrm{F}$ state (1D: $Q = 4k_\mathrm{F}$, 3D: $Q = 2\sqrt[3]{2}k_\mathrm{F}$). The $2\sqrt{2}k_F$-DW induces a $\lambda = \pi/\sqrt{2}k_F$ superstructure, whose BZ is exactly half filled, i.e. the upper Hubbard band is empty. Due to the lifted spin degeneracy at half-filling the DW gap at the Brillouin zone boundary leads to a strong renormalisation of the non-degenerate lower band and thus lower ground state energy. As all Fermi vectors lie at the BZ boundary in this case, the system shows perfect nesting and forms a DWO Mott insulator. In isotropic systems these nesting vectors and the structures of the $2\sqrt{2}k_F$-DWO state will continuously adjust to changes of the FS volume. In systems with an underlying periodic potential, however, the system will minimise its energy by selecting discrete energetically favorable commensurate structures. The stability of these structure with respect to changes in the FS volume will depend on the potential energy difference relative to superstructures with similar densities.

This type of two stage metal-insulator transition occurs in systems with strong non-local and on-site interactions, where the former are driving the DW and the latter the Mott insulator. Depending on the mechanism responsible for the initial DW, these transitions are known as Peierls-Mott [138] or Wigner-Mott transition [139, 140, 141]. Examples of these transitions can be found in the strongly correlated electron systems $Ca_{2-x}Sr_xRuO_4$ and $TaSe_2$, where the systems spontaneously

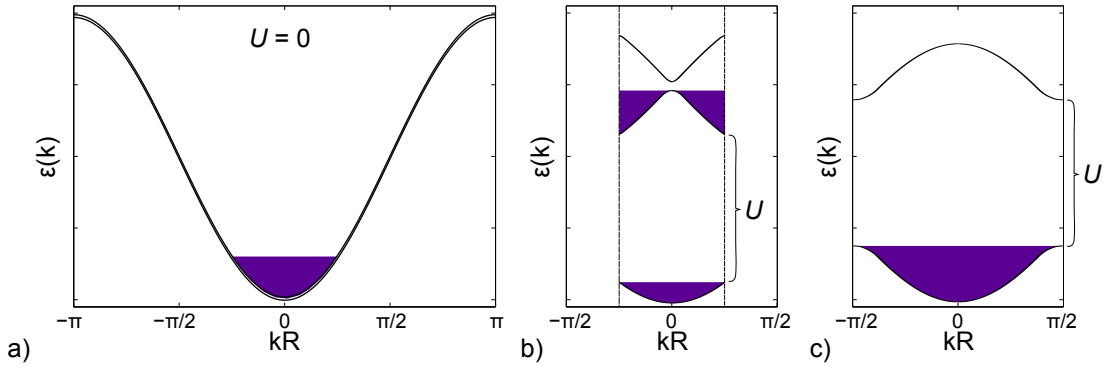

Figure 4.28: Wigner-Mott transition and superlattices: a) shows a spin-degenerate uncorrelated one-dimensional tight-binding band at $^1/_4$-filling b-c) show the reduced Brillouin zone for $Q = 2k_\mathrm{F}$ and $Q = \pi$ nesting vectors. In systems with strong on-site repulsion (b,c) $2k_\mathrm{F}$-nesting instabilities (b) are energetically unfavourable, due to the lifted degeneracy and Mott gap between the lower and upper Hubbard band. Such a system will favour a half-filled superstructure, leading to a completely filled lower Hubbard band (c).

breaks their translational symmetry into a $\sqrt{2} \times \sqrt{2}$ and $\sqrt{13} \times \sqrt{13}$ Mott insulating superstructure [142, 143].

In two dimensional ^{3}He on graphite there are two phases which can be interpreted as Wigner-Mott insulators, the first layer $\sqrt{3} \times \sqrt{3}\mathrm{R}30^o$ and the second layer $\sqrt{^7/_4} \times \sqrt{^7/_4}\,\mathrm{R}19.1^o$ phase. Both of which are based on commensurate charge-ordered states driven by strong on-site and inter-site interactions. Here the interactions are determined by the familiar LJ-potential (Fig. 4.29).

It has been shown that the first layer of ^{3}He on graphite stabilises a commensurate $\sqrt{3}\times\sqrt{3}\mathrm{R}30^o$ superlattice with respect to the graphite lattice at a density of $6.4\,\mathrm{nm}^{-2}$ [123, 144, 19]. It has been debated that this $\sqrt{3} \times \sqrt{3}\mathrm{R}30^o$ superlattice undergoes a transition into a higher density $\sqrt{^5/_2} \times \sqrt{^5/_2}$ structure on increasing the layer density beyond $6.4\,\mathrm{nm}^{-2}$. This transition would be an indicator for the nesting vector adjustment of the $2\sqrt{2}k_\mathrm{F}$-DWO state with increasing FS volume as described in the preceding paragraph.

Path-integral Monte-Carlo simulations have shown that the second layer of two-dimensional ^{3}He forms a commensurate $\sqrt{^7/_4} \times \sqrt{^7/_4}\,\mathrm{R}19.1^o$ superlattice with re-

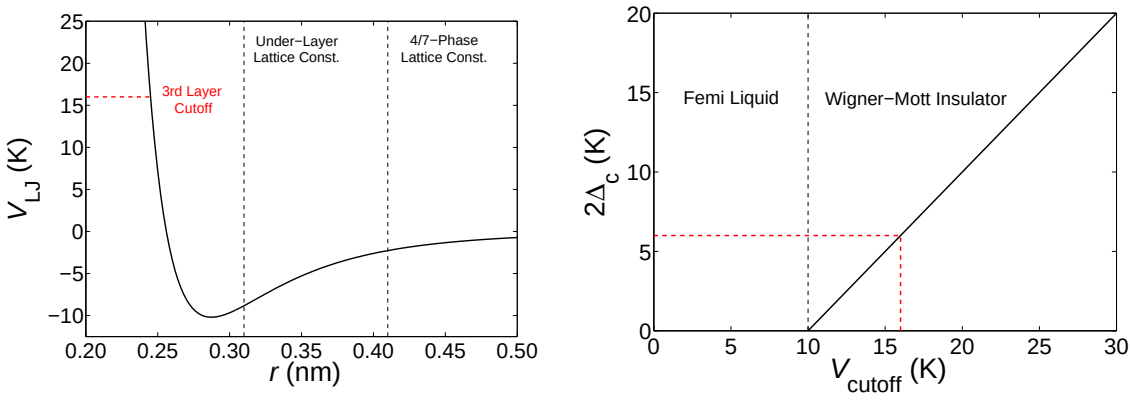

Figure 4.29: Interaction potential and Wigner-Mott phase: The left graph shows the ^{3}He Lennard-Jones interaction potential with $\epsilon = 10.2\,\mathrm{K}$ and $\sigma = 0.256\,\mathrm{nm}^{-2}$ [145]. The right graph shows the phase diagram of the $^4/_7$-phase as calculated by Watanabe and Imada [133, 146] with the Mott gap opening at a 3rd layer interaction cutoff of 10 K. The Mott gap corresponding to the chemical potential difference between the second and third layer is $\Delta_c = 6\,\mathrm{K}$.

spect to the ^{4}He under-layer at a density of $6.85\,\mathrm{nm}^{-2}$ [25, 147] (see Fig. 4.30 b)). The reciprocal lattice vectors and Brillouin zone of this superlattice are shown in Figure 4.27. Due to its density ratio of $^4/_7$ with respect to the ^{4}He under-layer this phase is also referred to as the $^4/_7$-phase. In this superlattice half filling corresponds to a real space density of $6.85\,\mathrm{nm}^{-2}$. Calculations by Watanabe et al. showed that by increasing the short range interaction limit, two-dimensional ^{3}He develops divergences in the charge susceptibility at reciprocal lattice vectors corresponding to the $^4/_7$-structure [133, 146]. Charge susceptibility divergences are usually precursors for a developing DW. The short-range interaction limit in this model is caused by the chemical potential difference between ^{3}He atoms in the second and third layer. If the chemical potential difference is exceeded by interactions atoms will be promoted into the third layer. In two-dimensional ^{3}He this difference is of the order of 16 K. Watanabe et al. showed that the system opens a charge gap corresponding to a Mott insulator for interactions limits above 10 K (see Fig. 4.29). For the case of a interaction limit of 16 K the Mott gap of the $^4/_7$-structure has been estimated as $\Delta_c = 3\,\mathrm{K}$.

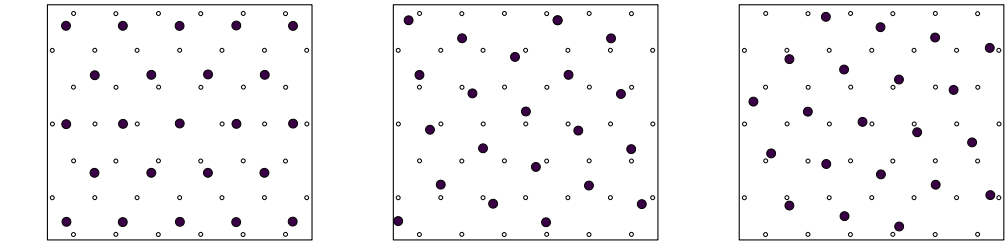

Figure 4.30: shows the ^{3}He superstructures in ascending order around $7.0\,\mathrm{nm}^{-2}$. The three proposed superstructures are a) $\sqrt{16/9}\times\sqrt{16/9}\,\mathrm{R}0^o$ corresponding to $6.75\,\mathrm{nm}^{-2}$ b) $\sqrt{7/4}\times\sqrt{7/4}\,\mathrm{R}19.1^o$ corresponding to $6.85\,\mathrm{nm}^{-2}$ and c) $\sqrt{12/7}\times\sqrt{12/7}\,\mathrm{R}10.9^o$ corresponding to $7.00\,\mathrm{nm}^{-2}$. The corresponding lattice vectors are $(^4/_3\,0\,0)$, $(^1/_2\,1\,0)$ and $(^2/_7\,^8/_7\,0)$.

However the stability of the $^4/_7$-phase against particle and hole doping is subject of ongoing debates. As has been discussed for the Wigner-Mott system, the $2\sqrt{2}k_\mathrm{F}$-DWO-state will adjust its nesting vector according to the FS radius and underlying lattice. By changing the second layer density or FS volume, the system would therefore undergo a cascade of commensurate DWO-sates. In general the stability of a particular superstructure depends on the potential energy gain compared to other superstructures with similar densities. An example of three similar superstructures with almost identical densities is shown in Figure 4.30. Due to its shorter commensuration length the $^4/_7$-structure is energetically favorable over the $^7/_{12}$ and $^9/_{16}$-structure and is therefore stable over an extended density range.

If this stability region extends far into the under-doped side of the phase diagram the question arises, how the system incorporates the density mismatch between the fluid and solid? Here two models (1) the doped Mott insulator and (2) a coexistence of half-filled $^4/_7$-solid with fluid might be considered.

In the first scenario the system consists entirely of $^4/_7$-structure stabilised by the DWO gap, where some of the sites are vacant. This model corresponds to the tight-binding Hubbard model on a triangular lattice and has been described by Kotliar, Dobrosavljevic and Rozenberg et al. [148, 149, 150, 151, 70]. On increasing the particle density this system will undergo a Lifshitz transition at $^3/_8$-filling, i.e. $5.1\,\mathrm{nm}^{-2}$, from a large particle FS centered around the Γ-point through six van-Hove

singularities at the M-points to six smaller hole FSs around the K-points of the BZ. This Lifshitz transition should be accompanied by divergences in the effective mass and transport sensitive measurements such as the transverse relaxation time due to the crossing of the van Hove singularities. Even if the hole-doped $^4/_7$-phase is stabilised beyond $5.1\,\mathrm{nm}^{-2}$ the system would still undergo a large to small FS transition as the translational symmetry is broken and show sudden changes in the thermodynamic and transport properties. The approach of half-filling at higher densities and resulting Mott transition are then described by the Brinkman-Rice scenario in the maximally frustrated Hubbard model [65, 70]. Even though the observed effective mass divergence and fluid-solid cross-over on approaching the Mott transition would coincide with this model, we do not see any evidence for a preceding Lifshitz transition.

In the second scenario the system consists of a mixture of local perfectly half-filled $^4/_7$-solid surrounded by strongly correlated fluid and hence has a partially broken translational symmetry. As the fluid approaches the $^4/_7$-density short range charge fluctuations will locally form $2\sqrt{2}$-DWO-solid. Due to opening of the DW gap the chemical potential of the DWO solid is lower than that of the surrounding fluid. Thus high density solid is expected to start growing around these nucleation points. This process will continue until the chemical potential of the fluid and solid are equalised due to the depletion of the fluid. This two-phase model is also supported by the observed collapse of the frequency shift data above 6.0 K. The collapse of these curves shows that structure of the magnetically dominating solid does not change throughout the coexistence region whilst is magnitude is growing.

Due to hybridisation of the fluid with the boundaries of the solid the two-phase region is characterised by a strong renormalisation of the fluid, where the effective mass is approaching infinity with increasing solid fraction. At highest densities the entire system consists of $^4/_7$-solid and the system is characterised by the DWO and Mott gap separating the fully filled lower from the empty upper Hubbard band.

Heat capacity measurements by Fukuyama and Greywall *et al.* [19, 152, 153] on the first and second layer of ^{3}He on graphite showed pronounced peaks around 3.0 and 1.1 K at the $\sqrt{3}\times\sqrt{3}$ and $\sqrt{^4/_7}\times\sqrt{^4/_7}$ commensurate densities. On the low density side of the two commensurate phases the critical temperature of these peaks shifts rapidly towards zero. In the $2\sqrt{2}$-DWO model these peaks correspond to the

second order phase transitions as the systems breaks its translational symmetry and opens the DW charge gap. By applying a BCS temperature dependence to the observed critical temperatures, the zero temperature charge gaps of both structures can be estimated. Here the heat capacity charge gaps of the $^1/_3$ and $^4/_7$-phase are $\Delta_{1/3} = 5.3\,\mathrm{K}$ and $\Delta_{4/7} \approx 1.94\,\mathrm{K}$ respectively. Comparing these values to the charge gap calculated by Watanabe et al. and the charge gap obtained from the band renormalisation (Sec. 4.3.3), we find that all three are in good agreement, supporting the hypothesis of a CDW driven Mott transition, i.e. the $2\sqrt{2}$-DWO Wigner-Mott transition.

The rapid decrease of the critical temperature away from the commensurate densities indicates that the induced charge gap is strongly density dependent. This density dependence can also be found in our band structure calculation, where the induced band renormalisation scales as ρ^2/ρ_c^2 and reaches a maximal value of $^1/_2\epsilon_F$ at the critical density. Unfortunately, at present, there are no reliable heat capacity data to compare the proposed density squared upturn of the critical temperature to.

To summarise, we conclude that the metal-insulator transition observed in the second layer of ^{3}He on graphite preplated with a monolayer of ^{4}He is of the Wigner-Mott type. Here the triangular lattice Wigner phase is stabilised by a CDW with three nesting vectors $Q = 2\sqrt{2}k_\mathrm{F}$, leading to prefect nesting and a reduced kinetic energy of the system. In the phase coexistence region it is believed that, on approaching the $^4/_7$-structure the system initially grows islands of perfectly half-filled $^4/_7$-solid which hybridise with the surrounding fluid, giving rise to the observed renormalisation of the surrounding Fermi fluid. The stability and existence of a hole-doped $^4/_7$-structure in the close vicinity of the critical $^4/_7$-density, however, remains unclear.

In the following section the emergence of the two low temperature fluids will be discussed. It will be argued that both the ultra-low and low temperature fluid might be interpreted as emerging zero-point vacancies and gapless quantum spin liquid in the triangular lattice solid.

4.4 The Mott Insulating State and Quantum Spin Liquids

As has been discussed in the previous section two-dimensional ^{3}He undergoes a putative Wigner-Mott transition into a triangular lattice spin-$^1/_2$ solid. This solid has been identified as the perfectly half filled $^4/_7$-phase whose growth can be observed throughout the phase coexistence region from 5.0 to 7.1 nm^{-2}. Due to the geometrical frustration and competing multiple spin ring-exchanges in the solid the triangular lattice solid is thought to be a good candidate to host a gapless quantum-spin liquid (see Sec. 2.3). This section thus looks closer at the magnetisation and spin-dynamics of the phase coexistence and solid samples.

4.4.1 Low Temperature Magnetism

As was discussed in the initial sections of this chapter, the magnetisation of ^{3}He|^{4}He|graphite does not follow the ideal Fermi liquid temperature dependence at lowest temperatures. It was shown that the low temperature magnetisation upturn, originating from the partial solidification of the system, is poorly described by a Curie-Weiss magnet, which to some extend is expected for $T \ll 5J$, but rather well by two Fermi liquids with low and ultra-low degeneracy temperatures.

Figure 4.31 shows the bare magnetisation of the low temperature upturn as calculated by subtracting the high temperature fluid magnetisation of the measured magnetisation. As can be seen the double logarithmically plotted temperature dependence is almost linear at highest temperatures, suggesting a power law temperature dependence in this region. However at lowest temperatures the temperature dependence becomes shallower. In order to discuss a possible power law temperature dependence, the temperature exponent has been calculated as a function of temperature and plotted in Figure 4.31. Here the exponents vary between -0.4 and -0.9. At lowest densities, i.e. 5.0, 5.5 and 5.61 nm^{-2}, the temperature exponents scatter around -0.5 with a tendency to go to -0.4 at highest temperatures. Thus the system is highly non Curie or Curie-Weiss law and might, due to the small deviations from a constant temperature exponent, be described by a power law.

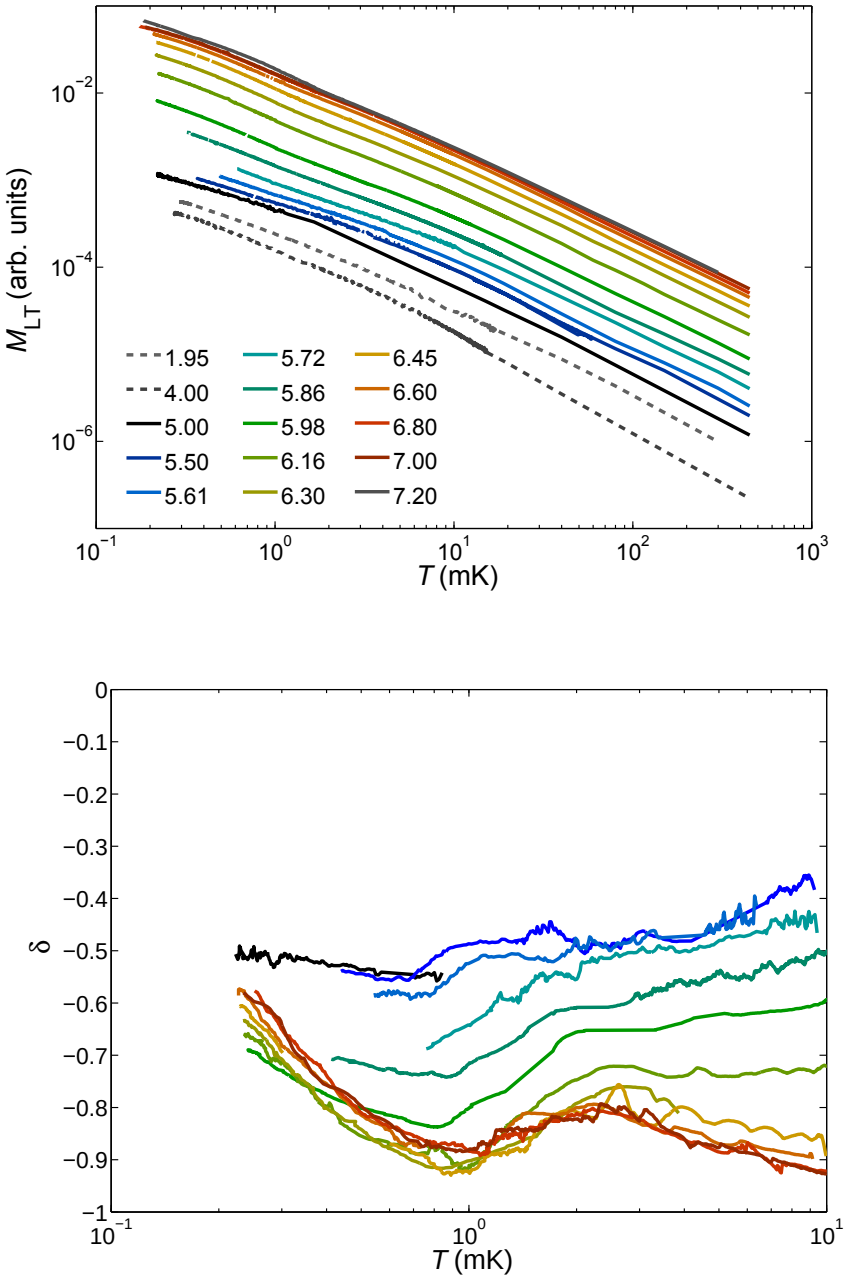

Figure 4.31: The upper graph shows the bare low temperature magnetisation upturn as calculated by subtracting the high temperature Fermi fluid magnetisation. The lower graph shows the temperature exponent of the upturn magnetisation as as calculated from the derivative of the upper graph.

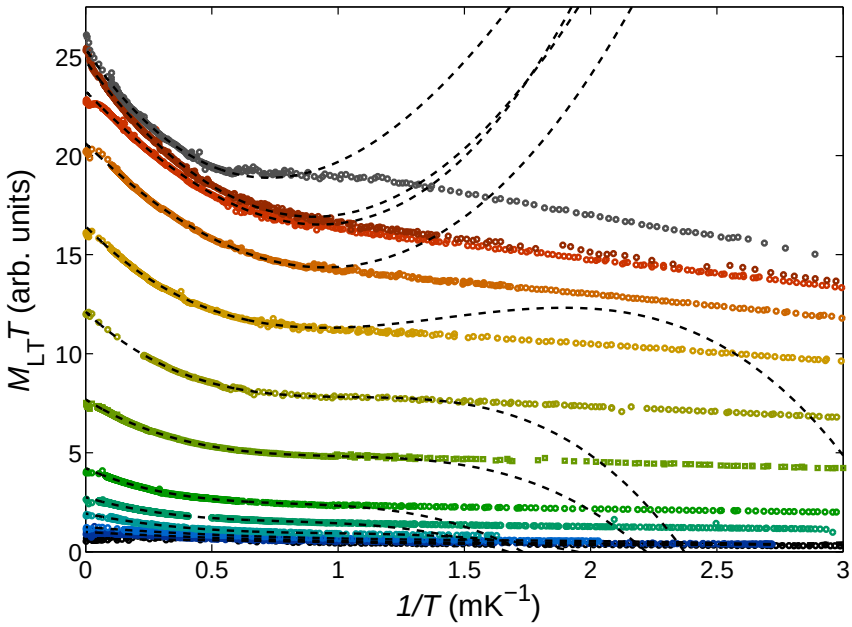

Figure 4.32: The graph shows the HTSE fits of the MSE model to the low temperature magnetisation upturn data. Fit parameters are shown in Fig. 4.33.

At densities above 5.72 nm^{-2}, however, the exponents starting at -0.5 to -0.7 at lowest temperatures, goes through a minimum around 1 mK, followed by a subsequent increase, which becomes shallower with increasing density. At highest densities the exponent even decreases again and approaches -1 at highest temperatures, as would be expected for the high temperature limit of a Curie-Weiss magnet. This non-trivial behaviour suggests that the excess magnetisation for coverages above 5.72 nm^{-2} is not described by a simple power law.

Another more sophisticated model which might be used to express the low temperature magnetisation upturn is the high-temperature series-expansions (HTSE) of the multiple spin exchange model (see Sec. 2.3.2). Multiple spin exchange in the solid leads to competing ferro- and antiferromagnetic interactions, depending on the parity of the particle permutation resulting in a non-trivial temperature dependence around the characteristic exchange constants.

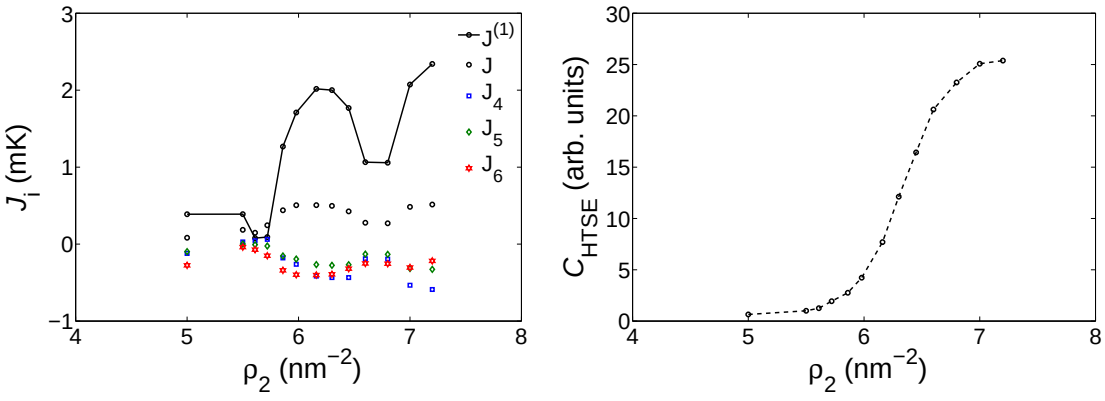

Figure 4.33: The left graph shows the density dependence of the exchange constants in the MSE model. Here the J_n are the exchange constants associated with n-particle ring exchange. J^1 is the effective exchange constant (see also Sec. 2.3.3).The right-hand side graph shows the corresponding Curie constant of the HTSE contribution.

Figure 4.32 shows the $M_\mathrm{LT}T$ of the low temperature solid plotted against the inverse temperature. This is to highlight discrepancies from a simple Curie-Weiss law. As can be seen the apparent Curie constants are almost linear in inverse temperature, in the high temperature limit, showing that the system is close to Curie-Weiss law as described in the previous paragraph and Section 4.3.1. At lower temperatures, however, the system starts to diverge from the initial linear behaviour and makes a transition to a much shallower slope. In order to extend the range of convergence of the solid magnetisations down to 1 mK, HTSEs according to the coefficients of Roger [75] up to the third order in J/T were fitted. Below 1 mK, however, a fast divergence of the the fits with respect to the measured magnetisations is observed. The fitted magnetisations and multiple spin exchange constants are shown in Figure 4.33. At this stage it should be mentioned that the fitted exchange constants strongly depend on the fitted temperature range.

The fitted total Curie constants of the HTSE fits (Fig. 4.33) are in excellent agreement with the high temperature Curie-Weiss fits in Section 4.3.1. The effective $J^{(1)}$, even though in the same order of magnitude as $\Theta/3$, does not follow the general trend of Θ and is a factor 3 too large. Thus the general model to describe the low temperature magnetisation or coefficients calculated by Roger might be flawed. If,

however, the model is to be believed, then the ratios of the inferred J_4 to J are always negative for coverages above $5.86\,\mathrm{nm}^{-2}$ and increases from about 0.33 at lowest to 1.1 at highest densities. Therefore two-dimensional ^{3}He on graphite lies deep within the quantum-spin liquid phase as proposed by Misguich and LiMing et al. [27, 28] (see also Sec. 2.3.4).

In the quantum spin liquid phase the Mott insulator is governed by fermionic excitations producing a finite magnetisation of the system. Similarly to electrons in metals these excitations are described by a band structure which might be gapped or ungapped (see Sec. 2.3.4). One method which is usually applied to determine whether an electronic or magnetic system is gapped or ungapped is to plot the corresponding thermally activated property (magnetisation) in an Arrhenius plot (see Fig. 4.34).

The quantum spin liquid ground state opposes magnetic order, e.g. a 120^o Neel ordered state as expected for 2D triangular quantum spin-$^1/_2$ magnets [27, 28]. If following Collin et al. [154] we assume a gapped magnon dispersion of the form:

$$\epsilon(k) = \Delta + k_\mathrm{B} JS|(k - k_0)|^n - \mu B, \tag{4.14}$$

with a magnon gap Δ and band exponent n, this leads to the thermally activated magnetisation:

$$M(T) \propto \frac{C}{T}\left(\frac{T}{JS}\right)^{2/n} \exp\left\{-\frac{\Delta}{T}\right\}. \tag{4.15}$$

In their analysis a magnon gap of about $\Delta \approx 100\,\mu\mathrm{K}$ was inferred from the linear behaviour of the Arrhenius plot at lowest temperatures [155, 154]. Furthermore, by plotting their data as $-dlog(M)/dT^{-1}$ against temperature, Collin *et al.* were able to determine the band exponent as $n = 6$. Using their magnetisation Equation 4.15, the logarithmic derivative can be calculated as:

$$\beta = -\frac{d\ln M}{dT^{-1}} = \Delta - \left(1 - \frac{2}{n}\right) T. \tag{4.16}$$

However, inference of a gapped magnon dispersion was later contradicted by NMR measurements by Masutomi *et al.* [30], who showed that the low temperature

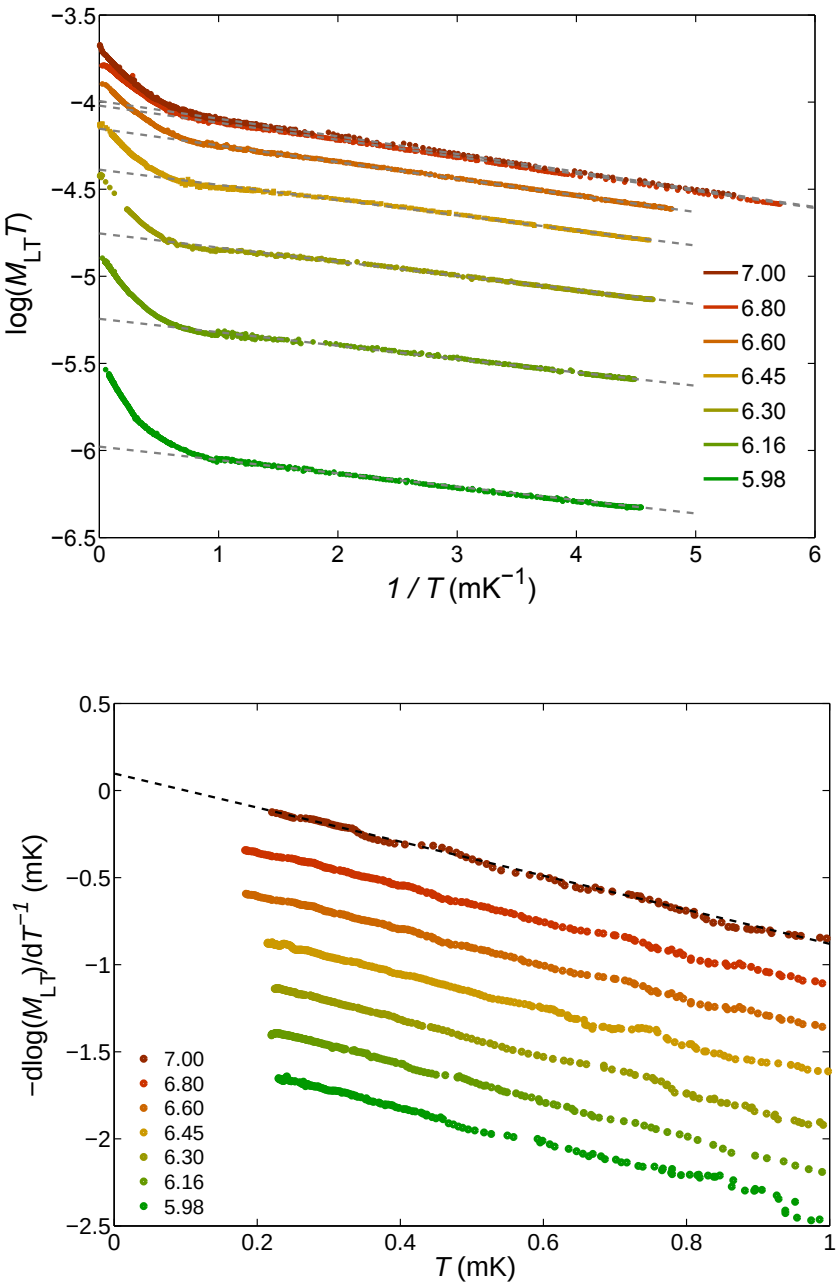

Figure 4.34: The upper graph shows the ultra-low temperature upturn magnetisation plotted in an Arrhenius plot where the slope is the negative magnon dispersion gap Δ. The lower graph shows the logarithmic derivative of the upturn magnetisation, where the slope $\beta = 2/n - 1$ and the intercept is Δ. Lower data are offset by -0.25 relative to the 7.00 nm^{-2} curve.

magnetisation increases down to 10 μK contrary to the behaviour expected from a finite spin gap, for which the low temperature magnetisation should be suppressed to zero by the thermal activation term. In their measurements Masutomi et al. found that the ^{3}He magnetisation increases down to lowest temperatures and starts to show the onset of a Pauli magnetisation plateau as expected from a Fermi fluid.

We repeated the analysis of Collin *et al.* for our data and found a comparable slope of the Arrhenius plot of $\Delta \approx 75...100\,\mu$K for all coverages (see Fig. 4.34). However the band exponent inferred from the logarithmic derivative differs significantly. The fitted slopes of the lower graph in Figure 4.34 are $\beta = -1.00 \pm 0.05$ meaning that $2/n - 1 = -1$, i.e. n is larger than 40 or infinite and thus unphysical.

As we already saw in Section 4.3.2, our magnetisation data can be fitted by three Fermi fluids over the entire temperature range, where the highest temperature fluid vanishes at the Wigner-Mott transition and is replaced by a low and ultra-low temperature fluid. By calculating the logarithmic derivative of an ideal Fermi fluid, as described by the Dyugaev form [131], we find that $\beta = -1$ for $T \leq T^*$ and $\beta \approx -(T/T^*)^3$ for $T \gg T^*$, which agrees with our observation. Furthermore by expanding the Dyugaev form, as plotted in an Arrhenius plot, around the degeneracy temperature:

$$\log(MT) = \log\left\{\frac{C}{\sqrt{1+\frac{T^{*2}}{T^2}}}\right\} \tag{4.17}$$

$$\log(MT)|_{T^*} \approx \log\left\{\frac{C}{\sqrt{2}}\right\} - \frac{T^*}{2}\Theta + \frac{T^{*3}}{12}\Theta^3 + \mathcal{O}(\Theta)^4 \tag{4.18}$$

where $\Theta = 1/T - 1/T^*$, we find that the Fermi fluid produces a linear dependence of $\log(MT)$ with respect to $1/T$ like a gapped magnon system. The slope of the Fermi fluid in the Arrhenius plot is $T^*/2$. Thus the fitted slopes of the Arrhenius plots reproduce the known Fermi temperatures of the ultra-low temperature Fermi fluid of 150 to 200 μK (Sec. 4.3.2). Here the observed upturn at high temperatures in the Arrhenius plot can now also be explained by the intervening low temperature Fermi fluid. Here the steeper gradient corresponds to the much higher Fermi temperature of the second fluid component. The degeneracy temperatures of both fluids have already been fitted in Section 4.3.2). Both temperatures are only weakly density

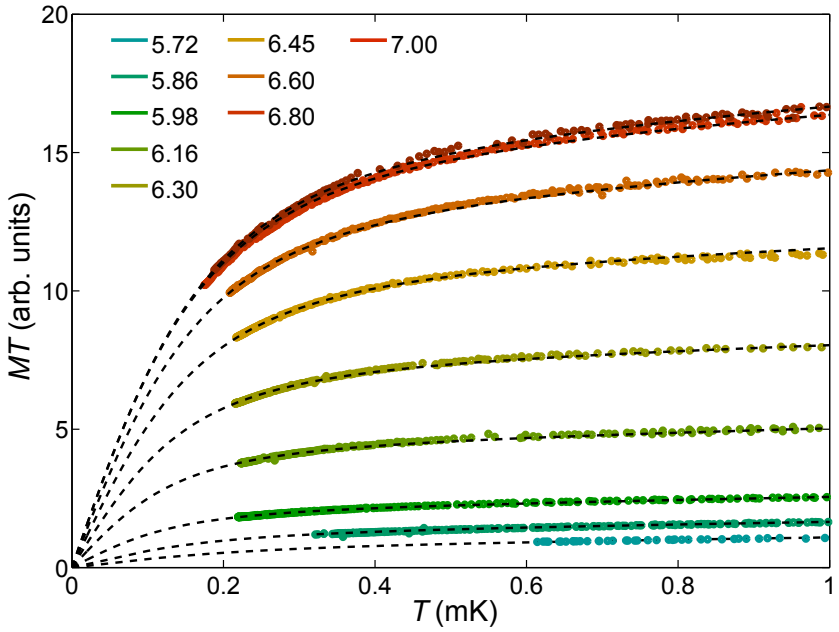

Figure 4.35: The graph shows the ultra-low temperature magnetisation of ^{3}He|^{4}He|graphite and the extrapolated three Fermi fluid fit down to zero temperature

dependent, suggesting that the underlying solid structure does not change. The magnetisation of the corresponding fluids, however is growing rapidly throughout the entire coexistence region. The magnetisation of the ultra-low temperature fluid saturates at temperatures far beneath the degeneracy temperature as evidenced by the linear increase of MT close to zero temperature (see Fig. 4.35). The occurrence of two fluids and their particular magnetisation ratios of $1/3$ and $2/3$ are still unresolved. The existence of two fluids might be explainable by the presence of two spinon bands with different effective masses or a mixture of a single band spinon system and an extremely heavy hole band as introduced by zero-point vacancies in the solid. Here the latter scenario is supported by the proposal that the spinon Fermi temperature is smaller than the characteristic exchange energies in the system, i.e. $T^* \ll J^{(1)} \leq 2\,\mathrm{mK}$.

Another way to confirm that there is no magnetically ordered ground state in the

system is by measuring a magnetic field dependence of the magnetisation and the NMR frequency. We measured the magnetisation of a 6.80 nm^{-2} sample at to usual Larmor frequency of 100 kHz and additionally at 25 kHz. Here the ^{13}C-frequency was used as magnetic field probe inside the NMR-cell. The measured magnetic fields and ^{3}He-Larmor frequencies, were proportional to each other. Thus considering a $\hbar\omega_{\mathrm{L}} = \sqrt{\Delta^2 + (\hbar\gamma B_0)^2}$ behaviour of the ^{3}He NMR resonance frequency as expected for a gapped Heisenberg triangular lattice spin-$^1/_2$ solid [156] the magnon dispersion gap must be significantly smaller than $\Delta \ll h \times 25\,\mathrm{kHz} = k_{\mathrm{B}} \times 1.2\,\mu\mathrm{K}$ and $\Delta \ll T^*$. As a consequence the magnetisation scales with the magnetic field as can be seen in Figure 4.36.

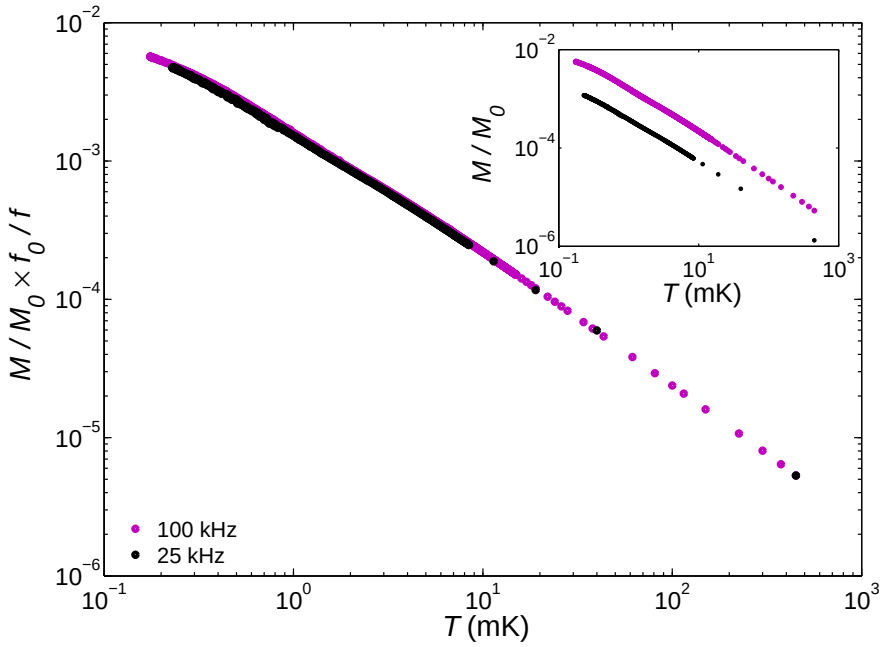

Figure 4.36: The graph shows the polarisation of the 6.80 nm^{-2} sample measured at a Larmor frequency of 25 and 100 kHz (inset). Rescaling the 25 kHz data by the frequency produces a perfect match with the 100 kHz magnetisation.

4.4.2 Spin-lattice Relaxation Times

In addition to the magnetisation, the spin-lattice relaxation time has been measured. This was the first the first attempt to measure T_1 on a ^{3}He sample on graphite at ultra-low temperatures, relying on the ability to measure in low magnetic fields with reduced eddy current heating. As has been shown in Section 2.4.2 the spin-lattice relaxation time is a probe of local field fluctuations at multiples of the Larmor frequency.

We first measured the longitudinal relaxation of 2D ^{3}He (fig. 4.37) by applying a 180^o-$\tau - \theta$ pulse sequence where the readout tipping pulse was a standard $\theta = 7.1^o$ tipping pulse. Initial experiments at sub-millikelvin temperatures showed that the applied 180^o pulse leads to a 15 % reduction of the observed equilibrium magnetisation at long delay times. This effect was attributed to eddy current heating within the silver and graphite. The time scale governing the subsequent warm-up of the helium-nuclei is T_1. The observed longitudinal relaxation is therefore a superposition of the T_1-recovery due to the 180^o-pulse and reduction of the longitudinal magnetisation due to the eddy current heating. Since both time scales are equivalent, the resulting total relaxation curve is highly deformed. In order to reduce this heating effect, the amplitude of the initial 180^o pulse was reduced to 90^o, which reduced the eddy-current heating by a factor of 4, and the equilibrium magnetisation loss to less than 5 %. Even with the reduced initial tipping pulse, we observed a secondary heating effect with a thermal relaxation time of 10 minutes, which has been attributed to the thermal relaxation of the NMR-cell with respect to the nuclear demagnetisation stage. The repetition time of the T_1-experiments was therefore chosen to be at least five times longer than this thermal relaxation time.

Figure 4.37 shows two examples of longitudinal relaxations following a 180^o and 90^o pulse. The 180^o pulse initially inverts the equilibrium magnetisation, whereas the 90^o pulse just reduces the longitudinal magnetisation to zero by tipping all spins into the xy-plane. In both cases, the following relaxation is a superposition of two exponential relaxations. The frequency and temperature dependence of both relaxation times and magnitudes are shown in Figure 4.38 for sample $6.80\,\mathrm{nm}^{-2}$.

As can be seen both relaxation times are weakly linearly frequency dependent with a zero-frequency intercept of 40 and 140 ms respectively. Both magnetisations

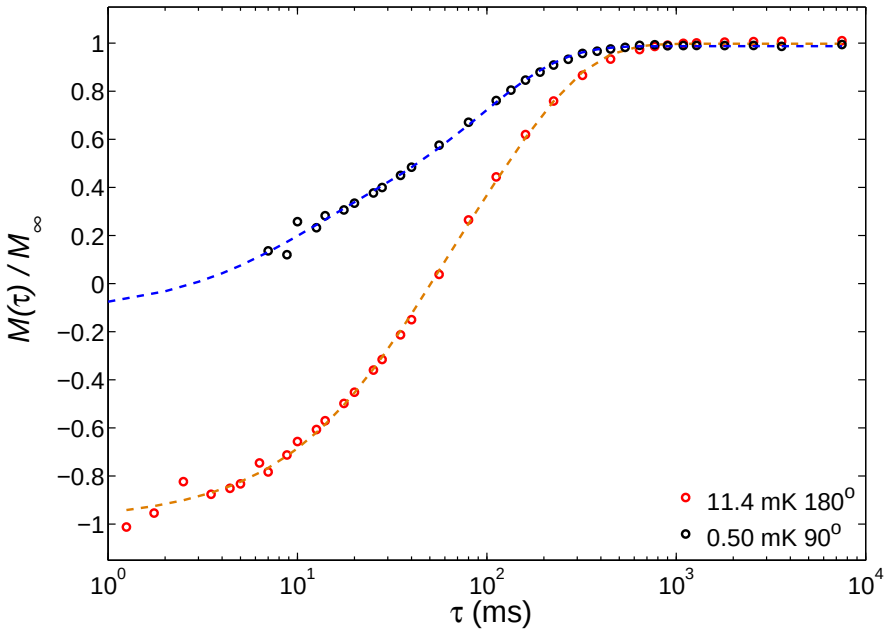

Figure 4.37: The graph shows the recovering longitudinal magnetisation following a 90 and 180^o-tipping pulse for a 6.80 nm^{-2} sample.

grow with increasing magnetic field, albeit with different rates. The relative weight of the two components shifts with frequency. The temperature dependence of both T_1's is described by a weak power law of about $T_{1L} \propto T^{1/9}$ and $T_{1S} \propto T^{1/12}$ for the long and short component respectively (see Fig. 4.39). Here both magnetisations grow at slightly different rates with decreasing temperature, leading to the observed shift of their relative weight.

The double exponential relaxation observed in the system stems from the different longitudinal relaxation times of ^{3}He atoms close to substrate inhomogeneities and ^{3}He atoms in the bulk. It is thought that atoms close to substrate inhomogeneities are more strongly coupled to its lattice and therefore exchange energy and spin more quickly. In this model the bulk relaxation originates predominantly from spin diffusion towards the substrate inhomogeneities and the observed long component can be interpreted as the intrinsic longitudinal relaxation time due to spin diffusion. The short relaxation time, however, reflects the interactions with other magnetic

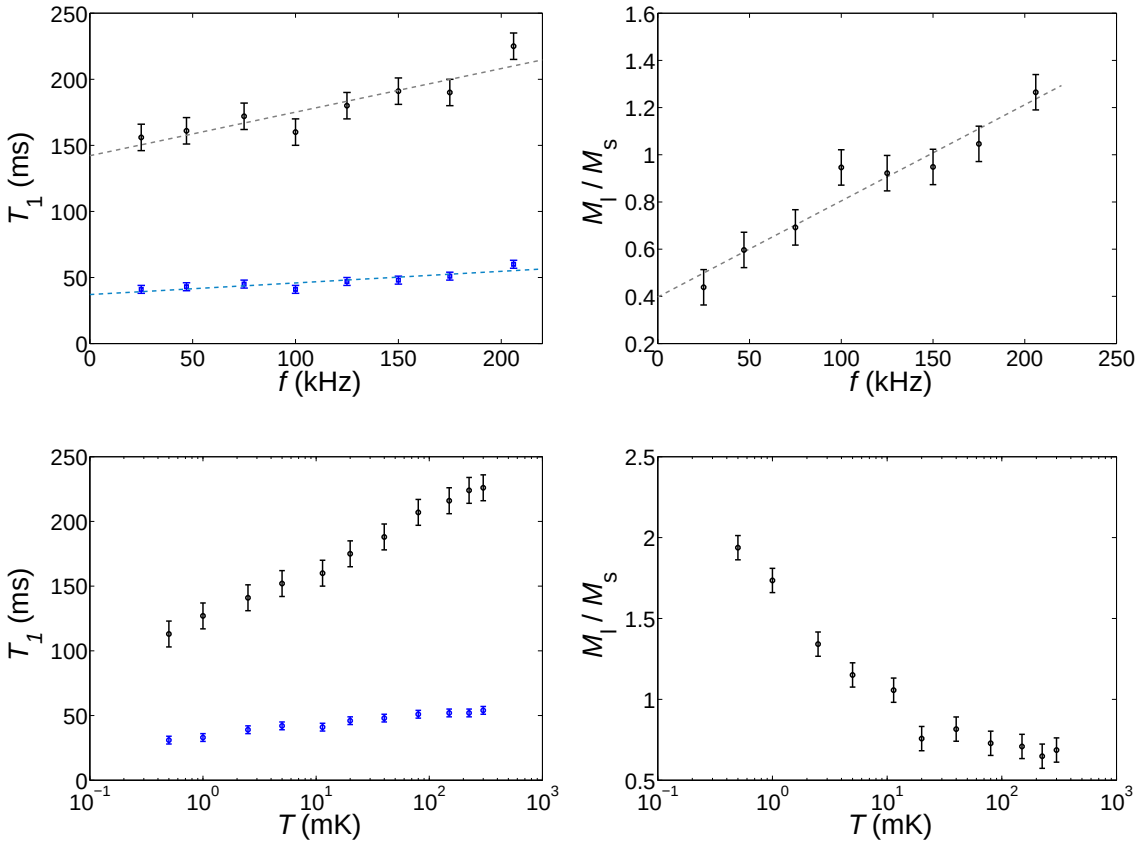

Figure 4.38: Frequency and temperature dependence of the spin-lattice relaxation time in a 6.80 nm^{-2} ^{3}He sample: The upper two graphs show the frequency dependence of the spin-lattice relaxation times of the double exponential longitudinal magnetisation recovery and ratio of the associated magnetisations at 11.4mK. The lower two graphs show the temperature dependencies of the same quantities at a fixed Larmor frequency of 100.4 kHz. Dashed lines are linear guides to the eye.

species in the substrate. In this model, the correlation times within the bulk are much larger than around inhomogeneities. Comparing both T_1's to the intrinsic transverse relaxation time measured in Section 4.2.3, we find a good agreement between the short component T_{1s} and transverse relaxation time whilst the long component T_{1l} is much larger than T_2. This comparison agrees with the proposed model of short and long correlation times of the intrinsic fields in the vicinity of inhomogeneities and the bulk [77]. Here T_{1l} is far longer than T_2, hence the associated

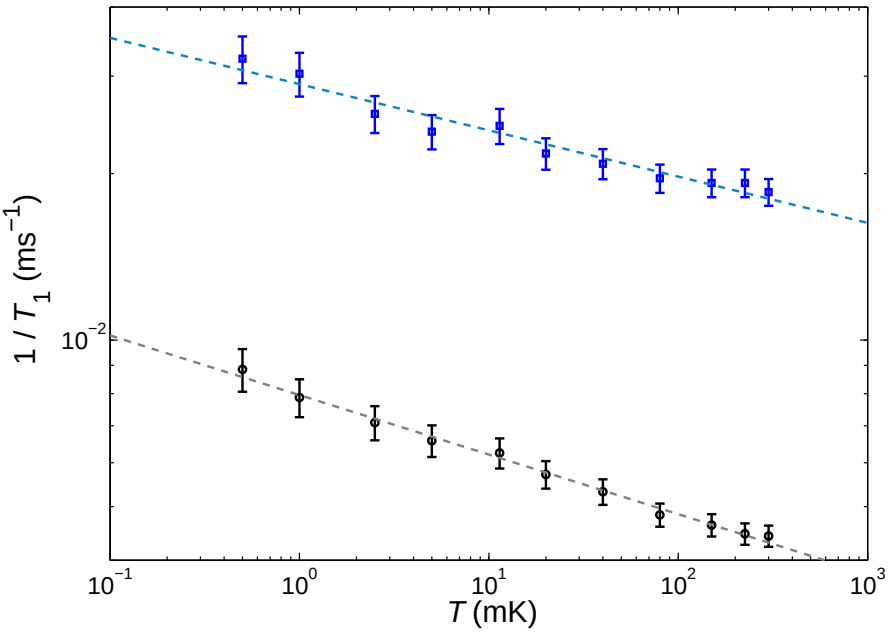

Figure 4.39: Temperature dependence of the long and short spin-lattice relaxation rate of a 6.80 nm^{-2} ^{3}He sample at 100.4 kHz.

correlation times in the bulk must be much longer than the Larmor period. This is also evidenced by the stretched exponential behaviour of the FID and Gaussian spin echoes (see Sec 4.2.3).

Unfortunately, at this moment there is no microscopic model that would link the T_1 data to intrinsic properties of the Fermi fluid or spin liquid. At present the only conclusions that we can draw from the data are that both components follow a smooth temperature and frequency dependence and show no evidence of structural or magnetic phase transitions. Secondly, neither of the two relaxation times follows a Korringa law [86].

In conclusion, we have analysed the low temperature magnetisation in terms of a magnetically frustrated solid and quantum spin liquid. We applied the high temperature series expansion for a triangular lattice solid with multiple spin exchange, and found that based on the fitted exchange constants the system lies deep within the quantum spin liquid phase as proposed by Misguich and LiMing [27, 28]. The

measured low temperature magnetisation shows a finite zero temperature magnetisation, contradicting an antiferromagnetically ordered state with gapped excitation spectrum. Dyugaev Fermi fluids have been fitted to the low temperature magnetisation upturn and showed that the low temperature magnetisation is composed of two Fermi fluids. The fluid with the lowest degeneracy temperature is interpreted as a gapless quantum spin liquid, whilst the high temperature fluid might originate from an extremely heavy hole band in the Mott insulator as introduced by zero-point vacancies in the solid. The renormailsed Fermi temperatures of both fluids have been determined as $T^*_{LT} \approx 4...7\,\mathrm{mK}$ and $T^*_{LT} \approx 150...200\,\mu\mathrm{K}$. As evidenced by longitudinal and transverse relaxation time measurements, we hypothesis that relaxation in the sample is governed by short correlation times of the internal fields around substrate inhomogeneities and long correlation times in the bulk. Neither of the two relaxation time measurements showed signs of an abrupt phase transitions in the system. Thus supporting the hypothesis of a smoothly evolving coexistence phase and stability of the magnetic ground state of the triangular lattice solid.

5 Transport Phenomena in Graphite

Graphite is a quasi-two dimensional semimetal described by the Slonczewski-Weiss-McClure band model [32, 56] (see Section 2.2.3). Its crystal structure can be interpreted as an infinite number of ABAB stacked graphene sheets [55]. Owing to its high crystallinity and semimetallic band structure charge carriers in graphite are characterised by extremely high Fermi velocities, mean-free paths and mobilities, whilst their density is extremely low. Due to these extraordinary properties graphite hosts a number of correlated electron and finite size effects.

As was discussed in the previous sections we used graphite, and in particular exfoliated graphite, as a highly homogeneous substrate for the adsorption of two-dimensional ^{3}He-films. Parallel to the experiments presented in this thesis, a new exfoliated graphite substrate was developed by Kristian Kent trying to increase the step free, coherent size of the graphite adsorption facets [121]. As part of this project the physical properties of these substrates and their starting materials were characterised by electrical transport and magnetisation measurements.

Here we analyse the influence of finite sizes and crystal defects, introduced by the chemical exfoliation of graphite, on the low temperatures electrical conductivity and magnetism. In a general characterisation effort, the magneto-transport properties of the graphite and its allotropes were studied up to 60 T.

Particular interest was paid to the density-wave anomaly in the magneto-transport of graphite above 30 T. We explored the correlation effects arising due to a dimensionality reduction and strong Coulomb interaction in the ultra quantum limit of graphite by applying magnetic fields of up to 60 T to a high purity graphite single-crystal. Our data shows conclusively for the first time that the density-wave anomaly in graphite is induced by charge-density waves in the lowest occupied Landau levels.

5.1 Graphite Samples

Our study was based on different poly- and single-crystalline graphites as well as mesoscopic exfoliated graphites. The polycrystalline natural graphites, Madagascan, Kish and Tanzanian graphite, were sourced from AMG Mining AG [157], NGS Naturgraphit GmbH [158] and Naturally Graphite [159] respectively. The nanocrystalline highly-oriented pyrolitic graphite (HOPG) and exfoliated ZYX and Grafoil were produced by Union Carbide [106, 160].

The batch of Madagascan graphite consisted of polycrystalline graphite flakes with diameters of 2 to 5 mm and thicknesses of up to 100 μm. Laue x-ray diffraction measurements showed that each flake has of the order of ten crystallites [121]. The matt appearance of these natural graphite flakes suggests a rather high degree of disorder on its outer surfaces. Additional gas adsorption experiments, similar to the helium adsorption isotherms presented in Section 4.1, showed a large specific surface area of these flakes, suggesting large internal cavities as would be induced by some form of natural exfoliation.

Kish graphite is a byproduct of iron smelting. It forms on top of the molten iron in the form of millimeter sized crystals. Due to the smelting process Kish graphite contains high levels of iron and other metallic impurities, but shows larger crystallites in comparison to natural graphites.

Tanzanian graphite crystals are embedded in dolomite rock found in Moshi, Tanzania. The crystals were extracted by chemically dissolving the rock. The size of these crystals was comparable to the Madagascan graphite flakes. Their shiny appearance and hexagonal shape suggests a much better quality compared to Madagascan graphite, which was later proven by higher residual resistivity ratio (see Fig. 5.2).

The nanocrystalline HOPG is an artificially grown graphite, which is produced by graphitising carbon above 2000^{o}C and annealing the resulting graphite at temperatures above 3000^{o}C and high pressures [161, 162]. HOPG shows a high chemical purity. However, its structure is dominated by lamellar crystallites with widths of the order of 50 nm [163].

Exfoliated graphite, like ZYX, is a nanocrystalline graphite, where the crystallites are only loosely packed and oriented. It is produced by rapid heating of chemically

intercalated natural graphite or HOPG [164]. The rapid heat treatment of the intercalated compound leads to a random separation of graphene sheets and break up of the graphite crystal into multiple graphite platelets. The resulting graphite platelet powder is often recompressed into a foil, which preferentially aligns the platelets parallel to the foil surface. Depending on the starting material these foils are known as Grafoil and ZYX for natural graphite and HOPG respectively. The crystallite sizes of these foils are of the order of 60 and 80 nm. The full-width half-maximum of the c-axis alignment angles of Grafoil and ZYX are 12^o and 4^o respectively, as determined by x-ray diffraction [121, 165]. Exfoliated graphites like Grafoil and ZYX continue to hold scientific interest due to their use as substrates for noble gas adsorption experiments, such as our helium studies, energy storage applications and high temperature gasket materials.

5.2 Low Field Transport and Quantum Oscillations

In order to characterise the quality of the individual graphites the zero-field resistance was measured in a Quantum Design Physical Property Measurement System (PPMS) [166]. The Madagascan, Kish and Tanzanian graphite samples were measured uncut and uncleaved. Their typical sizes were $1\,\text{mm} \times 1\,\text{mm} \times 25\,\mu\text{m}$ up to $3\,\text{mm} \times 3\,\text{mm} \times 75\,\mu\text{m}$. The HOPG, Grafoil and ZYX sample were cut to a standard size of about $3\,\text{mm} \times 3\,\text{mm} \times 150\,\mu\text{m}$. Resistances were measured using a LakeShore 370 AC Resistance Bridge with an excitation current of 1 to 5 mA and frequency of 16 Hz. The samples were mounted flat onto a PPMS electrical transport puck, i.e. with their crystallographic c-axis parallel to the magnetic field, and electrically separated from the metallic puck by a layer of cigarette paper and GE varnish. Electrical contacts were made along the perimeter of the samples by using $25\,\mu$m gold wire and silver loaded epoxy (EpoTek H20E, Dupont 6838). Both contact types were cured for 15 minutes under atmosphere and at 80^oC. Longitudinal and Hall resistances were measured using the van der Pauw method [167]. Generally temperature and magnetic field dependencies were measured by sweeping the temperature or magnetic field at a rate of 0.5 to 1.0 K/min or 30 Oe/s whilst logging the resistance every 5 to 10 s.

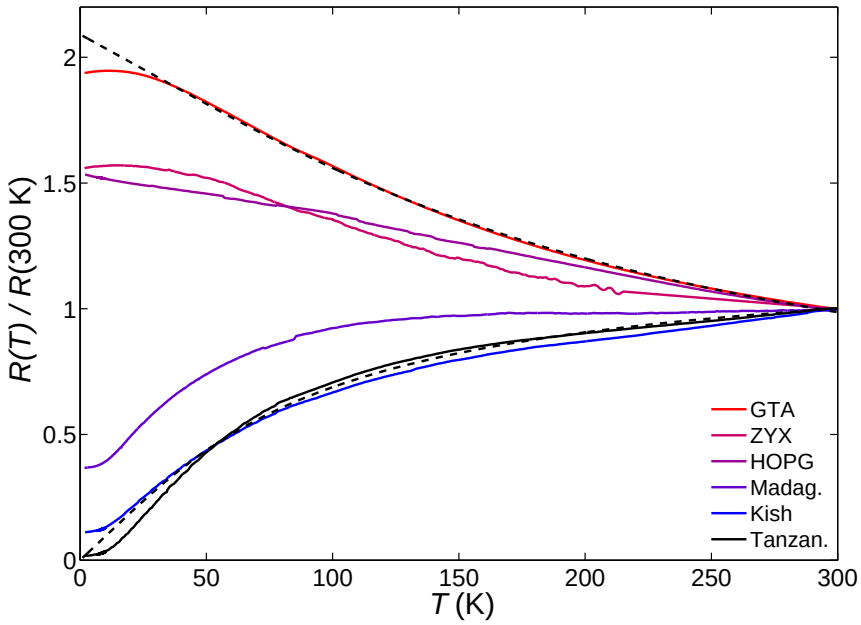

Figure 5.1: The graph shows the zero-field resistance of various graphite allotorpes renormalised by their room-temperature resistance. Dashed lines are fits to the resistance ofTanzanian graphite and Grafoil GTA using the standard two-band model of Zhang *et al.* [168].

Figure 5.2 shows the zero-field in-plane resistance of the four polycrystalline and two exfoliated graphite samples renormalised by their room-temperature resistances. As can be seen the polycrystalline samples show a residual-resistivity ratio (RRR) greater than one, whereas the nanocrystalline HOPG and exfoliated samples show a RRR smaller than one. Unlike ordinary metals, the resistance of the polycrystalline samples does not follow a T^2-behaviour and might thus be referred to as strange metal. The resistance of HOPG and the exfoliated graphites on the other hand, increases on lowering the temperature, forms an intermediate resistance maximum around 20 K and saturates at lowest temperatures. This unusual temperature dependence was first described by Uher and Sander in 1983 [169]. Later Zhang *et al.* interpreted this temperature dependence in the context of a two-band model, with a finite band overlap Δ between the electron and hole-band [168]. This model was extended by a temperature dependent charge carrier mobility μ to account for

phonon and other temperature dependent scattering mechanisms:

$$\rho = \rho_0 + \frac{1}{e\mu n} \qquad \text{with} \qquad n = n_0 k_\mathrm{B} T \ln\left\{1 + \exp\left(\frac{\Delta}{k_\mathrm{B} T}\right)\right\} \tag{5.1}$$

$$\text{and} \qquad \mu = (\mu_0^{-1} + A_0 T)^{-1}. \tag{5.2}$$

Fitting this model to our data produced strongly varying band overlaps and mobilities. Even though the model follows the general temperature dependence of both types of graphite samples at high temperatures, it fails at lowest temperatures (see dashed lines Fig.). Thus the fitted standard two-band model parameters are subject to large errors and depend strongly on the chosen temperature interval.

Based on the residual-resistivity ratios of the polycrystalline graphites: Tanzanian 58, Kish 9.0, Madagascan 2.7, HOPG 0.65, we find that Tanzanian graphite shows the best sample quality followed by Kish and Madagascan graphite. The particularly low RRR of our HOPG indicates a poor sample quality. Typical RRRs of HOPG range between 4 and 18 [170].

Due to the extremely low charge carrier densities in compensated semimetals like graphite a large Hall effect is expected. Thus in a magnetic field their resistances and conductivities are to be expressed by the conductivity tensor:

$$\sigma = \begin{pmatrix} \sigma_{xx} & \sigma_{xy} \\ \sigma_{yx} & \sigma_{xx} \end{pmatrix} \qquad \Rightarrow \qquad \sigma(\omega_c, \tau) = \frac{\sigma_0}{1 + \omega_c^2 \tau} \begin{pmatrix} 1 & -\omega_c \tau \\ \omega_c \tau & 1 \end{pmatrix} \tag{5.3}$$

where σ_{xx} describes the longitudinal and σ_{xy} the transverse conductivity. In a magnetic field, the Drude model conductivity tensor transforms into the expression on the right, where $\omega_c = eB/m^*$ is the cylotron frequency, τ the Drude scattering time and $\sigma_0 = ne^2\tau/m^*$ the zero-field longitudinal conductance [171]. In this model the resistivities are:

$$\rho_{xx} = \frac{\sigma_{xx}}{\sigma_{xx}^2 + \sigma_{xy}^2} \qquad \text{and:} \qquad \rho_{xy} = -\frac{\sigma_{xy}}{\sigma_{xx}^2 + \sigma_{xy}^2}. \tag{5.4}$$

In multi-band systems or systems with high Fermi surface anisotropy, this leads to the well known B^2 magneto-resistance of metals and their B-linear Hall resistance.

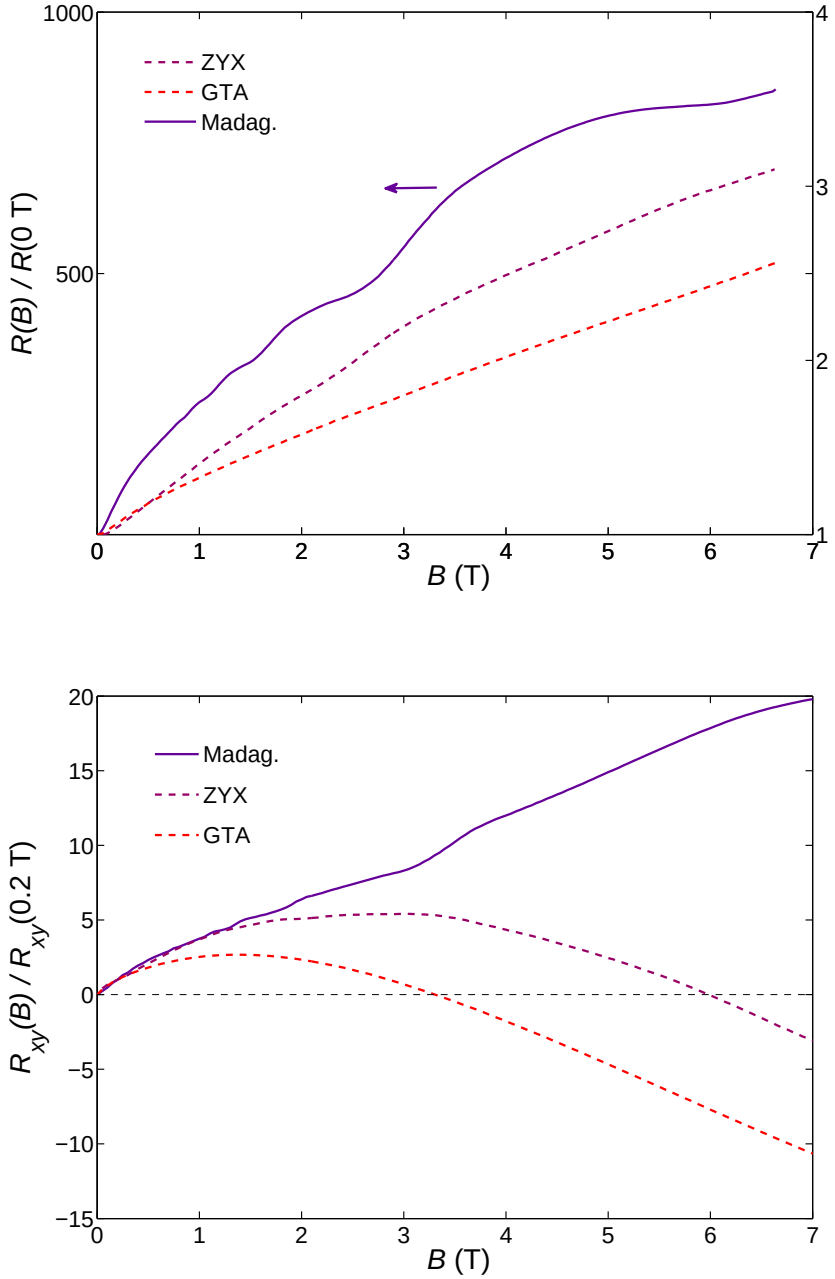

Figure 5.2: Longitudinal and Hall resistance of graphite at 4.2 K and magnetic fields up to 7 T. The graphs show a comparison between Madagascan (solid line) and two exfoliated graphites (dashed lines). Longitudinal and Hall resistances are renormalised by the zero-field longitudinal resistance and Hall constant respectively.

In metals with closed Fermi surfaces, the magneto-resistance will saturate due to the cyclotron motion of the electron around the Fermi surface and the associated vanishing of the drift velocity. The in-plane resistance shows a B^2 magneto-resistance at magnetic fields $B \ll 1\,\mathrm{T}$ followed by a much weaker magnetic field dependence B^α with $\alpha \leq 1$ at higher fields. At the same time the Hall resistance is almost linear in Madagascan graphite and shows a transition from a positive to a negative Hall constant in the exfoliated samples. Both the magneto- and Hall resistance of Madagascan graphite show pronounced Shubnikov-de Haas oscillations [172, 173]. As will be seen in Section 5.3 the magneto-resistance of graphite saturates at magnetic fields above 15 T, indicating the presence of closed Fermi surfaces as predicted by the SWM-model.

As the band structure of graphite is described by an electron and hole band crossing the Fermi energy, its conductivity is a superposition of the electron and hole conductivities. This interplay of the electron and hole conductivity enables the observed B-linear behaviour of the magneto-resistance. The sign and magnitude of the Hall coefficient are strongly dependent on the charge carrier densities and mobilities in almost compensated semimetals like graphite. Here the Hall constant is given as [171]:

$$R_\mathrm{H} = \frac{1}{e}\frac{n_\mathrm{h}\mu_\mathrm{h}^2 - n_\mathrm{e}\mu_\mathrm{e}^2}{(n_\mathrm{h}\mu_\mathrm{h} + n_\mathrm{e}\mu_\mathrm{e})^2} \tag{5.5}$$

A Hall sign reversal as observed in the exfoliated graphite can be caused by a changing relative charge carrier density or mobility. Brandt *et al.* were the first to discuss the influence of "magnetic freeze-out" on the charge carrier densities in graphite [174]. Their measurements on Kish graphite showed a strongly increasing positive Hall coefficient, peaking around 20 T and subsequently crossing zero and becoming negative at 50 T. Kumar *et al.* later reproduced Brandt's results on HOPG and found a comparable Hall sign reversal at magnetic fields around 42 T [175]. In Brandt's model, charge carriers are "frozen out" by increased binding to defects and impurities at high magnetic fields. In the magnetic field range studied in our experiments the freeze-out of electrons is dominant, leading to the cross-over of the Hall resistance from positive to negative (see Fig. 5.2). However, unlike Brandt's and Kumar's measurements the Hall sign reversal in exfoliated graphites occurs at 3.2

to 6.0 T, a factor ten lower in magnetic field than in natural graphite. This hints towards self-doping or stronger localisation of electrons, i.e. enhanced "magnetic freeze-out" due to an increased number of defects in graphite .

Self-doping of graphite should manifest itself in a noticeable change of the Fermi energy and Fermi surface volume due to the exceptionally low density-of-states in graphite. However the standard two-band model fits show only marginal differences of the band overlap ($\leq 1\,\mathrm{meV}$) comparing between exfoliated and natural graphites. Another way to determine changes in the electron density is by measuring the Fermi surface volume.

One method to determine the Fermi surface topology of metals is to measure the full angular dependence of their quantum oscillation frequencies [172]. In two-dimensional systems, however, it is sufficient to measure the Fermi surface cross-section within the ab-plane.

Quantum oscillations are caused by the Landau quantisation of electronic bands in high magnetic fields. In the presence of a magnetic field the Hamiltonian, Equation 2.10, is extended by the vector potential term $eA/2m$ where $B = \nabla \times A$. The resulting eigenstates are called Landau levels and are quantised in $\hbar\omega_c$. Furthermore it follows from the Onsager relation that these quantised energy levels correspond to electron orbits enclosing a multiple of the magnetic flux quantum [176]. Increasing the magnetic field causes the flux-quantised Landau levels to expand in reciprocal space and shift in energy. If a Landau level reaches the Fermi energy, the level depopulates and the associated electronic states redistribute to lower Landau levels. The mentioned flux-quantisation of these levels leads to a $1/B$-periodic repetition of these events, resulting in an oscillatory variation of the density-of-states at the Fermi energy and free energy. Here the magnetic de Haas-van Alphen (dHvA) and electrical Shubnikov-de Haas (SdH) effect are connected to the oscillatory part of the free energy by partial derivatives and can be described by the Lifshitz-Kosevich formula [177, 172]:

$$\tilde{M} = -\left(\frac{e}{2\pi\hbar}\right)^{3/2} \frac{\mu_m B^{5/2} F}{\sqrt{\pi \ddot{A}_{\mathrm{extr}}}} \sum_{\mathrm{p}} \frac{R_{\mathrm{T}} R_{\mathrm{D}} R_{\mathrm{S}} R_{\mathrm{M}}}{\mathrm{p}^{3/2}} \sin\left(2\pi \mathrm{p}\left[\frac{F}{B} - \frac{1}{2}\right] \pm \frac{\pi}{4}\right) \tag{5.6}$$

$$\text{with:} \qquad \mu_m = \frac{e\hbar}{2m_c} \qquad \text{and:} \qquad F = \frac{\hbar}{2\pi e} A_{\mathrm{extr}} \tag{5.7}$$

where $\tilde{M}$ is the oscillatory part of the magnetisation. Their frequency F is proportional to the extremal Fermi surface cross-section perpendicular to the magnetic field A_{extr}. Here p is the fundamental harmonic of the quantum oscillation frequency and R_T, R_D, R_S, R_M are the reduction terms associated with the thermal broadening, broadening of the Landau levels by a finite life time τ, spin-splitting of the Fermi surface and mosaic spread in polycrystalline samples. Most importantly the temperature and Dingle reduction term, R_{T} and R_{D}, can be used to determine the effective mass and scattering times of charge carriers in the system [178, 172]:

$$R_{\mathrm{T}} = \frac{\mathrm{p}\pi k_{\mathrm{B}} T}{\mu_m B \sinh\left(\mathrm{p}\pi k_{\mathrm{B}} T/\mu_m B\right)} \qquad \text{and:} \qquad R_D = \exp\left(-\frac{\mathrm{p}\pi k_{\mathrm{B}} T_{\mathrm{D}}}{\mu_m B}\right). \tag{5.8}$$

Figure 5.3 shows the oscillatory part of the graphite magnetisation at 1.8 K. The magnetisation and susceptibility of Madagascan graphite were measured using a PPMS-AC Susceptibility and Magnetisation Measurement option (ACMS) [166]. The ACMS option consists of a second order gradiometer and surrounding excitation coil inserted into the PPMS sample chamber. In ac-susceptibility mode the sample susceptibility is calculated from the mutual inductance of the excitation coil and gradiometer with the sample being subsequently placed at different positions in the gradiometer. In our measurements an excitation field of 10 Oe at a frequency of 321 Hz was applied. Static magnetisations were measured at zero and maximal field by moving the sample rapidly through the gradiometer and integrating over the induced voltage. The magnetisation shown in Figure 5.3 is integrated from the ac-susceptibility and corrected by the diamagnetic background of of $\chi = -0.051$ emu/T. The right-hand side graph of Figure 5.3 shows the dHvA spectrum of Madagascan graphite at 1.8 K as determined from a fast Fourier transform of the magnetisation oscillations in the left graph. Here two dominant frequencies at 4.85 and 6.25 T are visible. The two frequencies correspond to the extremal cross-sections of the majority hole and electron Fermi surfaces with the magnetic field aligned along the crystallographic c-axis [32, 179, 56, 173].

Similar measurements on Grafoil and ZYX show the same fundamental dHvA frequencies within the accuracy of $\Delta F = \pm 0.1$T of our measurements. However the amplitude of the dHvA oscillations in Grafoil and XYZ are strongly reduced due to

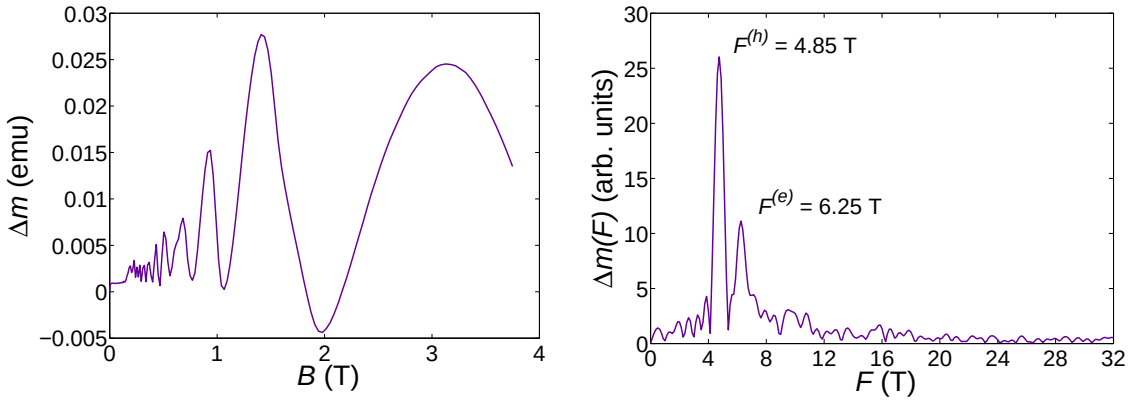

Figure 5.3: The left-hand side graph shows the magnetic moment of Madagascan single crystal graphite, measured at 1.8 K, subtracted by a constant diamagnetic susceptibility. The right-hand side graph shows the de Haas-van Alphen spectrum of the magnetisation oscillations on the left..

the large mosaic spread and resulting large mosaic reduction. Due to the excellent agreement of the measured dHvA frequencies with band structure calculations [32, 33] and previously reported values [173] a significant inflation of the Fermi surfaces or shift of the chemical potential can be excluded. However the existence of separate impurity bands close to the Fermi energy, which contribute to the electrical transport but are not measurable by quantum oscillations, can not be excluded.

Attempts to fit the effective masses and scattering times of the charge carriers in graphite were complicated by the limited number of observable quantum oscillations due to a poor signal-to-noise ratio of the magnetisation measurements at lower fields. A mean effective mass of $(0.044 \pm 0.003)\, m_\mathrm{e}$ was determined for Madagascan graphite by fitting the temperature reduction term R_T (Eqn. 5.8) to the temperature dependence of the dHvA amplitude at 2.2 T. This effective mass lies within previously reported masses for the electron and hole band in graphite of $0.057\, m_\mathrm{e}$ and $0.039\, m_\mathrm{e}$ respectively [173].

By including a beating frequency of about 1.4 T it was possible to fit a mean Dingle temperature and scattering time of the charge carriers. The scattering times vary strongly between 4×10^{-12} s in the Madagascan graphite and 1×10^{-12} s to 2×10^{-13} s in ZYX and Grafoil.

Therefore we conclude that exfoliation or the reduction of the crystallite size does

not significantly influence the bulk band structure of graphite, but increases the defect scattering rate. The increased defect concentration enhances the magnetic "freeze-out" by defect scattering and hence shifts the Hall sign reversal field to lower magnetic fields. The increased defect concentration also shortens the scattering time τ and reduces $\omega_c\tau$, which leads to a lower effective magnetic field and hence suppression of the magneto-resistance ratio in the exfoliated samples compared to the natural graphites. However, a simultaneous self-doping of graphite can not be excluded. For this a much more detailed transport or dHvA study to lower temperatures and higher magnetic fields would be necessary.

5.3 Landau Quantisation and Charge Density Waves in the Quantum Limit of Graphite

In the magnetic quantum limit, where $\hbar\omega_c \geq \epsilon_F$, and only the lowest Landau levels are occupied, the band structure of metals can no longer be described by their original Fermi energy and momenta. Here the remaining Landau levels dominate the band structure of the metal. In the ultra-quantum limit where the formerly cylindrical Landau levels become "Landau sheets" perpendicular to the magnetic field, the density-of states becomes essentially one dimensional. Consequentially these systems are prone to undergo nesting instabilities, such as charge-, spin-, or valley-density waves (CDW, SDW, VDW) or become an excitonic-insulator (EI) [40].

In semimetals like graphite and bismuth the magnetic quantum limit can be reached in moderate magnetic fields due to their low band width and charge carrier density. We studied the magnetic quantum limit of graphite by means of electrical transport measurements in pulsed magnetic fields. Pulsed magnetic field experiments were performed at the Dresden High Magnetic Field Laboratory in a KS21-type pulsed field coil. For experimental details please see Appendix B.

For this study, we used Tanzanian graphite crystals, due to their superior sample quality, sourced from Naturally-Graphite [159]. Samples were cut to bars of $\approx 1 \times 3 \times 0.08\,\mathrm{mm}$ for in-plane transport and cuboids of $\approx 0.75 \times 0.75 \times 0.15\,\mathrm{mm}$ for out-of plane transport measurements. Electrical contacts were made to the top

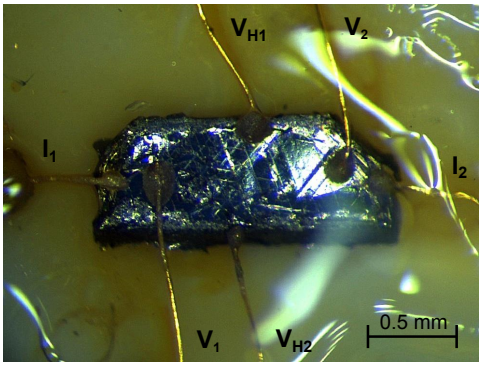

Figure 5.4: The photo shows the in-plane graphite sample presented in the following section. The samples c-axis is parallel to the direction of view. I,V and V_H mark the current, longitudinal and Hall resistance contacts.

surface of the samples using 25 μm gold wire and silver loaded epoxy (see Fig. 5.4). The EpoTek H20E and Dupont 6838 contacts were cured for 20 minutes at 120^o and atmosphere. Subsequently the samples were glued onto PEEK holders using GE varnish and covered in Dow Corning vacuum grease to stabilise the contact wires and to avoid vibrational pick up noise. The sample holders were installed on a pulsed field transport probe containing two calibrated magnetic field pick-up coils and a calibrated Cernox 1050 thermometer [89]. During the measurements the transport probe was inserted in a flow cryostat with variable sample chamber temperature. Above 4.2 K, the sample temperature was stabilised by an external PID controller using the cryostat's impedance heater and Cernox thermometer. Below 4.2 K, temperatures were stabilised by regulating the input impedance and pumping power of the sample chamber.

Figures 5.5 shows the in- and out-of plane resistance of graphite for magnetic fields applied parallel to the crystallographic c-axis. The in-plane resistance first increases steeply at low fields superimposed by SdH oscillations. Above 15 T the resistance starts to saturate due to the presence of closed Fermi surfaces. On increasing the magnetic field a step-like increase of the in-plane resistance can be observed around 30 T followed by an sharp resistance upturn at around 40 T. This behaviour is followed by another step-like resistance increase at 46 T before the resistance drops rapidly to below its initial saturation value with two steps at 52 and 54 T.

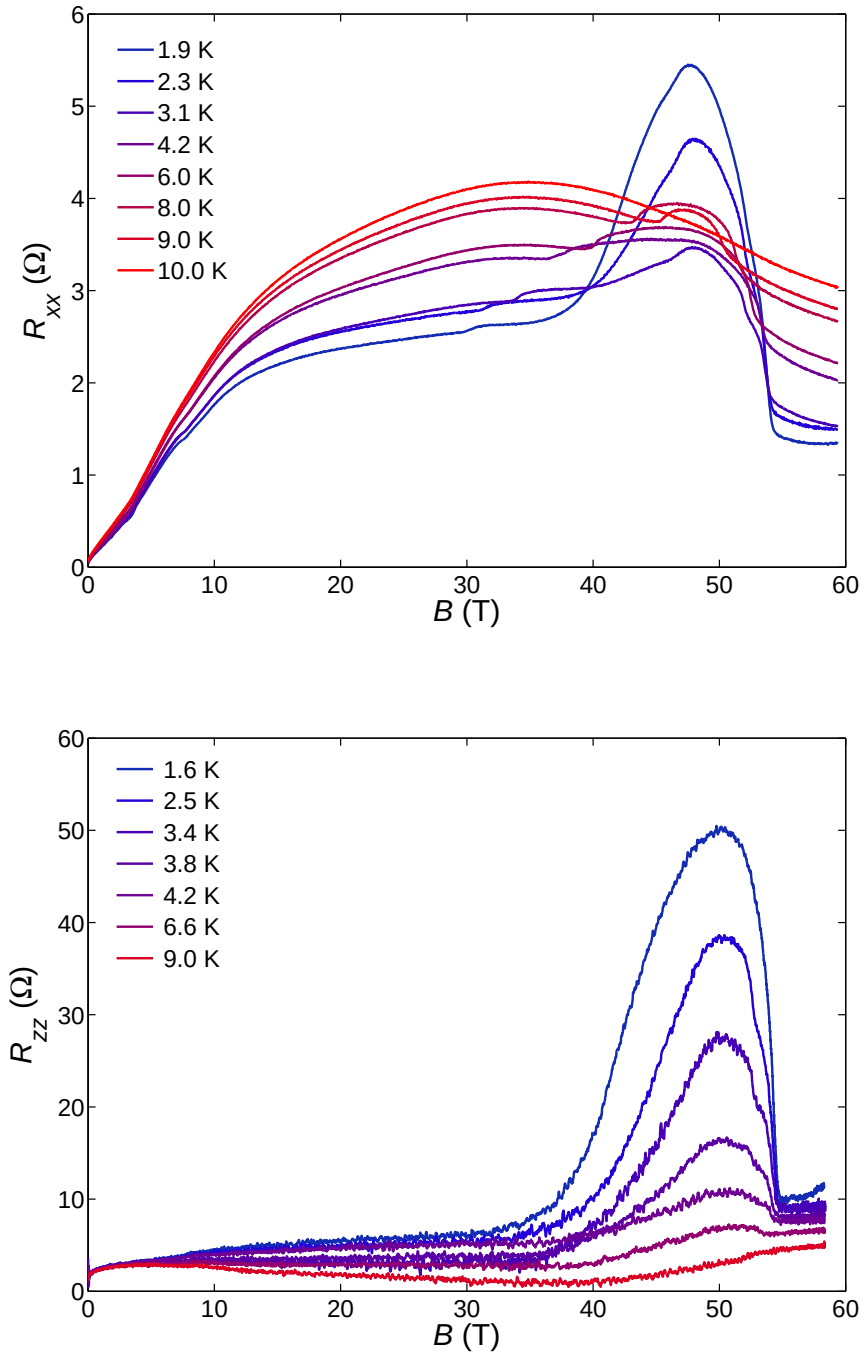

Figure 5.5: In- and out-of plane magneto-resistance of Tanzanian graphite at high magnetic fields: The upper and lower graph show the magnetic field dependence of the in-plane and out-of plane resistance graphite up to 10 K respectively.

The out-of plane transport on the other hand, does not show any considerable magneto-resistance up to the sharp resistance upturn at 46 T. Above 46 T the out-of plane transport is characterised by the same resistance features as the in-plane transport. In accordance with existing literature, these transitions are named in ascending order of their transition fields, α, β, γ, α' and β'-transition. Iye and Yaguchi *et al.* [41, 180, 181, 42] were the first ones to report these resistance anomalies in graphite in the 1980s and 90s. Nakao, Yoshioka and Fukuyama later attributed the observed resistance anomalies to a CDW in the lowest occupied Landau levels and developed a theory based on the increased interactions within these levels [182, 183]. However, the microscopic interpretation and identification of these features remained an open question. Recently Fauqúe *et al.* found another resistance anomaly at magnetic fields between 60 and 75 T, which could only be observed in the out-of plane transport, adding to the mystery of these field induced states.

In order to determine the exact transition fields in our data, the differential magneto-resistance of the in-plane resistance was calculated (see Fig. 5.6). Peaks and dips in the differential magneto-resistance correspond to upward and downward steps in the magneto-resistance.

Below 10 T the differential magneto-resistance shows strong SdH oscillations. Above these oscillations the system enters its quantum limit and becomes eventually one-dimensional. At 30 T a first peak-like structure (α) appears at lowest temperatures, which gradually moves towards higher magnetic fields with increasing temperature, before it vanishes at around 10 K. Together with a dip starting at 52.3 T (α'), whose transition field is slightly decreasing with increasing temperature, the α-transition encloses a presumed density-wave phase. Within this phase, a broad hump-like feature appears around 43 T followed by a sharp peak at 47 T (γ). The hump-like feature is an artifact of the steep resistance upturn associated with the β-transition and the subsequent resistance saturation. Furthermore, a second more pronounced sharp dip (β') appears beyond the α'-transition at 54.2 ,T, which merges with the α'-transition at around 6 K. Here the β and β'-transition enclose another density-wave phase. The full phase diagram of all transitions can be found in Figure 5.7. In this phase diagram, we chose to extract the β-transition from the field at which the pseudo-linear behaviour either side of the sharp upturn cross each other.

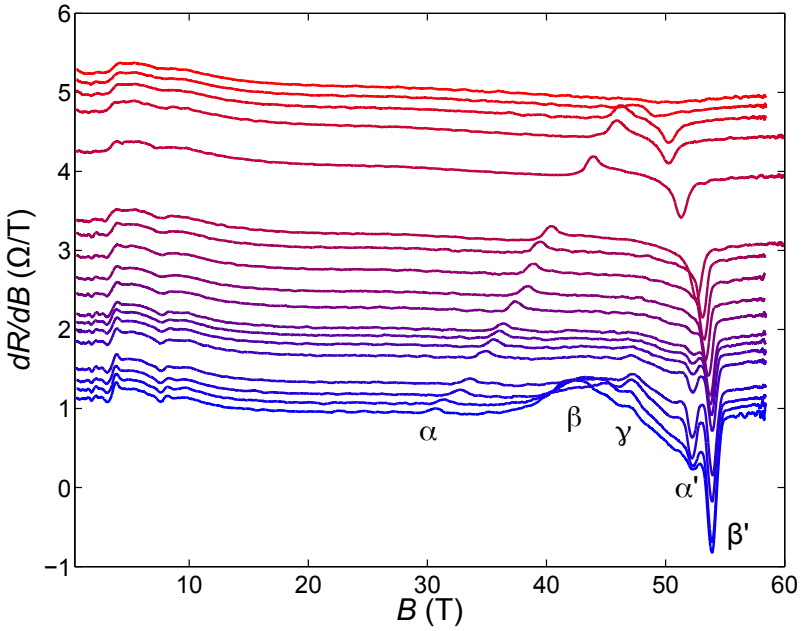

Figure 5.6: Derivatives of the in-plane magneto-resistance of graphite: The graph shows the derivatives of the in-plane magneto-resistance Fig. 5.5 with respect to the magnetic field. The data has bee offset proportional to temperature by 0.5 ΩTK.

In the phase diagram it can be seen that the α and β-transitions enclose two distinct overlapping phases, where the onset temperatures of α and β follow the theoretical prediction by Yoshioka and Fukuyama (YF) [183]. The dashed lines are fits to the YF-theory:

$$T_c(B) = T^* \exp\left\{-\frac{B^*}{B}\right\} \tag{5.9}$$

where T^* and B^* of both phases have been fitted as: α : 230 K, 148 T and β : 300 K, 195 T respectively.

Following the ideas of Takada and Goto [46], A. Isidori and M. Eschrig calculated the Landau level structures of graphite in the magnetic quantum limit [47]. Based on the bare SWM band structure $\epsilon_0(k_z)$ (see Sec. 2.2.3, the Landau level structure

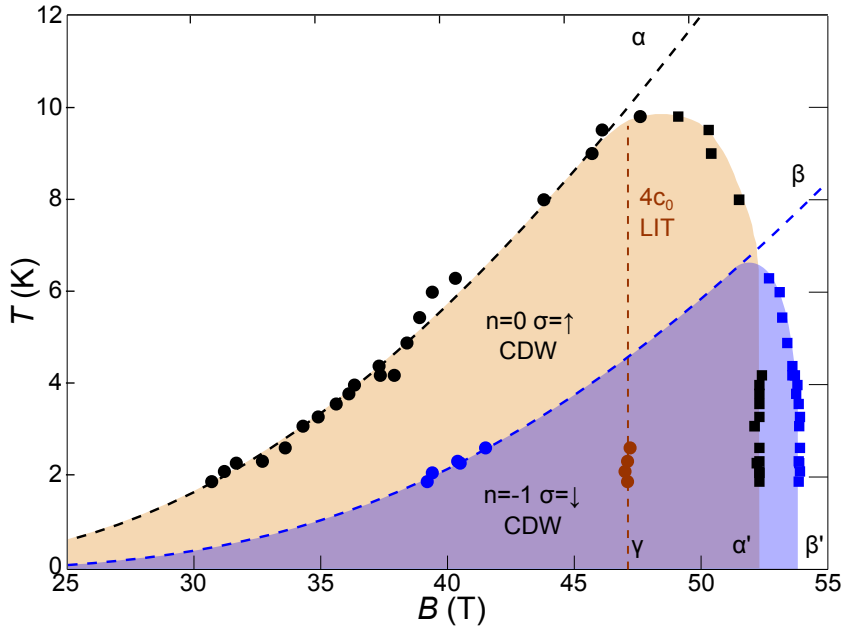

Figure 5.7: Phase diagram of the charge-density waves in graphite: The two shaded areas show the phase diagram region over which the $(0, \uparrow)$ and $(-1, \downarrow)$ charge-density waves extend. Black, blue and ocher markers represent the phase transitions as determined by Fig. 5.6 and extrapolation (see text). The dashed lines are fits to the YF-theory [183].

$\epsilon_\nu(k_z)$ was calculated by including the electron self-energy correction $\Sigma_\nu(k_z)$:

$$\Sigma_\nu(k_z) = \Sigma_{\nu',k_z',q_\perp} n_F^{\nu'}(k_{z'}) \left[|F_{\nu\nu'}(0)|^2 V_{\text{eff}}(0) - \delta_{\nu\nu'} |F_{\nu\nu'}|^2 V_{\text{eff}}(q_\perp, k_z' - k_z) \right] \quad (5.10)$$

, which was calculated from a self-consistent Hartree-Fock approximation. Here $n_F^{\nu'}(k_{z'})$ is the Fermi-Dirac distribution of the renormalised LLs, $F_{\nu\nu'}$ the corresponding form factors and $V_{\text{eff}}(q)$ the effective electron-electron interaction. In these calculations, short range electron-electron interactions were included by a local field correction to the random-phase approximation [184, 185]:

$$V_{\text{eff}}(q) = V_0(q) - \frac{[(1 - G_q)V_0(q)]^2 \Pi(q; i0)}{1 + [(1 - G_q)V_0(q)]\Pi(q; i0)}. \quad (5.11)$$

Here $V_0(q) = 4\pi e^2/\epsilon_r\epsilon_0 q^2$ is the bare Coulomb interaction, G_q the local field correction factor and $\Pi(q)$ the one loop electron polarisation as shown in Figure 5.9. For more details please see the supplemental online material of Arnold *et al.* [47]. In this self-consistent model, the only free parameter is the relative permeability of graphite ϵ_r, which was chosen such, that the calculated and observed α'-transitions match.

The resulting Landau level structures are shown in Figure 5.8. In the quantum limit of graphite only, the two lowest spin degenerate $n = 0$ and $n = -1$ LLs are occupied and give rise to the quasi-one dimensional character of the LL structure. Higher order Landau levels are already depopulated and reside far away from the Fermi energy and are therefore neglected in our model.

Comparing the phase diagram with the calculated LL structures, it can be seen, that the α' and β'-transitions correspond to the depopulation of the $(0, \uparrow)$ and $(-1, \downarrow)$ LL at 52.3 and 54.2 T respectively. Together with the observation of a third resistance anomaly above 60 T by Fauqúe *et al.*, we can for the first time identify these phases as CDWs. SDW, VDW and EI can be excluded as these are nesting instabilities that occur between different bands. Thus the lack of nesting possibilities above 54.2 T would prevent the formation of a third SDW, VDW or EI. This hypothesis is also supported by calculated divergences of the charge susceptibility in Figure 5.9). Here the quasi-one dimensional LL dispersion shows divergences of the charge susceptibility occurring at the Fermi momenta of the four lowest LLs. These divergences are restricted to a narrow region around the Fermi energy, hence intraband CDWs can be excluded and the observed CDWs are of the $2k_F$-type as described in Section 2.2.4.

The induced CDW gaps of both phases have been estimate by applying BCS-theory to the observed critical temperatures as $\Delta_\alpha \approx 1.5\,\text{meV}$ and $\Delta_\beta \approx 1.0\,\text{meV}$ for the α and β-phase respectively.

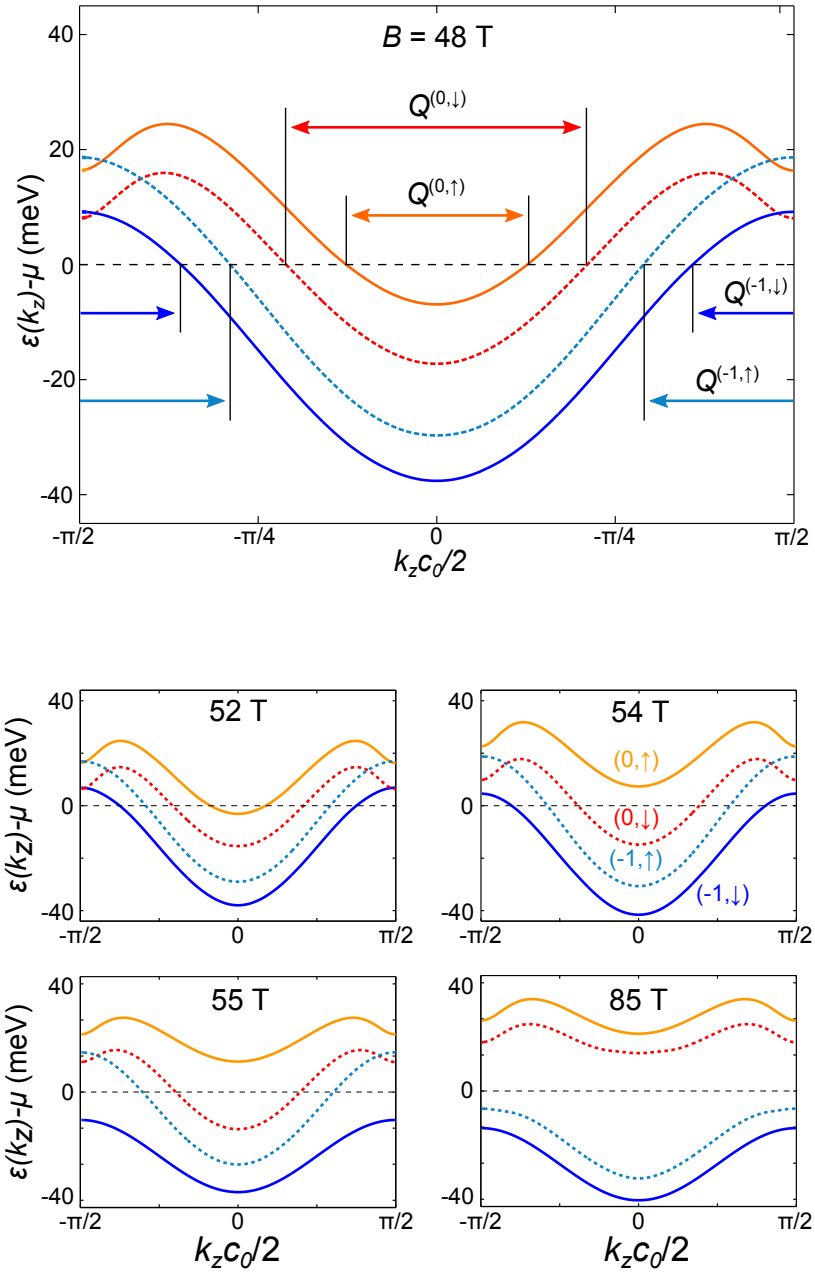

Figure 5.8: k_z-dependence of Landau level structure of graphite in the magnetic quantum limit along the HKH-edge of the hexagonal Brillouin zone. The arrows indicate the nesting vectors in the electron and hole-like Landau levels.

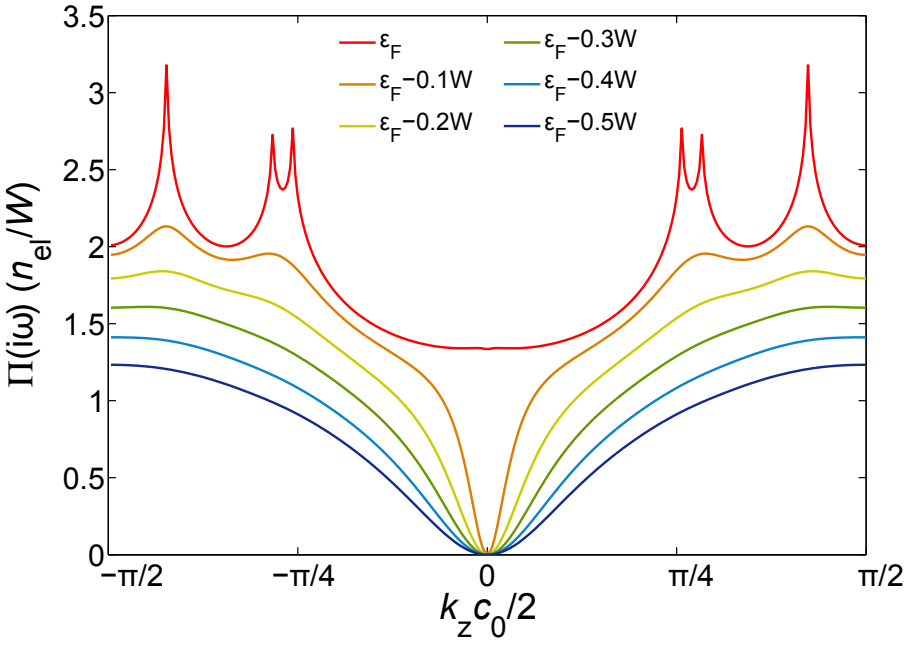

Figure 5.9: Quantum limit charge susceptibility of graphite at 48 T: The graph shows the k_z dependence of the charge susceptibility of graphite along the HKH-edge of the hexagonal Brillouin zone for energies between the Fermi energy ϵ_F and the bottom of the $n = 0$ and $n = -1$ Landau levels, where the band width $W = 40\,\mathrm{meV}$.

By plotting the magnetic field dependence of the calculated CDW nesting vectors (Fig. 5.10), it can be seen that the nesting vectors within all four LLs are continuously decreasing with magnetic field. This is due to the upward and downward shift of the $n = 0$ electron-like and $n = -1$ hole-like LLs through the Fermi energy with increasing magnetic field. At 52.3 and 54.2 T the bottom of the $(0, \uparrow)$ and top of the $(-1, \downarrow)$ LL pass through the Fermi energy leading to their depopulation and vanishing of the associated CDWs. The vanishing of the CDWs is reflected in the magneto-resistance by two distinct resistance drops. The sudden vanishing of the nesting vector and observable resistance hysteresis around $B_{\alpha'}$ and $B_{\beta'}$ (Fig. 5.3) indicate a first order character of these transitions.

The onset of both CDWs, on the other hand, is described by the BCS-like YF-theory for the critical temperature, where the magnetic field dependence of the

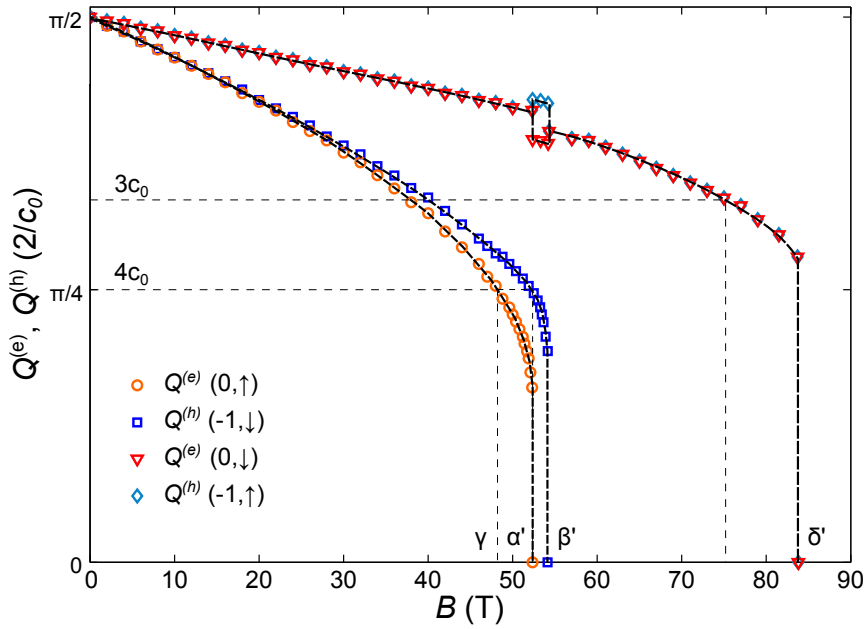

Figure 5.10: Fermi and charge-density wave nesting vectors in the quantum limit of graphite: The graph shows the magnetic field dependence of the Fermi wave vectors of the lowest four Landau Levels in graphite up to 90 T. The dashed lines mark the commensuration of the respective Landau level charge-density waves with the graphite lattice.

interaction constant leads to the observed exponential magnetic field dependence [183]. Here the higher band width of the $(0,\uparrow)$ LL compared to the $(-1,\downarrow)$ LL causes the higher critical temperature of the α-phase compared to the β-phase. The higher band width is also reflected in the higher T^*-value in the YF-theory fits.

In addition to the onset and vanishing of the α and β-phase, the magnetic field dependence of the Fermi momenta in Figure 5.10 shows that both nesting vectors become commensurate at 48 and 52 T respectively. The commensuration of the α-phase CDW at 48 T causes the γ-transition at 47.1 T. The commensuration of the β-phase CDW, however, is masked by the simultaneous collapse of the α-phase. Here it is believed that the much weaker signature of α'-transition compared to β' can be explained by a cancellation of a resistance increase due to the commensuration of the β-phase and simultaneous resistance decrease due to the collapse of the α-phase.

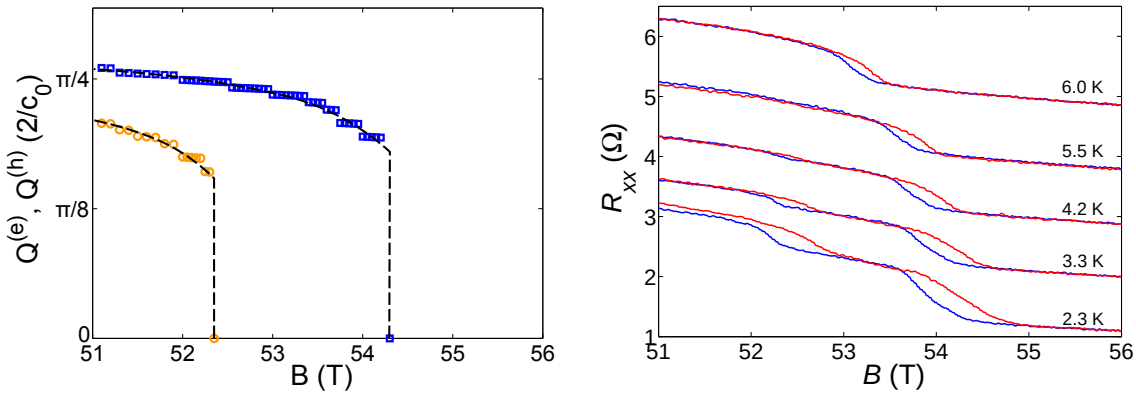

Figure 5.11: The left graph shows a close-up of Fig. 5.10 around the 1st-order α' and β' transitions. The right-hand side graph shows the according magneto-resistance hysteresis observed around these fields. Here red curves mark magnetic field up-sweeps and blue curves down-sweeps.

Above 54.2 T only the $(0,\downarrow)$ and $(-1,\uparrow)$ LL remain occupied. The imposed charge neutrality in our model forces the sum of all electron-like Fermi momenta to be equal to the sum of all hole-like Fermi momenta. This condition leads to the splitting of the $(0,\downarrow)$ and $(-1,\uparrow)$ nesting vectors between 52.3 and 54.2 T and their equality above. Thus the third CDW-state observed by Fauqúe *et al.* is doubly degenerate and gaps both the $(0,\downarrow)$ and $(-1,\uparrow)$ LL simultaneously with the same CDW-nesting vector.

By comparing the observed in-plane resistance anomalies with the calculated magnetic field dependence of the four lowest LLs, it was possible to identify the observed phase transitions as the onset, commensuration and vanishing of CDWs in the four lowest LLs. Furthermore it was possible to ascribe the phases to individual LLs. The absence of the CDW-signature, associated with the $(0,\downarrow)$ and $(-1,\uparrow)$ LLs, in-plane transport, however, remained unclear.

The answer to this question, lies within the surface and bulk states in the magnetic quantum limit. So far the entire discussion was based on the bulk LL-structure and induced CDWs and missed the crucial role of surface states for the electrical transport.

Below the onset field of the α-phase electrical current is mainly transported

through the bulk of the sample and surface states play only a minor role. The opening of the CDW-gaps and depopulation of bulk LLs at higher fields, eliminates these conduction channels and eventually results in a bulk insulator. On approaching the sample edge, however, the bulk LL dispersion is shifted towards higher energies, leading to the collapse of the associated CDWs and crossing of deep lying hole-like LLs close to the sample edge. In a fully gapped bulk or bulk insulator, these surface states remain conductive and the sample is in a quantum Hall state [186].

Below 52.3 T graphite is characterised by two gapped and two ungapped bulk LLs and four surface states. Here conduction is equally carried by the remaining bulk and surface states. Both the in and out-of plane transport are thus sensitive to changes in the bulk LL structure. Above 54.3 T, where the $(0, \uparrow)$ and $(-1, \downarrow)$ bulk LLs vanished and the $(0, \downarrow)$ and $(-1, \uparrow)$ LL are gapped, conduction is entirely carried by surface states. Due to the different surface penetration depth of these states, spin-up and down channels are spatially separated, resulting in ballistic transport along the sample edge perpendicular to the magnetic field. In this regime, the in-plane transport becomes independent from the bulk LL structure and looses its sensitivity to the opening of CDW gaps or crossing of bulk LLs. At the same time the out-of plane transport remains diffusive as it is governed by interlayer hopping processes, between graphene sheets [187, 188]. It is this difference between the ballistic in-plane and diffusive out-of plane transport that explains the absence of the third CDW signature in the in-plane transport.

Furthermore, as it can be assumed that the Fermi velocities of all surface states are different, the resulting edge current shows a finite spin imbalance. The resulting edge current is therefore chiral due to the dominance of one spin-species. This is in particular true where the number of spin-up and down surface states are not equal, as is the case above 54.2 T.

5.4 Point-Contact Spectroscopy

Point-contact spectroscopy is a powerful technique to probe the local density-of-states and excitation spectrum in metals [189, 190, 191]. It is therefore a suitable technique to measure the opening of a putative CDW gap in graphite.

Electrons which are accelerated by an electric field across a narrow contact, i.e. a point-contact, with dimensions smaller than the inelastic electron mean-free path, enter the adjacent metal ballistically at an elevated energy with respect to its Fermi energy. The resulting point-contact current might described by a simple tunneling model [192]:

$$I \propto \int g_1(\epsilon) g_2(\epsilon + eV) \left[f_{\mathrm{F}}(\epsilon) - f_{\mathrm{F}}(\epsilon + eV) \right] \mathrm{d}\epsilon. \tag{5.12}$$

in which the current is proportional to the density-of states $g_1(\epsilon)$ and $g_2(\epsilon)$ either side of the contact. In electronically non-trivial systems the energy dependence of the density-of states leads to a strong non-linearity of the $I(V)$-characteristics, i.e. non-ohmicity of the point-contact. Such injected non-equilibrium states subsequently decay by the emission of phonons, magnons and other excitations. In the absence of these excitations, i.e. relaxation, injected electrons lead to the macroscopic population or saturation of the non-equilibrium state and the point-contact current vanishes. It is therefore apparent that the point-contact spectrum not only depends on the density-of-states but also the excitation spectrum of the metals. Inelastic scattering processes, like the excitation of phonons, are incorporated into the point-contact conductivity by the Eliashberg function, which connects the phonon or magnon spectrum $F(\omega)$ to the second derivative of the point-contact conductivity [190]:

$$\frac{\mathrm{d}^2 I}{\mathrm{d}V^2} \propto -\alpha F(eV). \tag{5.13}$$

By measuring the bias voltage dependence of the differential conductance it is therefore possible to infer information about the density-of-states and excitation spectra of the point-contact metals.

Point-contacts with short electronic mean free paths or large dimensions on the

other hand, will be governed by scattering of electrons within the contact. Here the energy distribution of the injected electrons broadens, resulting in an ohmic contact. Point-contacts in this limit are called "thermal" contacts, as inelastic scattering induces strong local heating of the contact and sample. Where the electron mean free path and contact dimensions are equal the contact is in its Knudsen regime, which connects the ballistic and thermal limit. A good measure for the effective dimensions of a contact is its conductance. Here the conductance can be characterised by the number of conductance quanta $\sigma_0 = 2e^2/h \approx 7.75 \times 10^{-5}\,\mathrm{S}$, i.e. the number of single electron conductance channels. Generally a low conductance corresponds to a small contact.

In order to directly measure the opening of the CDW-gap in graphite, point-contact spectroscopy measurements were performed at the Dresden High Magnetic Field Laboratory. Initially a series of low temperature, low magnetic field spectra were measured as reference and proof of principle for the pulsed field measurements. A new pulsed magnetic field point-contact spectroscopy technique was developed to access the magnetic field range required to induce the CDW-instabilities [193].

The following sections are describing the point-contact spectra of a polycrystalline Madagascan graphite and exfoliated Grafoil sample measured in low static and high pulsed magnetic fields. For a description of the technique please see Appendix C.

5.4.1 Low Field Spectra

Low field, low temperature point-contact spectra of graphite were measured in a Quantum Design PPMS using a home made point-contact spectrometer (see Appendix C.1) [166]. Initial experiments were performed on a fixed point-contact spectrometer, which used a tripod-like construction to position a sharpened aluminium needle over the graphite sample. Later experiments used a more sophisticated setup containing three piezo-actuators to allow for the *in situ* adjustment and positioning of the point-contact (see Appendix C.1). The point-contacts in these setups were established by placing an electrochemically etched aluminium or tungsten needle onto the surface of the sample. This type of point-contact is referred to as spear-anvil point-contact.

Using a wet chemical etching technique we achieved aluminium tip radii of a few

micrometers (see Appendix C.2), which is of the order of typical electron mean-free paths in aluminium. By fine tuning the position of the needle, it was possible to alter the contact resistance over three orders of magnitude from about 10 Ω to 10 kΩ.

By using different materials for the sample and needle the resulting point-contact spectrum is a convolution of the two individual homocontact spectra. Homocontacts use the same material for both parts of the point-contact. Since the semimetallic graphite has a rather small bandwidth and Fermi surface compared to aluminium, electrons transiting from one side of the constriction to the other experience a large Fermi momentum mismatch. Like in classical optics this difference of the two momenta imposes a minimal scattering angle for electrons passing through the constriction. Electrons with smaller scattering angles are reflected back into the original electrode at the interface. The critical momentum k_c of an electron passing the constriction and the associated minimal scattering angle $\theta_{\min}$ are [194]:

$$\theta_{\min} = 2\sin^{-1}\left(\frac{k_c}{k_{\mathrm{F,Al}}}\right) \qquad \text{with:} \qquad k_c = \sqrt{k_{\mathrm{F,Al}}^2 - k_{\mathrm{F,Gr}}^2} \tag{5.14}$$

Considering the c-axis injection of charge carriers and the associated Fermi momenta of graphite and aluminium, we obtain a minimal scattering angle of about 145^o. Here we use $k_{F,Gr} = \pi/2c_0 = 4.7\,\mathrm{nm}^{-1}$ corresponding to contact point of the cigar shaped electron and hole pockets in the graphite BZ as well as $k_{F,Al} \approx \overline{\Gamma X} = 2\pi/2a_0 = 15.5\,\mathrm{nm}^{-1}$, which is a good estimate for the Fermi momentum on aluminium [195, 196]. The large Fermi momentum mismatch and scattering angle leads to a strong damping of the non-ohmicity and negligible influence of the aluminium spectrum to the overall point-contact spectrum [194]. Examples of graphite and aluminium homocontact spectra can be found in [197, 192].

Static field point-contact spectra are measured using a dc+ac bias method. Here a dc-bias voltage with an ac-modulation is produced by a Stanford Research SR830 lock-in amplifier in conjunction with an external voltage adder circuit (see Appendix C). The in-phase component of the resulting ac-bias current and voltage were measured using a lock-in amplifier. Similarly the dc-biases were measured using the dc-inputs of the lock-in amplifier. Typical parameters for the static field measurements were: an ac-excitation of 0.5 mV at a frequency of 15.16 kHz and bias step width of 0.5 mV. Depending on the contact resistance a 100 or 1000 Ω serial

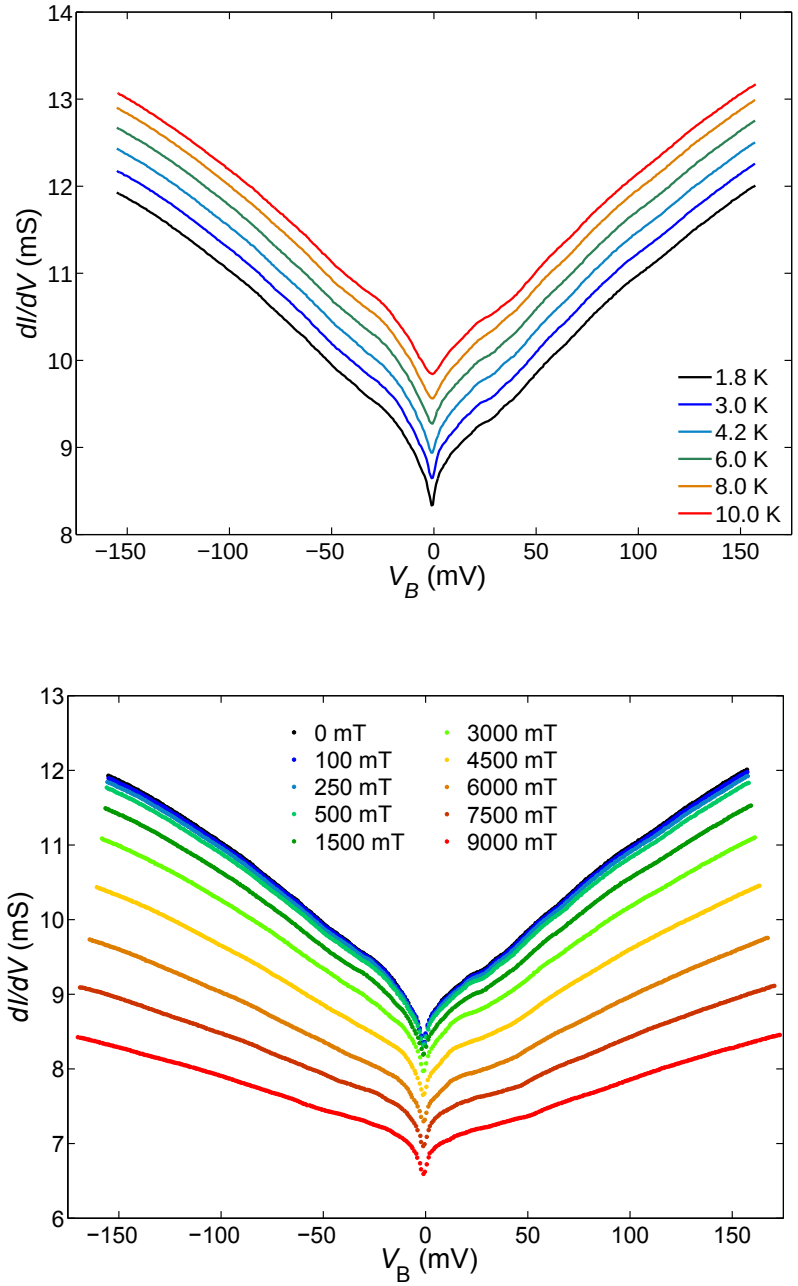

Figure 5.12: The upper graph shows the zero-field temperature dependence of the differential conductance spectrum of a 120 Ω aluminium-Madagascan graphite point-contact. Data are offset by 0.25 mS relative to the 1.8 K curve for clarity. The lower graph shows the magnetic field dependence of the same contact at 1.8 K.

Table 5.1: Phonon modes and energies in graphite as taken from [199]. A and O referre to accoustic and optical modes, where Z, L and S are the associated out-of plane, in-plane and shear modes.

Phonon Branch	ZA	ZA	ZO	SA	ZO	LA	SO	LO
Energy (meV)	15	59	78	77	109	124	177	200

shunt resistor was used to measure the bias current.

Figure 5.12 shows the low temperature point-contact spectrum of a Madagascan graphite-aluminium point-contact. The sharpness of the observed spectrum is an indication that the contact was in its ballistic regime. The zero-bias resistance of this 120 Ω contact is equivalent to 100 conductance quanta demonstrating a small contact area.

The overall shape of the Madagascan graphite point-contact spectrum follows an almost symmetrical v-shape centered around zero-bias. This v-shape arises due to the peculiar band structure and density-of-states of graphite [198]. The touching hole and electron-bands in graphite lead to a van Hove singularity with vanishing density-of-states at the Fermi energy. McClure calculated the density-of-state based on the SWM-model (see Sec. 2.2.3) [32]. Here the hole-like ϵ_1-band and electron-like ϵ_2-band give rise to a v-shape of the density-of-states at high energies, whilst the two ϵ_3-bands induce a slight deformation of this v-shape within the bandwidth of ±20 meV. Sampling this v-shaped density-of-states of graphite with the almost constant metallic density-of states of aluminium leads to the v-shape observed in the point-contact spectrum [198].

The v-shaped spectrum of Figure 5.12 is superimposed by additional features. These superstructures originate from phonon modes in graphite. Vitali *et al.* compared their point-contact spectra of HOPG to DFT-LDA phonon spectrum calculations and found a good agreement between dips in the second derivative of the point-contact spectrum with their calculated phonon modes [199]. A table of their calculated energies of the phonon modes is shown in Table 5.1.

Using the Eliashberg function Eqn. 5.13 each phonon mode induces a minimum in the second derivative of the I(V)-characteristic, i.e. flattening of the differential conductance at the energy of the phonon mode and leads to the modulation of the v-shaped point-contact spectrum as shown in Figure 5.12. The observed energies

are in good agreement with the calculated phonon energies Table 5.1.

As can be seen the observed zero-bias anomaly as well as superstructures are weakening with increasing temperature. This effect can be related to thermal broadening of the energy distribution of the electrons passing the point-contact. Hence formerly sharp energy features appear smeared out. Furthermore, we observe a general flattening of the point-contact spectrum on increasing the magnetic field. At the same time the zero-bias conductance drops significantly. The general decrease of the conductance in an magnetic field field can be explained by the sizable magneto-resistance in graphite. The flattening of the point-contact spectrum, however, remains an open question.

Point-contact spectra of aluminium-Grafoil spear-anvil hetero-point contacts were measured in the same temperature and magnetic field range. The measured spectra were equivalent to the point-contact spectra shown for Madagascan graphite and are therefore not shown. In general, point-contact spectra of graphite were highly reproducible, given a similar zero bias resistance, speaking for the uniformity of our point-contact needles and samples.

5.4.2 Anomalous Spectra and Possible Superconductivity

During our measurements with aluminium-Grafoil contacts, we found an "anomalous" point-contact spectrum (see upper curves in Fig. 5.13). At large bias voltages the point-contact spectrum of Grafoil is identical to the v-shape observed in Madagascan graphite. At lower bias voltages, however, a broad plateau appears at lowest fields, spanning 4.2 meV. On applying a magnetic field this low-bias plateau, is suppressed and eventually vanishes at around 450 mT. Further measurements, trying to measure the precise magnetic field and temperature dependence of this signature, were interrupted by a jump of the point-contact (see lower curves in Fig. 5.13). Here mechanical vibrations are likely to have caused the needle to jump to a neighboring position.

Efforts to reproduce the plateau signature with other contacts failed so far. A complete list of all point-contacts measured can be found in Table C.1. Here measurements with equivalent aluminium and tungsten needles were performed on Grafoil, Madagascan graphite and quasi-two dimensional graphite (KDG).

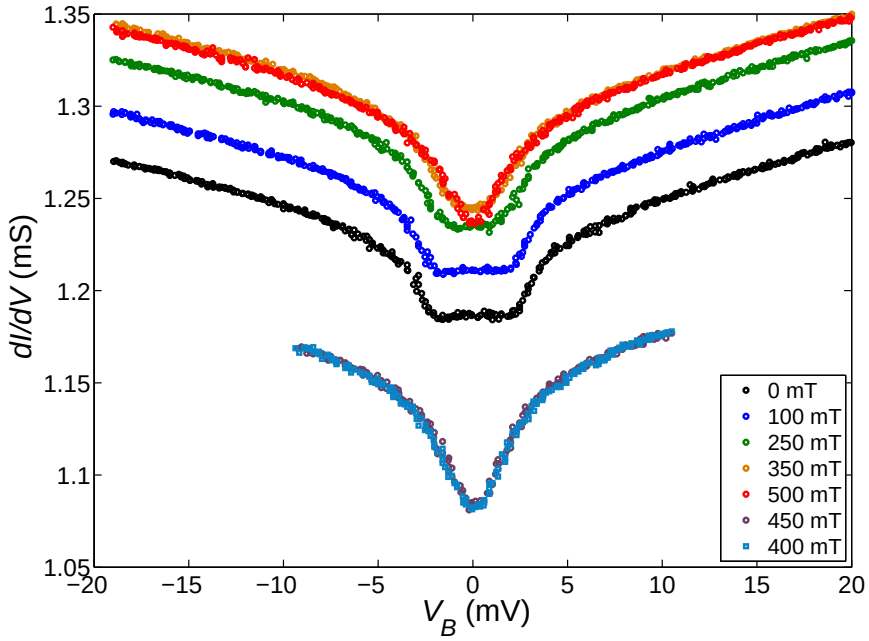

Figure 5.13: Anomalous point-contact spectra of Grafoil: The graph shows the magnetic field dependence of a 830 Ω aluminium-Grafoil point contact measured at 1.8 K. The upper curves show a distinct gap of up to 4.2 meV closing with increasing field. The curves have been offset by 0.1 S/T for better visibility. The zero-bias conductance of the upper curves is equivalent to 15 conductance quanta. The lower curves show spectra in the same field range after the contact jumped.

Plateaus as observed in the spectra of Figure 5.13 are usually attributed to gaps in the electronic band structure where the density-of-states is zero [200]. Figure 5.14 shows the putative gap size as extracted from the crossings of the pseudo-linear behaviour either side of zero-bias with the conductance plateau. The gap sizes and magnetic fields in Figure 5.14 have been renormalised by the zero-field gap $\Delta = 2.1\,\mathrm{meV}$ and critical field of 450 mT.

The particular magnetic field dependence of this putative gap suggests a connection to superconductivity, where the superconducting gap can be suppressed by applying a large magnetic field. As can be seen in Figure 5.14) the experimentally determined gap sizes follow the magnetic field dependence of a fully field penetrated

BCS-superconductor, i.e. where the superconducting domains are much smaller than the London penetration depth [201, 202, 110]. In Figure 5.14 the theoretical magnetic field dependencies of field penetrated superconductors are plotted for different ratios of the superconducting domain size d and London penetration depth λ. In the presence of a magnetic field the superconducting order parameter is increasingly suppressed with magnetic field. As the magnetic field penetrates a superconductor only on the length scale of λ these effects become prominent when the superconducting domain size and London penetration depth are of equal size.

As can be seen our data is best fit by the theoretical curve for $d/\lambda \approx 0$, meaning that the apparent superconducting domains are much smaller than the London penetration depth and the Meišner effect is almost completely suppressed.

If the measured signature, indeed, stems from a BCS-superconductor then its critical temperature can be estimated by applying the BCS-formula: $\Delta_0 = 1.764 k_\mathrm{B} T_c$ to the measured zero-field gap. Using $\Delta = 4.2\,\mathrm{meV}$ we find that the critical temperature superconducting state is $T_c \approx 14\,\mathrm{K}$.

Even though the flat region around zero bias might be interpreted as conductivity increase compared to the underlying v-shape, there is no clear indication of Andreev reflections in our spectra [203]. In normal metal-superconductor junctions, electrons in the metal whose energy is within $\pm\Delta$ of the Fermi energy are not allowed to enter the superconductor, Cooper pairs on the other hand are. Thus these electrons are reflected back into the normal metal as a hole under the generation of a Cooper pair at the interface. Due to the additional hole current, the resulting conductivity of such a junction therefore increases within $|V_\mathrm{B}| \leq \Delta$. This phenomenon was later analytically described by the Blonder-Tinkham-Klapwijk formula, which can be used to determine the barrier strength and superconducting order parameter symmetry [200].

If this is indeed a BCS-state, the question arises, which of the two involved materials (aluminium or graphite) could host superconductivity. Aluminium is known to become superconducting at a critical temperature and field of $T_c = 1.18\,\mathrm{K}$ and $B_c = 10.5\,\mathrm{mT}$, which is far below the temperature and magnetic field range studied here. Previous measurements on nanogranular aluminium films have shown that this critical temperature and field can be strongly enhanced by nanostructuring aluminium up to 2.4 K and 500 mT [204, 205, 206]. Similar nanoclusters might also

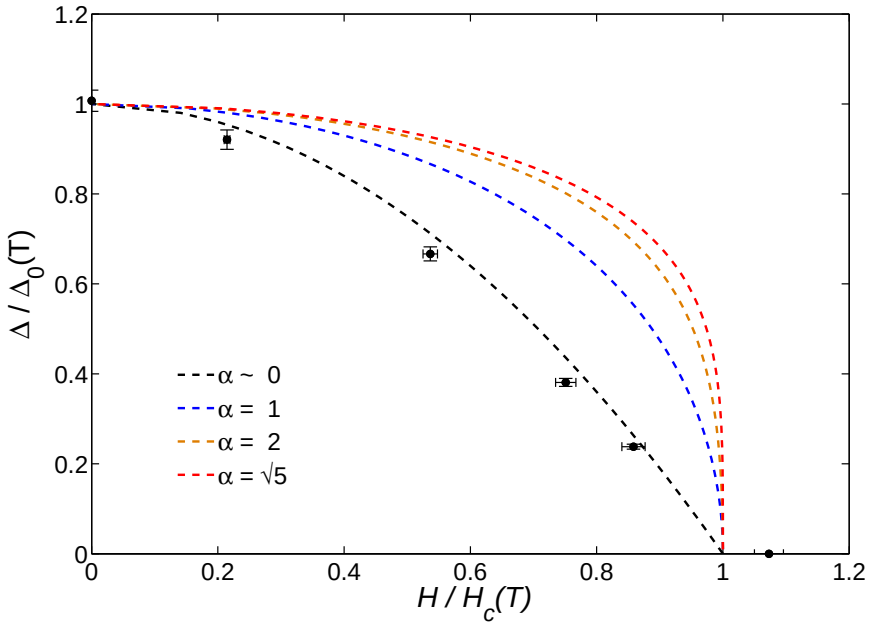

Figure 5.14: Magnetic field dependence of the point-contact gap: The graph shows the magnetic field dependence of the point-contact gap Δ at 1.8 K (see Fig. 5.13) renormalised by its zero-field value $\Delta_0(T)$. The dashed lines are theoretical predictions for BCS-superconductors in the limit where the London penetration depth is larger or equal than the superconductor thickness $\alpha = d/\lambda$ [201, 202].

be embedded in the alumina surrounding our aluminium needles. The critical fields reported in the nanogranular films would agree with our findings. The superconducting gap, however, is a factor seven higher than the ones observed in the nanocluster films ($\Delta \approx 300\,\mu$eV) and disappears when the needles moves to another position. Therefore we believe that aluminium superconductivity can be excluded.

Over the past five years a new idea has been proposed by P. Esquinazi *et al.*, who have argued that graphite interfaces can host superconductivity [207, 208, 209]. Backed up by band structure calculations it is proposed that graphite interfaces and in particular zig-zag edges can give rise to flat bands close to these defects [210]. In flat bands the effective mass and density-of-states are strongly enhanced enabling superconductivity at moderate temperatures [211, 209].

Given that Grafoil is a highly inhomogeneous graphite, with a large number of crystal defects and dislocations, we believed that the superconducting gap observed in our experiment is caused by a special crystal boundary, interface or defect. It is therefore plausible that finding such a "superconducting hot spot" is serendipity and hard to reproduce.

5.4.3 Point Contact Spectroscopy in Pulsed Magnetic Fields

In order to measure the magnetic field driven CDW-gap in graphite a new point-contact spectroscopy technique was developed. Previous point-contact methods were based on dc+ac techniques as described in the previous section and limited to static magnetic fields up to 45 T. In pulsed magnetic fields (see Appendix B) averaging, like in static field methods, is not possible. Here a more time efficient technique had to be devised.

The solution to this problem was the use of a quasi-dc technique (see Appendix C.3) in which the bias voltage is swept at a frequency of a few kiloherz. A high sampling rate of the bias voltage and current measurements ensures a high bias voltage resolution and enables averaging within each bias sweep. To reduce the noise even further, multiple subsequent bias sweeps were averaged together.

Pulsed field point-contact experiments were performed at the Dresden High Magnetic Field Laboratory in a KS3-type coil with a maximum magnetic field of 70 T and a overall pulse length of 150 ms using a home-made spear-anvil point-contact spectrometer (see Appendix C.3) [193].

We measured the point-contact spectra of Madagascan graphite and Grafoil samples in magnetic fields up to 50 T. The 4.2 K spectra of the Madagascan and exfoliated graphite are shown in Figure 5.15 and 5.16. Both contacts were established at room-temperature and gradually cooled down to 4.2 K. The contact resistances were monitored during the entire cool down by a digital voltmeter. Several attempts were needed to achieve a stable contact in the desired resistance range. However only a minority of contacts changed their resistance or disconnected during cooling. A larger fraction of contacts were unstable against applying large magnetic fields. In these cases the Lorentz force exerted on the point-contact during a magnetic field pulse forced the needle into another position and changed the contact resistance.

Like at lower fields, the high-field point-contact spectrum of Madagascan graphite shows a pronounced v-shape. Due to additional vibrational and electrical noise in the pulsed field setup, the high field spectrum is strongly rounded. The zero bias anomaly as well as the phonon induced superstructures are therefore strongly suppressed. The observable fast oscillatory modulations in the point-contact spectra (Fig. 5.15 and 5.16) are artifacts of a parasitic rectangular waveform noise signal, which coupled into our experiment via the common building ground. As was already seen in the low field measurements, the overall spectrum shows a strong reduction of the zero-bias conductivity and flattening of the v-shape towards higher magnetic fields. Unfortunately the elevated noise level meant that the opening of the millielectronvolt CDW-gap could not be resolved.

The point-contact spectrum of Grafoil (Fig. 5.16) shows much stronger features. The overall v-shape of the spectrum changes around 35 T. Below 35 T the spectrum follows the known v-shape. Above 35 T, the spectrum flattens and develops a shoulder either side of the zero-bias minimum. By analysing the second derivative of the $I(V)$-characteristic (Fig. 5.17), a clear break can be identified. Starting from zero bias a new minimum develops in the second derivative at 35 T (see dashed line) pro-

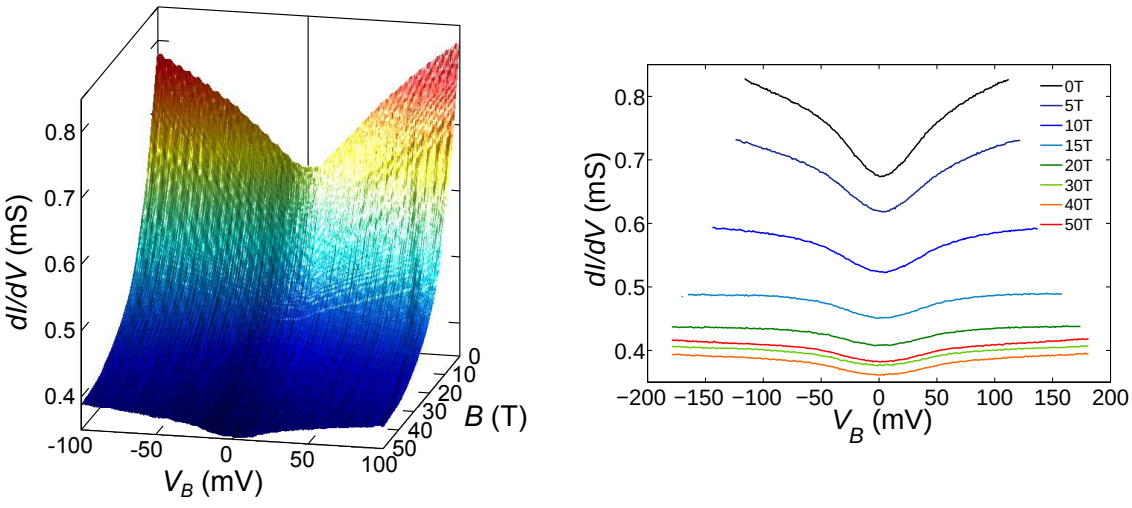

Figure 5.15: The graphs show the 4.2 K high field point-contact spectrum of an aluminium-Madagascan graphite 1.8 kΩ contact up to 50 T.

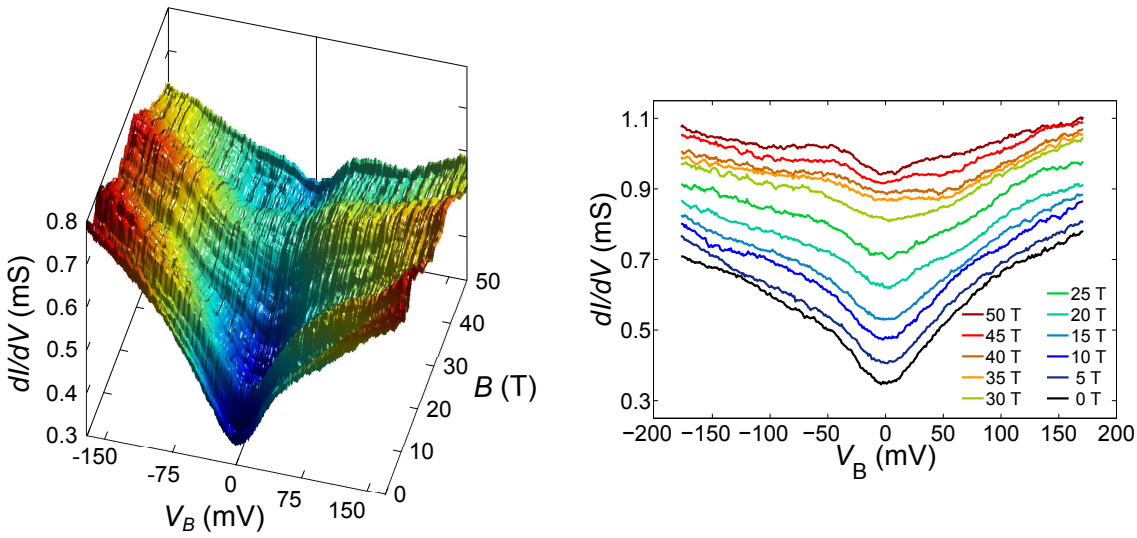

Figure 5.16: The graphs show the 4.2 K high field point-contact spectrum of an aluminium-Grafoil 3.2 kΩ contact up to 50 T. The spectra on the right-hand side have been offset by 50 μS relative to the zero-field spectrum.

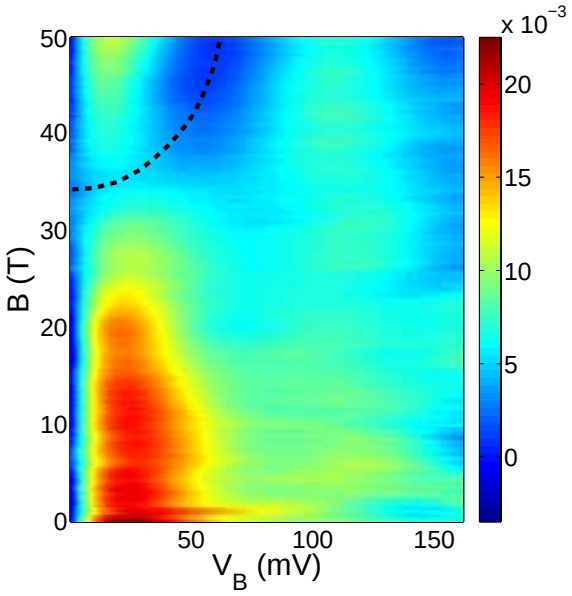

Figure 5.17: The graph shows the second order derivative of the $I(V)$-characteristic of na aluminium-Grafoil point-contact at 4.2 K.

gressing towards 70 meV at highest fields. This new minimum is likely to be caused by a lattice deformation due to the CDW. Even though the CDW is of purely electronic origin, its charge modulation will weakly influence the structure and phonon spectrum of graphite. However, the electron-phonon coupling is extremely weak in graphite and the observed minimum in the point contact spectrum might be an artifact due to the onset of the resistance anomaly.

In their interlayer tunneling spectroscopy Latyshev *et al.* found a strong suppression of the zero-bias conductance and flattening of the overall v-shape with increasing magnetic field in their HOPG mesostructure [212]. Their tunneling spectrum showed the emergence of two pronounced shoulders at ± 35 meV, which were associated with the opening of a pseudo-gap above 17 T. At present it is unclear whether the pseudo-gap measured by Latyshev is related to the presumed new phonon mode in our measurements.

Due to the high noise levels and mechanical instability of point-contacts, we were unfortunately not able to observe the opening of the CDW gap in graphite. Further improvements are needed to resolve the stability and noise problems and to advance the pulse-field point-contact technique into the submillivolt resolution range. A second point-contact spectrometer with *in situ* adjustability of the contact and better shielding showed a significant improvement of the signal-to-noise ratio, at the cost of lower contact stability. At the moment a fundamentally new design is needed to address the issues of point-contact stability in pulsed magnetic fields.

6 Conclusions and Outlook

In this thesis strongly correlated two- and quasi-two dimensional Fermi systems have been studied under extreme conditions. We analysed the ultra-low temperature behavior of two-dimensional ^{3}He and established the high field phase diagram of graphite.

For the study of two-dimensional ^{3}He a new SQUID-NMR set-up was built and run on an existing nuclear demagnetisation refrigerator requiring a significant reconstruction. Composite ^{3}He films were grown onto a chemically exfoliated graphite substrate, i.e. Grafoil. The Grafoil was preplated with a non-magnetic monolayer of ^{4}He to minimise the influence of substrate inhomogeneities and the corrugation potential originating from the graphite honeycomb lattice on the two-dimensional Fermi system. At low ^{3}He densities this system behaves like a weakly correlated Fermi fluid. On increasing the film density, correlations within the fluid increase and the system eventually solidifies. The increase of these correlations and subsequent solidification were measured by means of the magnetisation, frequency shift and relaxation times of this nuclear spin system. The temperature dependence of the two-dimensional fluid magnetisation was analysed by a highly successful form due to Dyugaev, which interpolates from the classical to the quantum degenerate regime. The characteristic temperatures of this Dyugaev formula, T_F^{**}, were used to determine the effective masses of the helium fluid. These effective masses show a divergence at a critical ^{3}He film density of $7.1 \pm 0.1\,\mathrm{nm}^{-2}$. The inverse effective mass, which starts at about one in the limit of zero density, goes almost linearly to zero at the critical density throughout the entire fluid phase. The observed frequency shifts and fluid-solid cross-over in the phase coexistence region, hint towards a gradual growth of the insulating solid on approaching the critical density. The observed mass divergence and phase coexistence have been interpreted as a Wigner-Mott transition, the analog of a one-dimensional $4k_\mathrm{F}$-density wave instability in systems with high on-site repulsion. These density waves break the translational

symmetry of the Fermi fluid, leading to a Brillouin zone folding and generation of an exactly fully filled lower Hubbard band. This type of density driven metal-insulator transition is also referred to as Wigner-Mott transition. In systems with strong periodic lattice potentials the nesting vectors of these density waves do not grow with the Fermi momentum as in isotropic systems, but are pinned to commensurate lattice vectors. In the case of two-dimensional ^{3}He, the commensurate structure is the putative triangular $\sqrt{7/4} \times \sqrt{7/4}\,\mathrm{R}19.1^o$ superlattice. Based on the ultra-low temperature magnetisation data and its Fermi fluid like behaviour, we have evidence that the geometrically and magnetically frustrated triangular lattice solid hosts a gapless quantum-spin liquid with a characteristic spinon Fermi temperature of 200 μK. However our measurements did not reach low enough in temperature to conclusively rule out a magnetically ordered ground state.

The second system studied in this thesis is the quasi-two dimensional electron system graphite, which can be visualised as an infinite number of ABAB stacked graphene sheets. The band structure and resultant thermodynamic properties of graphite are described by the Slonczewski-Weiss-McClure model. In this model two degenerate electron- and hole-bands give rise to an electron and two hole-Fermi surfaces in each HKH-edge of the hexagonal Brillouin zone. The electrical transport of graphite is governed by both charge carrier species. On applying a magnetic field electrons are magnetically frozen-out, leading to a shifting charge carrier balance in graphite and hence sign change of the Hall coefficient. By exfoliating graphite, we increased the defect concentration and scattering rate leading to a lower magneto-resistance and increased magnetic freeze-out as evidenced by the magneto- and Hall-resistance measurements.

On applying magnetic fields larger than 15 T parallel to the crystallographic c-axis, graphite enters its magnetic quantum limit in which the band structure is described by two-spin degenerate Landau levels. The one-dimensional character of these Landau levels triggers charge-density wave instabilities within all four Landau levels. By measuring the magneto-transport in pulsed magnetic fields up to 60 T and calculating the Landau level structures, we were able to identify the observable resistance anomalies as charge-density waves in specific Landau levels. We proposed that at highest fields, where the bulk Landau levels are either gapped by the charge-density waves or depopulated by crossing through the Fermi energy, graphite becomes a

topological insulator and in particular a quantum-Hall system.

Efforts to measure the induced charge-density wave gaps directly by point-contact spectroscopy, led to the development of a new experimental technique for point-contact spectroscopy in pulsed magnetic fields and the discovery of an unusual point-contact spectrum in exfoliated Grafoil, which might be identified as a superconducting BCS-gap in the fully field penetrated limit where the superconducting domains are much smaller than the London penetration depth. The critical temperature and field of this state have been estimated as 18 K and 450 mT.

The two-dimensional ^{3}He and graphite studied in this thesis are good model systems for low-dimensional Landau Fermi liquids. As was already proposed by Peierls, Fröhlich, Overhauser and Halperin low-dimensional systems are prone to undergo Fermi surface nesting instabilities, due to their high Fermi surface symmetry. Both systems, two-dimensional ^{3}He and graphite, lower their ground state energy by the formation of charge-density waves and gapping of the associated Fermi surface. In graphite the resulting state is a one-dimensional charge modulation along the crystallographic c-axis, whilst helium develops a triangular lattice Mott insulator.

Further work on both systems will be required to resolve several outstanding questions. In two-dimensional ^{3}He the question remains whether the proposed Wigner-Mott scenario holds and whether the triangular lattice 4/7-solid hosts a gapless quantum-spin liquid. Here a new theoretical framework is needed that incorporates the dynamics and strong short range correlations in this system. Furthermore heat capacity and thermal transport measurements are desirable to test the quantum-spin liquid state against the proposed power law temperature dependencies discussed by Motrunich [29]. In graphite a series of experiments should be carried out, testing whether superconductivity can be reproduced by controlled nanopatterning. Magneto-striction and magneto-caloric measurements on the charge-density wave instability in graphite are currently performed by Behnia and Brando *et al.* trying to find thermodynamic evidence of the charge-density wave transitions and to clarify the influence of electron-phonon interactions.

7 Acknowledgements

As experimental physics and ultra-low temperature and high field experiments in particular are generally a team effort, I would like to take the opportunity and thank the people without whom this thesis would not have been possible.

First and foremost, I would like to thank my supervisor Prof. John Saunders, who gave me the opportunity to do a Ph.D. in ultra-low temperature physics in his group. John was a great source of knowledge over the last years, always open for ideas concerning new experiments and tried hard to make me a better physicist.

Secondly I would like to thank Dr. Jan Nyeki and Dr. Ben Yager, who introduced me to ultra-low temperature physics and helped me to run my SQUID-NMR experiments. Without their continuing support, this thesis would not have been possible.

Also a very big "thank you" goes to the entire technical and administrative staff, here in particular Francis Greenough, Harpal Sandu, Richard Elsom, Paul Bamford and John Taylor for supplying us with liquid helium and vital parts for our experiments, as well as Tim Simmonds, Ian Murray, Andy Alway and Carmela Froggatt for dealing with various administrative and technical queries.

Furthermore, I would like to acknowledge all the people who were involved in various in house and external collaborations, in particular Aya Shibahara, Andrew Casey and Lev Levitin as well as Erik Kampert, Matthias Eschrig and Aldo Isidori for their efforts in the noise thermometry and high field graphite projects.

I would also like to thank, my fellow PhD students, here in particular Kristian Kent, George Nichols, Katie Porsch, Harriet van der Vliet and Terence Giles for sharing the pains and troubles of a PhD student and offering me the occasional helping hand.

Last but not least, I would like to thank my family and friends in Germany for their continuing support and efforts over the last years and my friends from the Old Windsor Rifle and Pistol Club for distracting me from physics every so often.

I would like to close this thesis with a rhyme by our
local German Ore Mountain poet Anton Günther:

Erscht musst diech schinden, kümmern un plogn,
nort lässt sich's Gute besser ertrogn!

First you have to slave, labour and to care,
then the good things are easier to bear!

Appendix A

The Ultra-Low Temperature Setup

A.1 New SQUID and Magnet Wiring of ND1

This section describes the newly installed SQUID and magnet wiring of the nuclear demagnetisation refrigerator ND1. A major part of the rebuild ND1 was the installation of the infrastructure for up to four SQUIDs in order to perform SQUID-NMR, magnetometry and Johnson noise and ^{195}Pt thermometry. Due to time constraints on the project only two of the planned four SQUIDs were installed and are currently in use.

SQUID Wiring

Each of the four two-stage SQUID planned to be installed on ND1 is controlled by a Magnicon XXF FLL electronic and requires a bare minimum of seven wires connecting the SQUID to the FLL electronics. Two additional wires are installed per SQUID for the optional Q-spoiler modulation. In order to minimise cross talk and electrical noise, each set of SQUID wires is run through a separate shield and is connected to its own heat sinks.

The dual channel Magnicon XXF electronics, used in our setup, were connected to our cryostat via 24-pin Lemo connectors. A vacuum leak tight room temperature break-out box with two 24-pin connectors was build to accommodate both Magnicon electronics. This break-out box is directly connected to the inside of the IVC via a $^1/_4$-inch access port of the cryostat and a OD = 10 mm flexible vacuum line. Leak tight connections between the box, the vacuum line and access port were made by a KF16 and a rubber o-ring sliding seal. The dimensions of the cables and shielding

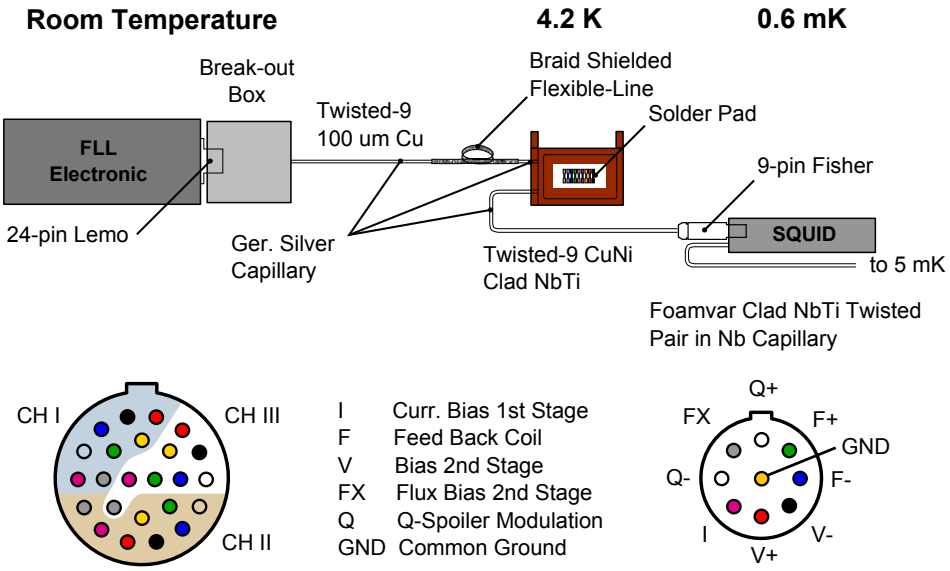

Figure A.1: The schematic shows the SQUID wiring from room temperature to 5 mK Followed by the pin out (front side of socket) and colour coding of the sockets and wires.

capillaries running through this link were limited by the inner diameter of the $^1/_4$-inch access port. Thus 1.1×0.1 mm German silver capillaries were used to shield the four sets of SQUID wiring and Q-spoiler modulation lines.

The twisted-7 cables, connecting the individual SQUIDs from room temperature to 4.2 K, were made from 100 μm colour coded copper wire. Each twisted-7 consisted of two twisted pairs, one for the feed-back coil and another one for the current and flux bias of the first and second stage SQUID and a twisted trio for the current bias of the second stage and common ground. The colour scheme of the twisted-7 cables is equivalent to the colours of the 9 and 24-pin connectors shown in Figure A.1. In order to stabilise the twisted-7s, the pairs and trios were twisted around each other and fixed with GE-varnish. A separate twisted-8 was made for the Q-spoiler modulation lines from 80 μm Constantan-wire.

Both the twisted-7s and 8s were pulled through Teflon sleeve in order to avoid mechanical damage and electrical shorts at sharp edges. 1.2×0.1 mm Teflon sleeve was stretched to an outer diameter of about 0.7 mm to fit inside the 1.1×0.1 mm

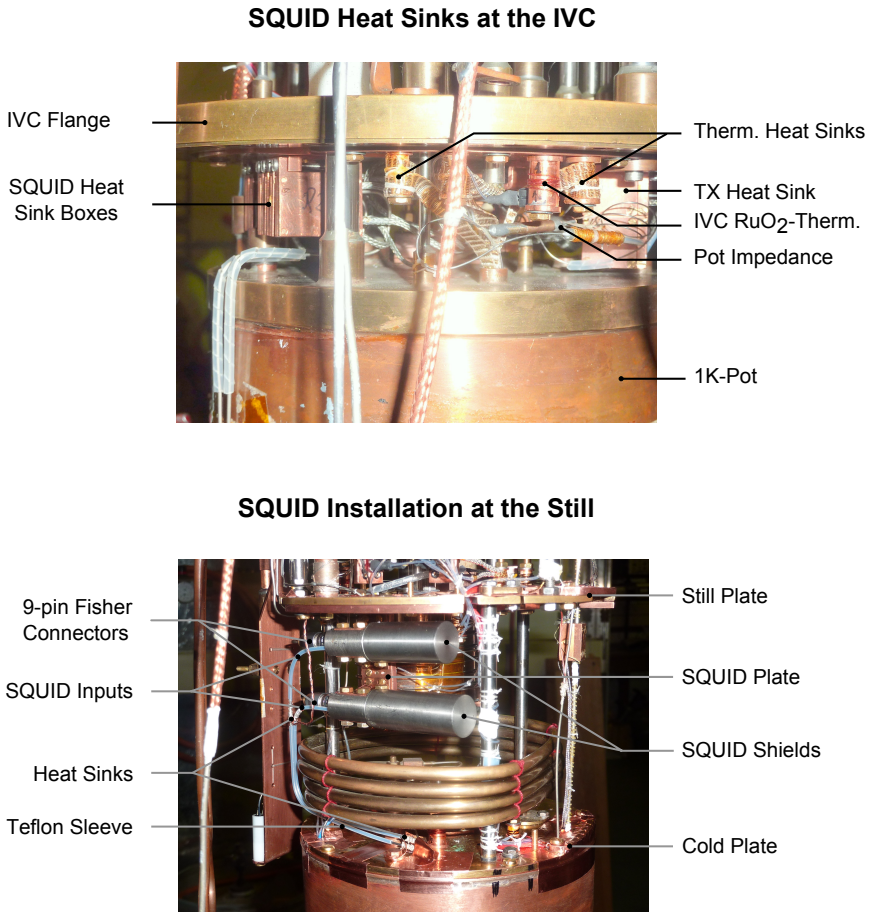

Figure A.2: The photos show the implementation of the heat sinking and SQUID mounting at the IVC and still (Photo by courtesy of Jan Nyéki).

German silver capillaries. The Teflon sleeves were pulled over the twisted-7s and 8s before the cables were pulled through the capillaries. 20 mm long Copper braids were soldered around the capillaries to thermally heat sink the capillaries to the inside wall of the $^1/_4$-inch access port. These heat sinks were located at the IVC flange and further upwards in steps of 130 mm along the access port.

Due to space limitations between the IVC flange and the 1K-pot an efficient heat sink design for the SQUID wiring had to be devised. A copper rail system was designed, which is attached to the IVC flange and has place to accommodate

five copper heat sink boxes. A picture of the heat sinks is shown in Figure A.2. This design guaranteed access to all five boxes whilst taking up minimal space. Individual boxes could be removed from the rail and worked on without disturbing other wiring. The draw back of this design was that the incoming wiring had to be flexible in order be able to move the boxes outwards. This problem was solved by using braided shields rather than rigid capillaries. Here the shield of a RG178 coaxial cable was used to replace the German silver capillary between the lower exit of $^1/_4$-inch access port and the SQUID heat sink boxes. A spare length of about 10 cm was build in to generate more flexiblity with the boxes. The shields of the in and out-going wiring were clamped to the heat sink boxes to prevent damage due to mechanical stress in the wires. In order to be able to clamp the braided shields additional 7 mm long German silver capillary pieces were soldered into the end of the braid.

Inside the heat sinks, solder pads with nine dog bone shaped contacts printed onto a thin Mylar foil were used to heat sink the wiring. The solder pads were glued to the copper heat sink box using a thin layer of Hysol 3430 [213]. Special care was taken that the in and out-going wires are soldered to the pads from the same side to avoid open wire loops.

Superconducting 106 μm CuNi-clad NbTi wire was used to connect the wiring inside the heat sink boxes to the SQUIDs mounted on the still. Here the superconducting twisted-9s (including the Q-Spoiler) were routed through the same German silver capillaries as were used above 4.2 K. In order to avoid thermal shorts between the 4.2 K heat sinks and the 1K-pot, the capillaries were wrapped in two layers of Teflon sleeve at potential contact points (see Fig. A.2). Controlled thermal links between the capillaries and the 1K-pot or still were established via oxygen annealed copper wires wound around the capillaries. The thermal contact of these wires to the capillaries was increased by a layer of silver loaded epoxy.

9-pin connectors were installed at the lower end of the twisted-9s and in the SQUID shields to simplify the exchange of SQUIDs in our setup. This way SQUIDs could simply be plugged into the setup or swapped without unsoldering their wiring. The pin out of these connectors is shown in Figure A.1. A SQUID package consisted of a standardised niobium shield with an internal Stycast 1266 former onto which the SQUID carrier was mounted and secondary heat sink for the SQUID and its wiring.

The wiring connecting 9-pin socket and internal heat sink to the SQUID was made from copper wire as the SQUID is partially thermalised through its contacts.

The input side of the SQUIDs was connected to the superconducting input circuit by niobium screw terminals which were built into the SQUID carrier. The superconducting input circuit itself was made from formvar-clad NbTi twisted pairs shielded in a 1.0×0.1 mm niobium capillary. In order to avoid pick up noise originating from vibrating wires, the twisted pairs of the input circuits were fixed with GE varnish inside the Teflon sleeves and niobium capillaries.

Magnet Wiring

In order to be able to run more persistent magnets on the cryostat three new magnet circuits were installed. The current in our magnet circuits is typically limited by the superconducting spot welds to 2.5 A. In order to supply these currents, 500 μm copper wires were routed from a room temperature break-out box at the top of the cryostat through the bath to the persistent switches. The persistent switches were mounted on an additional copper plate inside the helium bath about 200 mm beneath the IVC flange. A picture of the plate and the installed switches is shown in Figure A.3.

The persistent switches were connected to the experiments inside the IVC via a low temperature vacuum feed-through made from Stycast 2850 and 300 μm single filament Cu-clad NbTi-wire. The feed-through was from Stycast 2850 cap which was glued onto a $^1/_4$-inch stainless steel tube with attached brass bush. Six narrow holes were drilled through the cap for the NbTi-wires. The wires were stripped for the length of the feed-through to avoid vacuum leaks between the cladding and wire. After pulling the wires through the holes in the cap the inside of the feed-through was potted with Stycast 2850 and degassed for 10 minutes under vacuum. Subsequently a protective layer of Stycast 2850 was applied to the outside of the feed-through.

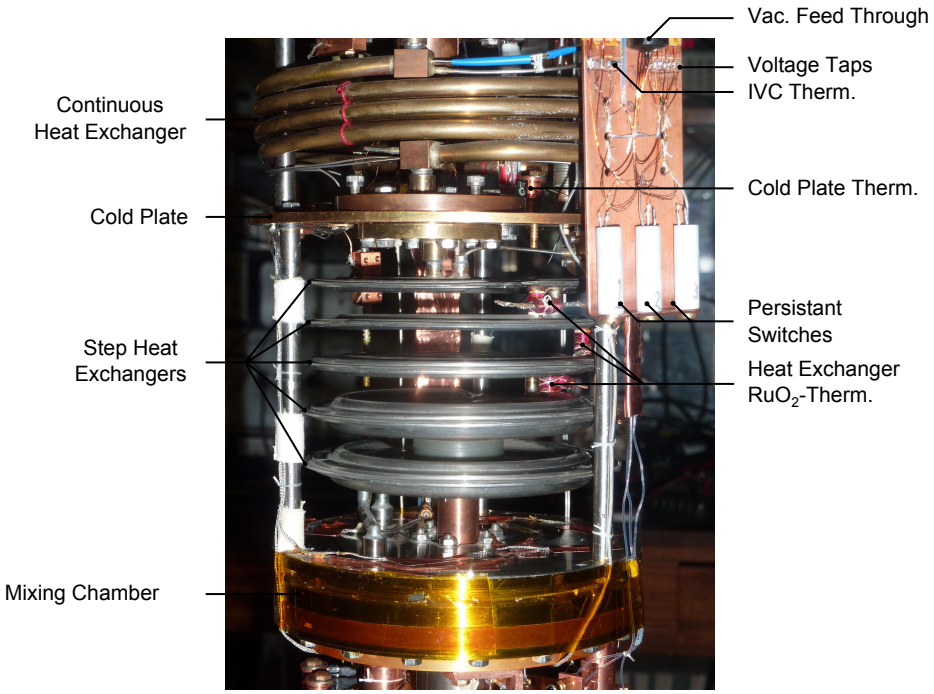

Figure A.3: The picture shows the heat exchangers of the ND1 dilution unit and the persistent switch plated located outside the IVC in the helium bath (Photo by courtesy of Jan Nyéki).

The feed-through as well as the persistent switch plate were attached to a $^1/_4$-inch copper tube which was soldered to a $^1/_4$-inch port going through the IVC flange. This tube was shaped like a candy cane, where the short end was attached to the IVC and the vacuum feed-through and persistent switch plate were mounted to the long end. The NbTi-wiring inside the $^1/_4$-inch tube was twisted in pairs and run in Teflon tubing to prevent electrical and thermal shorts to the walls.

On the inside of the IVC the 300 μm NbTi-wires were wrapped around the 1K-pot and fixed to a plate directly beneath the 1K-pot. This plate served as heat sink for the wires as well as mechanical support of the spot welds connecting the 300 μm NbTi-wires to the 100 μm NbTi-wire extending from the low temperature NMR magnet. Spot welds were made by stripping the copper and CuNi-cladding of the NbTi-wire using nitric acid. The cleaned NbTi-cores were crossed and spot welded at their crossing point. Following an optical inspection the spot weld was

covered in Hysol 3430 [213] to protect it from mechanical stress. On its way to the magnet, the 100 μm NbTi-wire is further heat sunk by wrapping it around copper bobbins at the still and cold plate. Here the Teflon sleeve through which the wire was routed was interrupted.

In the bath the 300 μm NbTi-wires were spot welded to the 100 μm CuNi-clad NbTi-wire from which the persistent switches were constructed. These spot welds were also fixed in Hysol 3430 and covered by cigarette paper and adhesive copper tape. The voltage taps and incoming magnet leads were soldered to the superconducting magnet circuit at two pairs of solder pads (see Fig. A.3).

The persistent switches were made from 100 μm CuNi-clad NbTi wire wound around a 477 Ω metal film resistors. In order to mount the switches on the plate the switches were potted with Stycast in a Teflon mold. Initial test of the switches in liquid helium showed a fast response time of less than 5 s and opening current of 5 mA i.e. about 2.5 V. Additional twisted pairs of 80 μm copper and 100 μm Constantan-wire were routed from 10-pin Fisher connectors at the bath break-out box to the persistent switch plate to operate the persistent switches, monitor the back-emf of the magnet circuit and measure the temperature of the persistent switch plate through an installed 2.2 kΩ RuO_2 thermometer (see Fig. A.3).

A.2 The ND1 SQUID-NMR Coil Set

In this section the design and manufacture of the ND1 SQUID-NMR coil set are discussed.

The design of this coil set was governed by the available vertical and lateral space on the new ND1 experimental platform as well as available sizes of niobium shields. The general demands on the design were: a) to maximise the experimental volume b) to achieve a high field-current ratio and homogeneity of all coils c) to shield the coil set by an outer continuous and inner overlapping niobium shield d) to minimise magneto-acoustic resonances.

The design concept of the coil set was taken from an existing coil set made by Ben Yager for his experiments on one-dimensional helium on a 1K-pot cryostat [214]. It consisted of a hollow cylindrical copper magnet former for the NMR-magnet, surrounded by a slightly bigger and longer niobium cylinder. The transmitter saddle

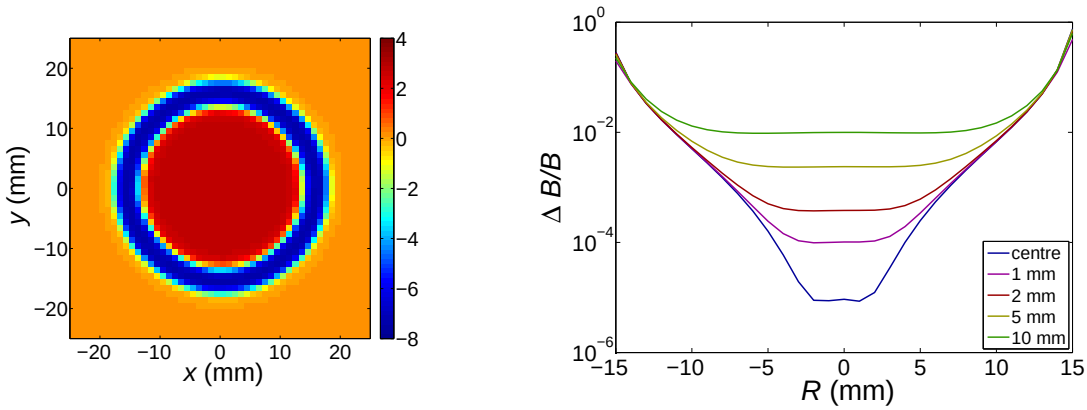

Figure A.4: Simulated NMR-magnet homogeneity: The left panel shows the magnetic field profile of a cross section through a 95 mm long 32 mm diameter magnet inside a 36 mm diameter superconducting niobium shield. The right-hand side panel shows the magnet homogeneity renormalised to the centre of the coil.

coil inside the NMR-magnet, was wound onto a Stycast 1266 former, with an air gap between the copper and Stycast coil formers. An overlapping niobium-foil Hechtfischer shield [215] between the transmitter and NMR coil was inserted to shield the copper magnet-former from rf-fields (see also Fig. A.7).

In order to optimise the field-current ratio as well as field homogeneity, a program was written that could calculate the magnetic field profile of coils in the presence of superconducting shields. Fig. A.4 shows the z-component and homogeneity of the magnetic field in the centre of the NMR coil.

In conjunction with the spatial dimensions of the other coils and shields, we opted for a 95 mm long and 32 mm diameter NMR magnet. The outer shield is a 36 × 0.5 mm niobium tube of 105 mm length centered around the magnet. The field homogeneity of this specific case is shown in Fig. A.4. The maximal simulated magnetic field inhomogeneity over a 10 × 10 × 10 mm NMR cell is of the order of $\Delta B/B \approx 2.5 * 10^{-3}$, which is a factor five larger than the experimental value obtained from a ^{13}C T_2^* frequency dependence (see Fig. 3.15). The copper magnet former was vacuum annealed for six hours at 850^{o}C. The magnet itself was wound from four layers of 100 μm, single-filament, CuNi-clad, NbTi-wire [216]. In order to protect the wire from shorting to the copper former, a Kapton foil was glued into the

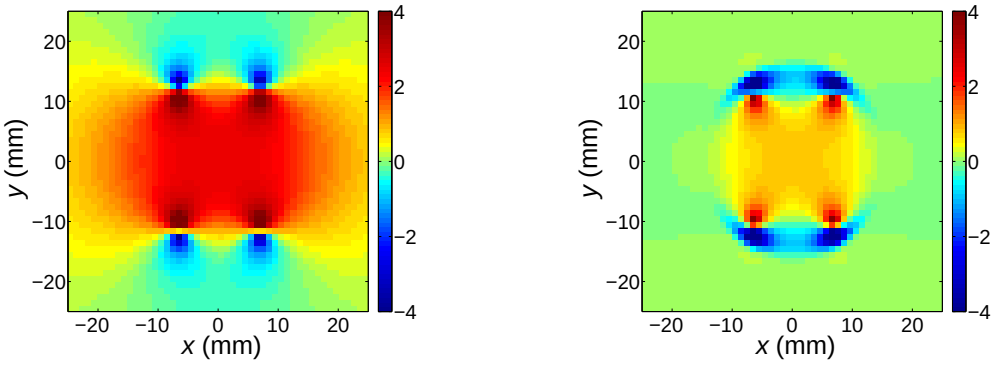

Figure A.5: Transmitter coil simulation inside a Hechtfischer shield: The left and right-hand side panel show the x-component of the magnetic field along a horizontal cross section through its centre of a 38 mm long 25 mm diameter saddle coil with 120^o opening angle. In the presence of an overlapping Hechtfischer shield (right-hand side) the transmitter field gets strongly distorted and the field-current ratio for the centre region drops significantly.

magnet former recess before the magnet was wound. Both the magnet windings and foils were fixed with GE 7031-varnish. The field-current ratio of the NMR-magnet was later confirmed by NMR experiments to be 5.24 mT/A.

Similarly to the NMR-magnet, the transmitter coil has been simulated using the same program. Here additional boundary conditions had to be introduced for the Hechtfischer shield to incorporate its laminar nature. The Hechtfischer shield enhances the homogeneity of the NMR-field and more importantly shields the copper NMR-magnet former from the rf-fields of the transmitter coil. This is achieved by prohibiting perimetric screening current through the use of coiled insulated niobium foils rather than a tube. In our case the Hechtfischer shield was built in a composite technique, where a sandwich of glass-fibre fabric and niobium foil was wound around a Teflon former and soaked with epoxy resin. The shield was made from 25 g/m^2 glass fibre fabric and 50 μm niobium foil and set in a 50:50 mixture of Stycast 1266 and 2580. After curing for two days the shield was removed from the Teflon former.

Following the simulation of various transmitter coil geometries inside the Hechtfischer shield, we opted for a 38 mm long and 25 mm diameter saddle-coil with an opening angle of 120^o. Figure A.5 shows how the Hechtfischer shield distorts the

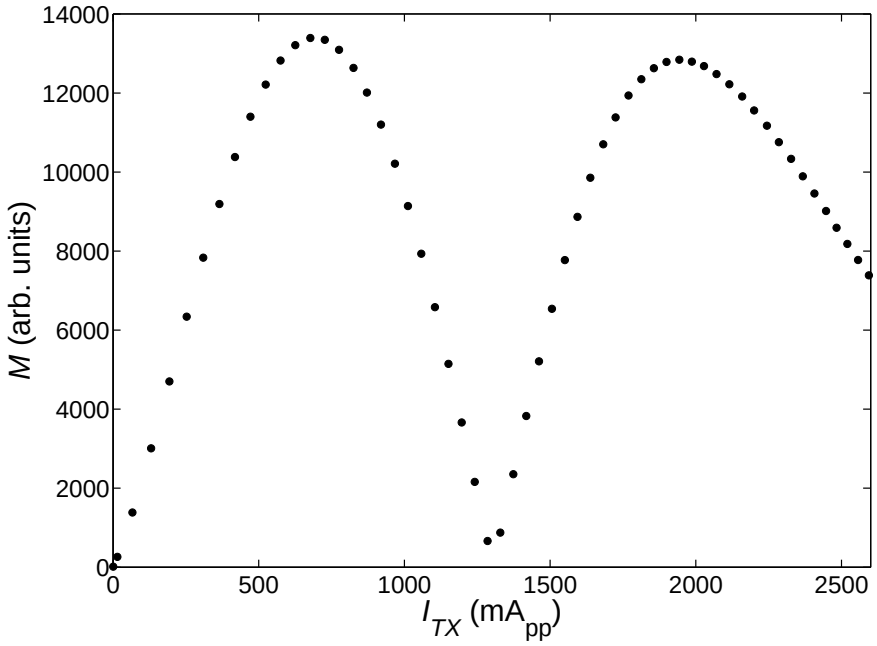

Figure A.6: Transmitter current dependence of the magnetisation of a $\rho_2 = 7.1\,\mathrm{nm}^{-2}$ ^{3}He sample preplated with a monolayer of ^{3}He at a Larmor frequency of 58.3 kHz. Transmitter pulses of ten Larmor periods and different currents, were applied to measure the tip angle of the ^{3}He magnetisation. Maxima correspond to 90^o and 270^o, whereas the minima correspond to 0^o and 180^o tipping.

transmitter field and reduces the field-current ratio significantly. The transmitter coil was wound from 105 μm multi-filament CuNi-clad, NbTi-wire onto a Stycast 1266 former. The unshielded inductance of the transmitter coil is 83 μH, as determined from resonance methods, and its shielded field-current ratio is 0.275 mT/A, as determined from a ^{3}He NMR tip-angle dependence (see Fig. A.6). An additional Hall sensor (model: THS119 Toshiba) has been installed into the magnet, located 20 mm inside the magnet along its axis, to detect potential quenches and magnetic field changes.

As the receiver coil is part of the experimental NMR cell, its design and manufacture will be discussed in the following section.

An overview of the ultra-low temperature NMR setup is shown in Figure A.7.

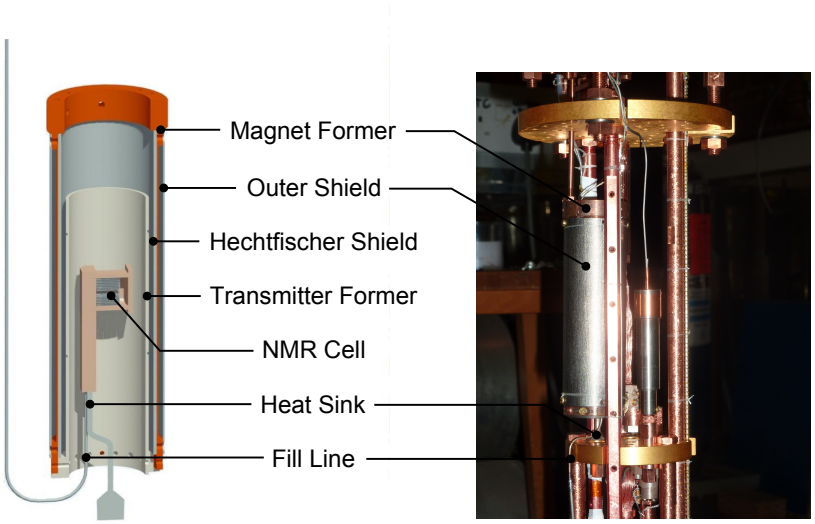

Figure A.7: The left-hand side panel shows a cross section of the coil set. The right-hand side photo shows the coil set and NMR-cell as installed on the nuclear demagnetisation refrigerator ND1 (Photo by courtesy of Jan Nyéki).

Here the transmitter coil, outer and inner shield are fixed to the NMR coil by radial screws at the top and bottom end of the NMR coil former. The transmitter coil can be rotated inside the NMR magnet to adjust its position relative to the receiver coil.

The entire coil set is supported of a magnet support plate located 25 mm above the 300 μK plate (see Fig. 3.5). This plate is connected to the lower mixing chamber plate by three copper rods, providing a thermal extension of the mixing chamber. The NMR-magnet former has been heat sunk to the mixing chamber, as eddy-current heating in the magnet former during NMR-field tuning would otherwise warm up the nuclear demagnetisation stage. The magnet former itself is connected to this plate via three 3 mm copper rods, which pass through the 300 μK plate without touching it. The positioning of the connecting rods is fixed in the magnet former and can be slightly adjusted via elongated holes in the magnet support plate. The wiring of the NMR magnet and Hall sensor is fixed to this mixing chamber link to avoid thermal shorts between the mixing chamber and demagnetisation stage.

A.3 The NMR-Cell

The previous section of Appendix A discussed the NMR-coil set providing the static and transmitter field for the NMR experiments. The design and build of the NMR adsorption cell and wound on receiver coil will be described in this section.

The optimised NMR coil set left us with an internal diameter of 24 mm. The highly homogeneous field region of both the NMR and transmitter coil extends over region of about $10 \times 10 \times 10$ mm at the centre of the coil set. The cell size was thus limited to these dimensions. The general design specifications of the NMR-cell were: a) to maximise the amount of exfoliated graphite in the cell b) to achieve an optimal filling factor of the receiver coil c) to optimise the heat sinking of the graphite and helium whilst reducing possible eddy-current heating d) the cell must be absolutely helium leak tight, helium can only be added or removed from the cell through a narrow fill line.

The final design (see Fig. A.7 and A.3) comprised of an almost cubic cell of $9 \times 9 \times 10$ mm enclosed in a Stycast cap and lid. Both parts were machined from solid blocks of Stycast 1266. In the case of the lid a greased piano wire (22 SWG) was installed in the Stycast mould, running along the centre mold and tensioned by a weight. After removing the piano wire a narrow fill line channel was left in the Stycast body. The upper end of this channel was filled with Stycast 1266 up to the point were the cell inlet branches off and an vacuum annealed silver capillary was glued into the other using a 50:50 mixture of Stycast 1266 and 2850.

In the mean time 36 Grafoil-Silver-Grafoil sandwiches were prepared. Firstly the 150 μm thick Grafoil was cut into 9×10 mm rectangles and baked out under high vacuum at 1000^{o}C for 24 hours. Silver foils were cut into rectangles of 8.5×8.5 mm with an attached 35×1.6 mm long heat sink tab on one side. About ten cuts were made into each foil, separating the rectangular part into 11 fingers. After cutting, the foils were vacuum and oxygen annealed at 750^{o}C for 15 hours, where during the 12 hour oxygen anneal dry air was added to produce a constant pressure of $2*10^{-4}$ mbar at the gauge of the pumping trolley. The annealed foils were each subsequently bonded to two Grafoil sheets. A stainless steel bonding vice was machined and cleaned at 1000^{o}C for 24 hours (see Fig. A.3). The insides of the vice were covered by 140 μm molybdenum foils and sheets of Grafoil to avoid any contamination of

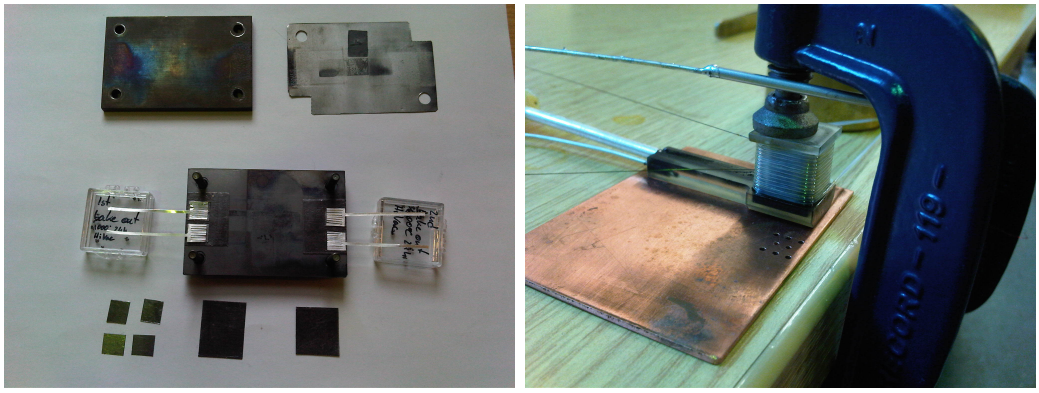

Figure A.8: NMR Cell Manufacture: The left-hand side picture shows the diffusion bonding vice during alignment of the sandwiches. The right-hand side picture shows the NMR-cell after assembly, held by a G-clamp, whilst the receiver coil is wound on.

the sandwich and bonding to the vice. Four sandwiches at a time were placed into the vice, with their heat sink tabs sticking out of the vice. The vice was closed and tensioned by four M5 bolts (1.5 Nm each). The whole setup was then transferred into a furnace and diffusion bonded for eight hours at 650^{o}C under vacuum. In order to ease the gas distribution in the cell eight 0.5 mm holes were drilled through the finished Grafoil-silver stack. Subsequently the cell was preassembled to align all heat sink tabs, trim their length and to clamp them to the central silver heat sink post. The clamped assembly was transferred into the furnace and diffusion bonded for another 30 minutes at 750^{o}C .

For the final assembly, 10μm thick Mylar foils were cut into the shape of the silver foils, pierced and placed in between each sandwich. The stack of Grafoil-silver sandwiches was compressed and inserted into the cap to make a tight fit. A mixture of Stycast 1266 and 2850 was applied to the heat sink tabs and Mylar foils coating both sides of each foil, before the cell was closed by putting the lid onto the cap. During curing the cap was pressed onto the lid and the silver taps were held down into their grove. After the initial curing, an additional layer of Stycast was added to the critical areas around the cap-lid joint and along the silver tabs.

Subsequently the cell was leak tested and a receiver coil was wound on. The inductance of the receiver coil was matched to the input inductance of the XL116T-SQUIDs $L_i = 1.8\mu$H(see Sec. 3.5.3). In order to guarantee a homogeneous spacing

of the 13 windings, a 800 μm Teflon sleeve was first wound around the cell followed by the 80μm bare single filament NbTi-wire (see Fig. A.3). A length of about 2 m of NbTi-wire was left on either side of the coil to connect the coil to the nearest heat sink box on the nuclear demagnetisation cryostat. After the coil had been set in Stycast 1266, the remaining wire was twisted and pulled through a Teflon sleeve and niobium capillary, which later got attached to the NMR-cell, by dental floss and Stycast.

Appendix B

Pulsed Magnetic Fields

B.1 Generation of High Magnetic Fields

Due to the current limitations in superconductor technology, where the best commercially available superconductors show critical fields of the order of 25 T, magnetic fields above 25 T can only be produced by normal resistive coils. Here the large currents in combination with the normal resistive wiring produce large amounts of heat and the high magnetic fields will give rise to tremendous Lorentz forces. So far two design are commonly used to overcome both of these issues.

Magnetic fields below 38 and 45 T are produced by Bitter magnets (invented in 1936 by Prof. Francis Bitter) [217] and Bitter-Superconductor hybrid magnets [218]. Bitter magnets are made of helically stacked thick semi-circular copper alloy plates, which are connected in series to form the windings of the coil [219]. Here high tensile strength alloys are used to stabilise the magnet windings against the moderate Lorentz forces. Bitter magnets are powered by large dc power supplies producing static currents of the order of 50 kA for the largest systems. At maximal field Bitter magnets can reach power consumptions of up to tens of megawatts, requiring a highly efficient cooling system. Here the Bitter plates are especially slotted and drilled to allow large quantities of cooling water to flow through the magnet. In order to reduce running costs of these systems, hybrid magnets were introduced. Hybrid magnets are made of an outer superconducting magnet producing a static background field of up to 14 T and an inner Bitter magnet. At low fields the hybrid magnet runs almost entirely on the superconducting outer magnet, thus saving on power of the Bitter magnet and cooling plant. Even by using hybrid technologies, static magnetic fields are still the most expensive way to produce high magnetic

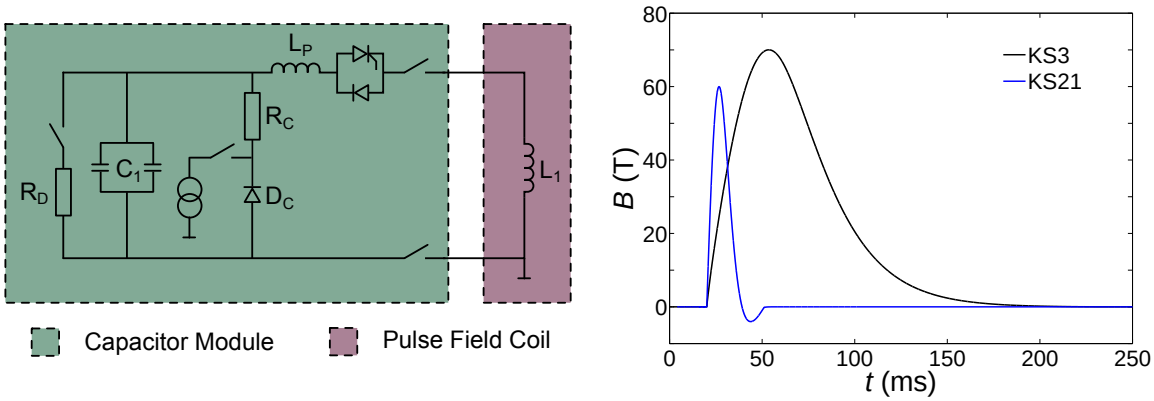

Figure B.1: Pulsed Field Schematics and Pulse Durations: The left panel shows a schematics of the capacitor bank-pulse field coil circuit. The right-hand side graph shows the time dependencies of a full field pulse of the pulse field magnets used in our experiments.

fields.

The second approach taken to generate even higher magnetic fields is based on pulsed magnets. Here rather than using static currents the coil is driven by current pulses generated by a capacitor bank. Using this method magnetic fields of up to 300 T are produced [220]. In pulsed coils the combination of large currents and magnetic fields of up to 300 T give rise to gigantic Lorentz forces or radial pressures in excess of the tensile strength of copper. Thus pulsed magnets are divided into destructive, i.e. single-shot, and non-destructive coils. Here non-destructive pulse field magnets are limited to maximal fields around 100 T and are usually reinforced by a Zylon fibre composite. Here Zylon has a tensile strength of 5.8 GPa exceeding that of copper (0.25 to 1.0 GPa) and other synthetic fibres like Aramid or Carbon fibre [221].

In order to produce magnetic field pulses, the capacitor bank is charged and subsequently discharged through the pulsed field magnet. During charging the capacitors are separated from the pulsed field coil by a thyristor switch. Once the designated charge voltage of the capacitors is reached, the control system triggers the thyristor and data acquisition system followed by the discharging of the capacitors through the coil. The magnitude and duration of the produced magnetic field pulse is mainly

governed by the capacitance of the capacitor bank C_1 and inductance of the pulse field magnet L_1, leading to an over-damped sinusoidal time dependence. Additionally the protection coil L_P and crowbar circuit (D_C and R_C) will shorten the up and down-sweep respectively. A schematics of the coil-capacitor circuit is shown in Fig. B.1 [222].

The overall pulse length of the coils used in our experiments were 25 ms for the KS21 and 150 ms for the KS3-type coils, where the maximal magnetic field of both coils are 60 and 70 T respectively [223] (see Figure B.1). Pulse field magnets are usually precooled in liquid nitrogen in order to reduce their resistance and end temperature after the pulse. Following a full field pulse, a time of typically 45 minutes for the KS21 and 3 hours for a KS3 magnet is needed to cool the pulsed magnet back down to liquid nitrogen temperatures. This cooling time is the main limiting factor determining the repetition time of experiments.

B.2 Pulsed Field Transport Measurements

Due to the shortness of the magnetic field pulses and high noise environment, standard dc-measurements can not be used in pulsed magnetic field. Instead, resistivities are measured using high frequency excitations and digital lock-in post-processing techniques.

Depending on the sample resistance and contact quality small ac-excitation currents of typically less than 5 mA and frequencies below 200 kHz are applied to the sample. Constant excitation currents are produced by function generators in conjunction with a high ohmic shunt resistor. The sample voltages as well as the current reference are measured by Yokogawa DL75 oscilloscopes (1 MS/s, 16 bit resolution) [224] or National Instruments PXI 5922 scopes (5 MS/s, 20 bit resolution) [104]. Signals below the input noise of the oscilloscopes can be amplified and filtered by Stanford Research SR560 preamplifiers. In pulsed field setups the typical voltage noise levels are of the order of 10 μV originating from magnet vibrations and high voltage surface discharges.

Recorded signals are subsequently post-processed by applying a digital lock-in procedure. Here the current signal serves as reference for all other voltages. Time constants of one to ten excitation frequency periods are used to integrate and smoothen

the signals.

A pick-up coil (typically 10 windings with 5 mm diameter) is installed close to the sample to measure the magnetic field (see also bottom right picture of Fig. C.4). According to Faradays law the pick-up coil induces a voltage proportional to the magnetic field sweep rate. The pick-up voltage is recorded concurrently with the sample data and later numerically integrated and calibrated to produce the magnetic field reference. Generally pick-up coils are calibrated against systems with well known phase transitions or high frequency quantum oscillations. One commonly used standard is the spin flip transition of MnF_2 at (9.27 ± 0.02) T and 4.2 K. The resulting field uncertainties with this method are of the order of 0.5 %. However for most measurements the field-current ratio of the pulse field magnet can be used to determine the magnetic field within 2 %.

Due to the high magnetic fields and field sweep rates special care needs to be taken when preparing samples and routing wires. Even the small currents flowing through the contact wires will exert a significant force onto the sample contacts, leading to their destruction after a few pulses. Thus in order to make sample contacts more stable two-component silver-loaded epoxies (EpoTek H20E and Dupont 6838) are used to attach wires (typically 25 μm gold wires) to the sample. Noise and pick-up signals are reduced by minimising inductive loops, twisting and fixing any connecting wires as far as possible. Additionally wiring inside the cryostat is shielded by metal capillaries and coaxial cables outside the cryostat in order to avoid high frequency cross-talk between different channels.

Appendix C

Point-Contact Spectrometers

C.1 Low Field Spectrometer

Generally point-contact spectrometers consist of a fixed sample holder and adjustable needle or contact holder. The sample and needle are fixed in their respective holders and are subsequently brought into contact by fine adjusting their position [225, 226, 227]. In order to perform point-contact spectroscopy at moderate magnetic fields and low-temperatures, two spectrometers were designed and built, utilising the variable temperature insert and magnet of a Physical Property Measurement System (PPMS) [228].

The first prototype setup, only consisted of a polycarbonate needle holder platform held by three fine pitch M3 screws above the aluminium sample holder plate. Here fine approaching the needle was only possible at room temperature before the sample was loaded into the PPMS. However due to differential thermal contraction and vibrations about 50 to 75 % of the contacts established in this way, disconnected or deformed the contact on cooling. Additionally, this initial spectrometer lacked the possibility to adjust the planar position of the contact.

Thus a more sophisticated spectrometer was built using AttoCube piezo-electric scanners and positioners [229]. Piezo electric Scanners are actuator that expand/contract if a constant voltage is applied. Positioners, however, are actuator operating in slip-stick mode, where the actuator position is changed stepwise by applying voltage pulses. Due to size restrictions inside the PPMS, we opted for a scanner-positioner stack consisting of an ANSxy50 xy-scanner and ANPz30 z-positioner with maximal travel of $12 \times 12\,\mu$m and 2.5 mm respectively at 4.2 K. A schematic of the whole setup can be found in Figure C.1.

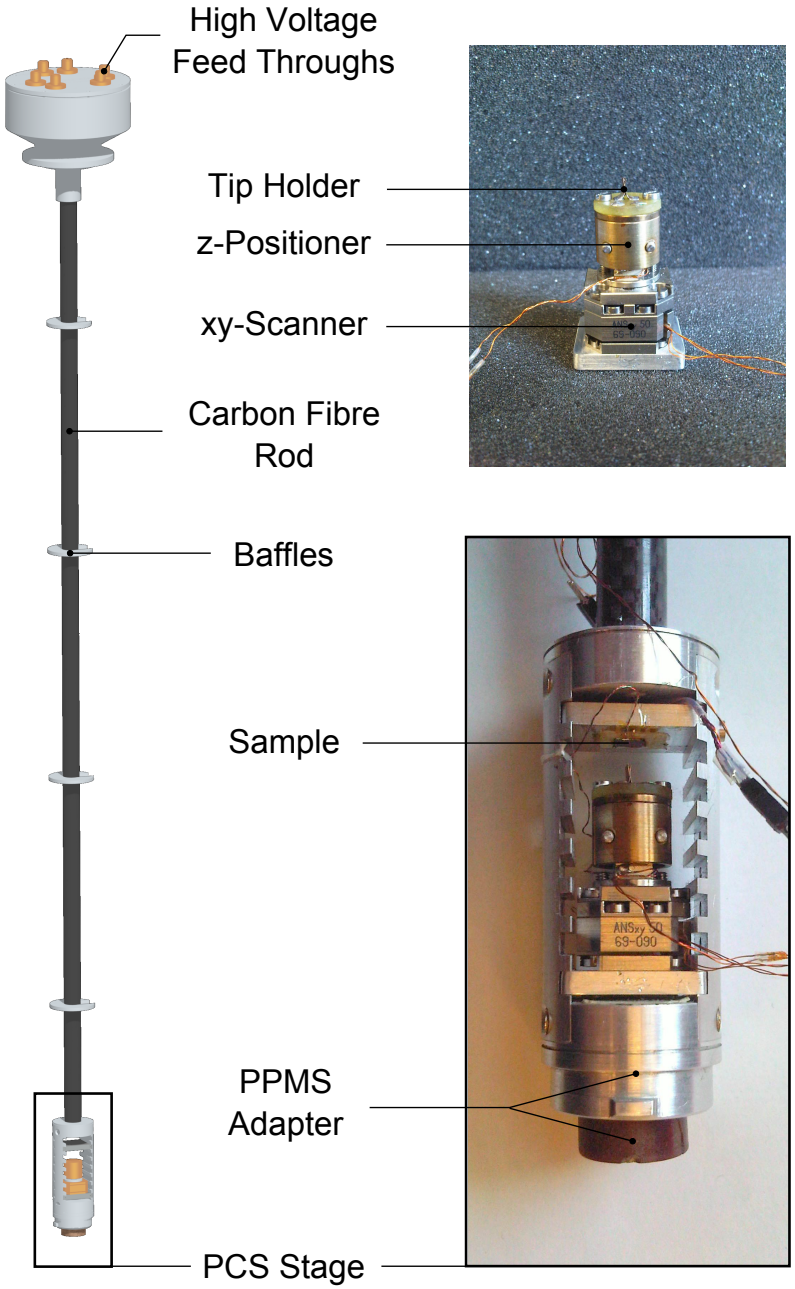

Figure C.1: PPMS Point-Contact Spectrometer: On the left a CAD model of the entire PPMS point-contact spectrometer is shown. The right-hand side shows two photos of the piezo-actuator stack (top) and the low temperature part of the spectrometer (bottom).

Here the piezo-stack and sample holder are enclosed in an aluminium frame that plugs into the socket at the bottom of the PPMS sample chamber. This connection is used for thermometry and the point-contact bias lines. The high voltage wiring, driving the piezo-actuators, was fed in through a room temperature break-out box, routed down the centre of the carbon-fibre probe into the low temperature PCS-stage. Both the piezo-actuator stack and sample were mounted on removable aluminium trays. The PCS-needle was held by a clamp on top of the piezo-actuator stack, made of two CuBe springs.

The piezo-actuators are controlled by an AttoCube ANC300 Piezo Controller, where two ANM300 modules are used to drive the xy-scanner and an ANM150 module to operate the z-positioner. Voltages of up to 150 V are applied to the xy-scanner at low temperatures (60 V at 300 K). The z-positioner is driven by assymetric voltage pulses with an amplitude of up to 60 V. The low temperature travel of both stages is about 80 nm/V for the xy-scanner and 10 nm for a minimal voltage pulse on the z-positioner. The travel of the piezo-actuators is temperature dependent and scales with the capacitance of the piezos (see Fig. C.1). At constant temperature the travel of the xy-scanner is highly reproducible. The z-positioner, however, due to its slip-stick mode, does not respond consistently to equivalent voltage pulses.

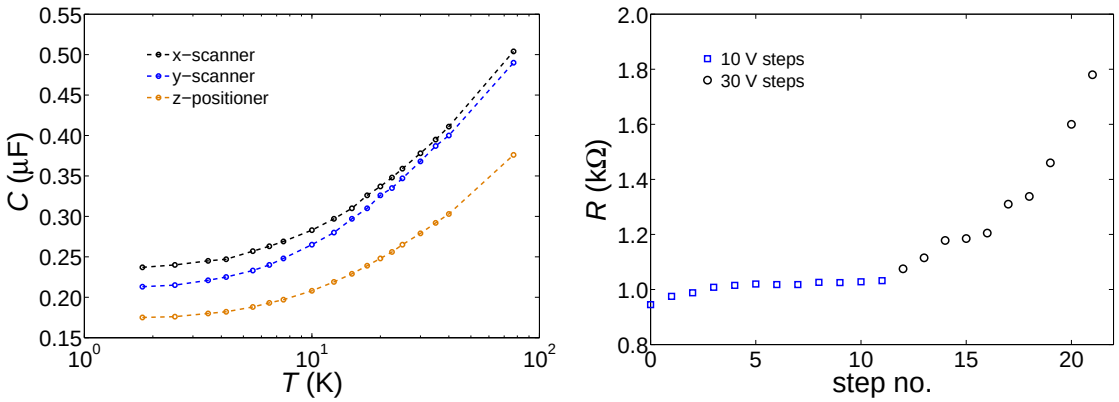

Figure C.2: The left-hand side graph shows the temperature dependence of the capacitance of all three piezo-actuators. The right-hand side graph shows the zero bias contact resistance of a Madagascan graphite-aluminium point contact as the tip is pulled out of the sample.

Figure C.1 shows the zero bias resistance of a point-contact whilst the needle was pulled out of the sample by applying 10 and 30 V pulses to the z-positioner. At first the contact is stabilised by the spring force of the needle. Once the needle tension is removed the contact starts to disconnect and the contact resistance grows.

The resistance and differential resistance of the point-contact are measured by two Stanford Reasearch SR830 DSP Lock-In amplifiers. The primary Lock-In produces a constant voltage as well as a low frequency modulation. Both signals are added using an INA103 instrumentation amplifier [230]. The output of the adder is fed through a shunt resistor whose voltage serves as current reference. The shunt resistor is chosen similarly to the contact resistance to optimise the bias voltage range and signal size. The ac- and dc-part of the current reference and bias voltage are both 10-fold amplified by INA103 amplifiers and simultaneously measured by the primary and secondary lock-in amplifier. The resistance and differential resistance are calculated from the ratio of the dc- and ac-signals respectively. Typical time constants, frequencies and bias modulations for the graphite PCS experiments were of the order of 300 ms, 15 kHz and 0.4 mV.

C.2 Point-Contact Needles

Point contact needles were prepared by electrochemical etching [227]. In our experiments we chose aluminium and tungsten as spear materials. The soft non-magnetic aluminium, which forms a natural 1 to 2 nm thick oxide-layer on its surface, is an ideal spear material for the use in spectrometers with poor needle positioning. Here the aluminium oxide builds a natural barrier reducing the contact cross section. Tungsten on the other hand is a very hard and does not form a natural oxide. The hardness of tungsten means that rather than deforming the spear, as with aluminium needles, the sample is damaged if the spear is misplaced.

The electrochemical process used to manufacture both needle types is very similar only the electrolytes and applied voltages differ between the two materials. Initially a high purity, 100 μm thick wire is partially submerged into a solution of 10 ml 35 % HCl, 2.5 ml 65 % HNO_3, 35 ml ethanol and 35 ml water for aluminium and a 2M NaOH solution for tungsten. In the case of aluminium a 3 V dc-voltage, with a superimposed 2 V ac-modulation at 250 kHz, is applied between the aluminium wire

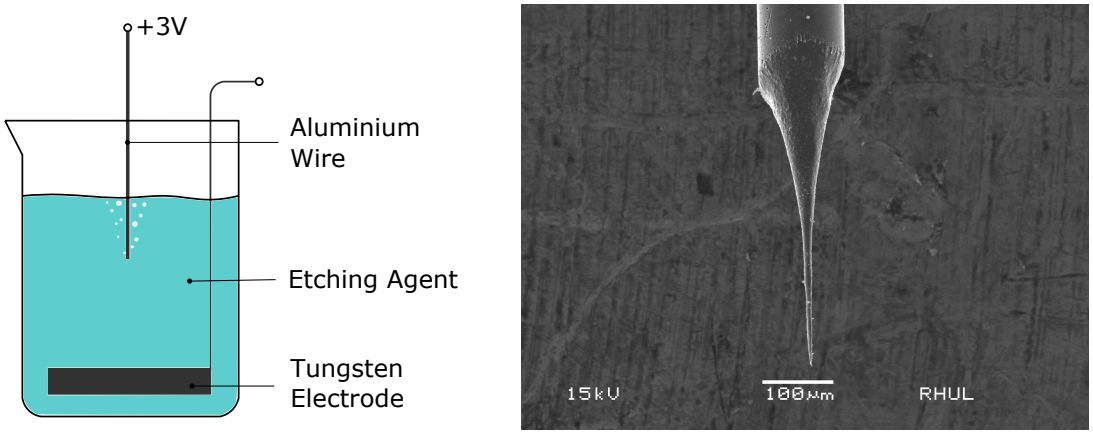

Figure C.3: Point-Contact Spectroscopy Needles: The left-hand side schematics shows how aluminium and tungsten wires were etched to point-contact needles by electrochemical etching. The right-hand side photo shows an SEM image of an etched aluminium needle [193].

and a secondary submerged tungsten electrode (see also Fig. C.3) [193]. Immediately after applying the voltage, gas bubbles will form around the aluminium wire and the submerged part of the wire will start to dissolve. After about half a minute the wire will start to pinch off at the electrolyte surface, producing a sharpened tip. In order to achieve ideal reproducible etching results electronics are used to cut off the voltage supply as soon as the etching current, i.e. the wire surface inside the electrolyte, falls below a set value. As we did not have such an electronic, the etching voltage was manually switched off as soon as the wire pinched of at the surface. Thus most needles in our experiments were slightly under-etched. A SEM image of an etched aluminium tip is shown in Figure C.3.

In the case of tungsten [231, 232], the applied voltage is purely dc, with an amplitude of about 0.7 to 1.5 V. Similarly to aluminium, the wire will start to become thinner until it pinches off at the electrolyte surface. Due to the fast progression in the final stage, better results were achieved by reducing the etching voltage to 0.7 V as soon as the initial etching current halfed.

The finished, sharpened wires were rinsed in water to remove any residual electrolyte. An SEM image of an aluminium spear is shown in Figure C.3. Typical tip radii were of the order of 1 μm.

C.3 High Field Spectrometer

Due to the short pulse duration in high field experiments, point-contact spectra could only be measured through dc IV-characteristics. Due to parasistic inductances and stray capacitances a potential ac-bias modulation well above 200 kHz would have lead to a large phase difference between the bias current and voltage.

We designed and built two spear-anvil point contact spectrometers for pulsed magnetic fields. Similarly to the low field setup, the pulsed field spectrometers consist of a needle and sample holder, where the needle position can be adjustable via fine pitch screws (see Fig. C.4). In order to eliminate eddy-current heating and vibrations the pulsed field PCS-stages were entirely made from polyether-ether-ketone (PEEK).

The first setup was designed to fit on an existing D-HMFL transport probe, where the needle position could only be adjusted when the probe was outside of the cryostat [193]. Later another spectrometer was build that allowed the *in situ* manipulation of the point contact. A schematic of both point-contact spectrometers is shown in Fig. C.4.

The second, more evolved spectrometer had a driving shaft running along the centre of the probe, with a M1.6 fine pitch threaded rod soldered into the lower end. The threaded rod was held in a threaded stainless steel bushing, which was glued into the PEEK holder. Under normal conditions the threaded rod protrudes beyond the bushing and pushes against the inside of the spring like needle holder. By screwing the threaded rod in and out, it is possible to adjust the position of the needle and contact resistance. Both the needle and sample holder have glued on contact pads, making it possible to prepare the needle and sample before assembling the probe.

Following the main ideas of Orlov and Latychev *et al.* [233, 212], we measured the IV-characteristics of our point contacts by applying a saw-tooth or triangle wave function with a frequency of about 5 kHz. The bias wave function was produced by an Agilent 33220A Function and Arbitrary Waveform Generator. The bias voltage and current reference were 10-fold amplified by INA103 instrumentation amplifiers and simultaneously

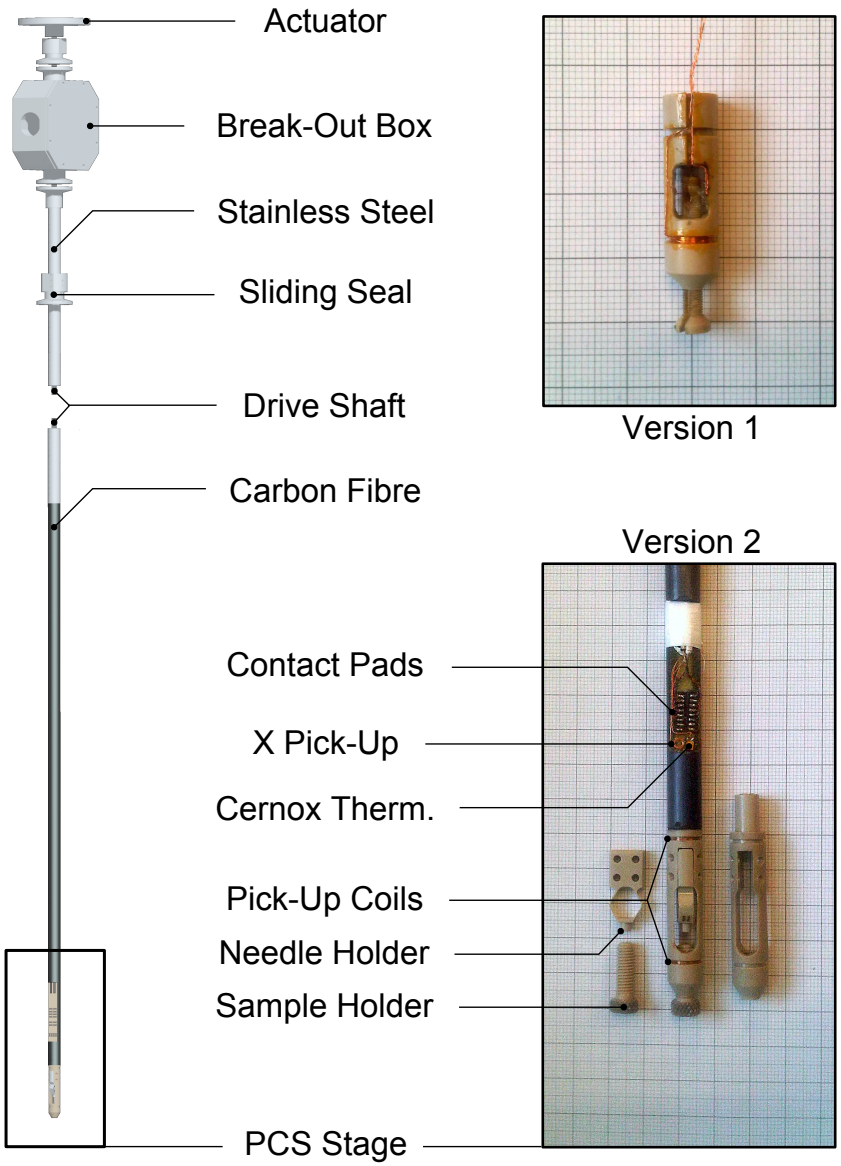

Figure C.4: Pulsed Field Spectrometers: The left drawing shows a CAD model of the second point-contact spectrometer version, where the photo on the bottom right shows the high field stage in more detail. The upper right-hand side photo shows the first spectrometer, which was connected to a D-HMFL transport probe.

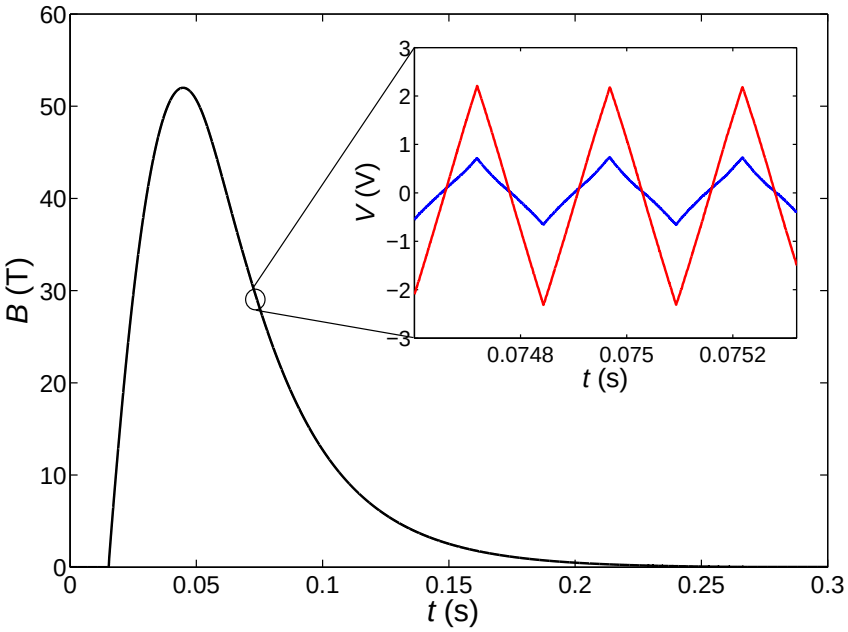

Figure C.5: The graph shows the integrated and calibrated pick-up coil signal. The inset shows a close-up of the 10-fold amplified recorded bias-voltage (red) and current (blue) of a aluminium-Grafoil point contact.

measured by a NI-PXI 5922 scope. Here the function generator was synchronised to the internal clock of the PXI system ensuring a simultaneous output and sampling of the bias voltage and current as well as guaranteeing a constant number of samples per sawtooth period. The sampling rate of the PXI-scope was chosen as 5 MS/s leading to a reduced resolution of 20 bit over a ± 5 V interval.

In order to achieve the best possible field and bias resolution, point-contact spectra were measured in a KS3-type pulsed field magnet (see Fig. B.1) an overall pulse length of 150 ms. The recorded bias and current traces were segmented into the individual slopes of the bias wave form and averaged along the bias voltage as well as over subsequent bias sweeps to produce the dc IV-characteristics of the point-contact. Differentiating the dc IV-characteristics along the bias voltage and assigning a magnetic field strength to the centre of the differential conductance produces the magnetic field dependent point-contact spectrum.

Table C.1: List of PCS Contacts: Each entry corresponds to one PCS needle-sample pairing. Entries with multiple resistances have been reestablished or repositioned laterally during a run to measure resistance or spatial dependencies. Measurements marked with (*) have been performed on the AttoCube spectrometer.

Date	Sample	Spear	Resistance (Ω)	Temperature (K)	Field (T)	Comment
16-18/11/12	Grafoil	Al		1.8	0-7.5	testing PCS setup
19-20/11/12	Grafoil	Al	830	1.8-15	0-0.5	gap measurement
24/11/12	Madag.	Al	120	1.8-10	0-9	in thesis
26/11/12	KDG	Al	120	1.8	0-9	sharp v-shape, no features
26-29/11/12	Grafoil	Al	100k	1.8	0 - 9	strong modulation, no gap
04/12/12	Grafoil	Al	140	1.8-14	0	strong modulation, flat v-shape, no gap
04/12/12	Grafoil	Al	400	1.8-20	0	strong modulation, no gap
04/12/12	Grafoil	Al	2000	4.2-20	0	unstable
15/03/13	Madag.	Al	43	1.8-10	0	similar to gapped spectrum $2\Delta \approx 20\,\mathrm{meV}$, linear background, inconsistent T-dependence
18/03/13	Madag.	Al	950	1.8-20	0 - 1.5	sharp v-shape, no modulation sharp spikes at $\approx \pm 50\,\mathrm{meV}$
07/06/13*	Grafoil	Al	125-17k	1.8	0	normal spectrum, no gap
08/06/13*	Grafoil	W	500-4k	1.8	0	xy-dependence, strong modulation, no gap
09/06/13*	Grafoil	W	600-7k	1.8	0	xy-dependence, strong modulation, no gap
10/06/13*	Grafoil	W	500-1k	1.8	0	strong modulation, no gap
27/06/13*	Madag.	Al	400	1.8	0	smeared out spectra, no gap
28/06/13*	Madag.	Al	1.5k-17k	1.8	0	R_0-dependence, partially unstable, no gap

Bibliography

[1] Bednorz, J. and Mueller, K. *Z. Phys. B Cond. Mat.* **64**, 189–193 (1986).

[2] Mott, N. *Proc. Phys. Soc. A* **62**, 416 (1949).

[3] Hubbard, J. *Proc. Roy. Soc. (London) A* **276**, 238 (1963).

[4] Hubbard, J. *Proc. Roy. Soc. (London) A* **281**, 401 (1964).

[5] Taillefer, L. *Annu. Rev. Condens. Matter Phys.* **1**, 51–70 (2010).

[6] Armitage, N., Fournier, P., and Greene, L. *Rev. Mod. Phys.* **82**, 2421–2487 (2010).

[7] Sebastian, S., Harrison, N., Altarawneh, M., Mielke, C., Liang, R., Bonn, D., Hardy, W., and Lonzarich, G. *PNAS* **107**(14), 6175–6179 (2010).

[8] Steglich, F., Aarts, J., Bredl, C., Lieke, W., Meschede, D., Franz, W., and Schaefer, H. *Phys. Rev. Lett.* **43**, 1892 (1979).

[9] Mathur, N., Grosche, F., Julian, S., Walker, I., Freye, D., Haselwimmer, R., and Lonzarich, G. *Nature* **394**, 39–43 (1998).

[10] Pfleiderer, C. *Rev. Mod. Phys.* **81**, 1551–1624 (2009).

[11] Shibauchi, T., Carrington, A., and Matsuda, Y. *Annu. Rev. Condens. Matter Phys.* **5**, 113–135 (2014).

[12] Putzke, C., Walmsley, P., Fletcher, J., Mallone, L., Vignolles, D., Proust, S., Badoux, S., See, P., Beere, H., Richie, D., Kasahara, S., Mizukami, Y., Shibauchi, T., Matsuda, Y., and Carrington, A. *Nature Comms.* **5**(5679) (2014).

[13] Sachdev, S. and Keimer, B. *Physics Today* **64**, 29–35 (2011).

[14] Levitin, L., Bennett, R., Casey, A., Cowan, B., Saunders, J., Drung, D., Schurig, T., and Parpia, J. *Science* **340**(6134), 841–844 (2014).

[15] Godfrin, H. and Lauter, H. *Prog. Low. Temp. Phys.* **XIV**, 213–320 (1995).

[16] Lusher, C., Cowan, B., and Saunders, J. *Phys. Rev. Lett.* **67**(18), 2497–2500 (1991).

[17] Casey, A., Patel, H., Nyeki, J., Cowan, B., and Saunders, J. *Phys. Rev. Lett.* **90**(11), 115301 (2003).

[18] Vollhardt, D. *Rev. Mod. Phys.* **56**(1), 99–120 (1984).

[19] Greywall, D. *Phys. Rev. B* **41**(4), 1842–1862 (1990).

[20] Miyake, K. *Prog. Theor. Phys.* **69**, 1794–1797 (1983).

[21] Takahashi, H. and Hirashima, D. *J. Low Temp. Phys.* **121**(1/2) (2000).

[22] Morhard, K., Baeuerle, C., Bossy, J., Bunkov, Y., Fisher, S., and Godfrin, H. *Phys. Rev. B* **53**(5), 2658–2661 (1996).

[23] Baeuerle, C., Bunkov, Y., Chen, A., Fisher, S., and Godfrin, H. *J. Low. Temp. Phys.* **110**(1/2), 333–338 (1998).

[24] Matsumoto, Y., Tsuji, D., Murakawa, S., Akisato, H., Kambara, H., and Fukuyama, H. *J. Low. Temp. Phys.* **138**(1/2), 271–276 (2005).

[25] Pierce, M. and Manousakis, E. *Phys. Rev. B* **59**(5), 3802–3814 (1999).

[26] Anderson, P. *Matter. Res. Bull.* **8**, 153–160 (1973).

[27] Misguich, G., Lhuillier, C., Bernu, B., and Waldtmann, C. *Phys. Rev. B* **60**(2), 1064 (1999).

[28] LiMing, W., Misguich, G., Sindzingre, P., and Lhuillier, C. *Phys. Rev. B* **62**(10), 6372 (2000).

[29] Motorunich, O. *Phys. Rev. B* **72**(045105) (2005).

[30] R, M., Karaki, Y., and Ishimoto, H. *Phys. Rev. Lett.* **92**(2), 025301 (2004).

[31] Fukuyama, H. *J. Phys. Soc. Jpn.* **77**(11), 111013 (2008).

[32] McClure, J. W. *Phys. Rev.* **108**(3), 612–618 (1957).

[33] Slonczewski, J. and Weiss, P. *Phys. Rev.* **109**(2), 272–279 (1958).

[34] Novoselov, K., Geim, A., Morozov, S., Katsnelson, M., Grigorieva, I., Dubonos, S., and Firsov, A. *Nature* **438**, 197–200 (2005).

[35] Castro-Neto, A., Guinea, F., Peres, N., Novoselov, K., and Geim, A. *Rev. Mod. Phys.* **81**, 109–162 (2009).

[36] Peierls, R. *Annalen d. Physik* **5**(4) (1930).

[37] Froehlich, H. *Phys. Rev.* **79**(5), 845 (1950).

[38] Overhauser, A. *Phys. Rev. Lett.* **4**(9) (1960).

[39] Overhauser, A. *Phys. Rev.* **167**(3), 691–698 (1968).

[40] Halperin, B. *Jap. J. Appl. Phys.* **26**, 1913–1919 (1987).

[41] Iye, Y., Tedrow, P. M., Timp, G., Shayegan, M., Dresselhaus, M. S., Dresselhaus, G., Furukawa, A., and Tanuma, S. *Phys. Rev. B* **25**(8), 5478–5485 (1982).

[42] Yaguchi, H. and Singleton, J. *J. Phys.: Condens. Matter* **21**, 344207 (2009).

[43] Fauque, B., LeBoeuf, D., Vignolle, B., Nardone, M., Proust, C., and Behnia, K. *Phys. Rev. Lett.* **110**, 266601 (2013).

[44] Yoshioka, D. and Fukuyama, H. *J. Phys. Soc. Japan* **47**(2), 394–402 (1979).

[45] Takahashi, K. and Takada, Y. *Physica B* **201**, 384–386 (1994).

[46] Takada, Y. and Goto, H. *J. Phys.: Condens. Matter* **10**, 11315–11325 (1998).

[47] Arnold, F., Isidori, A., Kampert, E., Yager, B., Eschrig, M., and Saunders, J. *ArXiv* **cond-mat:str-el**(1411.3323v1) (2014).

[48] Landau, L. *Sov. Phys. JETP* **30**, 1058 (1956).

[49] Landau, L. *Sov. Phys. JETP* **32**, 59 (1957).

[50] Landau, L. *Sov. Phys. JETP* **34**, 262 (1958).

[51] Abrikosov, A. and Khalatnikov, I. *Rep. Prog. Phys.* **22**, 329 (1959).

[52] Pomeranchuk, I. *Sov. Phys. JETP* **8**, 361 (1959).

[53] Bloch, F. *Zeitschrift f. Physik* **52**, 555 (1928).

[54] Wannier, G. *Phys. Rev.* **52**, 191 (1937).

[55] Bernal, J. *Proc. Roy. Soc. A* **106**(740), 749–773 (1924).

[56] Woollam, J. *Phys. Rev. B* **3**(4), 1148–1159 (1971).

[57] Wallace, P. *Phys. Rev.* **71**(9) (1946).

[58] Bardeen, J., Cooper, L., and Schrieffer, J. *Phys. Rev.* **108**(8), 1175 (1957).

[59] Overhauser, A. *Phys. Rev.* **128**(3) (1962).

[60] Hohenberg, P. and Kohn, W. *Phys. Rev.* **136**(3B), 864–871 (1964).

[61] Kohn, W. and Sham, L. *Phys. Rev.* **140**(4A), 1133–1138 (1965).

[62] Anderson, P. *Phys. Rev.* **115**(1), 2 (1959).

[63] Lieb, E. and Mattis, D. *Phys. Rev.* **125**(1), 164 (1962).

[64] Gutzwiller, M. *Phys. Rev.* **137**(6A), A1726 (1965).

[65] Brinkman, W. and Rice, T. *Phys. Rev. B* **2**(10), 4302 (1970).

[66] Gutzwiller, M. *Phys. Rev.* **134**, A923 (1964).

[67] Anderson, P. and Brinkman, W. *The theory of anisotropic superfluidity in He.* The Helium Liquids. Academic, New York, (1975).

[68] Anderson, P. and Brinkman, W. *The theory of anisotropic superfluidity in He, Part II.* The Helium Liquids. Wiley, New York, (1978).

[69] Greywall, D. *Phys. Rev. B* **27**, 2747 (1983).

[70] Vucicevic, J., Terletska, H., Tanaskovic, D., and Dobrosaljevic, V. *Phys. Rev. B* **88**, 075143 (2013).

[71] Liebsch, A., Ishida, H., and Merino, J. *Phys. Rev. B* **79**, 195108 (2009).

[72] Tamaribuchi, T. and Ishikawa, M. *Phys. Rev. B* **43**(1), 1283 (1991).

[73] Chernyshev, A. and Zhitomirsky, M. *Phys. Rev. B* **79**(144416) (2009).

[74] Thouless, D. *Prog. Phys. Soc.* **86**, 893 (1965).

[75] Roger, M. *Phys. Rev. B* **56**(6), R2928 (1997).

[76] Kim, Y.-B. Lighning Review On Quantum Spin Liquid; Talk at the Perimeter Institute, Waterloo Canada, June (2012). online version available under www.perimeter-institute.ca/videos/lightning-review-quantum-spin-liquid.

[77] Cowan, B. *Nuclear Magnetic Resonance and Relaxation.* Cambridge University Press, (1997).

[78] Ashcroft, N. and Mermin, D. *Festkoerperphysik.* Oldenbourg, 3 edition, (2007).

[79] Kittel, C. *Einfuehrung in die Festkoerperphysik.* Oldenbourg, 14 edition, (2005).

[80] Bloch, F. *Phys. Rev.* **70**, 460 (1946).

[81] Pobell, F. *Matter and Methods at Low Temperatures.* Springer, (2006).

[82] Enss, C. and Hunklinger, S. *Low Temperature Physics.* Springer, (2005).

[83] de Long, L., Symco, O., and Wheatley, J. *Rev. Sci. Instr.* **42**(147) (1971).

[84] Frosatti, G. *J. Low Temp. Phys.* **87**(595) (1992).

[85] Cousins, D., Fisher, S., Guenault, A., Haley, R., Miller, I., Pickett, G., Plenderleith, G., Skyba, P., Thibault, P., and Ward, M. *J. Low Temp. Phys.* **114**(5/6), 547–570 (1999).

[86] Korringa, J. *Physica* **16**(7-8) (1950).

[87] Fickett, F. *Mat. Sci. Engin.* **14**, 199–210 (1974).

[88] Wiedemann, G. and Franz, R. *Annalen der Physik und Chemie* **LXXXIX**(4) (1853).

[89] Germanium thermometers are sourced and calibrated from Lake Shore Cryotronics Inc., 575 McCorkle Boulevard, Westerville, Ohio 43082, United States - www.lakeshore.com.

[90] Oxford Instruments plc, Tubney Woods, Abingdon, OX13 5QX, United Kingdom - www.oxford-instruments.com.

[91] Paroscientific Inc., 4500 148th Ave. N.E. Redmond, WA 98052, USA - www.paroscientific.com.

[92] Casey, A. *Two Dimensional 3He Adsorbed on Grafoil Plated with a Bilayer of HD, PhD Thesis.* RHUL, (2001).

[93] Ruderman, M. A. and Kittel, C. *Phys. Rev.* **96**(1), 99 (1954).

[94] Kasuya, T. *Prog. Theor. Phys.* **16**(1), 45 (1956).

[95] Yosida, K. *Phys. Rev.* **106**(5), 893 (1957).

[96] Mueller, R., Buchal, C., Folle, H., Kubota, M., and Pobell, F. *Cryogenics* **20**, 395 (1980).

[97] NMR pulse generator/analyser for ultra-low temperature NMR-thermometry produced by RV-Elektroniikka Oy Picowatt, Veromiehentie 14 FI-01510 Vanataa, Finland, - www.picowatt.fi.

[98] Arnold, F., Yager, B., Nyeki, J., Casey, A., Shibahara, A., Cowan, B., and Saunders, J. *J. Phys. Conf. Ser.* **568**(032020) (2014).

[99] Johnson, J. B. *Nature* **119**(50) (1927).

[100] Nyquist, H. *Phys. Rev.* **29**(614) (1927).

[101] Casey, A., Arnold, F., Levitin, L., Lusher, C., Nyeki, J., Saunders, J., Shibahara, A., van der Vliet, H., Yager, B., drung, D., Schurig, T., Batey, G., Cuthbert, M., and Metthews, A. *J. Low. Temp. Phys.* **175**, 764 (2014).

[102] Physikalisch Technische Bundesanstalt, Fachbereich 7.21, Abbestr. 2-12, 10587 Berlin, Germany - www.ptb.de.

[103] Magnicon GmbH, Barkhausenweg 11, 22339 Hamburg, Germany - http://www.magnicon.com/.

[104] PXI platforms are a product of National Instruments Corporation, 11500 N MoPac Expwy, Austin, Texas, United States - www.ni.com.

[105] Lusher, C., Li, J., Maidanov, V., Digby, M., Dyball, H., Casey, A., Nyéki, J., Dmitriev, V., Cowan, B., and Saunders, J. *Meas. Sci. Technol.* **21**, 1–15 (2001).

[106] Grafoil is a product of GrafTech International Advanced Electronics Technology, 11709 Madison Ave. Lakewood, OH 44107 United States, formerly UCAR - http://www.graftech.com.

[107] Josephson, B. *Phys. Lett.* **1**(7), 251 (1962).

[108] Josephson, B. *Rev. Mod. Phys.* **46**, 251–254 (1974).

[109] J., C. and A.I., B. *The SQUID Handbook*. Wiley-VCH Verlag GmbH und Co. KGA, (2004).

[110] London, F. *Phys. Rev.* **74**(4), 562–573 (1948).

[111] Weast, R. *Handbook of Chemistry and Physics*. CRC Press, (1976).

[112] Abramowitz, M. and Stegun, I. *Handbook of Mathematical Functions*. Dover,NY, (1965).

[113] Carver, G. *Phys. Rev. B* **2**(7) (1970).

[114] Bloemberger, N. *Physica* **20**, 1130–1133 (1954).

[115] Wolf, D. *Spin-temperature and Nuclear-spin Relaxation in Matter*. Oxford Science Publications, (1979).

[116] Grykalowska, A. and Nowak, B. *Intermetallics* **15**, 1479–1482 (2007).

[117] Friemann, L., Millet, P., and Richardson, R. *Phys. Rev. Lett.* **47**(15), 1078–1081 (1981).

[118] Schuhl, A., Rasmussen, F., and Chapellier, M. *J. Low Temp. Phys.* **57**(5/6), 483–484 (1984).

[119] Geng, Q., Olsen, M., and Rasmussen, F. *J. Low. Temp. Phys.* **74**(5/6), 369–405 (1989).

[120] Solodovnikov, I. and Zavaritskii, N. *Pis'ma Zh. Eksp. Teor. Fiz.* **56**(3), 165–168 (1992).

[121] Kent, K. *Developement and Characterisation of New Exfoliated Graphite Substrates for the study of Adsorbed Helium Films, PhD Thesis*. RHUL, (2015).

[122] Brunauer, S., Emmett, P., and Teller, E. *J. Am. Chem. Soc.* **60**(2), 309–319 (1938).

[123] Lauter, H., Godfrin, H., Frank, V., and Leiderer, P. *NATO ASI Series* **267**(Phase Transitions in Surface Films), 135–151 (1991).

[124] Corboz, P., Boninsegi, M., Pollet, L., and Troyer, M. *Phys. Rev. B* **78**, 245414 (2008).

[125] Roger, M., Baeuerle, C., Godfrin, H., Pricoupenko, L., and Treiner, J. *J. Low Temp. Phys.* **112**(5/6), 451–478 (1998).

[126] Lauter, H., Godfrin, H., Frank, V., and Schildberg, H. *Physica B* **165-166**(1), 597–598 (1990).

[127] Neuman, M. *Experimental Investigation of 3He Films Adsorbed on Graphite, PhD Thesis*. RHUL, (2008).

[128] Secca, M. *NMR Studies of Helium Absorbed on Graphite, PhD Thesis*. RHUL, (1983).

[129] Takayoshi, S., Obata, K., Sato, D., Matsui, T., and Fukuyama, H. *J. Phys. Conf. Ser.* **150**, 032104 (2009).

[130] Ishida, K., Morishita, M., Yawata, K., and Fukuyama, H. *Phys. Rev. Lett.* **79**(18), 3451–3454 (1997).

[131] Dyugaev, A. M. *Sov. Sci. Rev. A Phys.* **1** (1990).

[132] Greywall, D. and Busch, P. *Phys. Rev. Lett.* **65**(1), 64–67 (1990).

[133] Watanabe, S. and Imada, M. *J. Phys. Soc Jpn.* **76**(11), 113603 (2007).

[134] Casey, A., Patel, H., Siquiera, M., Lusher, C., Nyeki, J., Cowan, B., and Saunders, J. *Physica B: Condes. Mat.* **284**, 224–225 (2000).

[135] Sato, D., Takayoshi, S., Obata, K., Matsui, T., and Fukuyama, H. *J. Low. temp. Phys.* **158**, 544–549 (2010).

[136] Casey, A., Neumann, M., Cowan, B., Saunders, J., and Shanon, N. *Phys. Rev. Lett.* **111**, 125302 (2013).

[137] Herrero, C. *J. Phys.: Condes. Matter* **19**, 156208 (2007).

[138] Hellmann, S., Rohwer, T., Kallaere, M., Hanff, K., Sohrt, C., Stange, A., Carr, A., Murnane, M., Kapteyn, H., Kipp, L., Bauer, M., and Rossnagel, K. *Nat. Comms.* **3**(1069) (2012).

[139] Camjayi, A., Haule, K., Dobrosavljevic, V., and Kotliar, G. *Nat. Phys.* **4**, 932–935 (2008).

[140] Li, C. and Wang, Z. *Phys. Rev. B* **80**(125130) (2009).

[141] Merino, J., Ralko, A., and Fratini, S. *ArXiv* **cond-mat.str-el**(1304.1700v2) (2013).

[142] Neupane, M., Richard, P., Pan, Z., Xu, Y., Jin, R., Mandrus, D., Dai, X., Wang, Z., and Ding, H. *Phys. Rev. Lett.* **103**(097001) (2009).

[143] Colonna, S., Ronci, F., Cricenti, A., Perfetti, L., Berger, H., and Grioni, M. *Phys. Rev. Lett.* **94**(036405) (2005).

[144] Ikegami, H., Obara, K., Ito, D., and Ishimoto, H. *Phys. Rev. Lett.* **81**(12), 2478–2481 (1998).

[145] de Boer, J. and Michels, A. *Physica* **5**, 945 (1938).

[146] Watanabe, S. and Imada, M. *J. Phys. Soc. Jpn.* **78**(3), 033603 (2009).

[147] Takagi, T. *J. Phys.: Conf. Ser.* **150**, 032102 (2009).

[148] Rozenberg, M., Kotliar, G., and Zhang, X. *Phys. Rev. B* **49**(15), 10181 (1994).

[149] Fisher, D., Kotliar, G., and Moeller, G. *Phys. Rev. B* **52**(24), 17112 (1995).

[150] Kajueter, H., Kotliar, G., and Moeller, G. *Phys. Rev. B* **53**(24), 16214 (1996).

[151] Kotliar, G., Murthy, S., and Rozenberg, M. *Phys. Rev. Lett.* **89**(4) (2002).

[152] Nakamura, S., Matsui, K., Matsui, T., and Fukuyama, H. *ArXiv* **con-mat.other**(1210.0391v1) (2012).

[153] Nakamura, S., Matsui, K., Matsui, T., and Fukuyama, H. *ArXiv* **con-mat.other**(1406.4388v1) (2014).

[154] Collin, E., Bunkov, Y., and Godfrin, H. *J. Phys. Cond. Matter* **16**, S691–S699 (2004).

[155] Collin, E., Triqueneaux, S., Harakaly, R., Roger, M., Baeuerle, C., Bunkov, Y., and Godfrin, H. *Phys. Rev. Lett.* **86**(11), 2447 (2001).

[156] Zvyagin, S., Kamenskyi, D., Ozerov, M., Wosnitza, J., Ikeda, M., Fujita, T., Hagiwara, M., Smirnov, A., Soldatov, T., Shapiro, A., Krzystek, J., Hu, R., Ryu, H., Petrovic, C., and Zhitomirsky, M. *Phys. Rev. Lett* **112**(077206) (2014).

[157] AMG Mining AG, Langheinrichstr. 1, 94051 Hauzenberg, Germany - http://www.graphite.de/.

[158] NGS Naturgraphit GmbH, Winner Str. 9, 91227 Leinburg, Germany - http://www.graphit.de/.

[159] Naturally Graphite, Nanotech Innovations, Michigan Technological University, 1400 Townsend Drive, Houghton, Michigan 49931-1295, United States - http://www.naturallygraphite.com.

[160] Bretz, M. *Phys. Rev. Lett.* **38**(9), 501 (1971).

[161] Brown, A. and Watt, W. *Ind. Carbon and Graphite Papers Conf.* , 86–100 (1957).

[162] Pappis, J. and Blum, S. *J. Am. Ceramic Soc.* **44**(12) (1961).

[163] Barzola-Quiquia, J., Yao, J., Roediger, P., Schindler, K., and Esquinazi, P. *Phys. Stat. Sol. A* **205**(12), 2924 (2008).

[164] Dresselhaus, M. and Dresselhaus, G. *Advances in Physics* **30**(2), 139–326 (1981).

[165] Kent, K., Arnold, F., Yager, B., Nyeki, J., Saunders, J., Howard, C., Kampert, E., and Yager, T. to be published, (2015).

[166] Quantum Design, Inc., 6325 Lusk Boulevard, San Diego, CA 92121-3733, United States - www.qdusa.com.

[167] van der Pauw, L. *Phillips Tech. Rev.* **20**(8), 220–224 (1958-59).

[168] Zhang, Y., Small, J., Pontius, W., and Kim, P. *Appl. Phys. Lett.* **86**(073104) (2005).

[169] Uher, C. and Sander, L. *Phys. Rev. B* **27**(2), 1326–1332 (1983).

[170] Kaburagi, Y., Yoshida, A., and Hishiyama, Y. *J. Mat. Res.* **11**, 769–778 (1996).

[171] Singleton, J. *Band Theory and Electronic Properties of Solids*. Oxford Master Series in Physics, (2001).

[172] Shoenberg, D. *Magnetic Oscillations in Metals*. Cambridge University Press, (2009).

[173] Hubbard, S., Kershaw, T., Usher, A., Savchenko, A., and Shytov, A. *Phys. Rev. B* **83**(035122) (2011).

[174] Brandt, N., Kapustin, G., Kotosonov, V. K. A., and Svistova, E. *Zh. Eksp. Teor. Fiz.* **67**, 1136–1147 (1975).

[175] Kumar, A., Poumirol, J. M., Escoffier, W., Goiran, M., Raquet, B., and Pivin, J. C. *Journal of Physics: Condensed Matter* **22**(436004), 5 (2010).

[176] Onsager, L. *Phil. Mag.* **43**(344), 1006–1008 (1952).

[177] Lifshitz, I. and Kosevich, A. *Sov. Phys. JETP* **2**, 636 (1956).

[178] Dingle, R. *Proc. Roy. Soc. A* **211**(1107), 517–525 (1952).

[179] Soule, D., McClure, J., and Smith, L. *Phys. Rev.* **134**(2A), 453–470 (1964).

[180] Yaguchi, H., Iye, Y., Takamasu, T., and Miura, N. *Physica B* **184**, 332–336 (1993).

[181] Uji, S., Brooks, J., and Iye, Y. *Physica B* , 299–302 (1998).

[182] Nakao, K. *J. Phys. Soc. Jpn.* **40**(3) (1976).

[183] Yoshioka, D. and Fukuyama, H. *J. Phys. Soc. Japan* **50**(3), 725–726 (1981).

[184] Hubbard, J. *Proc. Roy. Soc. A* **243**, 336 (1958).

[185] Singwi, K. S., Tosi, M. P., Land, R. H., and Sjoelander, A. *Phys. Rev.* **176**(2), 589–599 (1968).

[186] Young, A., Sanchez-Yamagishi, J., Hunt, B., Choi, S., Watanabe, K., Taniguchi, T., Ashoori, R., and Jarillo-Herrero, P. *Nature* **505**, 528 (2014).

[187] Balents, L. and Fisher, M. *Phys. Rev. Lett.* **76**(15), 2782 (1996).

[188] Cho, S., Balents, L., and Fisher, M. *Phys. Rev. B* **56**(24), 15814 (1997).

[189] Yanson, I. K., Kulik, I. O., and Batrak, A. G. *J. Low Temp. Phys.* **42**(5-6), 527–556 (1981).

[190] Jansen, A. G. M., van Gelder, A. P., and Wyder, P. *J. Phys. C: Solid St. Phys.* **13**, 6073–6118 (1980).

[191] Lee, W.-C., Park, W., Arham, H., Greene, L., and Phillips, P. *ArXiv* **cond-mat.str-el**(1405.6357v2) (2014).

[192] Sato, H., Sakamoto, I., Yonemitsu, K., and Hishiyama, Y. *J. Phys. Soc. Japan* **57**(7), 2456–2460 (1988).

[193] Arnold, F., Yager, B., Kamper, E., Putzke, C., Nyeki, J., and Saunders, J. *Rev. Sci. Instr.* **84**, 113901 (2013).

[194] Baranger, H. U., MacDonald, A. H., and Leavens, C. R. *Phys. Rev. B* **31**(10), 6197–6206 (1985).

[195] Harrison, W. *Phys. Rev.* **116**(3), 555–561 (1959).

[196] Segall, B. *Phys. Rev.* **131**(1), 121–122 (1963).

[197] Sato, H., Yonemitsu, K., and Bass, J. *Phys. Rev. B* **35 Rap. Com.**(5), 2484–2486 (1987).

[198] Li, G., Luican, A., and Andrei, E. *Phys. Rev. Lett.* **102**(176804) (2009).

[199] Vitali, L., Schneider, M. A., Kern, K., Wirtz, L., and Rubio, A. *Phys. Rev B* **69**(R), 121414 (2004).

[200] Blonder, G. E., Tinkham, M., and Klapwijk, T. M. *Phys. Rev. B* **25**, 4515 (1982).

[201] Jr., D. D. *Phys. Rev. Lett.* **6**(7), 346–348 (1961).

[202] Meservey, R. and Jr., D. D. *Phys. Rev.* **135**(1A), A24–A33 (1964).

[203] Andreev, A. *Sov. Phys. JETP* **19**(5), 1228–1231 (1964).

[204] Cohen, R. and Abeles, B. *Phys. Rev.* **168**(2), 444–450 (1968).

[205] Black, C., Ralph, D., and Tinkham, M. *Phys. Rev. Lett.* **76**(4), 688–691 (1996).

[206] Court, N., Ferguson, A., and Clark, R. *Supercond. Sci. Technol.* **21**(015013) (2008).

[207] Scheike, T., Boehlmann, W., Esquinazi, P., Barzola-Quiquia, J., Ballestar, A., and Setzer, A. *Adv. Mat.* **24**(43), 5826–5831 (2012).

[208] Barzola-Quiquia, A. B. J., Scheike, T., and Esquinazi, P. *New J. Phys.* **15**(023024) (2013).

[209] Esquinazi, P., Heikkila, T., Lysogorskiy, Y., Tayurskii, D., and Volovik, G. *ArXiv* **cond-mat:super-con**(1407.2060v3) (2014).

[210] Fujita, M., Wakabayashi, M., Nakada, K., and Kusakabe, K. *J. Phys. Soc. Jpn.* **65**(7), 1920–1923 (1996).

[211] Kopnin, N., Heikkilae, T., and Volovik, G. *Phys. Rev. B* **83**(220503(R)) (2011).

[212] Latyshev, Y. I., Orlov, A. P., Vignolles, D., Escoffier, W., and Monceau, P. *Physica B* **407**, 1885–1888 (2012).

[213] Hysol is a two component epoxy produced by the Henkel AG und Co.KGaA, Henkelstrasse 67, 40589 Duesseldorf, Germany - www.henkel.com.

[214] Yager, B. *A Pulsed NMR Study of ^{3}He Absorbed on Bare and ^{4}He Preplated MCM-41 Using DC-SQUID Detection, PhD Thesis.* RHUL, (2010).

[215] Hechtfischer, D. *Cryogenics* **27**(9), 503–504 (1987).

[216] NbTi wire has been sourced from Supercon Inc. 830 Boston Turnpike Shrewsbury, MA 01545, United States - www.supercon-wire.com.

[217] Wiegers, S., Rook, J., den Ouden, A., Perenboom, J., and Maan, J. *IEEE Trans. Appl. Supercon.* **22**(3), 4301504 (2012).

[218] Miller, J. *IEEE Trans. Appl. Supercon.* **13**(2), 1385–1390 (2003).

[219] Bird, M., Bole, S., Eyssa, Y., Gao, B.-J., and Schneider-Muntau, H.-J. *IEEE Trans. Mag.* **32**(4), 2542–2545 (1996).

[220] Jaime, M., Lacerda, A., Takano, Y., and Boebinger, G. *J. Phys. Conf. Ser.* **51**, 643–646 (2006).

[221] Zylon is a polymer fibre produced by Toyobo Co.,Ltd. Japan - www.toyobo-global.com/seihin/kc/pbo/.

[222] Herrmannsdoerfer, T., Krug, H., Pobell, F., Zherlitsyn, S., Eschrig, H., Freudenberger, J., Mueller, K., and Schultz, L. *J. Low Temp. Phys.* **133**(1/2), 41–59 (2003).

[223] Zherlitsyn, S., Herrmannsdoerfer, T., Wustmann, B., and Wosnitza, J. *IEEE Trans. Appl. Supercon.* **20**(3), 672–675 (2010).

[224] Product of Yokogawa Electric Corporation, 9-32, Nakacho 2-chome, Musashino-shi, Tokyo 180-8750, Japan - www.yokogawa.com.

[225] Leo, V. *Rev. Sci. Instr.* **52**, 997–1000 (1982).

[226] Heil, J., Wilde, Y. D., Jansen, A. M., Wyder, P., and Grill, W. *Rev. Sci. Instr.* **64**, 1347 (1993).

[227] Park, W. K. and Greene, L. H. *Rev. Sci. Instr.* **77**, 023905 (2006).

[228] 9T Magnet-Cryostat platform produced by Quantum Design Inc., 6325 Lusk Boulevard, San Diego, California 92121-3733, United States - www.qdusa.com.

[229] AttoCube Systems AG, Koeniginstrasse 11a, 80539 Muenchen, Germany - www.attocube.com.

[230] For INA103 instrumentation amplifier data sheets see: www.farnell.com/datasheets/1762589.pdf, or manufactures page: Texas Instruments Incorporated, 12500 TI Boulevard, Dallas, Texas 75243 USA - www.ti.com.

[231] Kelsey, G. *J. Electrochem. Soc.* **124**, 814–819 (1977).

[232] Ju, B.-F., Chen, Y.-L., Fu, M., Chen, Y., and Yuang, Y. *Sensors Actuators A Phys.* **155**, 136–144 (2009).

[233] Orlov, A. P., Latyshev, Y. I., Vignolles, D., and Monceau, P. *JETP Letters* **87**(8), 433–436 (2008).